DEVELOPMENT OF MILLI-KELVIN ADR TECHNOLOGY FOR SPACE MISSIONS

SHANE AKBAR WEATHERSTONE

MULLARD SPACE SCIENCE LABORATORY

DEPARTMENT OF SPACE AND CLIMATE PHYSICS

UNIVERSITY COLLEGE LONDON

A THESIS SUBMITTED TO UNIVERSITY COLLEGE LONDON (UCL)

FOR THE DEGREE OF DOCTOR OF PHILOSOPHY

JANUARY 2012

DECLARATION

I, Shane Akbar Weatherstone, hereby confirm that the work presented in this thesis is my own. Where information has been derived from other sources, I confirm that this has been indicated in the thesis.

ABSTRACT

Cryogenics is increasingly required for space applications as new detector technologies emerge offering improved performance, as is exemplified by future X-ray astronomy missions.

The IXO[1] (International X-ray Observatory) mission will carry an X-ray Microcalorimeter Spectrometer (XMS), requiring a 50mK operating temperature. Two space-demonstrated technologies are capable of maintaining milli--Kelvin temperatures: Adiabatic Demagnetisation Refrigerators (ADRs) and open-cycle Dilution refrigerators. ADRs are simpler, more reliable, and have a longer lifetime than open-cycle dilution refrigerators which deplete their Helium stores after ~3 years. For long-life (>5 year) missions, ADRs are the best practical choice.

MSSL have built an engineering model ADR for the XEUS (X-ray Evolving Universe Spectroscopy) mission. However, the ADR cannot achieve the required hold time and recycle time. This thesis shows how a magnetoresistive heat switch can improve performance such that the required hold time can be achieved.

Tungsten Magnetoresistive heat switch technology is developed through experimental investigation. Heat switch performance is found to be a function of purity; the difference between an otherwise identical 99.992% and a 99.999% pure sample is very significant, with switching ratios of 437 and 1×10^4 respectively at ~4K. The 'on' state thermal

[1] NOTE: During the writing of this thesis, the IXO mission ceased to be a candidate of the L-class missions under consideration by ESA. However, due to the strong science case of IXO; ESA, Astrium and the scientific community are investigating to what extent a European-led mission could preserve the original science goals of IXO. This new study is ATHENA (Advanced Telescope for High ENergy Astrophysics).

conductivity is limited by sample size as it is reduced to the electron mean free path and below. A Tungsten magnetoresistive heat switch mounted in the XEUS ADR via bolted joints lined with 0.13mm thick Indium foil can improve its performance to meet the design requirements.

MSSL are developing an ADR targeting the IXO XMS. The cooling chain required to support the ADR is presented. The design feasibility and compliance to requirements are verified by thermal and mechanical analyses, and it is shown that the ADR can be supported during holding and recycling for both warm and cold redundancy modes of higher temperature stage coolers in the chain.

CONTENTS

LIST OF FIGURES

LIST OF TABLES

LIST OF ABBREVIATIONS

ACS	Advanced Camera for Surveys
ADR	Adiabatic Demagnetisation Refrigerator
AFRL	Air Force Research Laboratories
AGN	Active Galactic Nuclei
AIV	Assembly, Integration and Verification
CAD	Computer Aided Design
CADR	Continuous Adiabatic Demagnetisation Refrigerator
CCD	Charge Coupled Device
CEA-SBT	Commissariat à l'Énergie Atomique - Service des Basses Températures
CFRP	Carbon Fiber Reinforced Polymer
CMB	Cosmic Microwave Background
CMN	Cerous Magnesium Nitrate
COBE	COsmic Background Explorer
COP	Coefficient of Performance
CPA	Chromic Potassium Alum
CVV	Cryostat Vacuum Vessel
dADR	double Adiabatic Demagnetisation Refrigerator
DGG	Dysprosium Gallium Garnet
DIRBE	Diffuse InfraRed Background Experiment
DMB	Direct Microwave Radiometer
EADS	European Aeronautic Defence and Space Company N.V.
EM	Engineering Model
ESA	European Space Agency
FAA	Ferric Ammonium Alum
FDM	Frequency Domain Multiplexing

FEE	Front End Electronics
FIRAS	Far InfraRed Absolute Spectrometer
G10CR	Cryogenic grade G10
GDMS	Glow Discharge Mass Spectrometry
GGG	Gadolinium Gallium Garnet
GM	Gifford McMahon
GSFC	Goddard Space Flight Center
GTO	Geostationary Transfer Orbit
HFI	High Frequency Instrument
HSC	Hybrid Sorption Cooler
HST	Hubble Space Telescope
HTRS	High Time Resolution Spectrometer
HXI	Hard X-ray Imager
ICM	Intra-Cluster Medium
INAF	Istituto Nazionale di AstroFisica (National Institute For Astrophysics)
IRAS	InfraRed Astronomy Satellite
ISAMS	Improved Stratospheric and Mesospheric Sounder
ISAS	Institute of Space and Astronautical Science
ISDC	INTEGRAL Science Data Centre
IXO	International X-ray Observatory
JAXA	Japan Aerospace eXploration Agency
JT	Joule Thomson
MIP	Moveable Instrument Platform
MLI	Multi Layer Insulation
MR	MagnetoResistive
MRI	Magnetic Resonance Imaging
MSSL	Mullard Space Science Laboratory

NASA	National Aeronautics and Space Administration
NFI2	Narrow Field Instrument, configuration 2
NGST	Next Generation Space Telescope
NIST	National Institute of Standards and Technology
OPTC	Orifice Pulse Tube Cooler
RAL	Rutherford Appleton Laboratory
ROSAT	Roentgen Satellite
RRR	Residual Resistance/Resistivity Ratio
SMBH	Super Massive Black Hole
SPICA	SPace Infrared telescope for Cosmology and Astrophysics
SQUID	Superconducting Quantum Interference Device
SRON	Stichting RuimteOnderzoek Nederland (Space Research Organization Netherlands)
STJ	Superconducting Tunnel Junction
SXS	Soft X-ray Spectrometer
TBD	To Be Determined
TDM	Time Domain Multiplexing
TES	Transition Edge Sensor
TLA	Thermal Link Assembly
TRL	Technology Readiness Level
TRP	Technology Research Programme
WFI	Wide Field Imager
XEUS	X-ray Evolving Universe Spectroscopy
XGS	X-Ray Grating Spectrometer
XMM	X-ray Multi-Mirror mission
XMS	X-ray Microcalorimeter Spectrometer
XPOL	X-ray POLarimeter
XRS	X-Ray Spectrometer

ACKNOWLEDGEMENTS

I would like to thank my supervisor, Dr Ian Hepburn, for his encouraging guidance, support and work throughout my research studies. I would also like to thank my second supervisor, Professor Graziella Branduardi-Raymont for her useful advice given in the supervisory panel meetings.

I would like to extend my thanks to Graham Hardy and Dr Jo Bartlett for sharing their extremely useful experience in running cryogenics experiments in the lab, and for the work they have done that has contributed to the foundations of some of the work presented in this thesis, as well as their assistance in the lab.

I am grateful to the MSSL Mechanical Engineering Workshop staff for their efficiency and quality in producing the test fixtures used during the Tungsten thermal conductivity investigations detailed in chapter 5.

My thanks go to Dr Jaime Reed, my industrial supervisor based at Astrium Stevenage, for his useful guidance, assistance and work during my time working on the IXO cooling chain detailed in chapter 6. I would also like to thank the IXO team at Astrium Stevenage for their cooperation and assistance.

On a personal note, I am extremely grateful to my parents, Scott and Tracey, for their ongoing support and for all they have done to provide me with the opportunities that have allowed me to aspire to achieve a Doctorate degree in a field of my interest.

I could not have completed this work without the ongoing support and love of my fiancée, Tejal, and to her I am extremely and eternally thankful.

OVERVIEW OF THESIS

This thesis presents developmental research on magnetoresistive heat switch technology for millikelvin space ADRs, in addition to development in the (cryogen-free) cooling chain technology that could support millikelvin ADRs onboard a long-life (>5 year) space mission. The context of technology development is focussed on the IXO (International X-ray Observatory) mission; however, the developments may be extended to wider applications in the field of space cryogenics.

The opening chapter provides a brief overview of X-ray astronomy, including its history, the processes that generate X-rays in space and some of the key past missions. The improvement in various observational properties over time, such as sensitivity, energy resolution and effective area are highlighted, leading on to an introduction to the IXO mission. The instrument payload is overviewed at top level, and the X-ray Microcalorimeter Spectrometer (XMS) is highlighted as an instrument that offers extensive improvement in spectroscopic observations, and is essential for the study of most of the IXO science goals. Some XMS science goals are discussed with examples of how the XMS might achieve them provided. The operational principles of the technology behind the XMS, Transition Edge Sensors, are described, and the need for the XMS to be cryogenically cooled to ~50mK is identified.

The second chapter introduces space cryogenics as the discipline of providing stable cryogenic temperature environments for space missions, in particular for detectors such as the IXO XMS. The thermal environment of a spacecraft at L2 such as IXO is described and the requirement for cryogenic cooling techniques highlighted. Further considerations for space cryogenics are described, including launch vibration

environments by example of the Ariane-5 launcher. Various cryogenic techniques are discussed; including common cryogen-based cooling methods, leading on to cryogen-free technologies such as Stirling coolers, Pulse tube coolers and passive radiative coolers. The millikelvin (sub-Kelvin) cryogenic technologies, sorption coolers, dilution refrigerators and Adiabatic demagnetisation Refrigerators (ADRs) are discussed, and it is clear that ADRs are an ideal, space-demonstrated, reliable technology for providing stable millikelvin cryogenic environments.

Chapter 3 then expands on ADRs, initially describing the theoretical principles of the magnetocaloric effect by which they operate. Building on this, the cooling cycle of an ADR is explained, and the key thermodynamic components that allow it to operate are discussed, including the salt pill refrigerants and heat switches. Several types of heat switch technology are discussed in terms of their advantages and limitations, and a new technology, magnetoresistive heat switches are introduced. The MSSL ESA ADR, an engineering model ADR designed for the XEUS (X-ray Evolving Universe Spectroscopy) mission, IXO's predecessor, is discussed. It is shown that magnetoresistive heat switches have the potential to significantly increase the ADR's performance. Finally, ADR solutions under development targeting the IXO XMS are discussed, including the double ADR (dADR) at MSSL. Chapter 3 shows that both the ESA ADR and MSSL dADR can benefit from magnetoresistive heat switch technology.

Chapter 4 introduces the theory of magnetoresistance in metals, beginning with discussion of how heat is transported in metals by both phonons and electrons. The limitations to the thermal conductivity caused by several types of scattering of these heat carriers are highlighted. Electron thermal conductivity is shown to dominate the phonon conductivity by several orders of magnitude in the liquid Helium temperature regime and below. Magnetoresistance is shown to be capable of significantly reducing

the electron component of the thermal conductivity, potentially to the extent that the lattice contribution dominates. Thus, the potential of using a magnetoresistive metal as a heat switch with a high (~10^{4}-10^{5}) switching ratio is indentified. Using established magnetoresistance theory, the criteria for the strongest magnetoresistive effect are defined, and the metals that meet these criteria are highlighted. Of these, Tungsten is shown to be the best choice for practical development for milli-Kelvin ADRs. The form of the magnetoresistive thermal conductivity of Tungsten is then derived based on magnetoresistance theory and published experimental data. This forms a basis for interpreting thermal conductivity measurements of Tungsten in a magnetic field.

Chapter 5 details the development of magnetoresistive heat switch technology by experimental investigations of the thermal conductivity of three samples of Tungsten in the presence and absence of a magnetic field. The results show that purity and crystal width determine the performance as a heat switch, and magnetoresistive effect is found to be strongly dependent upon purity, requiring the highest purity (>99.999%) for the greatest magnetoresistive effect and heat switch performance. A 99.999% pure sample had a measured switching ratio of 10^{4} at ~4K, compared to an otherwise identical 99.992% sample with a measured switching ratio of ~700. It is determined that thermal conductivity in the absence of a magnetic field is primarily limited by the sample crystal width, with smaller widths having detrimental effects as crystal width approaches and decreases below the electron mean free path, which is apparent from the poor performance of a 0.5mm width sample detailed in the published literature. The typical installation of a heat switch in an ADR would be at a pressed contact interface in the form of a bolted joint. The limitations of the thermal conductance due to such an interface are discussed, and it is shown that Indium foil between the interfacing contact points can increase the contact conductance by several orders of magnitude. Thus, it is recommended that this be implemented in any magnetoresistive heat switch

installation. The performance of the ESA ADR is predicted for the case of a magnetoresistive heat switch connecting the upper and lower temperature stages (salt pills) based on the results of the 99.999% pure Tungsten sample combined with Indium foil enhanced mounting interfaces to the ADR, and the results show a significant improvement upon current performance.

Chapter 6 investigates the technology development required to support the MSSL IXO dADR onboard the IXO spacecraft. The cooling chain is discussed, and a cryostat to contain it is designed. The cryostat/cooling chain is analysed in terms of its structural natural modes and thermal performance. The thermal and structural suspension analyses are detailed. The cooling chain requires a radiator which is located outside the cryostat, with a thermal link passing thorough the cryostat body in order to provide cooling to an 80K thermal shield. This requires a specialised feedthrough. Such a feedthrough is investigated and designed based on purely thermal considerations. The complete proposed cryostat and cooling chain design is shown to meet the requirements specified by ESA, and to be able to support the MSSL dADR during both recycling and holding at 50mK, even in the case of a single cooler failure at two redundant higher temperature stages.

Finally, chapter 7 summarises the thesis chapter by chapter, highlighting the main findings of each. To conclude, further work to consider in the field of magnetoresistive heat switch technology development and the development of the IXO cooling chain are highlighted.

Chapter 1:

X-RAY ASTRONOMY

This introductory chapter sets the scene for the motivation driving the research conducted for this thesis. Advancement in the field of Space Cryogenics is required in order to support the requirements of ever more sensitive detector instrumentation on scientific observatory satellites.

This thesis concentrates on technology development for a milli-Kelvin ADR (Adiabatic Demagnetisation Refrigerator) under development at MSSL (Mullard Space Science Laboratory). This ADR is being designed to cool an essential instrument onboard a future X-ray astronomy observatory, IXO (International X-ray Observatory). Hence, a brief introduction to X-ray Astronomy is provided, followed by an introductory description of the IXO mission. The instrument at the heart of the research motivation for this thesis, the XMS (X-ray Microcalorimeter Spectrometer), is highlighted, and an overview of some of the key science goals the XMS aims to achieve is given.

The principles of the operation of the XMS are discussed, and the requirement for a stable, 50mK cryogenically cooled environment is identified.

1.1 INTRODUCTION TO X-RAY ASTRONOMY

1.1.1 INTRODUCTION

The universe, its origins, and the physical laws which govern all that occurs within it have been the subject of ultimate fascination and inquisition throughout human history. The answers to many of the fundamental questions surrounding these topics can be sought within the most extreme environments in the universe. High energy astrophysical phenomena stretch the known laws of physics and events at the extremities of the observable cosmos hold the secrets of the origins of the universe.

High energy phenomena include black holes, neutron stars and supernovae, to name but a few. Accretion of material onto black holes, cooling hot neutron stars and shocks within the intra-cluster medium (ICM) of galaxy clusters all provide astronomical laboratories which can be observed to examine the laws of physics under conditions that are impossible to create on Earth. All of these extreme processes and phenomena share a common attribute; they are X-ray emitting. The most extreme environments in the universe are 'high energy', exhibiting hot (~10^6-10^8K [(1)]), and/or high velocity processes which are strongly luminescent in the X-ray region of the electromagnetic spectrum.

X-ray astronomy is the observational tool for the study of high-energy astrophysics. The X-ray waveband ranges from around 120eV to 120keV, which is sub-divided into two sub-bands based on the penetrative ability of the radiation through matter. This subdivision corresponds to weakly penetrating 'soft' X-rays, which have energies ~120eV – ~10-12keV; and strongly penetrating 'hard' X-rays with energies of ~12keV – 120keV. X-rays cannot penetrate the earth's atmosphere, thus in order to detect X-rays from extraterrestrial sources an observational platform must be placed above (or very high up in) the atmosphere.

1.1.2 X-RAY PROCESSES

The four main processes producing X-rays in space are Bremsstrahlung, synchrotron radiation, Compton scattering and atomic transitions. The first three processes are the result of the acceleration of charged particles emitting X-ray photons.

Bremsstrahlung

Free electrons, for example those present in the hot gas forming the ICM, frequently engage in interactions with other charged particles, typically atomic nuclei, due to their thermal motion. Such a collision causes an electron to rapidly decelerate, with its lost kinetic energy manifested as an X-ray photon emission. This is known as 'Thermal Bremsstrahlung' as the Bremsstrahlung (literally 'Braking radiation' in German) is a result of purely thermal interactions. This enables the temperature of such a gas to be inferred. Bremsstrahlung is not necessarily always a thermal process, and will be observed in any situation where high velocity electrons are decelerated by coulombic interactions, for example electrons colliding with shock fronts of a supernova remnant.

Synchrotron Radiation

Synchrotron radiation occurs where free electrons are in the presence of a magnetic field, where the electrons spiral around magnetic field lines. The resulting circular motion is acceleration, thus photons are emitted with a characteristic gyration frequency which is dependent on the magnetic field strength. Synchrotron radiation will be observed in any situation where there are free electrons interacting with a magnetic field. Many astrophysical phenomena demonstrate such conditions, perhaps the most obvious being neutron stars.

Compton Scattering

Compton scattering, or more strictly inverse Compton scattering, occurs when relatively low energy photons interact with relativistic free electrons. Upon scattering, the

relativistic electron imparts some of its energy to the photon, resulting in the photon emerging with a higher energy. Typically many successive scattering events occur before the photon gains sufficient energy to emerge in the X-ray or even gamma ray regime.

Atomic transitions

Electrons that are bound within in an atom can also cause X-ray emission. This is due to an electron dropping from a higher energy quantum state to a lower one, the energy difference being released as photon emission. X-ray photons are high energy, thus, only certain elements with the capability for electronic transition between sufficiently separated energy states will emit sufficiently energetic photons with X-ray frequencies. Emissions of this type produce peaks in the spectra, known as emission lines. The most common observed X-ray line emissions arise from transitions within Iron and Oxygen atoms. The redshift of known lines allows inference of the speed of the emitting object along our line of sight, and the broadening of spectral emission lines indicates the range of speeds within the observed object itself.

Typically astrophysical objects will demonstrate several of these X-ray emission processes; in an accretion disk surrounding a Black hole or neutron star for example, gaseous material is heated up to millions of degrees as it spirals inwards, as gravitational energy gets converted to kinetic energy. Friction within the accretion disk, along with the compression due to the strong gravitational field adds to the heating process. The hot dense gas emits thermal bremsstrahlung as well as synchrotron radiation, whilst elements within the gas are highly ionised thus generating spectral emission lines. It is clear to see that spectral analysis of such objects is essential to determining what processes are occurring within such extreme environments. Such analysis will indicate which physical processes are occurring and to what degree, the composition and temperature in addition to the speed and ionisation states of parts of the object under

study. This allows a powerful insight into the laws of physics in such intense conditions (see 1.3.1 for some examples).

It is clear that the study of extreme astrophysical phenomena requires detailed X-ray observations. Imaging and, more importantly, spectroscopic analysis of such environments allows rigorous testing of our laws of physics and the underlying astrophysical processes. In addition, the study of such high energy phenomena at high red-shifts provides a glimpse into the early stages of the evolution of the universe.

1.1.3 A Short History of X-Ray Astronomy

The history of X-ray astronomy began fairly recently, in 1949, when the USA Naval research laboratory launched a V-2 sounding rocket carrying an X-ray detecting payload [(2)]. On-board instruments included an X-ray detector housed in the nose-cone. This early, short observation of the order of minutes confirmed that the Sun emits X-ray radiation. From this initial result, the next step was to find X-ray sources outside of our solar system. There had been several failed attempts at this, until in 1962 when a team led by Riccardo Giacconi flew a payload with a detector 50-100 times more sensitive than any previously flown [(2)]. The first stellar X-ray source, Sco X-1, was discovered by this mission on June 12th, 1962. Several subsequent X-ray observations were made using similar rocket-based missions, but it was clear that the future of X-ray astronomy would require a dedicated platform capable of longer duration and wider-angle observations [(2)].

On December 12th, 1970, the first dedicated X-ray observatory satellite, Uhuru, was launched [(2)]. Its detector payload consisted of two simple proportional counters. This new observation platform allowed observations to last for years instead of mere minutes. Uhuru had the capability to survey the whole X-ray sky in three months. Uhuru led to the discovery and understanding of X-ray binary systems, and allowed the

properties of neutron stars to be studied, including their mass, radii and equation of state.

It was realised as early as 1959 (2) that in order to practically improve sensitivity further than the performance limits of the Uhuru -type instruments, a method of focussing X-rays from a large collecting area onto a small detector would be required. This design has the added advantage that high angular resolution can be achieved without the need for scanning motions. In order to achieve such focussing, reflective X-ray grazing-incidence optics had to be developed, since X-rays do not reflect on normal incidence. Grazing incidence optics had been first proposed by Hans Wolter in the context of microscopes, but practical limitations due to the tiny scales involved meant they would be impossible to construct. The scale of an X-ray astronomy telescope was much larger, metres as opposed microns, and this gave Giacconi the faith that it could be feasible to build a telescope based on the Wolter arrangement (2). The technology development required for the optics was not at a sufficient level to image weak signals from stellar X-ray sources until 1979, when the Einstein mission was the first mission to use an X-ray telescope capable of fully imaging its target sources. The Einstein mission also provided the first high resolution spectroscopy of supernova remnants [(3)].

The Einstein observatory was superseded by the Roentgen Satellite (ROSAT) in 1990, and then Chandra launched in July 1999. In Europe, ESA had developed XMM-Newton, launched in December 1999. The most recent addition to these contemporary X-ray observatories is the Japanese mission Suzaku, which launched in 2005 and demonstrated the first microcalorimeter X-ray spectrometer launched in space. For a detailed history of previous X-ray missions, see Bradt et al. (4) and Giacconi (2). The sensitivity of several previous X-ray Astronomy missions from 1970 - 2000 are

summarised in Figure 1, which shows how the sensitivity increased with time and observations of more phenomena became possible.

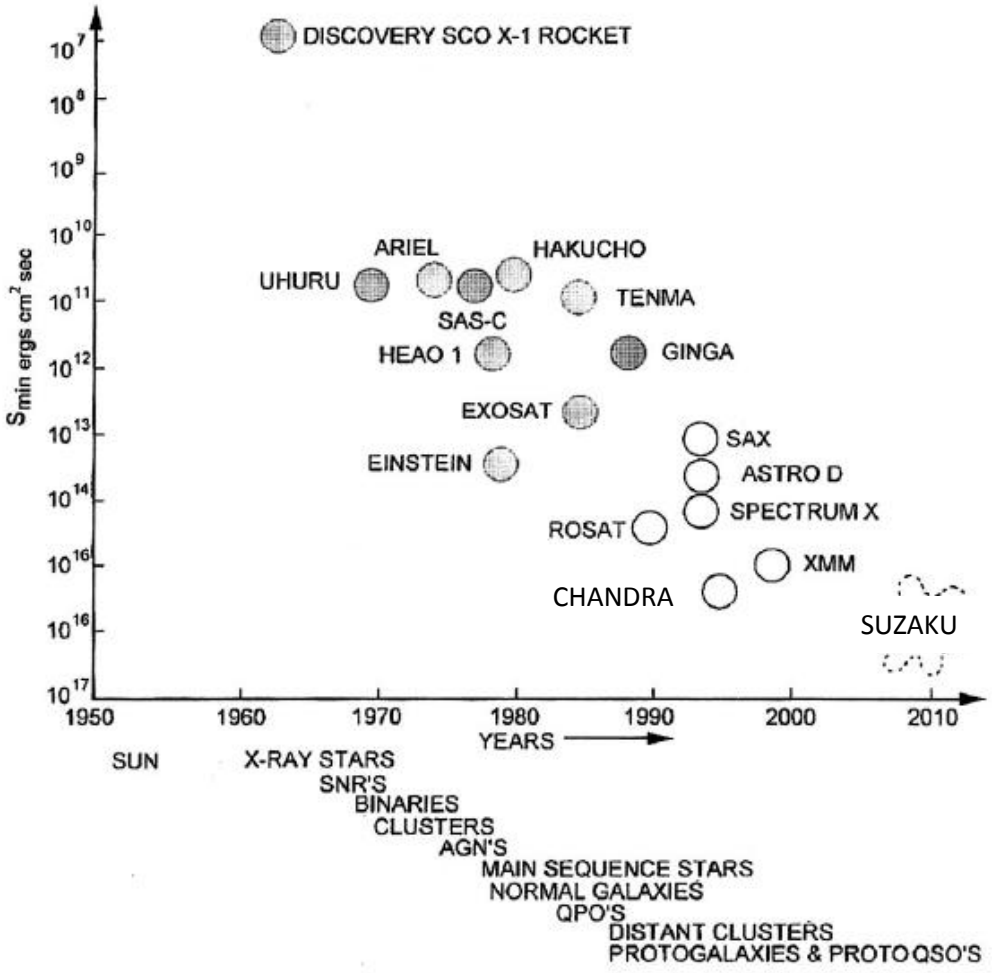

Figure 1: The sensitivity (In ergs, where 1 erg = 10^{-7} J = 6.24×10^{11} eV) achieved with various previous X-ray missions. Since the original publication of this figure [(2)] (2000) the question mark has been replaced by Suzaku launched in 2005, and AXAF was renamed Chandra. Adapted from (2).

A summary of current X-ray missions is provided in Table 1. It should be noted that 'Constellation-X' is the NASA mission concept which became superseded by the International X-ray Observatory IXO mission.

Comparison of Various X-ray Observatories																	
Observatory	XMM			Chandra					Suzaku		Constellation X		ASCA		ROSAT		RXTE
Detector	EPIC MOS	EPIC PN	RGS	ACIS back	ACIS front	HRC	HETG	LETG	XRS	XIS	Calori-meter	Grating	SIS	GIS	PSPC	HRI	PCA
Energy Range (keV)	0.2-12	0.2-12	0.4-2.5	0.1-10	0.4-10	0.1-10	0.6-10	0.1-6	0.3-12	0.2-12	0.2-10	0.2-2	0.4-12	0.6-12	0.1-2.4	0.1-2.4	2-60
Effective Area (cm^2)																	
@0.25 keV	133	460	-	30	-	150	-	25	-	-	3081	1235	-	-	240	40	-
@0.4 keV	360	771	44	120	35	50	-	12	-	-	864	2000	15	-	7	11	-
@0.6 keV	591	1061	94	345	70	65	-	25			5127	3720	35	-	70	8	-
@1.0 keV	922	1227	185	615	385	215	10	55	100	1600	11274	5327	230	50	210	80	-
@1.5 keV	1180	1304	160	500	525	162	45	105			13362	4100	300	145	180	60	-
@2.5 keV	696	779	-	320	320	65	20	50			7765	-	195	125	-	-	700
@6.0 keV	768	851	-	205	235	45	25	20	150	1000	6600	-	160	125	-	-	5000
@8.0 keV	390	557	-	45	60	10	7	4			4277	-	55	60	-	-	6000
@12.0 keV	19	56	-	-	-	-	-	-			638	-	-	-	-	-	4000
Energy Resolution (eV)																	
@0.25 keV	35	35	-	130	37	-	-	0.4	-	-	2	0.25	-	-	250	-	-
@0.4 keV	45	45	0.5	120	42	-	-	0.8	6.5	30	2	0.65	75	-	350	-	-
@1.0 keV	55	55	2.9	100	56	-	1.0	5.4	6.5	50	2	4.1	100	190	500	-	-
@2.5 keV	85	85	17	120	82	-	5.2	34	6.5	80	2	-	135	300	-	-	725
@6.0 keV	130	130	-	170	130	-	29	-	6.5	120	2	-	240	460	-	-	1125
@8.0 keV	150	150	-	190	150	-	50	-	6.5	140	2	-	265	540	-	-	1300
Angular Resolution (FWHM)	~6"	~6"	-	1"	1"	<0.5"	-	-	limited	<1.5'	6"	-	1'	1'	15"	5"	1 deg
Field of View	30'	30'	-	17'x17'	17'x17'	31'x31'	-	-	3'x3'	19'x19'	2.5'	-	22'x22'	20'x20'	114' dia	20'x20'	1 deg

Table 1: Table of contemporary and future X-ray missions. After (5).

The future of X-ray astronomy lies in missions such as the future International X-Ray Observatory (IXO) mission, which offers extensive improvements in sensitivity, spectral resolving power and effective area over previous missions, thus allowing for an unprecedented depth of observation. IXO is the mission on which this thesis bases its technology development, and is the focus of the next section.

1.2 IXO - INTERNATIONAL X-RAY OBSERVATORY

1.2.1 MISSION OVERVIEW

The international X-ray Observatory is a joint NASA (National Aeronautics and Space Administration), ESA (European Space Agency) and JAXA (Japan Aerospace eXploration Agency) mission based on the combined former ESA XEUS (X-ray Evolving Universe Spectroscopy) and NASA Constellation-X mission concepts. IXO will target high redshift Active Galactic Nuclei (AGN), clusters of galaxies and massive compact objects such as Neutron stars and Black holes; in order to study [(6), (7)]:

- Black holes and matter under extreme conditions
- Formation and evolution of galaxies, clusters and large scale structure
- Life cycles of matter and energy

IXO will operate from a halo orbit located at the Earth-Sun Lagrangian point L2, and will be launched on an either an Ariane-5 or an Atlas V 551.

The focal length is required to be long, at 20m, in order to accommodate the expansive collection area of the 3.3m diameter X-ray mirror telescope apparatus [(6)]. IXO will have a much larger effective collection area than any previous X-ray mission, as indicated by comparing the Constellation-X effective area to the current missions in Table 1. Figure 2 below shows how some of the key IXO performance criteria compared to the current leading X-ray observatory missions, XMM-Newton and Chandra [(7)].

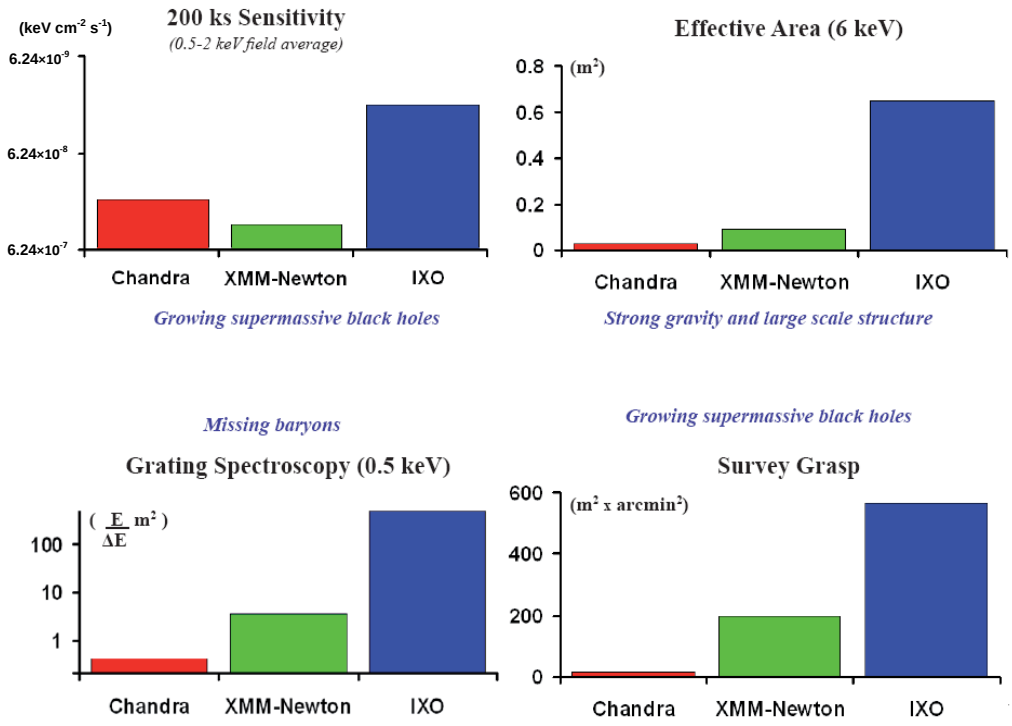

Figure 2: Comparison of key performance parameters between IXO and the contemporary leading missions. After (7).

IXO will have a deployable optical bench which will house the latest technology in grazing-incidence optics, based on either silicon pore technology (under development at ESA) or segmented glass (under development at NASA), and providing a $3m^2$ collecting area [7]. The optics will be arranged in a conical approximation to the Wolter I geometry [6],[7]. Incident X-rays will be focussed to a single point at the focal length of 20m, where the movable instrument platform (MIP) will align interchangeable detector instruments for data collection.

1.2.2 Instrument Overview

The MIP will contain a payload consisting of 5 X-ray analysing instruments, which operate in parallel with a fixed X-ray Grating Spectrometer (XGS). The details of the instruments are beyond the scope of this thesis; however, full details may be found in the IXO Assessment Study Report (7) and IXO Payload Definition Document (8). A brief summary of each instrument is given subsequently for completeness.

X-ray grating spectrometer (XGS)

The XGS instrument consists of a set of diffraction gratings at a fixed position between the X-ray mirror optics and the MIP. Fixed at the focal point of the gratings is a CCD (Charge Coupled Device) based camera which records the diffraction spectra. The XGS is designed such that it can provide continuous spectroscopy in the 0.3 keV – 1.0 keV waveband, without affecting instruments in the focal plane (i.e. the MIP). There are two concepts being considered for the XGS, as detailed in the IXO assessment study report (7).

Wide Field Imager (WFI)

The WFI comprises a silicon active pixel sensor with an energy resolution of 70eV at 1KeV. It has a large field of view, 18' × 18', and provides imaging in the 0.1 – 15keV energy band whilst simultaneously counting photons and providing spectral and timing data.

Hard X-ray Imager (HXI)

The HXI is mechanically coupled to the WFI, located directly beneath the WFI and sharing the same optical axis. The HXI extends the WFI imaging capabilities across the hard X-ray band up to around 40eV. The HXI consists of 3 confocal layers, two Silicon (Si) and one Cadmium Telluride (CdTe), providing a field of view of 12' × 12', and an energy resolution of better than 1 keV at 40keV.

The WFI and HXI are intended to be operated simultaneously in order to maximise observation efficiency, which is shown in Figure 3 for the WFI, HXI and combined operation of both instruments.

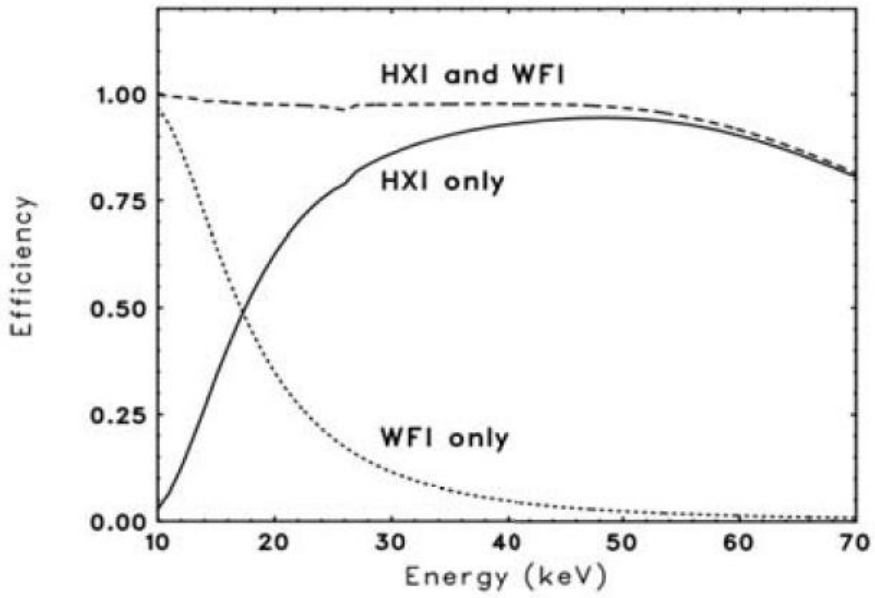

Figure 3: Observational efficiency with HXI and WFI instruments. After (7).

High time resolution spectrometer (HTRS)

The HTRS is a non imaging instrument designed to target matter under extreme conditions, where time-resolved spectroscopy and high count rates may be required. HTRS works in the 0.3-10keV energy band, and provides a spectral resolution of 150eV at 6keV. It provides a time resolution of 10μs with the capability of taking up to 2 million counts per second.

X-ray polarimeter (X-POL)

Polarisation measurements may be used to deduce the spin of a black hole or AGN [(7)]. The X-POL instrument enables the polarisation of X-rays to be determined in the waveband 2 keV – 10keV, alongside providing imaging (~5 arcsec resolution), spectroscopy (with energy resolution ~1.2 keV at 6 keV), and time resolution data (at the μs level).

X-ray microcalorimeter spectrometer (XMS)

The instrument of focus for the technology development detailed in this thesis is the XMS. The XMS is a Transition Edge Sensor (TES) microcalorimeter array with field of view

of 40”. It boasts an unprecedented energy resolution of <2.5 eV in the energy range 0.2 keV – 10 keV. This performance is impossible to achieve with current CCD based spectrometer technology. In order to achieve such impressive energy resolutions, the XMS must be operated at a temperature of around 30-50mK. The XMS is discussed in further detail subsequently in 1.3.

1.3 XMS – X-RAY MICROCALORIMETER SPECTROMETER

The resolution of the IXO XMS is unprecedented, <2.5 eV in the energy range 0.2 keV – 10 keV. An example of how this spectral resolving power compares to previous X-ray missions is shown by the simulated XMS spectra illustrated in Figure 4 below:

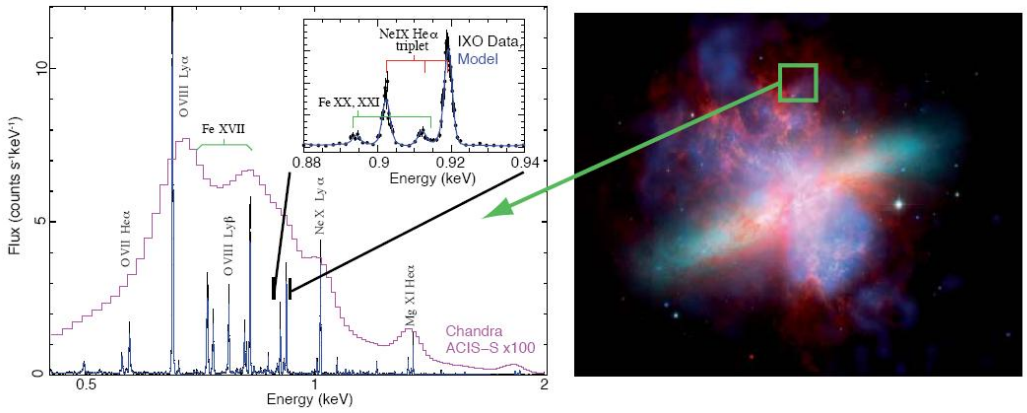

Figure 4: Left: IXO high-resolution X-ray spectra (blue) show the metal-enriched hot gas outflowing from starburst galaxy Messier 82, a part of the feedback process unresolvable with current X-ray CCD data (magenta). The insert shows that the He-like emission line triplet of NeIX can be resolved, and that not only velocities can be measured, but the plasma temperature and ionisation state can be diagnosed. Right: Superwinds in Messier 82, exhibiting a starburst-driven superwind. Diffuse thermal X-ray emission as seen by Chandra is shown in blue. HydroCarbon emission at 8μm from NASAs Spitzer telescope is shown in red. Optical starlight (cyan) and Hα+[NII] (yellow) are from HST-ACS (Advanced Camera for Surveys on the Hubble Space Telescope) observations. Figure and caption after (7).

As can be seen from Figure 4, the XMS provides a vastly superior power of resolution over current CCD X-ray spectrometer technology, thus allowing for the deeper observations required to achieve the IXO mission science goals.

The XMS instrument is the motivation behind the work published in this thesis, as it is the cutting edge technology of X-ray Astronomy instruments, and requires a cryogenic temperature environment of 30-50mK (see chapter 2 for cryogenics definition). Hence, the science reasons for requiring this instrument are briefly described in order to provide a 'big picture' view of the research justification for the work contained in this thesis. Following the science goals, the general principles of TES based technology and the XMS instrument itself are described.

1.3.1 IXO XMS Science Goals

A brief description of the XMS science goals is provided here. However, it must be noted that full details are beyond the scope of this thesis, which is in the field of space cryogenics. A general overview of IXO science goals is presented in Table 2.

THEME/QUESTION	WHAT IXO WILL DO	INSTRUMENT
CO-EVOLUTION OF GALAXIES AND THEIR SUPERMASSIVE BLACK HOLES (SMBH)		
The first SMBH	Find young growing massive black holes at the dawn of the Universe (z~6-10), by conducting multi-tiered surveys, in conjunction with observations at longer wavelengths. To test the growth mode of SMBH by measuring their spin.	WFI
Obscured growth of SMBH	Find and charectarise SMBH growing in an obscured phase at z~1-3, including Compton-thick AGN, and measure their energetics.	WFI, HXI, XMS
Cosmic feedback from SMBH	Measure feedback from growing SMBH in galaxies, groups and clusters, by relating AGN activity to star formation at high-z, and measure gas motions in galaxies and clusters induced by AGN .	XMS, WFI
LARGE-SCALE STRUCTURE AND THE CREATION OF CHEMICAL ELEMENTS		
Missing baryons and the Intergalactic Medium	Find the remaining missing baryons in the current Universe, likely in a Warm-Hot Intergalactic Medium phase, by detecting hundreds of intervening absorption systems towards bright background targets.	XGS, XMS
Cluster Physics and Evolution	Find out how gas dynamically evolves in the cluster dark matter potentials, by measuring gas motions and turbulence. Determine the physical processes behind the production of cosmic rays in clusters. Also find when and how the excess entropy was generated in clusters by studying their precursors at early epochs.	XMS, HXI
Galaxy cluster cosmology	Provide an independent measurement of Dark Energy density and its equation of state by counting clusters at various epochs and measuring their gas fraction.	WFI
Chemical evolution along cosmic time	Measure chemical abundances of the various families of elements in intracluster gas, find at which epoch they were dispersed and derive what is the main production mechanism .	XMS
MATTER UNDER EXTREME CONDITIONS		
Strong gravity and accretion physics	Measure black hole spin of stellar and supermassive black holes via time-averaged spectroscopy, reverberation mapping, timing and polarimetry; probe Genaral Relativity in the strong field regime by mapping the emission of the innermost regions of accretion disks; measure the kinetic energy of outflows produced by matter falling onto black holes.	WFI, HXI, HTRS, XPOL, XMS
Neutron Star Equation of State	Measure Mass and Radius of tens of neutron stars via a number of timing and spectroscopic techniques, and constrain the equation of state at supra-nuclear density. Detect vacuum polarisation effects in highly magnetised neutron stars.	HTRS, XMS, XPOL
LIFE CYCLES OF MATTER AND ENERGY IN THE UNIVERSE (Additional Science Goals)		
Supernovae : explosion mechanisms	Probe the supernova explosion material and its environment, by measuring temperatures, velocities, turbulences in Supernova Remnants.	XMS
Supernovae : nucleosynthesis	Measure nucleosynthesis products for the various types/subtypes of Supernovae, by detecting weak emission lines from radioactive elements in Supernova Remnants.	XMS, HXI
Cosmic ray acceleration in Supernova Remnants	Measure hard X-ray synchrotron emission due to fluctuating magnetic fields.	WFI, HXI, XPOL
Characterising the Interstellar Medium in the Galaxy	Determine the aggregation state of elements in the Inter-stellar Medium in the Galaxy (solid state, molecular, atomic, etc), by precise measurements of the edge energy of bound-free transitions .	XGS
Galactic Centre	Study the energetics and geomtery of the various components around Sgr A*.	WFI, XPOL
Accretion in Young Stellar Objects	Characterise the geometry of accretion disks in Young Stellar Objects, via time resolved high-resolution spectroscopy.	XGS
The atmospheres of Solar System planets	Study particle populations and their acceleration mechanisms occurring in the outer layers of the atmospheres of these planets and show their link to solar activity.	XMS

Table 2: IXO Science goals. After (7).

From Table 2, it can be seen that the XMS is required to satisfy more of the science goal themes than any other single instrument. This is due to the extremely high spectral resolving power offered by the instrument, which is essential for investigating most of the key themes of interest to the mission. The key science goals that require the XMS are described in brief subsequently; however, further details may be found in the IXO Assessment Study Report (7).

1.3.1.1 CO-EVOLUTION OF GALAXIES AND THEIR SUPER MASSIVE BLACK HOLES (SMBH)

Obscured Growth of SMBH

SMBHs (Super Massive Black Holes), typically found at the centre of a galaxy, and theorised to be related to the formation of the galaxy in which it resides. Theories suggest a significant proportion of SMBH growth in massive galaxies occurs when the SMBH is heavily obscured during a period of intense star formation [(7)]. Observations suggest that relatively unobscured and heavily obscured AGN are actually different phases which occur after a galaxy merger event, with the majority of the SMBH growth occurring in the obscured phase [(7)].

AGN X-ray emission spectra are obscured most in 'Compton thick' AGN, where the column density[2] of absorbing matter exceeds the inverse of the Thomson cross section, $\sigma_T^{-1} \cong 1.5 \times 10^{24}\text{cm}^{-2}$ [(9)]. It is thought that Compton thick AGN may represent a key phase in the co-evolution of a SMBH and its host galaxy, and these AGNs harbour a significant proportion of SMBHs. Observations of such Compton thick AGN at red-shifts of z ~1-3, where in the cosmic history star formation and mass accretion had peak activity, are essential to understand the SMBH-host galaxy co-evolution process [(7)]. Currently the presence of these AGN is determined by infrared observations, and the presence of an AGN can only inferred by a signature of X-ray emission at the highest energies. However, there is a large uncertainty in these observations and any further information about the AGN cannot be gained. Astro-H will be able to realise some of these AGN, but for the highest column densities (hence highest obscuration), the AGN will only be visible due to observable scattered X-rays. The IXO XMS will be able to reveal the presence of the Iron K emission line, which is a signature of a Compton reflection dominated source, and provide definitive evidence of an AGN. This, combined

[2] Number per unit area along the observer line of sight

with IXO XGS data, will help to reveal how much of the SMBH growth occurs in obscured objects [(7)].

Cosmic feedback from SMBH

IXO observations with the XMS will enable the investigation of whether and how SMBHs influence the stellar formation within distant galaxies. Two possible forms of interaction between the energy emitted by a growing, accreting black hole and the matter of the galaxy are postulated to exist: Mechanical and Radiative [(7)].

The mechanical type occurs most when a black hole is accreting below the Eddington limit[3], and significant proportions of the black hole energy output exits in the form of winds or jets. In this case, for a galaxy of mostly gas with embedded dust, the gas would be mechanically heated and accelerated to high speeds by ram pressure. For a gas of initially moderate temperature, this interaction would result in shock heating of the gas, making it so hot that it is only observable in X-rays [(7)].

The radiative type occurs most when a black hole is accreting close to its Eddington limit, and the black hole energy is emitted primarily in the form of electromagnetic radiation. If the galactic matter is mostly stars, no significant interaction would be expected. However, for a galaxy whose matter is mostly gas and dust, the radiation would heat the gas and accelerate it via radiation pressure. The gas would be expected to be cold and dusty, thus the interaction not directly observable in X-ray. However, the AGN may be revealed by X-rays and far-infrared radiation escaping from the inner regions of the interaction [(7)].

IXO will study these interactions by observing AGN, outflows and winds in galaxies at redshift z~1-3, where the majority of galaxy formation occurs. With the power of the

[3] Eddington limit: The maximum luminosity that can be radiated by a compact object of given mass. It marks the limit where the force due to outward radiation pressure balances the inward force of gravity.

XMS, IXO will be able to resolve all ionisation states from Fe I – Fe XXVI, thus probing all phases of interstellar and intergalactic gas, across a temperature range of tens of thousands of degrees [K] to millions of degrees [K]. Measurements of the velocities and energies of outflows will be performed right across the galactic radius; from the inner regions of outflow generation (~10^{-4} pc) to the outer halos around galaxies and clusters) regions of energy deposition (up to ~1Mpc) [(7)].

1.3.1.2 LARGE SCALE STRUCTURE AND THE CREATION OF CHEMICAL ELEMENTS

Missing Baryons and the Intergalactic Medium

Recent observations indicate 95% of the mass-energy of the universe exists in dark matter and dark energy. Ordinary, baryonic matter accounts for just 4.6%, and only 10% of baryonic matter exists in collapsed objects such as stars, galaxies and clusters [(7)]. Theory predicts most of the baryonic matter exists in a cosmic web of unvirialised[4] filaments interconnecting galaxies and clusters.

The formation of large scale structure such as clusters and galaxies is thought to be due to baryonic matter falling into dark matter potential wells, and large scale structure is hence more pronounced at late cosmological times. As large scale structure develops, the gas contained within becomes increasingly shock heated, reaching temperatures of up to $10^{5.5}$K – 10^{7}K at close redshifts (z<1).

Although current absorption line studies can detect some of the warm baryonic matter, around 30-50% is still undetected, hence the term ‘missing’ baryons. IXO, with the XMS and XGS, will be able to observe these missing baryons if they exist in the predicted ‘hot‘ phase, as such high temperatures and ionised gas result in absorption lines in the X-ray spectra.

[4] Having a kinetic energy not bound by gravitational potential

Cluster Physics and Evolution

The radiation from hot gas and galaxies in clusters may be studied to reveal an insight into the interactions between the hot and cold baryonic matter, and the dark matter, in order to determine the evolution and physics of clusters. Current observations of this type are limited to late time clusters, at z~0.5 and below. In order to understand the evolution and physics involved, it is required to observe the first low mass clusters, which formed at earlier times which are observable at z~2 with capable instrumentation [(7)].

The IXO XMS will provide the necessary capabilities to study in detail the evolution of baryonic gas in dark matter potential wells, by providing spatially resolved high resolution spectroscopy measurements. Figure 5 shows a spectrum of Fe XXV lines for a small area of the Hydra A cluster (~1 arcmin^2), where modelled spectra is shown alongside an IXO XMS simulation [(7)]:

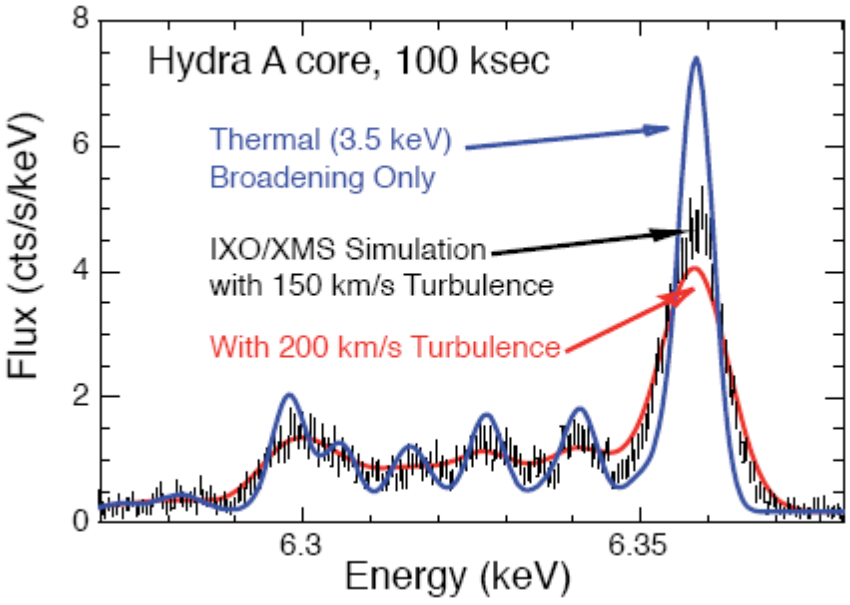

Figure 5: IXO spectrum of Fe XXV lines shows that turbulence of ~150 km/s or ~200 km/s may be distinguished from thermal broadening alone. This cannot be done at CCD resolution. Simulated IXO XMS data in black, models in colour. After (7).

The 2.5eV resolution allows for turbulent velocities down to about 100km/s to be distinguished from thermal broadening only. This will allow the gas motions and interactions to be studied in unprecedented detail, in order to provide an essential significant contribution into how baryonic gas evolves in dark matter cluster potential wells [7].

Chemical Evolution Along Cosmic Time

Supernovae are responsible for the initial creation of heavy elements in the universe. The most abundant heavy elements are the alpha-group elements (On Ne, Mg, Si, S, Ar, Ca) and the Fe-group elements. These elements, along with Carbon and Nitrogen, all have their k-shell transitions in the soft x-ray regime. The well known spectral lines for these elements means X-ray observations will allow for measurements of elemental abundances. Performing spectroscopy observations of supernova remnants at a range of redshifts (up to z~2) will allow for determination of when and where chemical elements were created and dispersed along the cosmic timeline [7].

1.3.1.3 MATTER UNDER EXTREME CONDITIONS

Strong Gravity and Accretion Physics

Black holes are notorious for their intense gravitational fields; they demonstrate strongest gravitational fields that are known to exist. As matter becomes trapped in such a strong gravitational potential, it spins and heats up, radiating at X-ray wavelengths. Hence, X-ray observations of these emissions can reveal the effects of strong gravity on both matter, and radiation, thus testing general relativity in the strong gravity limit.

The inner accretion discs of black holes, where the strongest gravity stable orbits are located, are illuminated with X-rays and provide an observable emission line spectrum together with a disc reflection spectrum, which is characteristic for an accretion disc.

Relativistic Doppler shifts together with gravitationally induced redshifts increasingly distort the emission line and reflection spectra for orbits radially closer to the central black hole, as predicted by general relativity. Modelling of these distortion effects can be used to ascertain the spin of a black hole, as is shown in Figure 6, where it can be seen how a spinning black hole has a disk much closer to the event horizon than a non spinning black hole. The increasing spin causes increasing broadening and red-shifting of the line spectrum [7].

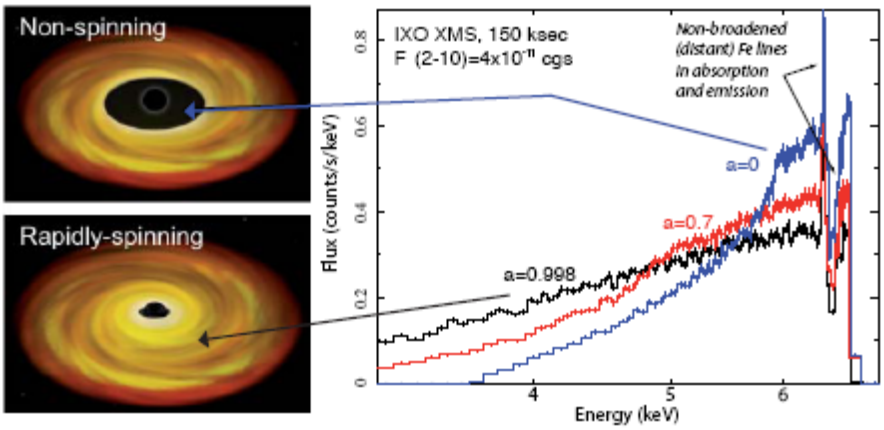

Figure 6: Left: X-ray illumination of the inner accretion disk provides a unique probe of the strong gravity environment near black holes. If the black hole is spinning the disk extends closer to the event horizon, resulting in a much broader, redshifted line profile. Right: Simulated IXO-XMS spectrum of a bright AGN, showing various broad Fe emission line profiles for different SMBH spins (with an equivalent width of 330 eV), superposed on the narrow emission and absorption features (typically of < 10 eV) resulting from more distant material. This shows that the XMS will be able to separate the narrow features from those produced by strong gravity. After (7).

Figure 6 shows (by simulated spectra) the XMS can distinguish between narrow emission/absorption features present due to more distant material (therefore unaffected by broadening/distortion due to strong gravity) and the broadened, red-shifted features produced by strong gravity [7].

Neutron Star Equation of State

The neutron star is the densest material object in the universe. Studying it allows for a unique laboratory in which to test Quantum Chromodynamics; which is thought to describe the fundamental behaviour of matter in neutron stars for most of the

temperature/density plane from the sub-nuclear scale upwards. The high temperature, low density regime of Quantum Chromodynamics is progressing in the field of particle physics; however, the opposite regime can only be investigated at the highest densities and low (with respect to the neutron Fermi energy) temperatures, i.e. neutron stars [7].

The relation between pressure and density – the equation of state, provides the insight into behaviour of bulk matter. Measurements of the mass and radius (M-R) of neutron stars can determine the correct equation of state for a neutron star by constraints imposed by several IXO instrument observations, as in Figure 7.

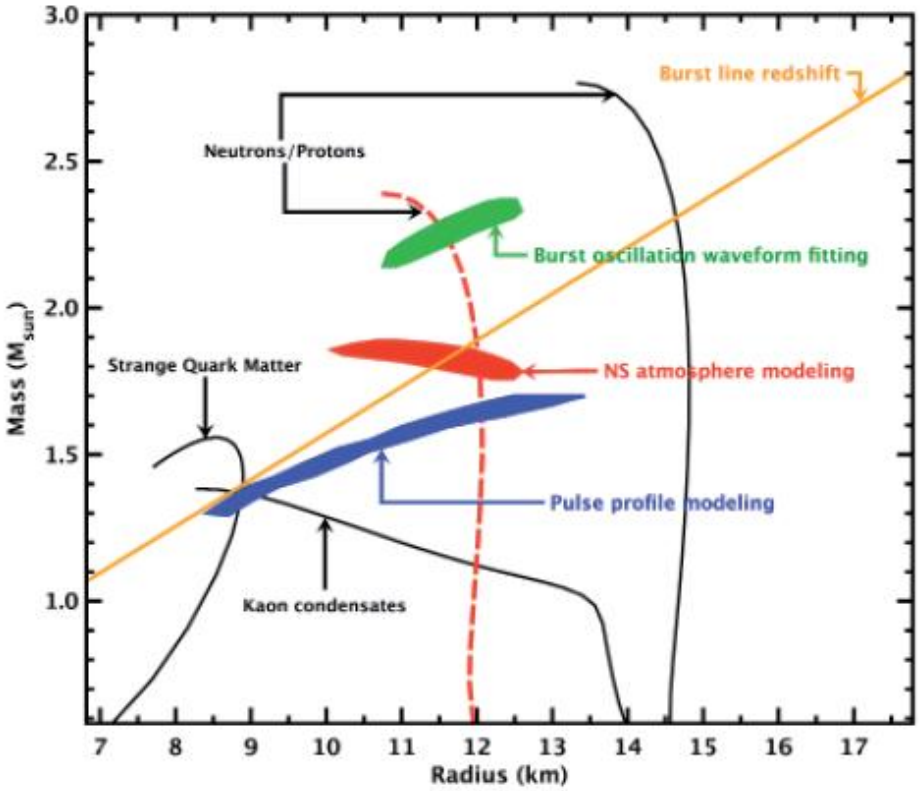

Figure 7: Mass-Radius relation for typical equations of state alongside constraints. The red dashed curve is the correct equation of state in this case. After (7).

Four curves for different equations of state predicted M-R relations are shown; strange quark matter, kaon condensates and 2 for ordinary nucleonic matter. The 'blob' type regions are constraints imposed from IXO instrument observations:

- **Green**: HTRS – pulse profile fitting of X-ray burst oscillations
- **Red**: - IXO XMS and WFI, 100ks observation – hydrogen atmosphere model fitting of the X-ray spectrum of a quiescent Neutron star in the globular cluster Omega Cen.
- **Blue**: - HTRS - waveform fitting of pulsations obtained from a 2 hour observation of an accreting millisecond pulsar.

Additionally, the orange line represents the detection of a gravitational redshift (z=0.35) from burst spectroscopy using the IXO XMS and HTRS. Only one of the M-R curves (the red dashed one) passes through all of these constraints, indicating that matter at super-nuclear densities consists of ordinary nucleonic matter [7].

1.3.2 Principles of Microcalorimetry

Microcalorimetry is the modus operandi at the heart of the latest technology in X-ray spectroscopy, and is the underlying physics of the IXO XMS. A microcalorimeter sensor is capable of measuring the energy of an individual X-ray photon. Figure 8 shows a schematic representation of a microcalorimeter:

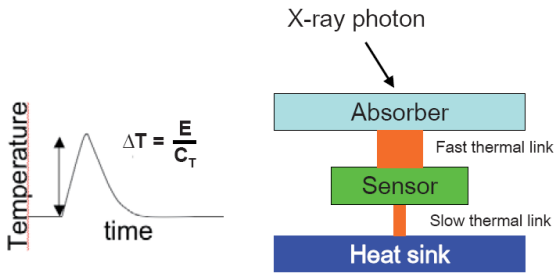

Figure 8: Schematic representation of a microcalorimeter. After (7).

The principle behind the sensor's operation is simple; a photon enters an absorber, causing a temperature rise ΔT equal to the energy deposited by the photon, E, divided by the absorber heat capacity C_T. The temperature rise is typically measured as a

resistance change by a thermistor. The heat energy deposited by a photon is typically equal to the energy of the incoming photon. Thus microcalorimetry provides a tool to directly measure the energy of individual X-ray photons.

In practise, the absorber must have a sufficiently low heat capacity, and kept sufficiently cold (tens of mK), so that the temperature rise caused by the incoming photon will be large enough to measure against the thermal energy of the absorber atoms. The absorber is connected via a thermal link to the thermistor. This thermal link provides partial isolation of the thermistor from the absorber to allow the absorber material to reach thermal equilibrium before the temperature rise is measured, to enable an accurate determination of the actual temperature rise. The thermistor temperature then warms up to the new absorber temperature, and its resistance changes accordingly. This resistance change is measured before the excess heat sinks into the heat bath, to which the thermistor is connected by a weak thermal link. Once the thermistor and absorber are back in thermal equilibrium with the heat bath, the system is ready to measure the energy of another photon.

1.3.3 TRANSITION EDGE SENSORS

The IXO microcalorimeter instrument consists of an array of Transition Edge Sensors (TES). These sensors utilise thermistors constructed of materials engineered to have a superconducting transition temperature in a convenient region, typically around 60-100mK. This extremely low temperature is essential in order to measure the tiny increase in temperature of the absorber caused by a single X-ray photon. The low temperature is required to maximise the resolving power of the TES, as is shown by equation (1), which shows a lower energy resolution ΔE is achievable using a low temperature of operation T, low absorber heat capacity C_T and high dimensionless

sensitivity α (described subsequently and in Figure 9), where $k_B$is Boltzmann's constant [(10)].

$$\Delta E \cong 2.35\sqrt{4k_B T^2 \frac{C_T}{\alpha}} \qquad (1)$$

The transition temperature region between the normal and superconducting states is typically around 1mK wide, thus this region has an extremely steep resistance-temperature gradient (change in resistance with respect to change in temperature/dimensionless sensitivity), as shown in Figure 9.

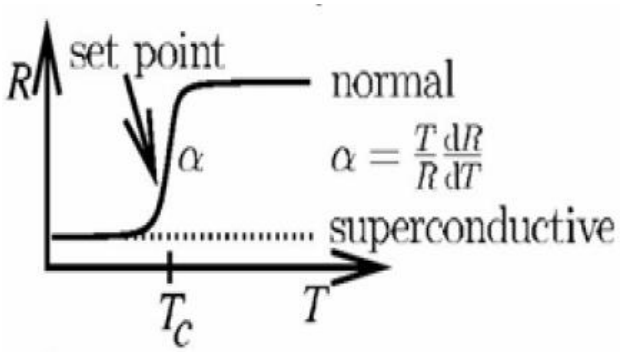

Figure 9: Operating principle of a Transition Edge Sensor (TES). After(8).

The TES is held at the lower end of this transitional temperature band by voltage biasing (i.e. held at a set point of the order of 20% the normal state resistance), so that when a photon strikes the absorber and imparts its energy as heat, the resulting small temperature change is measured as a large change in resistance. This allows for extremely sensitive measurements to be made, and accurate determination of the incident photon energy. The increase in resistance due to the temperature increase caused by an incoming photon is actually measured as a drop in current by SQUID (Superconducting QUantum Interference Device) read-out electronics inductively coupled to the TES circuit. SQUID read-out electronics are the only type of read-out systems with sufficiently high sensitivity and low noise necessary to permit

measurement of the drop in current of the TES circuit. The output of the SQUID is then subsequently amplified by conventional electronics to be processed by the spacecraft.

1.3.4 IXO XMS INSTRUMENT

The IXO XMS TES arrays are being developed for IXO by a consortium including SRON (Stichting RuimteOnderzoek Nederland - Netherlands), INAF (Istituto Nazionale di AstroFisica –Italy), ISDC (INTEGRAL Science Data Centre - Switzerland), GSFC (NASA Goddard Space Flight Center - USA), NIST (National Institute of Standards and Technology - USA), and ISAS (Institute of Space and Astronautical Science - Japan). A TES microcalorimeter under development at SRON is schematically illustrated in Figure 10.

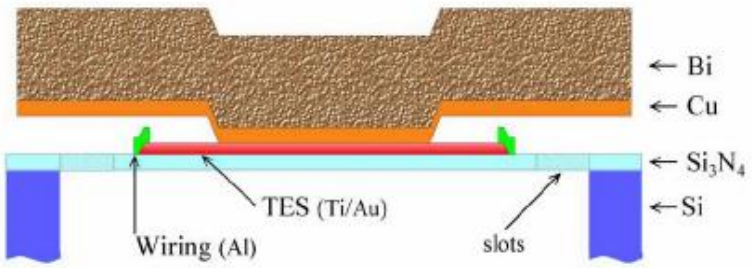

Figure 10: Schematic of a micro-calorimeter pixel (as developed at SRON), consisting of an X-ray absorber (in this case Bi/Cu), a phase transition thermometer (in this case Ti/Au) and a weak link (Si3N4-membrane) to the base temperature of the cooler. After (8).

The IXO XMS consists of two arrays of TES microcalorimeters; an inner array and an outer array. Each TES consists of a Mo/Au Bi-layer with a critical transition temperature of T_c ~100mK, voltage biased to an initial resistance set point of 20% of the normal state resistance [7]. The base temperature of the heat sink will be maintained 50mK, such that without voltage biasing the nominal detector temperature is well in the superconducting range. The XMS TES array arrangement is illustrated in Figure 11.

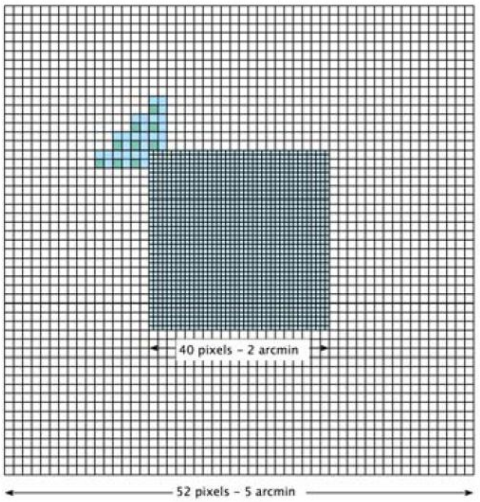

Figure 11: Possible layout of the XMS Field of View showing the difference between the inner and outer array clearly. The outer pixels are twice as large and 4 pixels are read-out by a single TES. After (8).

In the inner array, each 300µm × 300µm pixel has its own TES to measure the energy of a single X-ray photon at a time. In the outer array, a single TES is shared between 4 of the 600µm × 600µm pixels, with incidence position determined by analysis of the temperature rise time which is different for each of the pixels due to different thermal conductance links to the TES layer. This concept is illustrated in Figure 12.

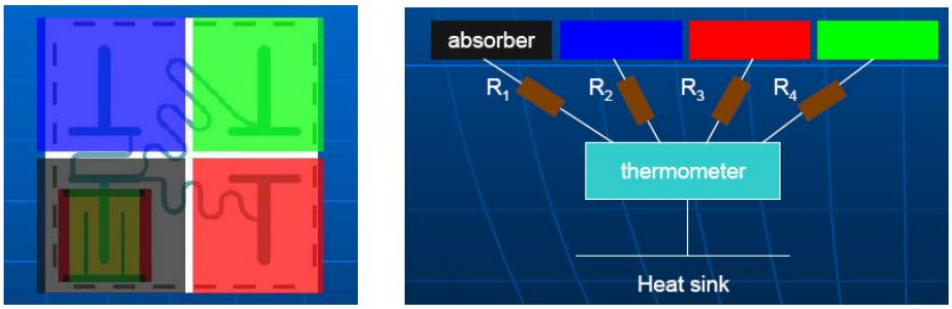

Figure 12: Schematic read-out of a super pixel illustrating the differences in thermal conductivity to the TES and bath temperature. After (8).

The complete XMS consists of 2176 individual TES's. The thermal loads due to the electrical harnesses required if each TES had its own SQUID would be far too high for the instrument to operate, hence, it is essential to minimise these loads by multiplexing the

TES signals so that they may be read by a single SQUID. There are ongoing investigations into both Time Domain Multiplexing (TDM) and Frequency Domain Multiplexing (FDM).

The design concept of the detector package housing the XMS is shown below in Figure 13.

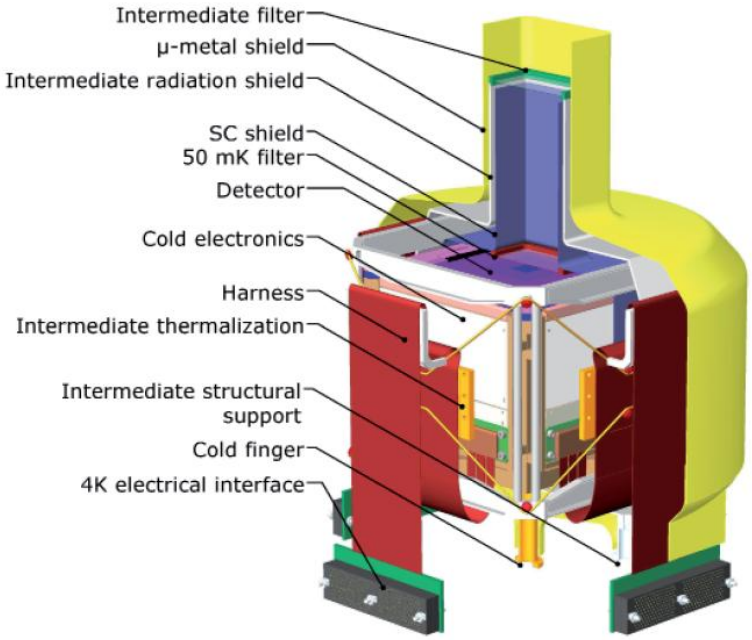

Figure 13: Conceptual design of the focal plane assembly of a microcalorimeter, showing the various steps in the cooling system. The FPA is laid out as a cube. The inner, outer, and anti-coincidence detectors are mounted at the upper horizontal plane of it. Along the sides of the cube the cold electronics are mounted and connected to the electrical harness. The central cube is surrounded by thermal and magnetic shields at the various temperature levels. Kevlar suspension is used for thermal isolation of these temperature stages. After (7).

This instrument package must be contained in a cryostat, and actively cryogenically cooled in order to support the stable 50mK environment necessary for the TES array to function at its operating temperature and not be affected by thermal noise. This thesis describes some of the technology development that will allow this cryogenic environment to be maintained reliably and effectively, and for the length of time required for sufficient observation duration.

1.4 SUMMARY

This chapter has introduced the field of X-ray Astronomy, and described how it can be used as a tool to contribute to understanding the laws of physics in extreme environments, and how observations at high red-shifts can provide clues as to the formation of structure in the universe.

X-ray astronomy has been shown to be a fairly recent but essential branch of astronomy, with several missions that have advanced astrophysics over the past several decades due to increasing sensitivity and observational performance of the observing instruments. The IXO mission has been identified as the future of X-ray astronomy, which will allow for unprecedented sensitivity (to look further back in time/observe at higher redshifts) and spectral resolution (to determine in unprecendented detail the physics of processes occurring in observational targets).

The IXO XMS instrument has been shown to be essential for IXO to achieve its science goals, and its operational principles and applications briefly described. The requirement for the XMS to be cryogenically cooled to a stable 50mK during operation has been highlighted, thus identifying one of the reasons why cryogenics is required for space missions.

Chapter 2:

SPACE CRYOGENICS

The previous chapter introduced X-ray Astronomy, and by presenting the future IXO mission, showed there is a need for cryogenic temperature production in space by example of the XMS instrument. X-ray Astronomy is certainly not the only application of cryogenics in space; however, it is the driver for the work published in this thesis.

This chapter introduces the discipline of cryogenics, and more specifically, space cryogenics. The environment of space introduces several further considerations that must be respected during the design and selection of cryogenic cooling technology, including sources of thermal radiation, vacuum, and the vibrations and shocks associated with the launch and ascent of the spacecraft.

Some of the common cryogenic technologies are described, in particular, those which are relevant to the work contained within this thesis, such as Stirling Coolers and Joule Thomson coolers. The Adiabatic Demagnetisation refrigerator (ADR) is identified as a favourable cooler for milliKelvin cooling applications such as required by the IXO XMS.

2.1 CRYOGENICS AND SPACE CRYOGENICS

2.1.1 INTRODUCTION TO CRYOGENICS

Cryogenics: From the Greek '*Kryos*' – Frost, and '*genic*' – production/generation.

Cryogenics is the production of, and study of effects at, low temperatures. 'Low temperatures' may have a variety of interpretations; however, it is generally accepted that cryogenic temperatures are anything below about -150^{o}C (123.15K) [(11)].

Cryogenics began with the liquefaction of oxygen in 1877 by both Cailletet and Pictet [(12)], but the term was first coined by Kamerlingh Onnes, who founded the Cryogenic laboratory at the University of Lieden in 1882 [(12)]. A historical introduction to cryogenics is given in a review paper by Scurlock (12); however, some key pioneering events in the field are summarised below [(12)]:

1877	Oxygen liquefied: Cailletet (Paris), Pictet (Geneva)
1895	Air liquefiers: Hampson (London)/Linde (Munich)
1898	Hydrogen liquefied: Dewar (London)
1908	Helium liquefied: Kamerlingh Onnes (Leiden)
1911	Superconductivity discovered in mercury: Kamerlingh Onnes (Leiden)
1930	Freons as refrigerants
1938	Superfluidity in Helium
1939	Air liquefied with turbine expander: Kapitza (Moscow)

Cryogenic temperature environments are required for numerous ground based applications, including (but not limited to):

- **Low temperature Physics**: - The study of low temperature physical phenomena such as superconductivity, superfluidity etc naturally requires low temperatures.

- **Particle Physics**: - Particle accelerators such as the LHC (Large Hadron Collider) require cryogenics to cool the powerful superconducting magnets used to control the particle beams.

- **Quantum computing**: - Generally the 'QuBits' – Quantum analog of the binary Bit that represent the data require cryogenic temperatures as they are typically stored and manipulated on and with superconducting materials. Qubits are analogous to binary bits, where the value '0' may be represented by an atom (for example) in its ground state, and '1' by the first excited state. Superpositions of these states are what give Qubits their unique advantage over bits, in that both states (and an infinite number of states in between) may also be represented simultaneously. The superpositional states are extremely sensitive, hence thermal agitations must be reduced sufficiently (by ensuring the atom is sufficiently cold) so that they to not disrupt the Qubit state.

- **Medicine**: - Cryosurgery, a common example would be the treatment of warts and verruccas using liquid Nitrogen. Cryosurgery is also being used to treat various cancers by killing the tumourous tissue by direct cryogenic freezing.

- An extremely important application of cryogenics is the use of liquid Helium to cool the superconducting magnets of MRI (Magnetic Resonance Imaging) machines. MRI scanners are a key tool in modern diagnostic medicine, and require magnetic fields that are so strong they are only practically achievable with superconducting magnets.

- **Production of liquefied gases**: - The liquefaction of nitrogen, oxygen, and all 'permanent' gases require cryogenic temperatures.

- **Cryogenic Storage**: - Food, biological and organic tissue samples etc are often stored in cryogenic environments when long-term preservation is required.

- **Detectors**: - Detectors for radiation, X-rays, Infra-red sensors etc. Often require cryogenics to achieve the best sensitivity and energy resolution.

This thesis, however, focuses on the application of cryogenics in space, in particular the cryogenic environment required to support the IXO XMS. Hence, 'ground' based/laboratory cryogenics shall not be discussed further in any detail.

2.1.2 Introduction to Space Cryogenics

Space cryogenics is the production of cryogenic temperatures in space, typically to provide cooling for detector based instruments, as this thesis demonstrates by example of the IXO XMS previously presented in Chapter 1. Generally, the need for cryogenic temperatures in space is to reduce the thermal 'noise' which is required to increase the sensitivity of detectors, according to the fundamental principles of detector physics [(13)].

The IXO XMS requires a 50mK environment, and many superconducting-based detectors also require sub-Kelvin temperatures as they must operate below their critical temperature. Common earth-observing missions such as military surveillance and climatic monitoring satellites require cryogenics as they typically use infra-red detectors which require temperatures of around 50K - 80K. An overview of the various types of photon detectors used in space is given below in Figure 14, where the target waveband and operating temperatures are also given [(14)].

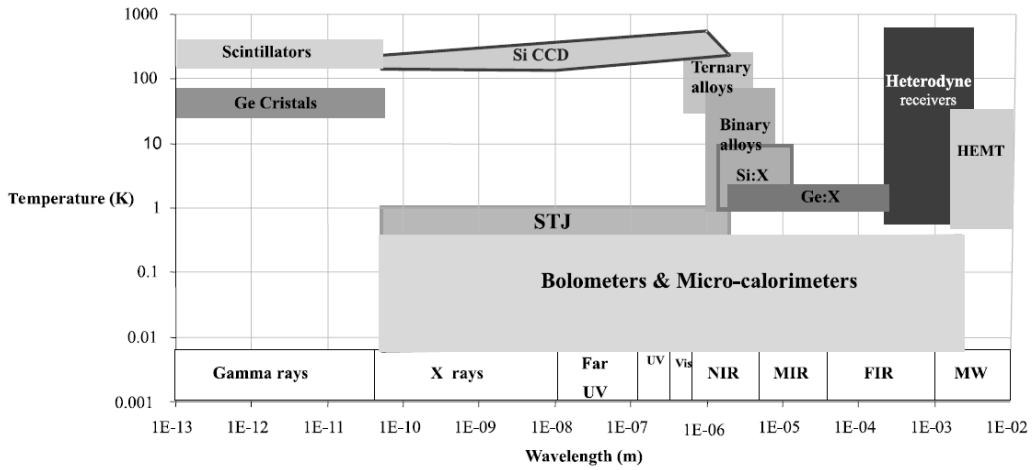

Figure 14: Overview of photon dectectors and their operational temperature requirements. After(14).

A thorough review of the missions and technologies employing space cryogenics is given in Collaudin and Rando (14).

2.1.3 The Thermal Environment of Space

Space cryogenics engineers and scientists are often asked 'why do you need cryogenics in space, when space is already so cold?'. It is true that deep space has a temperature of 2.73K due to the CMB (Cosmic Microwave Background) – the remnant radiation from the big bang event. However, for objects in view of a radiating black body (such as the sun, a planet etc) this extremely cold temperature will only be experienced by the parts that are not subject to any incident thermal radiation. Typically for satellites orbiting the earth, the sun-facing side will be at ~300K, and the side facing away from the sun could be extremely cold if no other radiation is incident upon it. However, additional radiation incident on an earth-orbiting spacecraft comes from the earth emitting its own blackbody radiation (planetary emission), as well as solar radiation reflected by the earth (known as *Albedo* radiation). Naturally, the same applies for a satellite orbiting any planet. Such a situation is depicted (for the common Earth case) schematically in Figure 15.

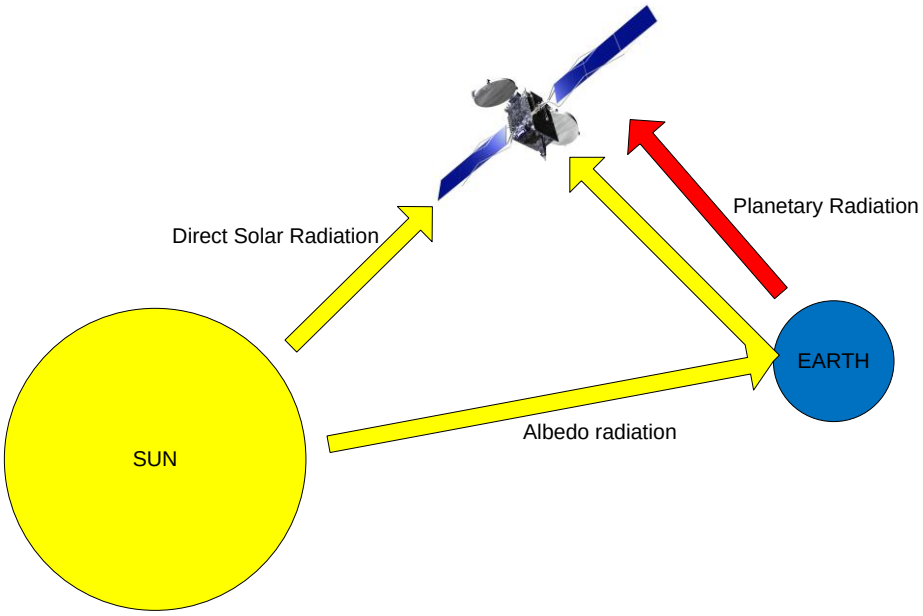

Figure 15: Typical thermal radiation incident on a general earth orbiting satellite

All of these radiation contributions are easily calculable, as outlined in (15), and must be considered for the general near-earth orbit case. However, IXO will be positioned at a halo orbit around the sun-earth lagrangian point L2, whose location is shown in Figure 16:

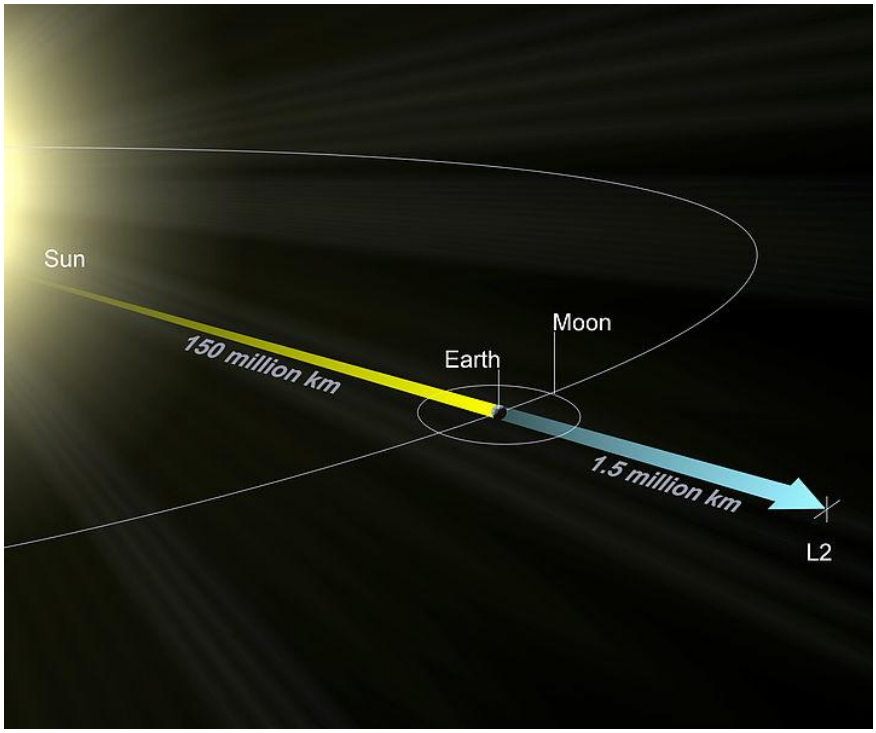

Figure 16: Illustration of L2. After (16).

The typical halo orbit such as intended for IXO is represented schematically in Figure 17.

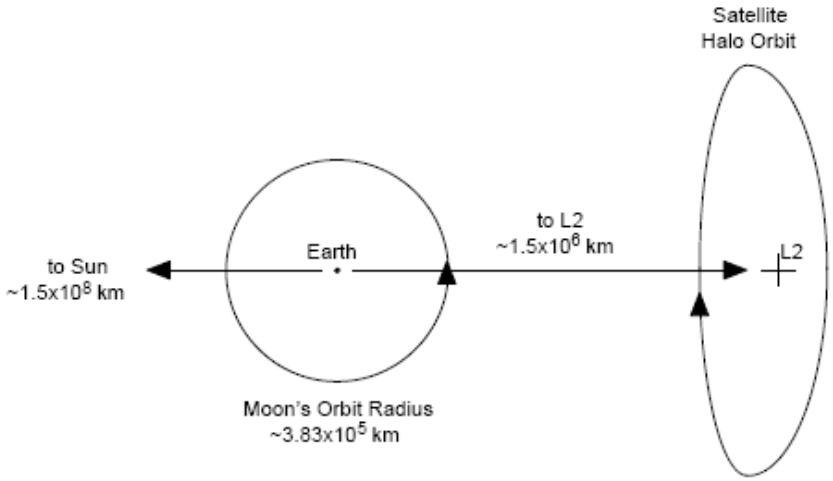

Figure 17: Typical satellite halo orbit at L2. After (17).

The L2 halo orbit depicted shows how the satellite is always at a constant angle to the earth on the 'dark' side, and at an almost constant distance from the sun. The resulting effect is that albedo and planetary (earth) radiation is negligible (unlike the near earth orbital environment) and only the solar thermal radiation need be considered [17]. Hence, the thermal environment is reasonably stable throughout the year, as shown by the thermal breakdown in Figure 18.

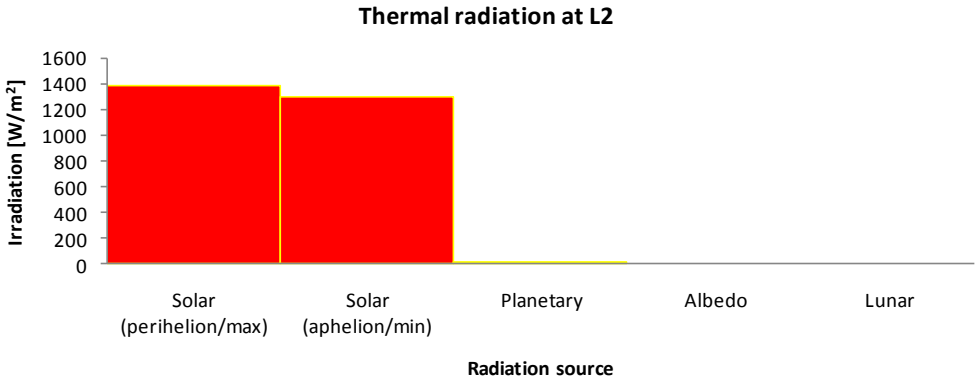

Figure 18: Thermal radiation sources at L2, as calculated for a 700,000 km halo orbit. Data after (17).

The values of the solar irradiances in Figure 18 come from an inverse square law calculation of the solar constant (the irradiance at a plane normal to the sun at the radial distance of 1AU – quoted as 1367±10Wm^{-2} [17]); and the albedo/planetary/lunar contributions assume a 700,000km orbit radius for the L2 halo orbit (as for the NGST – Next Generation Space Telescope) [17]. These values are summarised in Table 3.

Radiation source	Irradiation at L2 halo orbit [W/m^2]
Solar (perihelion/max)	1389
Solar (aphelion/min)	1296
Planetary	0.004
Albedo	0.0004
Lunar	0.0002

Table 3: Summary of irradiation experienced by a satellite at an L2 halo orbit of 700,000km

The electronic and mechanical components of a spacecraft typically operate within a temperature window that requires the spacecraft to be thermally controlled in order to allow operation in the thermal environment of the spacecraft orbit. Example temperature ranges of typical equipment are given in Table 4:

Component	Tmax (C)	Tmin (C)
Electronics	40	-10
Batteries	15	-5
Fuel	40	9
Mechanism (Bearing)	65	-45
Solar cells	55	-60

Table 4: Typical operating temperature ranges for satellite equipment. After (18).

Thermal control is also required due to the strong temperature gradients spacecraft may experience between the sun-facing and sun-opposing sides, which could impart significant stress on the satellite/spacecraft structure due to differing thermal contraction/expansion between different materials/parts. The spacecraft is typically

maintained at a temperature that suits the thermal-structural and operational temperature requirements of the onboard systems.

It is clear that in order to provide stable cryogenic temperatures for detector instruments, dedicated cryogenic cooling technologies must be employed.

2.1.4 CONSIDERATIONS FOR SPACE CRYOGENICS

Space provides a number of additional design challenges in comparison to ground based cryogenics applications. These include:

- **Lack of serviceability**: - Once in space, a spacecraft/satellite will be inaccessible for maintenance and service/repairs of its systems. Hence, any cryogenic system must be highly reliable and be able to run without requiring any maintenance that cannot be performed by the spacecraft itself (e.g. decontamination cycles with heaters).

- **Absence of gravity**: - Gravity dependent processes will not occur in space due to the zero-g environment. This affects the transfer and properties of cryogenic fluids in space.

- **Mass**: - Mass must be minimised for all spacecraft systems, in order that the spacecraft can be launched, as the payload must be below a given mass (for example, 10 metric tonnes for an Ariane-5 delivering a payload to a Geostationary Transfer Orbit – GTO [19]).

- **Vacuum considerations**: - In the vacuum of space, materials outgas as surface atoms sublimate due to the lack of external pressure. The absence of pressure enables the thermal excitations of surface atoms to overcome the forces attracting them to the material bulk [15]. Hence, material choice is crucial in

order to minimise outgassing, as outgassed particles can cause detrimental contamination to optically and/or electrically sensitive equipment.

In addition, spacecraft systems must survive the depressurisation that occurs due to venting during the launcher's escape from earth's atmosphere. Figure 19 shows how pressure decreases with flight time for a payload launched on an Ariane-5.

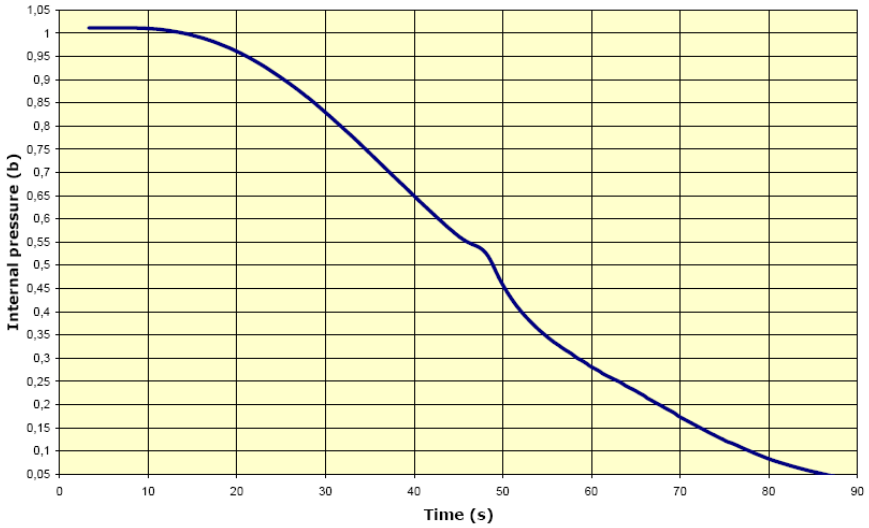

Figure 19: Static pressure decrease with flight time for the Ariane-5 payload module. After (20).

As the profile shows, the venting is engineered to enable the gradual, smooth decrease of pressure.

- **Vibration/shock**: - Spacecraft systems must be designed to survive the intense vibrations induced during launch, and the shocks that arise from the various phases of launch (e.g. separation of launcher components in-flight).

The acceleration profile of an Ariane-5 is shown in Figure 20.

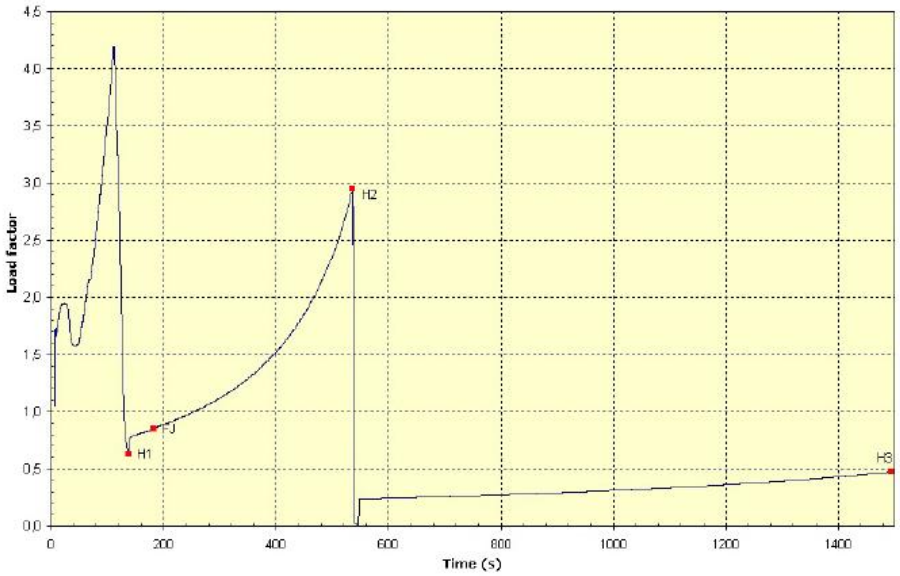

Figure 20: Typical longitudinal acceleration profile of Ariane-5 during ascent flight. Load factor (y-axis) is static acceleration in g. After (20).

The highest longitudinal static acceleration occurs at the end of the solid rocket boost phase (first peak on Figure 20) and is <4.55g. Lateral accelerations are <0.25g [(20)].

The main shocks that occur during ascent are:

- The upper stage separation from the main cryogenic stage
- The fairing jettisoning
- The spacecraft separation

The shock envelope for the first 2 shock events (at the spacecraft interface) is given in Figure 21.

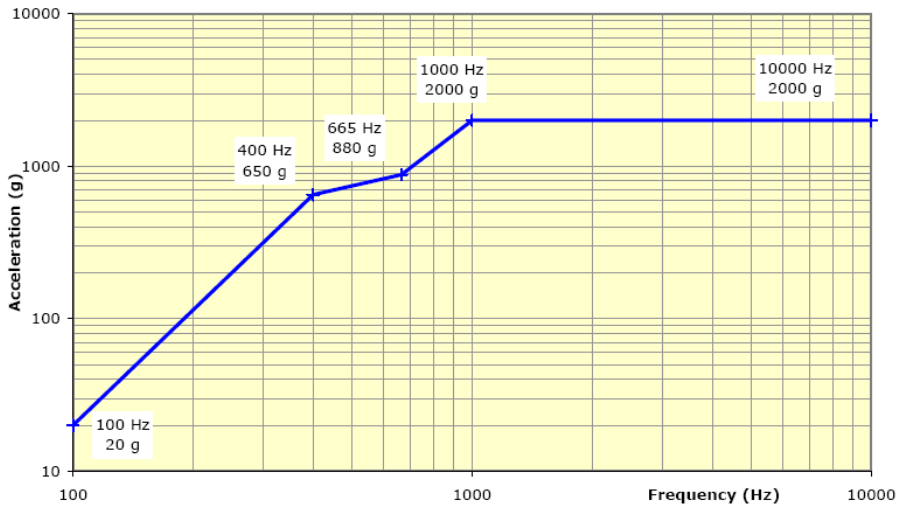

Figure 21: Shock spectrum envelope for upper stage separation and fairing jettisoning of Arainne-5. After (20).

The spacecraft separation shock spectrum depends on the launch adaptor used. However, it is clear to see that separation events deliver high shock loads to the spacecraft interface, and hence, spacecraft and all of its systems.

The typical vibration spectrum envelopes experienced by payloads during flight and launch are shown in Figure 22 for sine excitation and Figure 23 for acoustic excitation.

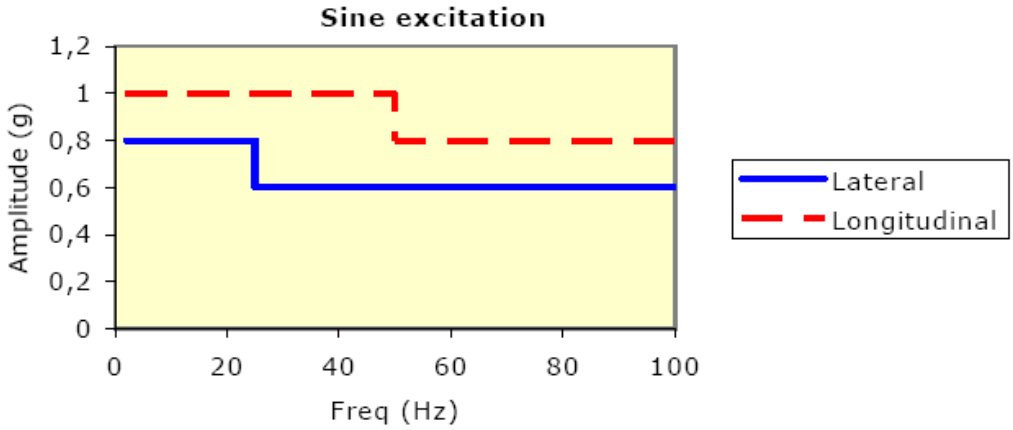

Figure 22: Sine excitation envelope at spacecraft base. After (20).

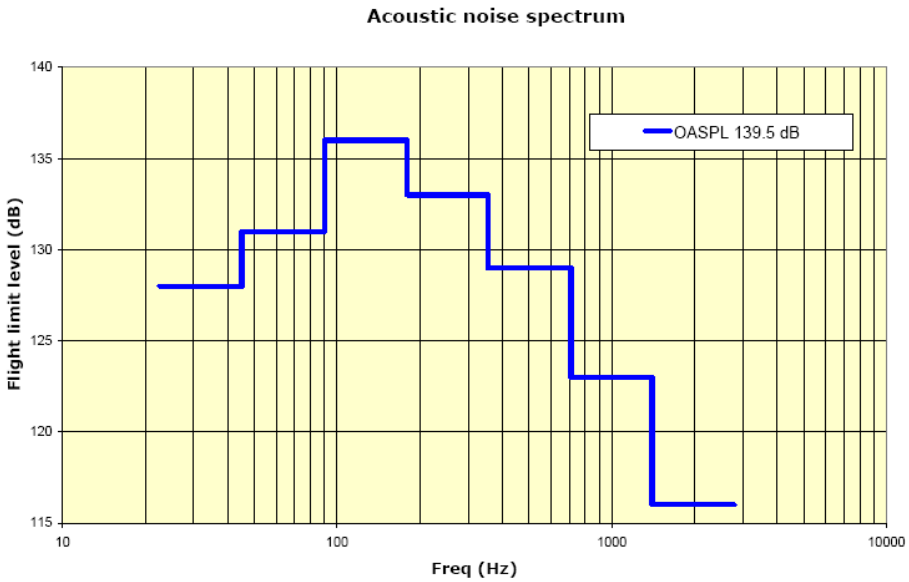

Figure 23: Acoustic noise spectrum averaged over the volume occupied by the spacecraft stack on Ariane-5. After (20).

The vibration excitations arise from the rocket engines themselves, and noise caused by the rocket moving through atmospheric air. These vibration environments lead to restrictions on structural resonances of the spacecraft and its internal systems. Inevitably, the spacecraft structure itself will cause the vibration excitation spectra to be modified at system and sub-system level due to the amplification and attenuation of different frequencies. Hence, spacecraft system design is a complex, cyclical process in which the spacecraft structure and systems must be engineered to have structural resonances in strategic frequency locations to prevent excitation of natural structural modes and coupling between them.

2.2 CRYOGENIC COOLING - TEMPERATURES > 1K

There is a natural divide around 1K above which cryogen[5]-based cooling technologies are typically used to provide the cryogenic cooling required for any application of cryogenics. Below this dividing temperature, cryogen-based cooling becomes increasingly impractical, and below 0.25K, impossible. Hence, achieving sub-kelvin cooling is generally quite different from the more common cryogen-based methods. In this section, typical cryogenic cooling techniques employed in space are described.

2.2.1 CRYOGENS

The most widely used method of producing cryogenic temperatures in general is through the use of cryogens such as liquid nitrogen and liquid Helium. Cryogens have their boiling points in the cryogenic temperature range, as shown in Table 5 where the thermodynamic properties of some common cryogens are summarised.

	Temperature (K)			Pressure			Latent Heat of Vaporization	
	Triple point	Normal boiling point	Critical point	Triple point (kPa)	Critical point (kPa)	Critical density (kg/m³)	L (J/g)	Density (g/ml)
Helium	2.1768[a]	4.222	5.1953	5.048	227.46	69.64	20.6	0.13
Hydrogen	13.8	20.28	32.94	7.042	1283.8	31.36	441	0.07
Neon	24.5561	27.09	44.44	43.35	2703	483.23	86	1.20
Nitrogen	63.15	77.36	126.26	12.46	3399	313.11	199	0.81
Oxygen	54.36	90.19	154.58	0.148	5043	436.14	213	1.14
Argon	83.8	87.28	150.86	68.9	4906	535.70	162	1.40
Krypton	115.76	119.77	209.39	73.2	5496	910.75	108	2.40
Xenon	161.36	165.04	289.74	81.6	5821	1100	96	3.10
CO_2	216.58	—	304.21	518.16	7384	466.51	571	1.56
Methane	90.69	111.63	190.55	11.7	4599	162.65	510	0.42
Ethane	90.35	184.55	305.33	0.0011	4871	206.73	489	0.55
Propane	85.47	231.07	369.85	0.1×10^{-6}	4248	220.49	425	0.58
Ammonia	195.49	239.81	406.65	0.0662	11627	237.57	1371	0.68

[a] *Triple point values for helium are those of the lambda point*

Table 5: Table of common cryogens and some of their thermodynamic properties. After (21).

Cooling is provided at the boiling point of a liquid cryogen. Whilst a substance undergoes a phase change, such as liquid into gas (evaporation), its temperature is constant. This is

[5] Cryogen: - A fluid (generally, a liquefied gas) which has a cryogenic boiling point. See 2.2.1.

because any heat added during a phase change increases the enthalpy[6] (a full definition of enthalpy may be found in Bowley and Sanchez (22)) of the cryogen but not the temperature, as the enthalpy increase is used by the system to perform the phase change by overcoming the intermolecular bonds associated with the liquid state. The amount of enthalpy increase required to perform the phase change is known as the latent heat of vaporisation.

The latent heat is essentially what provides the cooling. Hence, it is essential to minimise the rate of enthalpy increase caused by the external environment being at a higher temperature than the boiling cryogen, in order to minimise the rate at which the phase change occurs, and maximise the useful cooling capability (i.e. to maximise the use of enthalpy increase to provide cooling). Hence, heat loads on the cryogen (from the environment – known as parasitic heat loads) must be minimised. Thus, cryogens are stored and transported in thermally insulating dewars, and when used for cryogenic cooling, are contained in a cryostat. Both of these vessel types have vacuum spaces between the external and internal walls, to eliminate convective heat loads (in atmospheric environments) and minimise conductive heat loads. Typically, low emissivity coatings cover the faces of the walls to minimise radiative heat loads.

The cooling power of a cryogen is proportional to the vapour pressure, which falls exponentially with decreasing temperature as described by Maxwell-Boltzmann statistics. At and below the boiling point of ^{4}He (4.2K), all substances except Helium have negligible vapour pressure (since they are well into the solid or liquid phase), hence anything in thermal contact with liquid Helium will automatically become 'cryopumped' – the low temperature reduces the vapour pressure as vapour condenses onto the liquid Helium temperature surfaces.

[6] Enthalpy: - The internal energy of a system plus the energy required to displace the environment and establish its volume and pressure.

It is possible to reduce the boiling point of a cryogen, hence, reduce the temperature at which cooling can be provided. This can be achieved by reducing the vapour pressure by actively pumping the vapour away from above the liquid surface. Since liquid Helium cryopumps all other substances, only Helium can be pumped on to reduce the boiling point to temperatures <4.2K. The reduction of vapour pressure shifts the equilibrium between the forces preventing evaporation (provided by the vapour pressure) and the forces of evaporating liquid. As the vapour pressure is reduced, the energy required for a molecule to evaporate is reduced, such that more molecules in the energy distribution of the liquid cryogen have energy greater than the required evaporation energy. The rate of evaporation increases and the temperature drops as more evaporating molecules carry away heat, thus changing the energy distribution such that the fraction of molecules with energy greater than the evaporation energy is reduced. Hence, a new equilibrium at a lower boiling point is established. This is exactly the same process that allows water to boil at temperatures <100^{o}C in high altitude (lower pressure) environments.

However, since the cooling power is proportional to the vapour pressure, there is a limit to which the boiling point can be reduced, where the vapour pressure is reduced sufficiently that the cooling power becomes equivalent to the heat load on the cryogen. Further pumping will not lower the boiling point of the cryogen. The boiling point limitations for Helium, which exists in 2 stable isotopes, are ~0.7K for the common ^{4}He isotope, and ~0.25K for the rarer ^{3}He isotope [15]. Helium is described subsequently.

2.2.1.1 CRYOGENIC HELIUM

Helium in its common ^{4}He isotope is a product of alpha-decay (an alpha particle is a fully ionised Helium-4 nucleus), and most natural Helium-4 on earth is a product of alpha

decay of heavier elements within the earth's crust. A phase diagram of Helium-4 is provided in Figure 24.

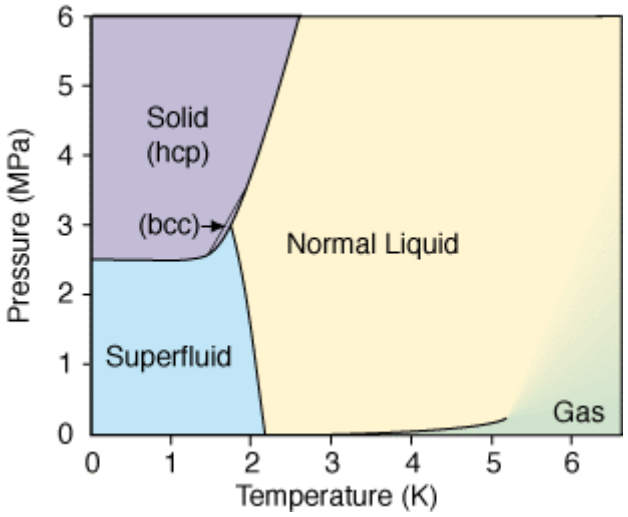

Figure 24: Phase diagram of Helium-4. After (23).

The atmospheric pressure at sea-level is ~0.1MPa, thus it is impossible to solidify Helium without high pressures (>~2.5MPa). Helium liquefies at 4.2K at atmospheric pressure – as was first discovered by Kamerlingh Onnes in 1908 (12).The interesting phase of Helium is the superfluid phase, which occurs <2.2K. This phase is an example of a Bose-Einstein condensate (see (22) for a full definition of Bose-Einstein condensates), where the atoms of the fluid enter in to one macroscopic ground state. Superfluid Helium has zero viscosity, and infinite thermal conductivity. It appears to defy gravity by forming a flowing layer of fluid film moving up the walls of its container, seeking warmer temperatures. This phenomenon is shown in Figure 25.

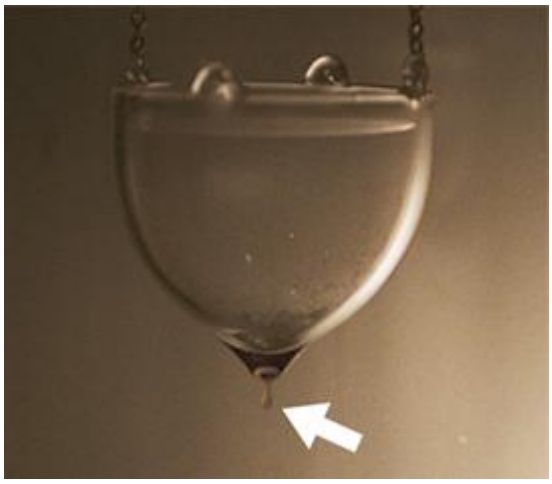

Figure 25: Superfluid Helium-4 creeping over the container walls. After (24).

As such, for temperatures below 2.2K, an extra heat load on liquid Helium arises from the superfluid film coating the container walls. Pumping on Helium-4 can achieve temperatures down to 0.7K [15].

The rare stable isotope of Helium, Helium-3, has one fewer neutron in its nucleus compared to the heavier Helium-4. This results in a half-integer quantum spin value, and means that unlike the bosonic Helium-4 nucleus, Helium-3 is governed by Fermi statistics. Helium-3 is present in only trace amounts on Earth, hence is extremely expensive to procure. It is typically produced from Tritium decay as a by-product of weapons production. Helium-3 can be used to obtain lower temperatures than achievable with Helium-4, since it has a vapour pressure 74 times greater when at 1K, and ~10^4 times greater at 0.5K [15]. Hence, it is possible to cool down to 0.25K by pumping on Helium-3. A Helium-3 phase diagram is shown in Figure 26.

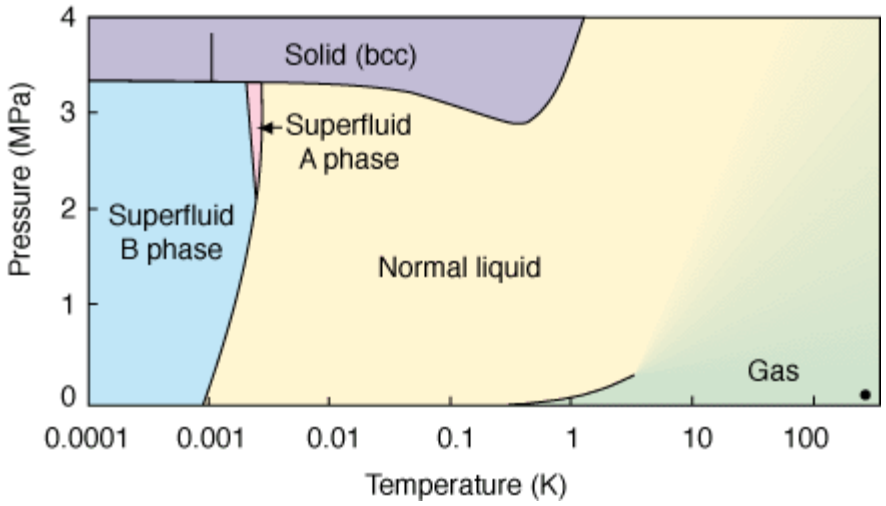

Figure 26: Helium-3 phase diagram. After (23).

Since the superfluid transition occurs by a different process than for Helium-4 (since the Helium-3 atom is a fermion and not a boson), it happens at much lower temperature, below the limitations of cooling achievable with a pumped Helium-3 cryostat. This means that when using pumped Helium-3 for cryogenic cooling, there is no extra heat load due to the superfluid film.

2.2.2 Cryogen use in Space

The first applications of cryogenics in space inevitably used the simplest method of cryogenic cooling – stored cryogen evaporation. IRAS (InfraRed Astronomy Satellite), launched in January 1983, was the first cryogenic space mission, and the first mission to survey the entire sky at infrared wavelengths. It used liquid Helium-4 to cool the focal plane detectors to ~3K [(14)].

COBE (COsmic Background Explorer) measured the cosmic background radiation left over from the big bang, confirming the predictions of a remnant blackbody spectrum expected from the big bang. Launched in November 1989, It flew a payload of 3 instruments; DMB (Direct Microwave Radiometer), FIRAS (Far InfraRed Absolute Spectrometer) and DIRBE (Diffuse InfraRed Background Experiment). FIRAS and DIRBE

operated at 1.6K [14], and were both cooled by a 'pumped' Helium-4 cryostat –the 'pumping' was achieved by venting the helium into space through a porous plug.

These early cryogenic missions depleted their stored cryogens after about ~10 months, and as such had a very limited service life as the detectors could not function at higher temperatures. Later missions improved on the mission lifetimes achievable with stored cryogens, however, there is only limited improvement that can be made using technology and methodology, and ultimately the mission lifetime is dependant on the amount of stored cryogen. Naturally, it is not possible to launch excessive masses of cryogens, as the mass must generally fit into a specified budget determined by the mass that can be launched. As such, it is not easily possible to use cryogen based cooling for missions with a lifetime >~3 years.

In order to facilitate cryogenic missions with longer lifetimes (>3 years plus), additional cryogenic cooling technologies must be employed. Typically, these involve a combination of passive cooling systems (see 2.2.4) and cryogenic coolers (cryocoolers), which are described subsequently. Cryocooling technologies for sub-Kelvin temperatures are described in 2.3.

2.2.3 CryoCoolers

Cryocoolers are machines which utilise some kind of thermodynamic cycle in order to lift heat from a colder temperature and reject it at a higher temperature. Essentially, such machines are heat engines operating in reverse. The Carnot cycle is perhaps the most familiar thermodynamic cycle to physicists from early studies in thermodynamics, and is the ideal heat engine:- The most efficient method of converting heat into work. Conversely, operating in reverse; a Carnot cycle becomes the most efficient method of using work to remove heat: Naturally, the most efficient refrigerator.

2.2.3.1 The Carnot Cooling Cycle

The second law of thermodynamics may be stated in the form [22]:

> *"It is impossible to construct a machine which, operating in a cycle, produces no other effect than to transfer heat from a colder to a hotter body"*

This form of the second law is the Clausius statement. It means that in order to transfer heat from a lower temperature to a higher one, work must be done.

A Carnot engine may be conceptually constructed by proposing a cylinder with a frictionless piston at one end, encapsulating an ideal gas. The piston is operated by a motor capable of moving the piston so slowly that its motion causes quasi-static compression and expansion of the contained gas, such that the system is constantly in thermal equilibrium.

In order to produce cooling, these quasi-static compressions and expansions of the ideal gas must occur between two thermal reservoirs of different temperatures, T_H and T_C. The operation of the cycle is as follows:

Firstly, the cylinder is connected with the hot reservoir via a link of infinite thermal conductance. The gas is then compressed quasi-statically from pressure P_1, volume V_1 to pressure P_2, volume V_2. The heat produced, Q_H, is rejected to the hot reservoir isothermally at T_H.

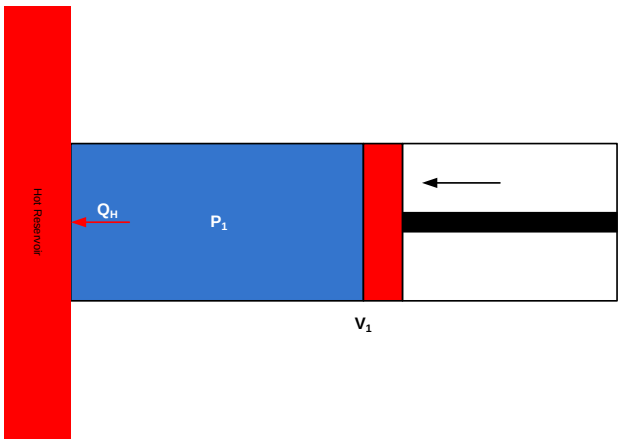

The thermal link to the hot reservoir is then removed, so that the cylinder is thermally isolated and no heat can flow into or out of the system. The gas is then expanded quasi-statically in an adiabatic, isentropic (constant entropy) process to pressure P_3, volume V_3. The temperature of the gas drops to T_C.

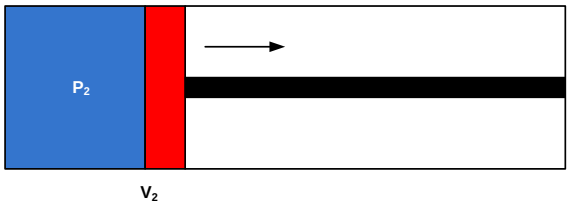

The cylinder is then connected with the cold reservoir via an infinite thermal conductivity link and the gas quasi-statically expanded to pressure P_4, volume V_4. During this process, the cylinder takes in heat Q_C from the cold reservoir isothermally at T_C.

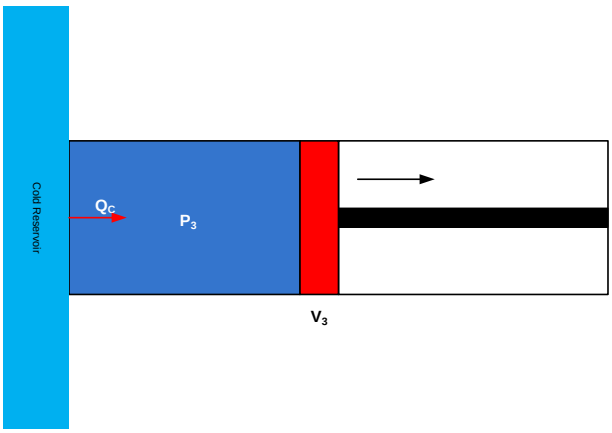

The thermal link to the cold reservoir is then removed, and the gas is compressed, returning to its original state of pressure P_1, volume V_1 and temperature T_H. The cycle is ready to repeat again.

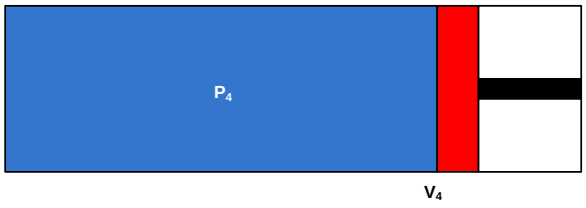

The complete cycle is shown on the pressure-volume plot below in Figure 27. The work required (W) to extract heat Q_C from a cold temperature T_C and reject it at a hotter temperature T_H is given by the shaded area enclosed by the cycle.

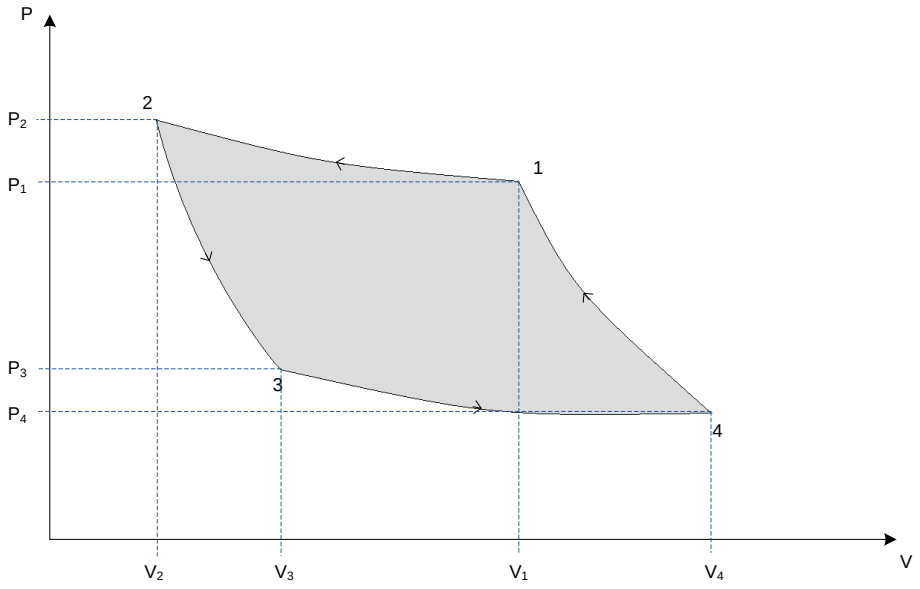

Figure 27: Carnot cycle P-V diagram

The carnot cycle is completely idealised, and represents the absolute maximum limit of cooling efficiency, as it consists of 4 completely reversible processes. Hence, if the cycle is operated in the reverse order to what has been described, it is the most efficient heat engine, and if heat Q_H is supplied to the cycle at T_H, and heat Q_C will be rejected at T_C whilst the engine outputs work W.

The efficiency of the Carnot cooling cycle is:

$$\eta = \frac{Q_C}{W} \tag{2}$$

Which is easily shown to be equal to equation (3) (see Steijaert (25)), which defines the Carnot Coefficient Of Performance (COP):

$$\eta = \frac{T_C}{(T_H - T_C)} \tag{3}$$

The Carnot COP definition shows it is increasingly difficult to cool as the temperature at which cooling is required is decreased.

Any real system will have efficiency below the Carnot COP. This is because in real systems, processes are typically non-reversible, thus some work is lost in increasing entropy. Additionally, non ideal behaviours introduce further losses (such as friction etc).

The efficiency of cryocoolers is typically quoted as a percentage of the Carnot COP. There are several types of cryocoolers used in space cryogenics; the most common are subsequently described.

2.2.3.2 STIRLING COOLERS

Stirling coolers are quite similar to the conceptual Carnot system described above. They exploit the thermodynamic principles of gaseous fluids by containing a fixed quantity of gas (Typically Helium for cryogenic applications) in a closed system and utilising pistons in order to induce pressure and volume changes to generate heating and cooling of the working fluid. The heat produced upon compression of the working fluid is extracted prior to the expansion phase of the cooling cycle, such that cooling may be produced.

Stirling coolers typically cool to around 50K; however, a dual-stage Stirling cooler developed by EADS Astrium UK for AFRL has reached 9.4K [(26)].

The simplest type of Stirling cooler may be thought of as a tube containing:

- Two pistons at each end
- A regenerative matrix between the 2 pistons. A regenerative matrix (regenerator) is a porous structure designed to have a high heat capacity and a low axial thermal conductance. Its function is to store heat imparted to it by the working fluid for part of the cooling cycle, and return it during a later stage.

Regenerator matrices are typically comprised of a stack of fine metal gauze discs.

The Stirling cooling cycle is shown in the familiar P-V diagram form in Figure 28 below:

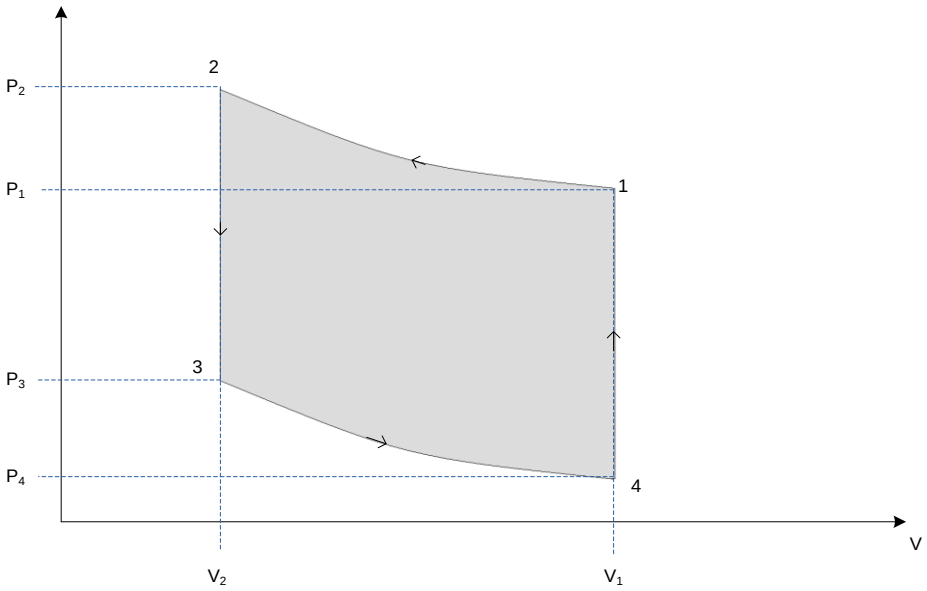

Figure 28: Stirling Cycle P-V diagram

Each stage in the cycle is now described:

1-2: Firstly, piston 1 moves inwards towards piston 2 whilst piston 2 remains stationary. The working fluid is compressed, causing heating. This heat, Q_H, is dissipated isothermally at T_H to the environment via a heat exchanger, which in practice is simply the body of the Stirling cooler compressor. The net effect is an isothermal compression depicted by the isotherm 1-2 on the P-V diagram.

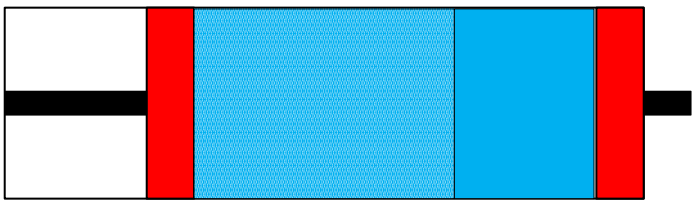

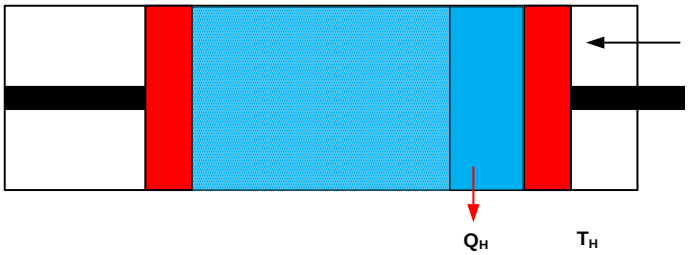

2-3: Piston 1 continues to move inwards towards piston 2, but piston 2 begins to move outwards away from piston 1 at the same rate. This results in the enclosed volume between the pistons remaining constant whilst the working fluid is forced through the regenerator matrix. The heat possessed by the working fluid is given up to the regenerator matrix upon passing through it, such that the gas emerging at the cold end of the regenerator (left on diagrams) is at a lower temperature (T_C) and pressure. This process is represented by the isochore 2-3 on the P-V diagram.

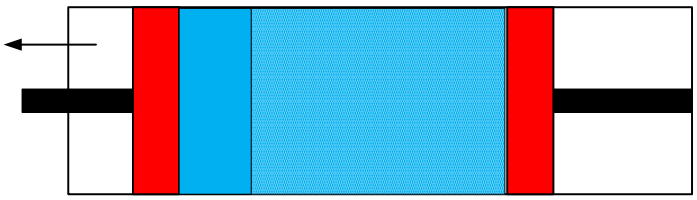

3-4: Piston 2 continues to move outwards away from piston 1 as piston 1 reaches its maximal displacement, thus resulting in expansion of the volume between the 2 pistons, and of the working fluid. The expanding working fluid draws in heat Q_C from its surroundings (i.e. produces cooling at the cold end) in order to maintain its temperature at T_C. This is the only phase of the cycle which actually produces cooling, and is represented by isotherm 3-4 on the P-V diagram.

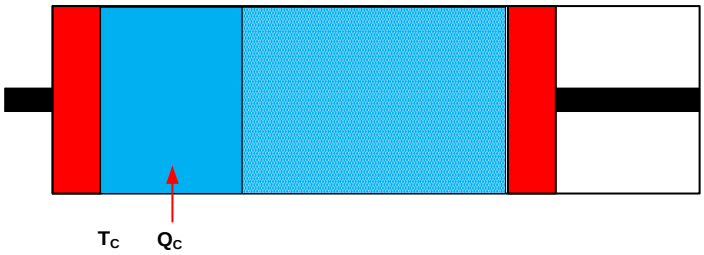

4-1: Finally, as piston 1 moves outwards away from piston 2, piston 2 begins to move inwards such that both pistons move at the same rate, forcing the working fluid back through the regenerator whilst maintaining a constant volume. Here, the heat that was deposited into the matrix by the working fluid in phase 2-3 is picked up again by the working fluid, increasing its temperature and pressure. This is represented by isochore 4-1 on the PV diagram. The cycle returns to its initial state and begins again.

An **ideal** Stirling cooler has the same COP as the Carnot cycle, hence, is inherently the most efficient thermodynamic cooling cycle.

In practise, Stirling coolers do not have two pistons and a fixed regenerator as described above. Instead, the regenerator itself moves as a piston (known as a 'displacer') through the working fluid which is compressed and expanded by a compressor piston.

Typical Stirling coolers for space applications are based on an original design developed by RAL and The University of Oxford for the ISAMS (Improved Stratospheric and Mesospheric Sounder) instrument, known as 'split-type' Stirling coolers. Split-type refers to the separation of the compression and regeneration processes into two separate mechanisms; the compressor and displacer respectively. The linkage between these two mechanisms is provided by a tube, known as a transfer line, which allows the working fluid to move between the compressor and displacer units. The typical 'Oxford' design of a split type Stirling cooler is presented in Figure 29.

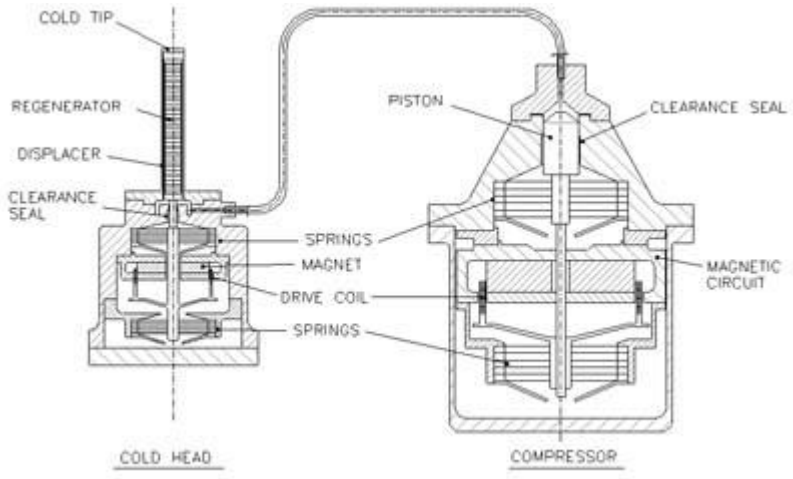

Figure 29: 'Oxford type' split stirling cooler. After (27).

In such a cooler, the Stirling cycle description has the compressor piston as piston 1, and the displacer regenerator as piston 2. The displacer regenerator may move passively (i.e. moved by the force of the working fluid compressing and expanding and restored by a spring) or actively by a small motor, as is shown in the split type design in Figure 29 above.

Stirling coolers have been used extensively for space applications, primarily in Europe by former companies now part of EADS Astrium. A detailed review of the heritage of these coolers may be found in Gibson et al. (28).

2.2.3.3 GIFFORD MCMAHON COOLERS

Gifford McMahon (GM) coolers work in the same way as Stirling coolers, and use the same thermodynamic cycle. However, the pressure variation of the working fluid is controlled differently. In Stirling coolers, a compressor alternately compresses and expands the working fluid in order to create an oscillation in pressure. In a GM cooler, the pressure oscillations are controlled by valves which switch alternately between a high pressure and a low pressure reservoir, provided by external pumps. The high and

low pressure reservoirs are of constant pressure. This allows for increased cooling power, however is much less efficient [29]. The additional complexity of GM systems means they are more massive and less reliable than Stirling coolers. Typically, GM coolers are favoured on ground based cryogenic applications, but Stirling on space based applications.

2.2.3.4 PULSE TUBE COOLERS

Pulse tubes are similar to Stirling coolers, utilising the same regenerative cooling cycle and oscillating pressure wave to move heat. Whilst a stirling cooler has a displacer with a piston/moving regenerator at the cold end, a pulse tube has a compressible gas volume which the working fluid expands against and a fixed regenerator.

Cryogenic pulse tube coolers are all based on the 'Orifice Pulse Tube Cooler' (OPTC), as shown below in Figure 30.

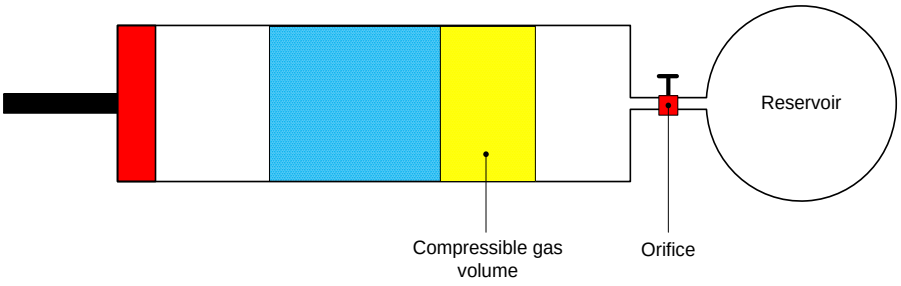

Figure 30: Schematic representation of an Orifice Pulse Tube Cooler (OPTC)

The OPTC has a fixed regenerator and a single piston. The orifice (a flow resistance) connects the main tube section to a buffer (a relatively large volume such that it is at effectively constant pressure). This allows for the phase relationship between the compressor piston pressure wave and moving gas to be offset to produce optimal cooling. The addition of the orifice by Mikulin in 1984 [30] is what gave the pulse tube cooler the performance required to produce cryogenic temperatures [25], [29], [31]. The

orifice has since evolved such that modern pulse tube coolers use inertance tubes to control the phase. The pulse tube operation is briefly described subsequently.

The piston moves inwards, compressing the gas in the tube and rejecting heat Q_{H1} to the environment at the hot end of the regenerator.

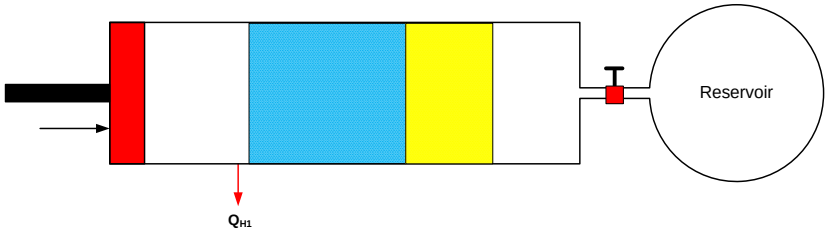

The piston continues to move inwards towards the regenerator, forcing the working gas through the regenerator where it gives up heat to the regenerator matrix. At the same time, the compressible gas volume begins to move towards the reservoir.

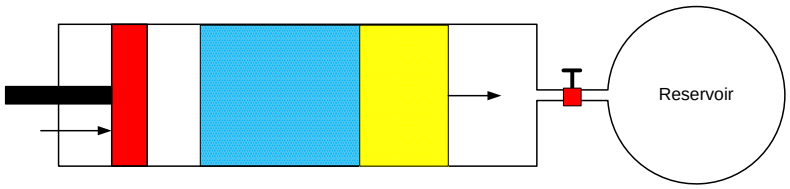

The piston reaches the regenerator and the compressible gas volume continues moving towards the reservoir, such that the working gas volume is expanded and the pressure drops. Heat Q_L is lifted at the cold end of the regenerator, whilst an equal amount of heat Q_{H2} is given up to the environment at the reservoir end of the pulse tube.

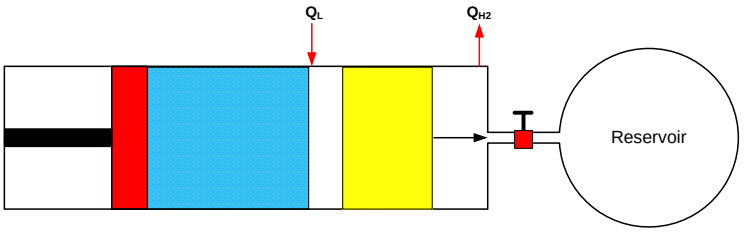

The piston begins to move back to its initial position, followed by the compressible gas volume, forcing the working gas back through the regenerator where the stored heat is returned to the gas.

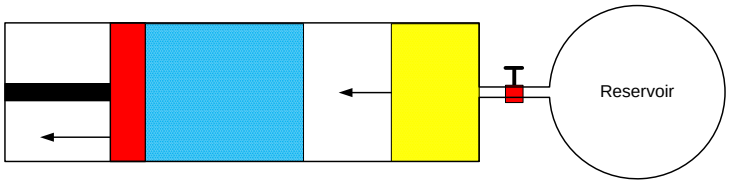

The pulse tube returns to its initial state ready to repeat the cycle (see 1.).

Pulse tubes are increasingly becoming capable of performances to rival Stirling systems, and offer inherent advantage in they typically produce lower exported vibration at the cold interface due to the absence of a mechanism at the cold end. Such an advantage is particularly attractive to missions flying sensitive detectors that must be isolated from vibration. Additionally, the fewer mechanisms a cryocooler has, the fewer failure modes exist; which is highly attractive for space applications. However, there are disadvantages to using pulse tubes for space applications; including far less heritage in comparison to Stirling coolers, and the performance in a gravitational field is only verifiable with the pulse tube aligned vertically. This is because as the pulse tube is aligned away from the vertical axis, their performance decreases, which requires consideration during test/verification on ground.

Pulse tubes have been developed for space use over the past decade by NASA backed programmes and Northrupp Grumman [(32)] and are being developed in Europe by Air liquide [(33)]; although all cryocooler based ESA missions have used Stirling coolers to date.

Pulse tube coolers typically provide cooling at tens of kelvin, but there are Pulse tubes that can reach 2.23K [(25)].

2.2.3.5 JOULE THOMSON COOLERS

Joule Thomson (JT) coolers utilise the Joule Thomson effect to produce cooling. The JT effect is where a gas changes temperature when expanded adiabatically through a throttling valve. A throttling valve is essentially a small pore or similar flow restriction that limits the flow of a gas. This concept may be illustrated by a sealed tube with a wall separating into two sides. The dividing wall has a flow restriction, which could be some kind of porous plug. Each side of the tube contains a piston. This situation is schematically illustrated in Figure 31 below.

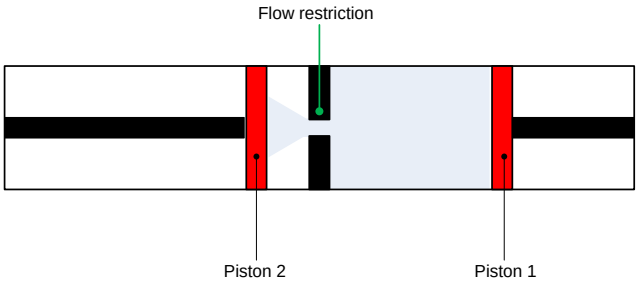

Figure 31: Schematic representation of the Joule Thomson effect

Initially, piston 2 is up against the dividing wall, and piston 1 on the far right of the tube with all the gas in the right hand side. The tube is perfectly insulated such that no heat can be exchanged with the external environment. Piston 1 moves in towards the left, approaching the dividing wall. The gas is forced through the orifice and expands against piston 2, which is retracted at a rate permitting the pressure on the left hand side of the tube to remain constant and the gas to undergo free expansion. The pressure on the left is always less than on the right. Once all the gas is transferred completely to the left side, it has a temperature which is not equal to the temperature of the gas before the expansion when all the gas was on the right. Whether this temperature is higher or lower than the initial temperature depends on the sign of the Joule Thomson coefficient, μ_{JT}, which is defined as the change in temperature T associated with a change in

pressure p at constant enthalpy H (a Joule Thomson expansion is isentropic by definition since it is adiabatic) [34]:

$$\mu_{JT} = \left(\frac{\partial T}{\partial p}\right)_H \tag{4}$$

This can be represented in terms of the easily measureable quantities; temperature T, Volume V and heat capacity C_p:

$$\mu_{JT} = \frac{T(\partial V/\partial T)_p - V}{C_p} \tag{5}$$

A theoretical **ideal** gas has $\mu_{JT} = 0$, hence it exhibits no Joule Thomson effect. The Joule-Thomson effect is observable in all real gases as it arises from the interactions between the molecules of the gas itself.

The concept of the Joule Thomson effect may be well understood by considering the Joule Thomson apparatus in Figure 31 filled with a gas subject to Van der Waals intermolecular interactions. The Van der Waals equation of state may be expanded as a power series in what is known as the virial form of the equation (35):

$$Z = 1 + \frac{1}{RT}\left(b - \frac{a}{RT}\right)p + \cdots \tag{6}$$

Where $Z = p\bar{V}/RT$, a is a term representing the attractive force between molecules, b represents the volume taken up by the molecules (i.e. the volume within V that is not space between the molecules) and $R$is the gas constant. Using the definition for Z, the above equation can be solved for V, so that the Joule Thomson coefficient for a Van der Waals gas may be represented to a first order by:

$$\mu_{JT} = \frac{2a/RT - b}{C_p} + \cdots \tag{7}$$

Such that in the low temperature limit it becomes:

$$\mu_{JT} = \frac{2a}{RTC_p} + \cdots \tag{8}$$

Which is always positive since all its constituents are positive. The positive sign of the JT coefficient translates to a cooling effect. In the high temperature limit, the JT coefficient becomes:

$$\mu_{JT} = -\frac{b}{C_p} \tag{9}$$

Which is always negative, implying a heating effect. Inevitably there is a point of inflexion where the JT coefficient equals zero, known as the *Inversion Temperature*. This may be found by setting $\mu_{JT} = 0$; however, does not give a true result in the first order van der waals approximation as described here, since in reality the inversion temperature depends on pressure.

There are two physical mechanisms which contribute to the Joule Thomson effect. Both arise from the fact that in the free expansion, average intermolecular distance increases and the only source of energy in the adiabatic process is the internal energy of the gas itself. The first mechanism is where the expansion of the gas increases the potential energy of the gas due to the attractive intermolecular forces; since the internal energy must be conserved, the average kinetic energy of the molecules decreases and the temperature drops. The second mechanism arises from the fact that in intermolecular collisions, kinetic energy is temporarily converted into potential energy. As the intermolecular distance increases, there are less collisions per unit time and the average potential energy decreases. Again, conservation of total energy requires that the kinetic energy must increase, resulting in a temperature increase.

Clearly, the first mechanism dominates below the inversion temperature and the second mechanism dominates above the inversion temperature. This can be seen from the low temperature limit form of the Van der Waals gas Joule Thomson coefficient, where it

depends on the attraction term a, which is absent in the high temperature limit expression.

For cryogenic cooling, Helium is typically used as is the case in most cryogen based coolers. However, its low inversion temperature requires the gas be pre-cooled sufficiently to be at a temperature below the inversion temperature upon the actual free expansion phase. This precooling is typically achieved by using counterflow heat exchanging pipes which are heatsunk at intermediate temperature stages between the cold (Joule Thomson) stage and the ambient temperature, as in Figure 32.

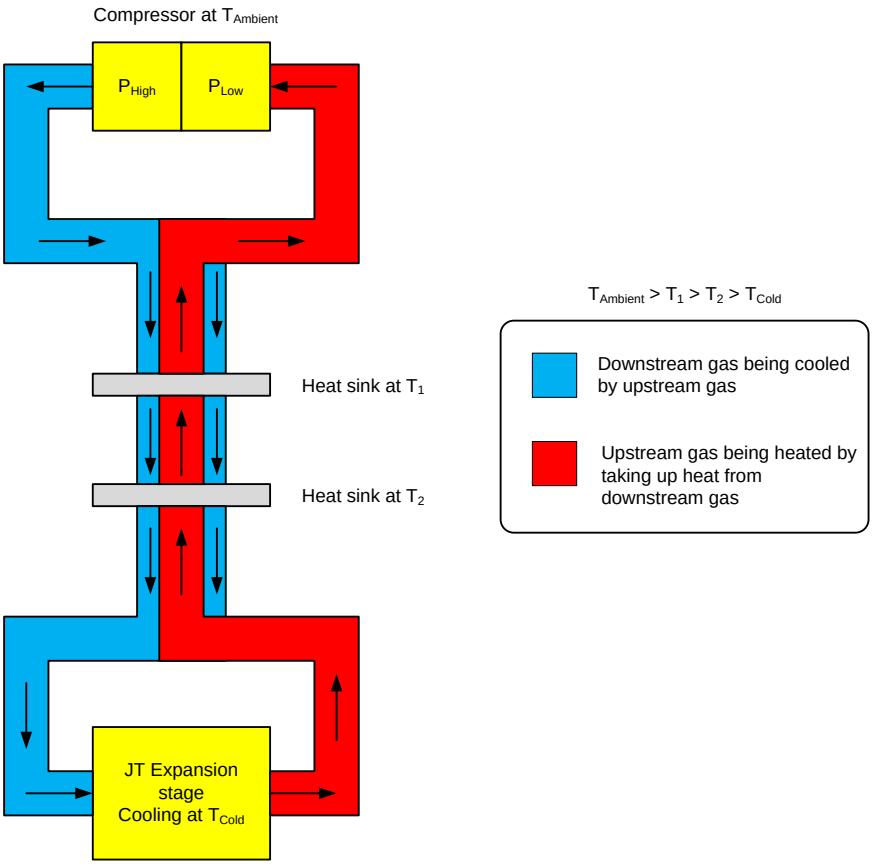

Figure 32: Counterflow heat exchanging and heat sinking in a JT cooler.

The complete JT cycle may be represented on an Entropy-Temperature plot, as in Figure 33.

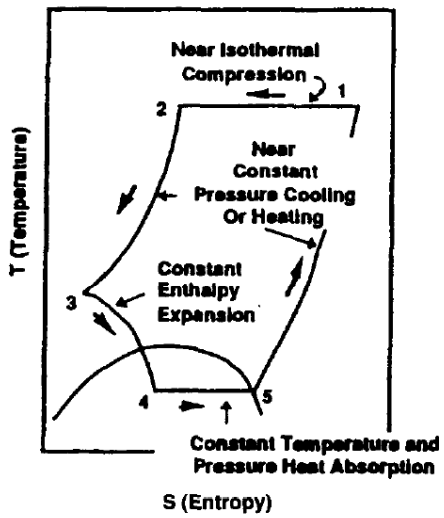

Figure 33: Temperature-Entropy variation during Joule Thomson cooling cycle. After (36).

In 2009 a Joule Thomson cooler developed at RAL in association with EADS Astrium UK was successfully flown on the Planck mission, and remains operational providing ~17mW mW of cooling at ~4K [37].

2.2.4 Passive Cooling

Passive cooling by definition requires no work input to produce cooling. This is achieved by radiating heat into cold space directly. The heat produced by all cryogenic cooling systems in space ultimately radiates to space, however, passive cooling relies on the ability to radiate sufficient energy to space to allow cryogenic temperatures to be produced. Hence, the radiating 'device' must be isolated from the view of any solar, planetary or albedo radiation by appropriate orientation and thermal baffles. Typically, passive cooling is achieved by external radiators mounted on the spacecraft.

2.2.4.1 Radiators

Spacecraft radiators rely on the emission of infrared radiation to reject heat to space. A radiator radiates according to [14]:

$$Q = \sigma \varepsilon A T^4 \qquad (10)$$

Which shows clearly that the radiated heat Q (cooling power) is dependent on the radiator emissivity ε, the surface area A and most strongly on the temperature T (weighted by the Stefan boltzman constant, σ).

The strong temperature dependence means that cooling power is reduced significantly with decreasing temperature. In practise, useful cooling cannot be obtained below ~60K [38], as the area of radiator required increases such that the necessary support structure introduces parasitic heat loads that outweigh the cooling capability. The typical performance of thermal radiators on earth-orbiting satellites is shown in Figure 34.

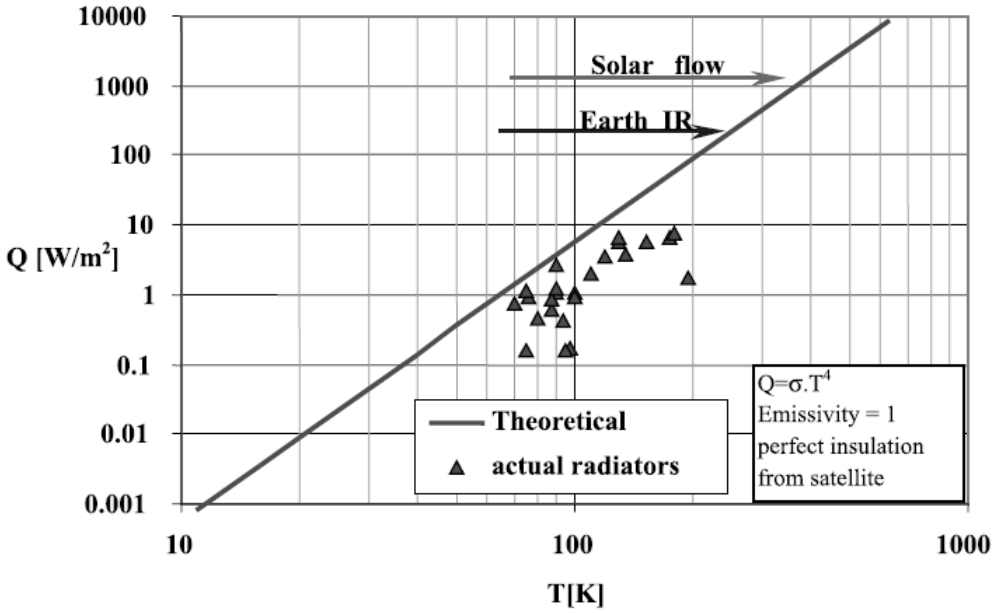

Figure 34: Typical radiator performance in the earth orbiting case. After (14).

In order to maximise heat rejection, radiators are typically coated with a high infrared emissivity coating $\varepsilon > 0.8$ which also has a low solar absorptance ($\alpha < 0.2$) to minimise the effect of any incident stray solar radiation. Such surface finishes include quartz mirrors, aluminised Teflon or white paint.

Radiators are used in one form or another for thermal control on all spacecraft. They may be dedicated radiators in the form of fixed or deployable panels, or an existing structural wall used as a radiator.

2.3 CRYOGENIC COOLING - TEMPERATURES <1K

Passive cooling is limited to several tens of Kelvin, and mechanical cryocoolers cannot cool below a few Kelvin. Hence, for applications requiring sub-Kelvin (in particular, millikelvin) cooling, different active cooling technologies are required.

Cryogen cooling using Helium can at best cool to 0.25K as discussed in 2.2.1, but requires the vapour pressure to be reduced. In space, this is achieved by a sorption pump, in a system known as a sorption cooler. The sorption cooler and other main cryogenic cooling technologies capable of achieving sub-Kelvin temperatures are described subsequently.

2.3.1 SORPTION COOLERS

A sorption cooler is essentially a recyclable pumped liquid cryogen bath suitable for space use. The system is a closed system, such that the cryogen gas is recycled after evaporation by re-condensing into a liquid. The cryogen vapour pressure is reduced using a sorption pump, which allows a Helium-3 based sorption cooler to cool down to ~300mK. The sorption pump is typically a vessel containing a material engineered to adsorb the working cryogen gas at the correct temperature. A schematic of a sorption cooler is given in Figure 35.

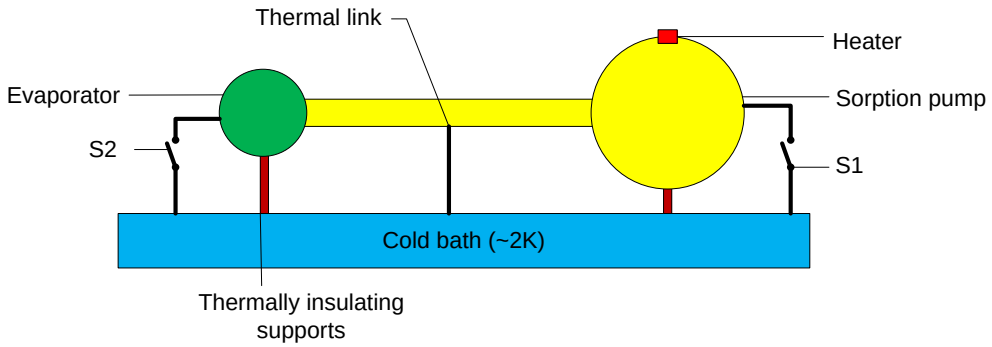

Figure 35: Sorption cooler schematic.

Initially, the complete system is at the temperature of the heat bath to which it is attached. This heat bath may be provided in practise by stored cryogens, mechanical

coolers or a Joule Thomson cooler. The operating cycle of the sorption cooler is as follows:

1. Heat switches S1 and S2 are closed, such that the system is at the temperature of the heat bath (~2K - 4K). All of the working gas is adsorbed within the sorption pump.

2. The heat switch S1 is then opened, such that the sorption pump is thermally decoupled from the heat bath. The sorption pump is heated via an integral heater, such that the gas within desorbs and the vapour pressure increases. As the vapour pressure increases, the warm gas moves down the pump tube to the cold evaporator where it condenses to form liquid.

3. Once all the gas is desorbed from the sorption pump, the evaporator contains liquid at the temperature of the heat bath. Heat switch S1 is then closed whilst S2 is opened. This thermally isolates the evaporator from the heat bath, and allows the sorption pump to cool to the temperature of the heat bath and hence reduce the vapour pressure such that the liquid in the evaporator boils (and provides cooling) at a lower temperature. The sorption pump adsorbs all the vapour, and cooling is provided while the liquid cryogen evaporates. Once this is complete, cooling cannot continue and the cycle must be restarted.

Sorption coolers are under development for space use at CEA-SBT (Commissariat à l'Énergie Atomique et aux énergies alternatives - Service des Basses Températures), France, where they are being combined with another type of cooling technology, Adiabatic demagnetisation Refrigerators [(39)] (A type of magnetic cooling, see 2.3.3 and Chapter 3). The sorption cooler cannot cool below ~250-300mK by itself, hence must

always be combined with some other technology to reach lower temperatures such as would be required by the IXO XMS.

2.3.2 DILUTION COOLERS

Dilution coolers/refrigerators offer the only method by which liquid cryogens can produce cooling in the sub-centurian milliKelvin range. They rely on the spontaneous phase separation that occurs when a mixture of the two different Helium isotopes, Helium-3 and Helium-4 (as discussed in 2.2.1.1) is cooled below ~0.86K (40). The phase diagram for a He-3/He-4 mixture is shown in Figure 36.

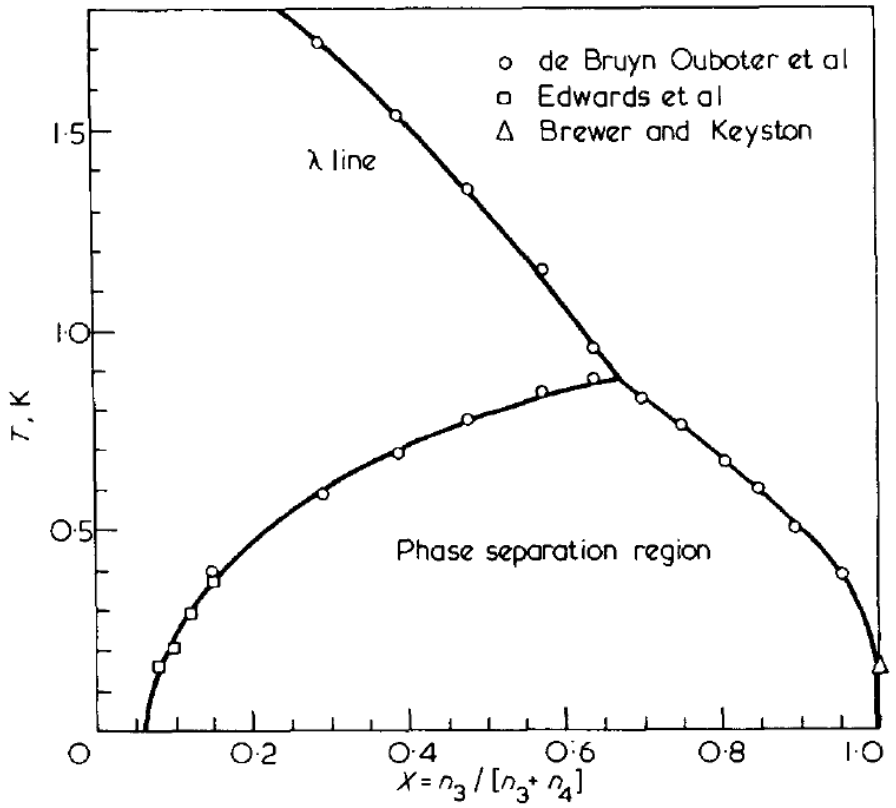

Figure 36: Helium-3/Helium-4 mixture phase diagram. x-axis is molar fraction of Helium-3, y-axis is temperature. After (40).

The phase separation manifests itself as a Helium-3 rich (concentrated) phase floating on top of a Helium-3 poor (dilute) phase, in equilibrium in a similar way to a liquid/vapour equilibrium. Hence, the chemical potential of Helium-3 is equal in both

phases. The Helium-4 is superfluid (below the λ line) in the dilute phase only. The phase diagram shows that even at absolute zero, the dilute phase will still consist of ~6% Helium-3. The superfluid properties of Helium-4 means that it can be effectively neglected, and the dilute Helium-3 treated as a gas of quasiparticles [(40)].

It can be shown that the enthalpy of Helium-3 in the two phases is different (see Radebaugh and Siegwarth (40)); the enthalpy in the concentrated phase is equal to the enthalpy in the dilute phase plus the heat of 'vapourisation' – the energy required to move the quasiparticles from the concentrated (liquid) phase to the dilute (gas) phase. Thus, if equilibrium is disrupted by removing Helium-3 from the dilute phase, Helium-3 will move from the concentrated phase into the dilute phase in an attempt to restore it. During this process (which is essentially pumping to reduce vapour pressure), as the Helium-3 makes the phase transition, it absorbs heat from the environment. This is how a dilution refrigerator cools. A schematic of a dilution refrigerator is shown in Figure 37.

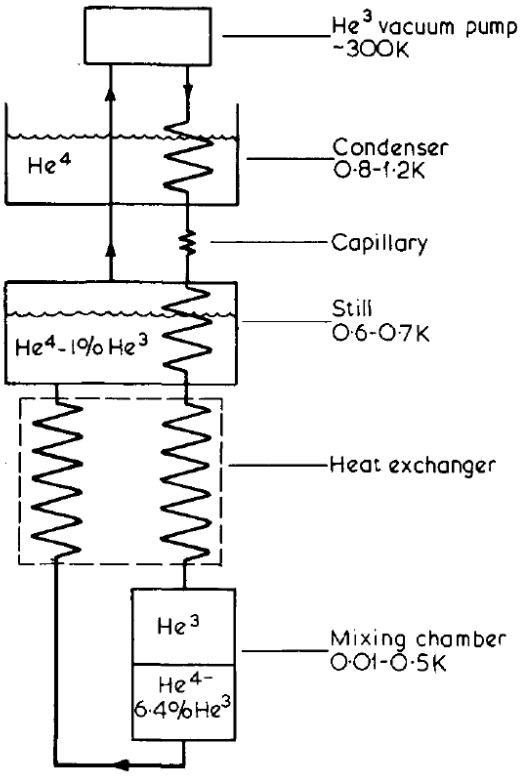

Figure 37: Schematic of a Dilution cooler. After (40).

The mixing chamber is where the phase separation and cooling effect occur. The diagram shows how the Helium is precooled before entering the mixing chamber.

Helium-3 gas is circulated by an ambient temperature vacuum pump, which pumps the Helium-3 vapour out of the dilute phase in the mixing chamber, down into the dilution refrigerator. The operation principle is briefly described subsequently in the form of a brief overview, however a detailed explanation is provided in Radebaugh and Siegwarth (40).

Starting from the ambient temperature pump stage of the cycle, the Helium-3 gas is typically cooled by passing through liquid Nitrogen and liquid Helium (or other cryocooler-cooled) stages (not shown on figure) before entering the condenser, or '1K pot'. This is a pumped Helium-4 chamber with a typical temperature of 0.8-1.2K, which cools the incoming Helium-3 gas sufficiently to condense it into a liquid, aided by the high pressure of the compressed Helium-3 gas (25 – 200 torr (40)). The gas is compressed as it is pumped into a volume with a flow restriction (capillary tube) at its only exit (between the condenser and the still). The liquid Helium-3 passes through the capillary tube through a 'still', where the pressure on the liquid is reduced. The still contains almost pure Helium-4 liquid at 0.6-0.7K and provides pre-cooling to the incoming Helium-3 liquid. Finally, the Helium-3 liquid flows through a heat exchanger where it exchanges heat with cold Helium-3 vapour leaving the mixing chamber, cooling further. The liquid Helium-3 leaves the cold end of the heat exchanger, entering the rich phase in the mixing chamber, allowing continuous dilution to produce cooling. Cooling is produced within the mixing chamber by the phase separation mechanism described previously. The vapour from the dilute phase is pumped out via the heat exchanger (where it heats by cooling the incoming Helium-3 liquid entering the mixing chamber)

into the still, where it is heated to 0.6-0.7K, such that the condensed liquid Helium-3 has a vapour pressure much larger than Helium-4. The gas returning to the pump is then almost pure Helium-3.

There have been several recent efforts to adapt dilution cooler technology for space use [41], [42] due to their attractive continuous cooling and lack of magnetic fields (unlike magnetic coolers). Naturally, dilution refrigerators require gravity to induce the liquid/vapour phase boundaries and to aid the flow of Helium around the cycle hence there are significant challenges in adapting this technology for space. However, an open-cycle dilution refrigerator is implemented on the Planck HFI instrument [43] cooling to ~10mK, however its lifetime is limited to ~3 years as the Helium vents out to space. A more efficient, longer-life, closed-cycle dilution cooler is being developed for the consideration of the SPICA and IXO missions [44], however, it is considerably difficult to produce a dilution cooler that can operate in zero gravity in a closed cycle configuration.

2.3.3 MAGNETIC COOLERS

Magnetic coolers utilise changes in entropy that occur in certain paramagnetic materials upon magnetisation and de-magnetisation to produce cooling. There are two types of magnetic cooler; the Adiabatic Demagnetisation Refrigerator (ADR) and Nuclear demagnetisation based cooling. The first type uses the entropy associated with molecular ionic magnetic moments (spins), the second uses the entropy associated with nuclear spins. ADRs are capable of cooling to tens of milliKelvin, and are under recent development for space use due to their inherent simplicity and high reliability. ADRs are the focus of the next chapter, where their comparative simplicity to dilution refrigerators and sorption coolers is made clear.

An ADR has successfully flown on Suzaku in 2005, successfully providing a 60mK environment to the XRS (X-Ray Spectrometer) instrument [45] before the Helium

reservoir (heat bath for the ADR) was unfortunately vented into space. Nuclear demagnetisation coolers are capable of cooling to microKelvin, and are not required for current space applications, hence will not be discussed further.

The MSSL cryogenics department is a leading space ADR authority, and have designed and built a space-qualified engineering model ADR (The 'ESA' ADR) with the IXO mission predecessor (XEUS) in mind. This thesis details the technical development required to improve the ESA ADR (and derived future systems) performance to meet the IXO mission (and future mission) cooling requirements. ADRs are the focus of Chapter 3 in this thesis.

2.4 CHAPTER SUMMARY

It is clear there is a requirement for cryogenic cooling in space. The environment experienced by a spacecraft in flight was shown to introduce several further considerations that must be respected by space cryogenics engineers. Such considerations include the vacuum of space, and the thermal radiation incident on the spacecraft due to solar emission, planetary emission and albedo reflection. This thermal radiation heats up the parts of the spacecraft upon which it is incident, and can lead to sharp temperature gradients across a spacecraft with cold parts in view of only deep space. Thus, the spacecraft must be maintained in a controlled thermal condition, typically of the order ~300K. Hence, stable cryogenic temperatures required by instruments such as the IXO XMS must be produced by dedicated cooling equipment.

Any cryogenic equipment on board a spacecraft must survive the harsh launch environment, where it will be subjected to various vibrations and shocks, as well as depressurisation upon ascent. Thus, intensive qualification regimes are required to ensure space cryogenic equipment will survive and remain fully functional during mission operations.

Early cryogenics missions utilised the familiar evaporative cryogen based cooling. Such cooling methods have lifetime limitations which render them unattractive for most modern missions, where long (>~5 year) lifetimes are increasingly required. The cooling that would be provided by cryogen based cooling can also be provided by several types of mechanical coolers, such as Stirling coolers, Pulse tube coolers and Joule Thomson coolers as well as passive radiators.

The very low (milli-Kelvin) temperature required by some instruments such as the IXO XMS are unachievable with passive or mechanical cooling technologies. Technology that exploits the properties of Helium may be used to obtain cooling down to a few hundred

milliKelvin (sorption coolers). However, by exploiting the properties of a Helium-3/Helium-4 mixture below a critical temperature of ~0.86K, a dilution cooler can cool down to tens of milliKelvin. These coolers are quite complex, and though being developed for space use, present inherent design challenges which must be overcome in order to produce a viable space cooler. However, the complexity of dilution refrigerators implies inherent low reliability in comparison to Adiabatic Demagnetisation Refrigerators (ADRs).

ADRs are a simple space-demonstrated technology capable of cooling at milliKelvin temperatures. The ADR is the focus of this thesis, and is described in the following chapter.

The suite of cryogenic cooling technologies available to the space cryogenics industry is illustrated in Figure 38.

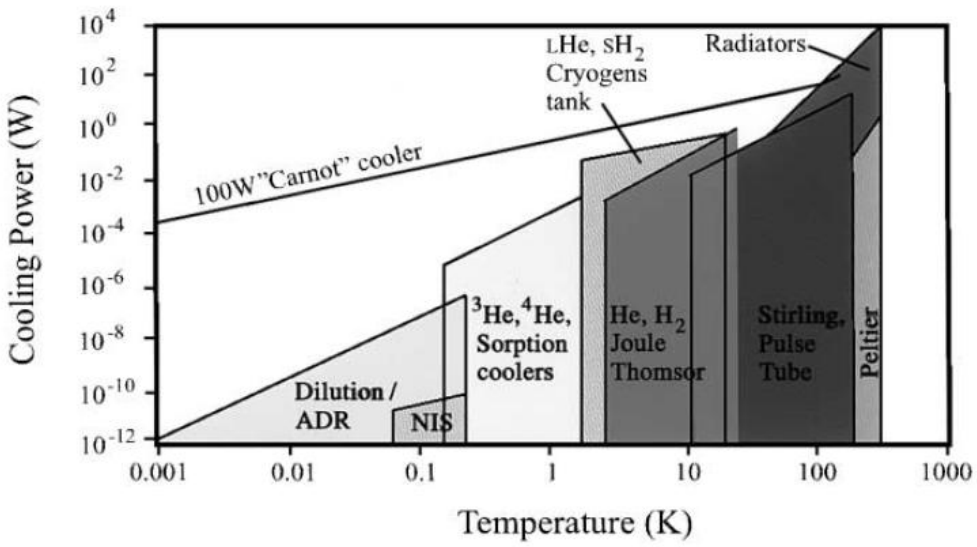

Figure 38: Typical performance and temperature ranges of Space cryogenic cooling technologies. After (14).

Figure 38 shows how in order to achieve the cooling requirements of instruments such as the IXO XMS, a 'cooling chain' of several cooling technologies must be employed, as

each technology only covers a small portion of the temperature range from the ambient spacecraft temperature down to the instrument temperature. This thesis details the development and analysis of a potential cooling chain to support the IXO XMS in chapter 6.

Chapter 3:

ADIABATIC DEMAGNETISATION REFRIGERATORS

Thus far, chapter 1 has presented the science goals for IXO and shown the need for X-ray microcalorimeter instruments such as the IXO XMS in space. The requirements for such instruments to be cryogenically cooled led to an overview of space cryogenics presented in chapter 2, where magnetic cryocoolers, ADRs, were presented as a demonstrated successful technology for cooling milli-Kelvin instruments.

This chapter describes ADRs in detail, beginning with the principle of their operation, magnetic cooling. The theory of ADR operation and their key components are described. ADR systems under development for space are discussed, including the MSSL ESA ADR, which was originally developed for XEUS. The performance of the ESA ADR is reviewed against the requirements, and it is shown that a substantial performance increase may be obtained by replacing one of the component heat switches with a new technology; a magnetoresistive heat switch.

Finally, ADR systems that are currently under development targeting the IXO XMS instrument are discussed, including a modified version of the MSSL ESA ADR.

3.1 INTRODUCTION TO ADRS

As stated in the previous chapter, ADRs are a type of magnetic cooler capable of providing milli-Kelvin cooling for space applications. This section gives a brief overview of the history and theory behind ADRs

3.1.1 INTRODUCTION TO MAGNETIC COOLING

In 1905, Langevin stated that for paramagnetic materials, magnetisation changes are generally accompanied by reversible temperature changes [(46)]. Not much more was developed on the subject until 1926, when data from various experiments combining low temperatures and magnetisations were gathered, leading to the conclusion that it was possible to utilise the 'magnetocaloric effect' to reach temperatures significantly below 1K. This realisation was made independently by both Giauque and Debye [(46)].

Kurti and Simon showed in 1933 that their measurements of the specific heat of gadolinium sulphate indicated this substance was highly suited to cryogenic cooling applications [(46)]. Giauque, in that same year, used gadolinium sulphate to cool down to 0.53K from 3.4K, with a magnetic field of 6.37×10^{5} Am^{-1} (8000 Oe in original source) [(46)]. Since this first success, magnetic cooling has evolved significantly with the wider availability of cryogenic fluids such as liquid Helium, and together with the advent of superconducting magnets, has become a common laboratory technique for achieving sub-Kelvin temperatures.

Their lack of moving parts means magnetic coolers, ADRs, are highly reliable, and can be re-cycled without suffering any wear or fatigue. In addition, they export no vibrations or motion forces. These properties means that ADRs are highly suited to milli-Kelvin space cryogenics applications such as cooling detectors like the IXO XMS.

3.1.2 PRINCIPLE OF MAGNETIC COOLING

Magnetic cooling exploits the magnetocaloric effect in paramagnetic substances in order to cool from temperatures on the order of a few Kelvin down to sub-Kelvin temperatures. A paramagnetic substance is one that gains magnetic properties in the presence of an externally applied magnetic field, due to unpaired electrons in the molecules/atoms providing a magnetic dipole which can be controlled by an external field. Paramagnets have a positive magnetic susceptibility. The magnetocaloric effect in certain materials allows for cooling down to the milliKelvin regime, as subsequently described.

In order to achieve a magnetocaloric effect that can provide effective milliKelvin cooling, a material is required that satisfies the condition of remaining approximately 'ideally paramagnetic' down to 1K [46]. The magnetic moments associated with the atomic electrons of such a substance are bound by extremely weak forces due to the presence of the vanishingly small interaction magnetic field, B_{Int}, hence they are essentially free to orient themselves randomly into any one of the available directions [46], [47]. The number of spatial orientations available to the magnetic moments is governed by the total angular momentum number J, and is limited to the degeneracy of the magnetic ion $(2J+1)$ [46]. The entropy S of such a paramagnetic substance comprises two components; the magnetic entropy, S_M, and the non-magnetic entropy of the lattice, $S_{Lat.}$, which is negligible in the temperature range of interest (<~4K) such that the magnetic entropy dominates.

$$S = S_M + S_{Lat.} \tag{11}$$

One mole of paramagnetic substance will possess a magnetic entropy of $S_M = R\ln(2J+1)$ [46], [47], where R is the ideal gas constant.

Supposing a suitable paramagnetic material has an initial temperature T_0 of the order of 1K, the difference in energy between each of the energy levels corresponding to adjacent spatial orientations is $U = g\beta B_{Int}$, where $U \ll k_B T_0$, g is the Landé splitting factor[7], β is the Bohr magneton[8] and k_B is the Boltzmann constant. The probability of the magnetic moment adopting a particular orientation is determined by the Boltzmann factor, $e^{U/k_B T}$ [(47)], which clearly depends on the ratio of the splitting between the energy levels of differing magnetic moment orientations to the thermal energy . If the temperature is decreased sufficiently (typically, the sub-kelvin range), the thermal agitations will eventually become small in comparison to the weak magnetic restraining forces, i.e. when T tends to zero, $k_B T_0 \ll U$, and the restraining forces will be sufficiently strong as to limit the number of spatial orientations available to the magnetic moments. The system will become more ordered as the magnetic moment of each paramagnetic ion is forced to occupy the direction associated with the lowest energy level. As a result, the magnetic entropy will decrease below $S_M = R\ln(2J+1)$ as the system tends towards a single ground state. The transition to a completely ordered magnetic state occurs at the material-specific ordering temperature (see 3.1.5.1) and is accompanied by a sharp drop in entropy.

This ordering effect can be reproduced at temperatures in the liquid Helium regime by application of an external magnetic field. This is the fundamental basis of the mechanism of magnetic cooling using the magnetocaloric effect. The presence of a sufficiently strong applied magnetic field, B_1 (on the order of 1 Tesla or more), causes the separation between each spatial/magnetic orientation energy level to 'artificially' increase sufficiently to be greater than the thermal agitation energy; $U \geq k_B T_0$ [(46), (47)].

[7] Lande splitting factor g: Material-specific constant depending upon electron spin and orbital momentum quantum numbers (see (46) for full definition). A larger g implies a greater change in entropy for a given change in magnetic field.

[8] Bohr Magneton: Physical constant defining the electron magnetic dipole moment $\beta = e\hbar/2m_e$ where e is the electronic charge, $\hbar$the reduced Planck constant and m_e the electron mass.

The effect is that the magnetic field increases the magnetic restraining forces acting upon the magnetic moments of the paramagnetic ions. Thus, the magnetic ions are forced to occupy the lowest energy states, which are those with a spatial orientation parallel to the external field [47]. As with the previous situation where the temperature was reduced, the magnetic entropy is significantly reduced below $S_M = R\ln(2J+1)$ due to the induced magnetic ordering. This effect is illustrated in Figure 39 in terms of the energy level populations (Initial state shown on the left; state with applied magnetic field shown in the centre), where the applied magnetic field is acting in the direction towards the top of this page.

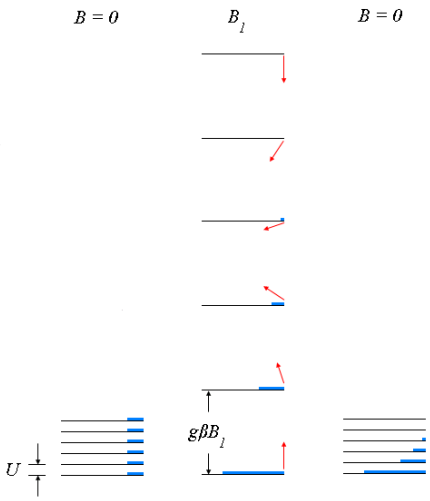

Figure 39: Illustrates how magnetic ordering is induced in a paramagnetic material under application of an external magnetic field and subsequently retained upon its removal. Image adapted from (47).

The magnetisation process shifts the magnetic moments of the paramagnetic ions into alignment with the external field. This can be thought of classically as a 'torque' acting upon the magnetic moments. This 'torque' imparts kinetic energy onto the magnetic ions in order to change their orientation, which naturally increases the thermal energy and causes the substance to heat up. What is happening is as the magnetic field

increases the level splitting (thereby increasing the energy of the upper levels), ions in the higher energy levels drop to lower energy levels, releasing the energy imparted by the magnetic field as heat. The ions then populate the lowest energy levels which are in line with the applied magnetic field.

3.1.3 MAGNETIC COOLING CYCLE

In order to achieve cooling, the magnetisation process must be carried out *isothermally*. The heat of magnetisation is ideally removed as soon as it is produced; hence the substance remains at a constant temperature. Once the system is ordered, it is then thermally isolated, thus allowing for a subsequent *isentropic* demagnetisation process. Such an isentropic process is adiabatic by definition, since $\Delta S = \int dQ/T$ [47] by the first law of thermodynamics. Removal of the external magnetic field collapses the energy level splitting back down to its original spacing; however the isentropic nature of the process ensures the magnetic ordering (energy level population) is retained, as shown on the right in Figure 39. As the thermal energy is again comparable to the splitting between energy levels associated with different spatial orientations, the magnetic moments begin to re-orient, thus converting their thermal energy into magnetic energy. The product of this is that the temperature of the substance falls, thus achieving the cooling effect. Figure 40 shows how the temperature and entropy of a paramagnetic material varies during the processes of isothermal magnetisation and isentropic demagnetisation.

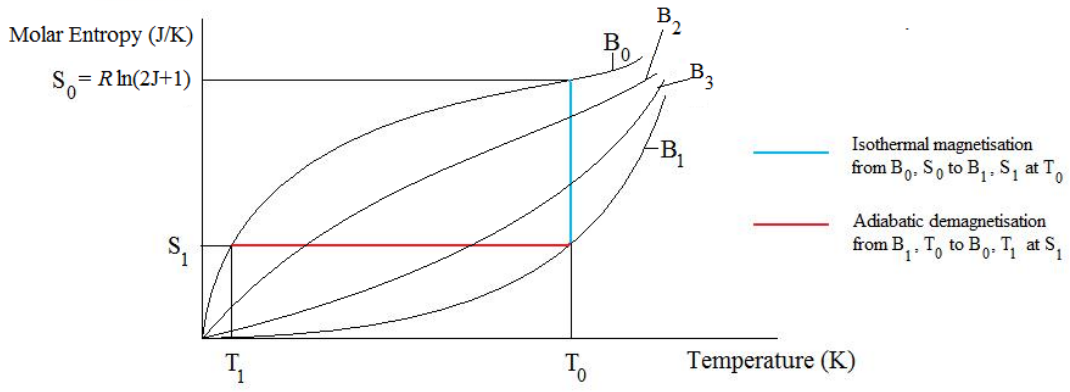

Figure 40: Variation of entropy with temperature during the isothermal magnetisation and adiabatic demagnetisation phases of the magnetic cooling cycle. Image adapted from (47).

The isentropic nature of the demagnetisation process means the initial degree of order is the same upon removal of the magnetic field as when the sample was fully magnetised. Hence, the distribution functions at each phase are required to be equal, thus, from Figure 40, we see:

$$e^{g\beta B_1/k_B T_0} = e^{g\beta B_0/k_B T_1} \tag{12}$$

Thus the final temperature must be:

$$T_1 = \frac{B_0\, T_0}{B_1} \tag{13}$$

This equation is a little misleading - if the external magnetic field is reduced to zero, T_1 will not equal zero because the magnetic dipoles interact with their weak interaction field, B_{Int}. This interaction can be accounted for by the following equation [48].

$$T_1 = \frac{(B_0^2 + B_{Int}^2)^{1/2}}{(B_1^2 + B_{Int}^2)^{1/2}} T_0 \tag{14}$$

The engine that drives the magnetic cooling cycle as it has been described is the Adiabatic Demagnetisation Refrigerator, or ADR. The focus of this thesis is on working towards the development of technology for an ADR for cooling the IXO XMS.

3.1.4 ADRs

ADRs are simple devices. A schematic representation of the basic ADR is shown in Figure 41.

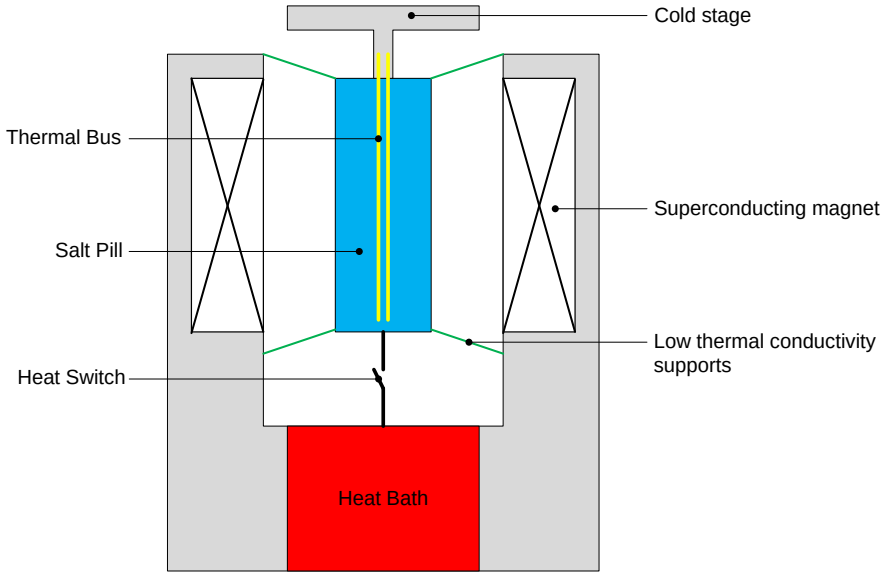

Figure 41: Basic ADR schematic.

At the heart of the ADR is the paramagnetic substance, the refrigerant, contained within a sealed enclosure known as a Salt Pill. The salt pill is suspended by low thermal conductivity supports, and connected to the cold (sub-kelvin/millikelvin) stage, or cold finger, by a highly conductive thermal bus. The thermal bus is typically multiple wires of high-thermally conducting Copper running through the salt pill, and anchored to the cold finger. The salt pill is also connected to a heat bath via a heat switch, a device which allows thermal conduction and isolation to be achieved at the appropriate points in the cycle (heat switches are discussed in further detail in section 3.1.6). The heat bath may consist of a cryogenic fluid such as liquid Helium, or a mechanical cooling device such as a pulse tube or Stirling cooler (see chapter 2). Typically the heat bath will provide a temperature reservoir of between 1K and 4.3K, and is also used to cool the superconducting magnets that control the magnetisation/demagnetisation of the salt

pill. ADR magnets have not been discussed in this thesis; however, Emes (15) provides a detailed discussion.

There are several types of ADR, depending on the arrangement of multiple salt pills and modes of operation. Some of these are discussed in sub-section 3.2.1.

3.1.5 SALT PILL

The most important component in an ADR system is the salt pill. The salt pill contains the magnetocaloric paramagnetic refrigerant that provides the cooling. The paramagnetic material may be in the form of a single crystal, which is grown around the wires of the thermal bus linking the paramagnetic refrigerant to the ADR cold stage, or powder compressed into a semi-solid rod around the thermal bus. Other salt pill configurations include loose powder packed into a container, with a substance added to improve the heat transfer between the thermal bus and the magnetocaloric material.

The salt pill is hermetically sealed to prevent any loss of water of crystallisation in hydrated salts, which serves to aid the cooling mechanism by reducing the interaction between magnetic ions, as will be discussed in the following paragraphs.

3.1.5.1 PARAMAGNETIC MATERIALS

In order to be a suitable candidate for magnetic cooling, the paramagnetic substance must contain paramagnetic ions which have a non-zero resultant angular momentum, or magnetic moment [47]. As previously stated in section 3.1.2, the dipole-dipole exchange interaction between magnetic ions should be sufficiently weak so that the energy level splitting between different orientations, U, is much less than $k_B T$ at ~1K. The induced energy level splitting, $g\beta B$, caused by application of a ~1Tesla external field should be greater than $k_B T$. Any higher energy levels should be high enough that they are quenched in the presence of no applied field, so as they have negligible effect on the distribution function. Providing these conditions are met, the material obeys Curie's law

to a reasonable approximation, for temperatures down to $T \sim \theta = U/k_B$ [47]. The temperature θ is the temperature at which the magnetic ions become fully ordered, and enter either a ferromagnetic or antiferromagnetic state, depending on the properties of the material. The ordering temperature represents the limit of cooling. This temperature is known as the *Néel* temperature for transitions to antiferromagnetism, and the *Curie* temperature for transitions to ferromagnetism.

Elements with an unfilled, partially shielded inner electron shell usually have the ability to possess suitable magnetic ions for producing magnetic cooling. Such elements usually fall into the categories of the transition elements, where suitable 'magnetic' electrons are located in the 3d shell, and the rare earth elements, where the 'magnetic' electrons are found in the 4f shell [46]. The magnetic ions within such elements are typically used to form salt compounds (hence the term *salt pill*), but some are formed into garnets and perovskite compounds.

The non-magnetic ions and water of crystallisation within a hydrated salt serve to increase separation between the magnetic ions, thereby reducing the interaction between them. This decreases the splitting of the lower energy levels, lowering the temperature at which the system orders and the sharp drop in entropy occurs (the ordering temperature). This usually results in lower achievable demagnetisation temperatures.

The amount of heat energy a paramagnetic refrigerant can absorb determines how long the desired cold temperature can be maintained [46]; the *hold time*.

The heat energy that can be absorbed by the material is calculated via integration of the heat capacity [46]:

$$Q = \int C dT = \int T dS \qquad (15)$$

The integration of the temperature over the entropy can be seen to be the area between the zero field curve (B_0 line for the heat that can be absorbed once the salt pill is completely demagnetised), and the entropy axis on the graph in Figure 40. Hence, the quantity of heat that can be absorbed is greater for larger values of T_1, the temperature at which the sharp drop in entropy occurs and the system orders. Thus, low demagnetisation temperatures and long hold times are generally mutually exclusive [(46)], and the paramagnetic refrigerant must be carefully chosen according to its application.

Modelling the magnetic ions as completely free, i.e. ignoring any interaction effects and assuming the zero-field entropy is $S_M(0,T) = R\ln(2J+1)$, independent of temperature; the entropy as a function of external magnetic field, B, and Temperature, T, can be derived [(46)]:

$$\frac{S(B,T)}{R} = \ln\left[\frac{\sinh(2J+1)\,x/2}{\sinh x/2}\right] + \frac{x}{2}\coth\frac{x}{2} - \frac{(2J+1)x}{2}\coth\frac{(2J+1)x}{2} \qquad (16)$$

Where $x = g\beta B/k_B T$. This is the *Free Ion Approximation*. It holds for hydrated salts with negligible interaction between magnetic ions.

In order to maximise the energy that can be absorbed by the salt pill, the magnetic material must have as large a *J* value as possible. This serves to maximise the initial zero field magnetic entropy, as there are more potential orientations the magnetic moments may adopt. In addition, a large Landé splitting factor, *g*, is favoured as splitting between energy levels will be maximised upon application of an external magnetic field. The resulting effect of this would be that the ordering will occur at a higher rate during the magnetisation process, and the entropy drop will be maximised. The most obvious method to maximise the heat energy that can be absorbed before the material begins to heat up is to use a material with as high a heat capacity as possible, especially in the

temperature region of demagnetisation, and at $T \sim \theta$, the ordering temperature. The ADR designer must take into account all of these properties, and trade them off against θ, to determine the best material for his purpose.

Common refrigerant materials include Chromic Potassium Alum (CPA), Cerous Magnesium Nitrate (CMN), Ferric Ammonium Alum (FAA), Gadolinium Gallium Garnet (GGG) and Dysprosium Gallium Garnet (DGG). A brief summary of the key properties of some of the commonly used paramagnetic materials is provided below in Table 6.

Material	J Value	g value	Θ [K]
Cerium Magnesium Nitrate (CMN) $Ce_2Mg_4(NO_3)_{12}.24H_2O$	1/2	2	0.001
Chromic Potassium Alum (CPA) $CrK(SO_4)_2.12H_2O$	3/2	2	0.009
Ferric Ammonium Alum (FAA) $FeNH_4(SO_4)_2.12H_2O$	4/2	2	0.026
Manganese Ammonium Sulphate (MAS) $Mn(NH_4)_2.6H_2O$	5/2	2	0.173
Dysprosium Gallium Garnet (DGG) $Dy_3Ga_5O_{12}$	1/2	8	~0.4
Erbium Orthoaluminate (ErOA) $ErAlO_3$	1/2	9	~0.6
Ytterbium Orthoaluminate (YbOA) $YbAlO_3$	1/3	7	~0.8
Gadolinium Gallium Garnet (GGG) $Gd_3Ga_5O_{12}$	7/2	2	~0.8

Table 6: Properties of some common Paramagnetic Materials. Upper (light blue) represent 'low' temperature stage materials, lower (pink) represent higher temperature stage materials. After (46).

3.1.6 HEAT SWITCHES

Heat switches are essential for operating the ADR cooling cycle. They allow for controlled thermal isolation and contact between different temperature environments within the system at the appropriate points in the cycle. An ideal heat switch would have the characteristics of infinite thermal conductivity in the 'on' (closed) state, and zero thermal conductivity in the 'off' (open) state.

There are many types of heat switch, exploiting a multitude of physical effects in order to provide two states with significantly differing thermal conductivities, so that there is a clear 'on' and 'off' state. Among the common cryogenic heat switches for use around the temperatures of magnetic cooling are superconducting, gas-gap, and mechanical heat switches. A new type of heat switch, a magnetoresistive heat switch, is also briefly introduced.

3.1.6.1 MECHANICAL HEAT SWITCHES

Mechanical heat switches rely on having separated mechanical components thermally anchored to two different temperature stages within the ADR. In the open ('off' state) mode, these components do not touch. In order to close the switch, some form of powered mechanism is required to move the components into contact. This is typically achieved by using electricity to drive a solenoid which forces the switch closed. Thus, closing the switch introduces a further heat load from the driving electrical current. The thermal conductance in the closed state is strongly dependent on the force with which the switch's mechanical components are held in contact. These switches are commonly used in ground applications, however are susceptible to 'cold welding' – sticking closed when attempted to open at cryogenic temperature.

Inevitably, the nature of these switches means they are not sufficiently reliable for space flight-ADRs, as the moving parts means they are more susceptible to failure than other technologies.

3.1.6.2 SUPERCONDUCTING HEAT SWITCHES

Superconducting heat switches exploit the difference in the thermal conductivity in the normal and the superconducting states of a superconducting element. Heat, in both states, is transported by 'normal' (non superconducting) electrons [(49)], and phonons (lattice vibrations, see chapter 4 for more details). The normal state sees electron conduction dominating, with the phonon contribution almost negligible. The superconducting state sees phonon conduction making a significant contribution, in fact dominating below a certain temperature, e.g. 100mK for thin Aluminium foil [(49)]. This is because in the superconducting state there are far less normal electrons present, as they begin to form Cooper pairs[9]. The number of cooper pairs increases with the number of normal electrons decreasing as the temperature continues to fall below the critical temperature. Cooper pairs, because of their nature, seldom scatter, thus do not transport heat. Figure 42 below shows experimental proof that the same piece of Aluminium can act as an excellent conductor, comparable to pure Copper, or as an insulator, comparable to Epibond 121 (an insulating adhesive).

[9] Cooper Pairs: A quasiparticle composed of two interacting electrons. The basis of the BCS theory of superconductivity. See Cooper (51), Bardeen et al. (53) and Bardeen et al. (53).

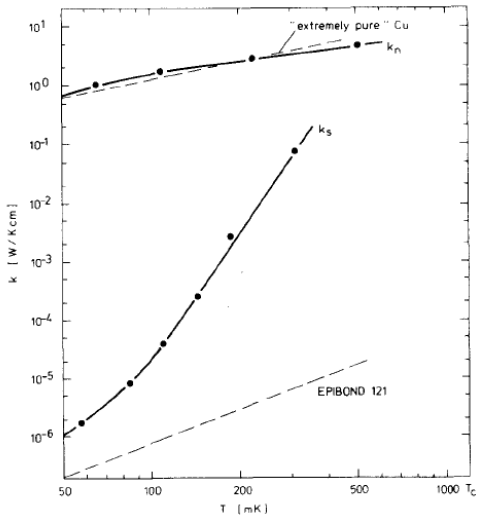

Figure 42: Comparison of the thermal conductivities of 0.1mm thick Aluminium foil in the normal (k_n) and superconducting (k_s) states. *After* (50).

The state of the switch is controlled by application of a magnetic field to drive the naturally superconducting switch into its normal state by crossing the phase boundary marked by the critical magnetic field. This introduces further heat loads to the system, as electric current is required to generate the magnetic field. Superconducting heat switches, however, can be excellent at serving their purpose when appropriately designed for a specific application. The superconducting heat switch described in Mueller et al. (49) has a switching ratio (ratio of thermal conductivities in 'on' and 'off' states) of $1600T^{-2}$.

3.1.6.3 GAS-GAP HEAT SWITCHES

The simplest Gas-gap heat switches rely on the temperature dependence of a gas vapour pressure to control heat conduction between two contact surfaces. Gas-gap heat switches are usually active; relying on a control mechanism to change the state of the switch. In the 'off' state (thermally insulating state), the conduction gas (typically ^{3}He or ^{4}He), is adsorbed onto a *getter* made of a specific type of material. This material may be a zeolite or some kind of purpose-engineered substrate. The space between the two contact surfaces is evacuated and the off-state conductance is limited simply by the

conductivity of the walls that enclose the gas-chamber. The walls are thus engineered to have minimal thermal conductivity. Power applied to a heater in contact with the getter causes the gas to be desorbed from the getter, and fill the chamber via a capillary. The gas is thus allowing thermal contact between the two contact surfaces and the switch is in the 'on' state (thermally conducting). The main disadvantage of such a heat switch is that when switched off, it takes some time for the gas to re-adsorb onto the getter, and the vapour pressure in the chamber to decrease sufficiently for the switch to actually be 'off'.

Passive gas-gap heat switches have been developed [(51)] that not only have a faster switch-off time, but require no external control mechanism. This means they have the advantage of being more simple and reliable, in addition to not having the extra heat load imposed by the control mechanism, i.e. heat conduction and joule-heating down current leads, which are inevitable in superconducting, mechanical and active gas gap heat switches. The passive gas gap heat switch developed at NASA Goddard Space Flight Center (GSFC) has been designed to switch off below ~0.15K, and on above ~0.2K [(51)]. When the mean free path of the conduction gas is of the order of the separation between the contact plates, the heat conduction mechanism is *molecular*. *Laminar* conduction arises when the mean free path of the gas molecules is around 100 times smaller than the plate separation distance [(51)]. In the laminar regime, thermal conduction is almost independent of vapour pressure, whereas in the molecular conduction regime, the thermal conductivity of the gas is proportional to vapour pressure. Gas-gap switches are usually designed to switch on in the laminar phase, to maximise the 'on' state conduction. However, engineering a passive gas gap heat switch to switch off quickly around a desired temperature requires the conduction mechanism be molecular in that temperature region, and the vapour pressure to be a strong

function of temperature [51]. The nature of the passive gas gap switch means it must have a lower 'on' conductance than an active gas gap switch.

3.1.6.4 MAGNETORESISTIVE HEAT SWITCHES

All heat switches described so far have drawbacks which limit their suitability or effectiveness in a real space ADR. Mechanical switches have low reliability, superconducting switches are generally limited in their achievable switching ratios and gas-gap switches are increasingly limited in their switching ratio performance as temperature decreases.

A new type of heat switch utilises the change in thermal conductivity that occurs in certain metals when exposed to a sufficiently strong (~1-2 Tesla) magnetic field. These 'magnetoresistive' heat switches are highly conductive in the 'on' state, and are able to achieve instantaneous switching to an 'off' state with the application of a localised magnetic field, thereby reducing their thermal conductivity by a factor of the order ~10^5. The development of this type of switch constitutes a significant portion of this thesis, and is described in detail in the dedicated chapters 4 (theory) and 5 (experimental development). The importance of this technology with respect to the ESA ADR and the IXO XMS is highlighted in 3.2.2.2 and 3.3.1 respectively.

3.2 ADR Systems

3.2.1 General Types of ADR

3.2.1.1 Single ADR

The simplest type of ADR is known as a *single ADR*, and contains a single salt pill and heat switch coupling it to the heat bath. A diagrammatic representation of a single ADR is shown in Figure 43:

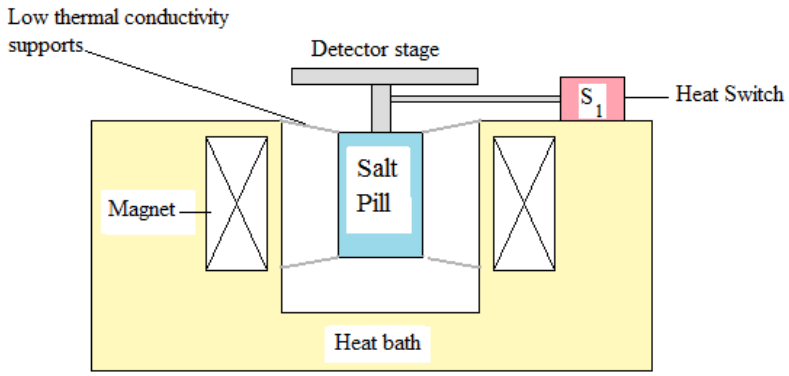

Figure 43: Configuration of a single ADR. The detector stage, or cold finger, is connected to the salt pill via a highly conductive thermal bus. Coupling to the heat bath is via heat switch S1. Superconducting magnets generate the magnetisation field. Image adaped from (52).

The cooling cycle for a single ADR is a simple single cycle of magnetic cooling. Initially, the heat switch S1 is closed to allow the salt pill and detector stage to cool to the temperature of the heat bath. The superconducting magnets are then ramped up to full field, fully magnetising the paramagnetic substance within the salt pill. The heat of magnetisation is continuously extracted to the heat bath via the closed heat switch S1, to allow for an effectively isothermal process. Once the salt pill is ordered, and its temperature is equal to that of the heat bath, the heat switch S1 is opened. This provides thermal isolation from the heat bath, and the superconducting magnets are ramped down until the detector stage is at the desired temperature. Upon reaching the desired temperature, the demagnetisation process continues at a rate sufficient to

maintain this temperature, providing just enough cooling to overcome the *natural heat leak* occurring from imperfect thermal isolation, and the heat load applied to the detector stage. When the magnets reach zero field no more demagnetisation can occur, and the salt pill will eventually begin to warm up. At this point the ADR must be recycled; the heat switch S1 is closed and the magnetisation process re-initiated.

More complex ADR configurations include the two-stage ADR, double ADR (dADR), and the continuous ADR (CADR). The two-stage ADR works in exactly the same manner as a single ADR, but has a second salt pill that demagnetises in parallel to the main/detector stage salt pill. This second salt pill cools an intermediate temperature stage (at a temperature between that of the bath and the detector stage pill) in order to provide a thermal 'buffer' to reduce the parasitic loads on the main salt pill to allow for a longer hold time. These ADRs are unlikely to be selected for future space applications as they can be outperformed by double ADRs and continuous ADRs without any significant increase in mass, complexity or cost that would outweigh the advantages of such systems.

3.2.1.2 DOUBLE ADR

The double ADR contains two stages in order to improve cooling power. Unlike the two-stage ADR, the double ADR stages are connected via a heat switch. The first stage of a dADR will demagnetise to a temperature in between that of the heat bath and that of the desired temperature of the cold finger. The second stage will be cooled by the first stage before acting as the final stage to cool the detector stage. The dADR configuration is illustrated in Figure 44:

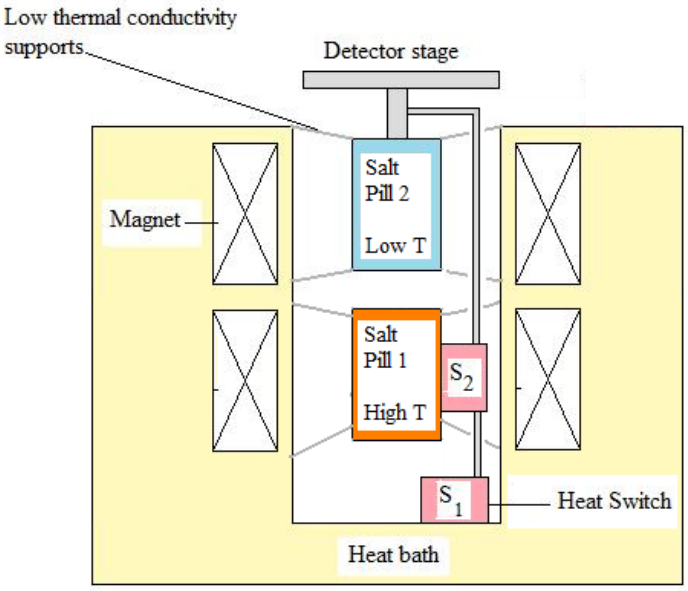

Figure 44: Configuration of a double ADR. The detector stage, or cold finger, is connected to the second stage salt pill via a highly conductive thermal bus. The second stage salt pill is then connected to the first stage salt pill via the heat switch S2. The first stage salt pill is coupled to the heat bath via heat switch S1. Superconducting magnets generate the magnetisation field at each stage. Image adaped from (52).

The operation of the double ADR requires initially that both heat switches S1 and S2 are closed. Both salt pills are cooled to the temperature of the heat bath, before being fully magnetised. Once both salt pills are magnetised, and at the temperature of the heat bath, heat switch S1 is opened, thermally isolating both salt pills from the heat bath, yet remaining connected to one another via heat switch S2. The first stage salt pill is then typically fully demagnetised, pulling the temperature of the second stage salt pill down to its demagnetisation temperature. Upon reaching thermal equilibrium, heat switch S2 is opened, thus thermally isolating the second stage salt pill from the first stage. The second stage is then demagnetised in exactly the same way as for a single ADR. Upon reaching zero-field in the second stage magnets, the whole system must be recycled. This process involves closing both heat switches S1 and S2, and re-magnetising both stages before demagnetising as already described.

3.2.1.3 CONTINUOUS ADR

The nature of the ADR cooling cycle means that in its nominal configuration, it can only provide cooling for a finite time before recycling is necessary. It is a 'single shot' cooling system. Thus, observation durations for the attached cryogenic instrument are typically limited by the ADR hold time; and the ADR recycle time is observational dead time where the cryogenic instrument will be out of commission.

There is considerable interest in developing the concept of the continuous ADR, or CADR into a practical space cryogenic technology. The continuous ADR aims to provide continuous cooling at the desired temperature, eliminating the period of the recycle time where cooling cannot occur. Current literature indicates there are two main designs for the continuous ADR, achieving continuous low temperature cooling via differing approaches.

NASA's Goddard Space Flight Center is developing a continuous ADR for consideration of the IXO mission (originally for the constellation-X) [53]. This design is described in 3.3.4.

Another CADR design is under development at MSSL, and adopts a different format. It essentially consists of two dADRs coupled to a continuous low temperature stage [54]. Figure 45 illustrates the concept.

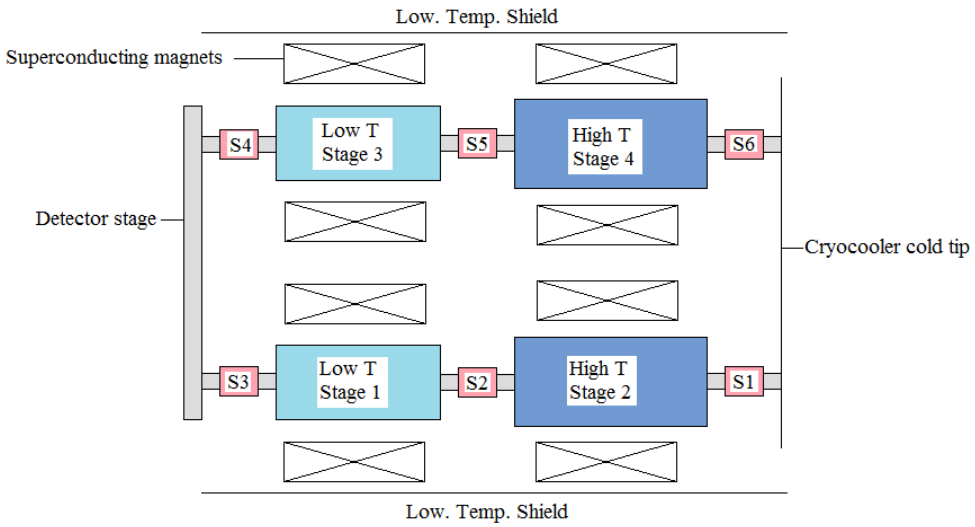

Figure 45: MSSL continuous ADR design. 2 dADRs sharing a common detector stage. Heat switches are labelled S1-S6. The basic concept is that one dADR can provide cooling whilst the other recycles. Image adapted from (54).

In this design, continuous cooling is provided by one ADR whilst the other recycles. The cycling method can be either parallel, or serial.

Parallel Mode

In Parallel mode, each dADR acts effectively independently; its cools and recycles as an ordinary dADR. Whilst cooling is provided by stage 1, heat switch S3 is closed, whilst S2 and S1 are open to minimise heat load. Heat switch S4 is open, isolating the cold stage from the recycling (magnetising) stages 3 and 4, which are transferring heat to the cryocooler heat bath via the closed heat switches S5 and S6. Once stages 3 and 4 are magnetised, switch S6 is opened and stage 4 is demagnetised, cooling stage 3. Upon thermal equilibrium, heat switch S5 is opened and stage 3 is demagnetised until the desired temperature is achieved, at which point heat switch S4 is closed and S3 is opened. Stage 3 is now cooling whilst stages 1 and 2 are free to recycle.

Serial Mode

In serial mode, heat is passed around the stages in a similar fashion to the NASA GSFC CADR (see 3.3.4). Assuming cooling is initially provided by stage 1, S3 is closed whilst S2

and S1 are open. S4 is open as is S5. S6 is closed whilst stage 4 magnetises, then opened whilst it demagnetises. S5 is then closed whilst stage 3 is magnetised, and the heat is transferred to stage 4. S5 is then opened whilst stage 3 demagnetises to the desired cooling temperature, at which point S4 is closed and S3 is opened, and stage 3 takes over providing the cooling. Stages 1 and 2 then recycle.

The MSSL CADR has a few advantages over the NASA GSFC design (see 3.3.4). The main advantage is that it provides an enhanced reliability in that it has redundancy. If one of the component dADRs were to fail, the other would be unaffected and cooling could still be achieved at the performance of the single dADR. It also has no single point failures, whereas if one of the stages fails on the NASA design the CADR would be rendered completely useless. It should also be possible to make the MSSL design smaller and lighter than the NASA design [(54)]. At this stage, however, the NASA design is more technologically mature, as a functional demonstration model has been produced. The MSSL design has been verified by modelling which in turn has been validated with the MSSL ESA ADR and experiment – See Bartlett (55).

3.2.2 MSSL ESA ADR

IXO's predecessor mission, XEUS (X-ray Evolving Universe Spectrometer), was a purely European mission concept under development and assessment study led by ESA. The original requirements for the XMS cooler were [(56)]:

1. A cold finger temperature of 50 mK (with a target of 30 mK) for 24 h with a 1 μW heat load and with a 4 h ADR recycle time.

2. A maximum heat load to the ADR heat sink of <5mW in order to allow cooling via a space cryocooler.

3. A magnetically shielded <5 μT (0.05 G) detector focal plane to house superconducting tunnel junction (STJ) or transition edge (TES) X-ray detector arrays and associated SQUID readout electronics.

4. Magnetic screening of the whole system to reduce the exported stray magnetic flux density to a level acceptable to a spacecraft (<67 μT, <0.67 G).

ESA contracted the development of an ADR meeting these requirements to MSSL and Astrium. An engineering model (EM) ADR was delivered to ESA in July 2008. Figure 46 shows an engineering schematic and photograph of the EM MSSL/Astrium ADR.

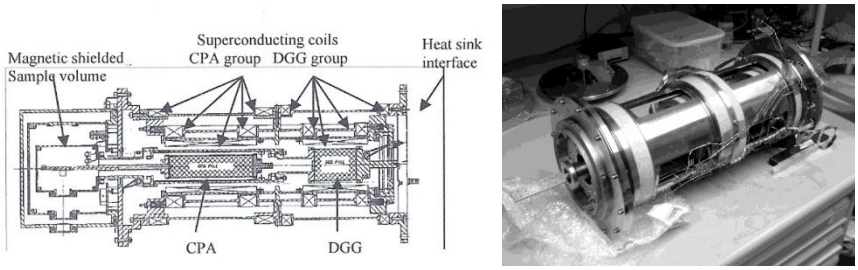

Figure 46: (Left) Engineering schematic of MSSL dADR. (Right) Photograph of engineering model of MSSL dADR. After (57).

The MSSL/Astrium ADR ("ESA ADR") met all the requirements bar the crucial hold time and recycle time, which are measured to be 10 hours and 15 hours respectively (with a 2.34μW average heat load) [(56)]. The detailed design of the ESA ADR is described in Hepburn et al. (57), Bartlett (55) and Bartlett et al. (56); however a brief description follows.

3.2.2.1 General Overview

The ESA ADR is a dADR designed to operate from a heat bath of 4K or lower, to be provided by mechanical coolers or similar (on ground testing at MSSL a laboratory Pulse tube cooler is used). The ESA ADR uses a DGG salt pill for the upper temperature stage, consisting of a single crystal of 0.9 moles DGG, designed to operate from 4K down to

0.6K (approximate ordering temperature). The DGG stage acts as the pre-cooling stage for the lower temperature stage, a CPA salt pill consisting of 0.56 moles of CPA crystals packed to an approximate packing density of 95% [(56)]. The CPA stage operates from 1.6K (heat switch limitations prevent the CPA beginning demagnetisation from ~0.6K/DGG ordering temperature) down to 25mK, which is significantly above its approximate ordering temperature of the order 10mK.

The ESA ADR has a gas-gap heat switch (developed at CEA-SBT (58)) connecting the DGG to the heat bath, and a superconducting Lead heat switch providing the thermal interface between the DGG and CPA stages. The DGG is connected to the heat bath interface via a Copper thermal strap, which dominates the gas-gap switch 'on' state conductivity. In addition, the 'off' state conductivity of the gas-gap switch is dominated by the structural walls of the heat switch (a titanium tube). An overview of the thermal performance properties of these heat switches is given below in Table 7.

Heat switch	'On' state	'Off' state
Superconducting lead (based on measured performance)	$0.01\ \mathrm{K} \leqslant T \leqslant 2.85\ \mathrm{K}$: $k = 0.52\ T^{2.97}\ \mathrm{W\ cm^{-1}\ K^{-1}}$	$0.01\ \mathrm{K} \leqslant T \leqslant 3.00\ \mathrm{K}$: $k = 0.0296\ T^{3.0569}\ \mathrm{W\ cm^{-1}\ K^{-1}}$
	$2.85\ \mathrm{K} < T \leqslant 4\ \mathrm{K}$: $k = 9\ \mathrm{W\ cm^{-1}\ K^{-1}}$ $4\ \mathrm{K} < T \leqslant 8\ \mathrm{K}$: $k = 36\ T^{-1}\ \mathrm{W\ cm^{-1}\ K^{-1}}$	$3.00 < T \leqslant 3.50\ \mathrm{K}$: $k = 0.2670\ T^{1.0543}\ \mathrm{W\ cm^{-1}\ K^{-1}}$ $3.50\ \mathrm{K} < T \leqslant 8.00\ \mathrm{K}$: $k = 0.4567\ T^{0.6256}\ \mathrm{W\ cm^{-1}\ K^{-1}}$
Gas gap [5]	$10 \times 10^{-3}\ \mathrm{W\ K^{-1}}$ at 1 K $42 \times 10^{-3}\ \mathrm{W\ K^{-1}}$ at 4 K Limited by copper strap[a]: $1.00 < T \leqslant 10.00\ \mathrm{K}$: $k = 0.9858\ T + 0.2816\ \mathrm{W\ cm^{-1}\ K^{-1}}$	$2 \times 10^{-6}\ \mathrm{W\ K^{-1}}$ at 1 K $18 \times 10^{-6}\ \mathrm{W\ K^{-1}}$ at 4 K Dominated by titanium tube [5]: $0.30\ \mathrm{K} \leqslant T \leqslant 2.00\ \mathrm{K}$: $k = 4.32 \times 10^{-4}\ T^{1.59}\ \mathrm{W\ cm^{-1}\ K^{-1}}$ $2.00\ \mathrm{K} \leqslant T \leqslant 13.00\ \mathrm{K}$: $k = 5.88 \times 10^{-4}\ T^{1.1}\ \mathrm{W\ cm^{-1}\ K^{-1}}$

[a] Based on measured performance.

Table 7: Overview of performance properties of the ESA ADR heat switches. After (56).

Thus far, the ESA ADR has undergone shock/vibration pre-qualification testing to Ariane-5 levels at the sub-system (component) level. Details may be found in (56).

3.2.2.2 PERFORMANCE

The ESA ADR is currently an engineering model at TRL (Technology Readiness Level) 5. It has demonstrated achieving a base temperature of 25mK. As already stated, for a heat bath temperature of 4K it can hold 50mK for 10 hours with an average parasitic heat load of 2.34μW, and recycle within 15 hours. These measured performances are

significantly non-compliant with respect to the original ESA requirements on performance; i.e. a 24 hour hold time (with a 1µW applied heat load) and a 4 hour recycle time. Detailed modelling [55], [56] of the ADR reveal the main hindrances to performance are due to:

- The performance of the superconducting heat switch. It is too conductive in the 'off' state, causing a high parasitic heat load to limit the hold time. The poor 'on' conductance means heat cannot transfer sufficiently quickly from the magnetising DGG stage to the heat bath upon recycling, thus resulting in a long recycle time.

- Thermal boundary resistance between the CPA crystals and the thermal bus (gold plated Copper wires around which the CPA crystals are grown) which prevents the cold finger getting as cold as the CPA crystals (i.e. why the base temp is 25mK and not closer to the CPA ordering temp of ~10mK).

Extensive Investigation and analysis (see Bartlett et al, (56)) using modelling has shown that the improvements required to remove the limitations caused by thermal boundary resistance will be impractical to implement, in that they require a 2 orders of magnitude decrease in the parasitic heat load incident on the cold finger/CPA (From 0.6µW to 5nw, which is impossible as parasitics are already minimised by design) and an increase of more than ten-fold on the contact area between the thermal bus and the CPA crystals (from 300cm^2 to 5000 cm^2). Any increase in this surface area would require more wire material and lead to significant increase in size and mass of the CPA salt pill, so much so that there would be no net benefit. Hence, this limitation will be extremely difficult to overcome.

The Lead superconducting heat switch between the two temperature stages of the ESA ADR (see Table 7) has a low switching ratio (ratio of 'on' state conductance to 'off' state conductance), of the order of $10^1 – 10^2$ in the 1K-4K temperature range. This is primarily down to the low 'on' state conductivity of the switch, which prevents fast recycle times and limits the rate at which the DGG can cool the CPA, hence the temperature the CPA can be cooled to (i.e. why it only cools to 1.6K not ~0.6K). Low temperature measurements of the thermal conductivity of single-crystal Tungsten in zero and non-zero magnetic fields shows the thermal conductivity can vary by as much as 10^5 simply by the application of a magnetic field of the order of a few Tesla [(59)] in the Kelvin temperature regime. This indicates the potential to form the basis of a heat switch with an extremely high switching ratio in the temperature range of operation of the lead superconducting heat switch. Bartlett et al (56) have performed thermal conductivity measurements of a Tungsten crystal [(55)] in the presence of a magnetic field of ~2 Tesla, and show a Tungsten heat switch of this type could significantly increase the hold time by reducing the parasitic heat load on the CPA stage. The reduction in parasitic load can be seen in the figure below, where modelled heat load on the CPA stage is computed for both the Lead superconducting and Tungsten (denoted 'MR' in figure) heat switch:

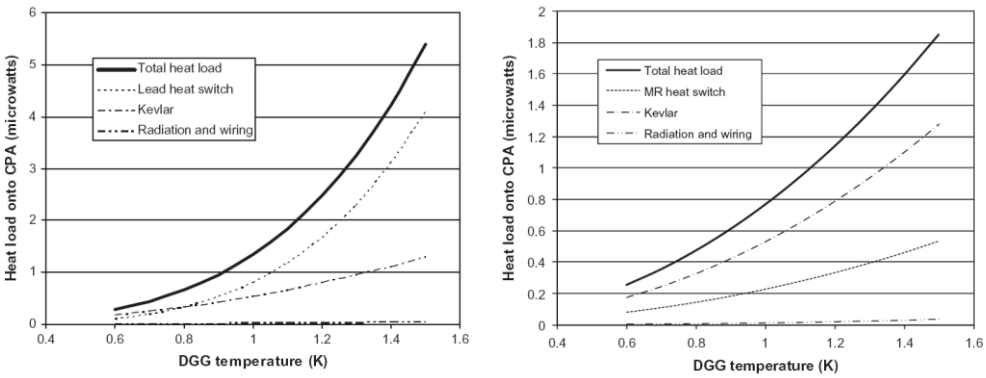

Figure 47: Comparison of modelled heat loads on ESA ADR CPA salt pill for Lead superconducting and Tungsten MR switches. After (56).

The reduction in heat load these modelled results show suggest the hold time of the ESA ADR can be increased to 29 hours with the Tungsten heat switch (with a 1μW heat load), and the higher 'on' conductivity (~90 W cm^{-1} K^{-1} at 1K, ~450 W cm^{-1} K^{-1} at 4K) would result in a 2 hour recycle time being achievable [56].

This novel heat switch technology, *Magnetoresistive*, or 'MR' heat switches, are thus a technology that shows great potential for improving the performance of the ESA ADR, and subsequent evolutions of ADRs for future space missions. Hence, this thesis devotes chapters 4 and 5 to the development of this technology, in order to provide an insight into what criteria a material must possess in order to achieve the best heat switch performance. The achievable improvements to the ESA ADR performance are ascertained in chapter 5 using real measured data for several magnetoresistive heat switches, including taking into account the interface thermal resistance between the magnetoresistive heat switch and its attachment points within the ADR structure.

It is clear that replacing the Lead heat switch within the ESA ADR should improve the hold time and recycle time [56] thus feeding into the development of a truly flight-worthy ADR system suitable for IXO.

3.2.3 ADRs IN SPACE

ADRs are a prime candidate for providing stable sub-Kelvin temperature environments for space missions, and are being considered for future X-ray missions such as IXO and Astro-H. They are highly advantageous in that they contain no mechanisms; hence have high reliability (limited only by the magnets and heat switches), are relatively simple and can operate unaffected by the absence or presence of gravity. The only real disadvantage to ADR systems is the high magnetic fields they require (typically 2-3 Tesla) must usually be in close proximity to magnetically sensitive instrumentation, thus

extensive stray-field reducing (magnetic shielding) technologies must be employed to counteract this.

To date, only one ADR has actually flown on a space mission. The Japanese led 'Suzaku' mission, formerly ASTRO-E II, was launched in July 2005 as a replacement for the failed ASTRO-E mission (which failed to achieve orbit and crashed into the ocean only 42 seconds after launch), and was the first mission to launch an X-ray Microcalorimeter (Suzaku XRS – X-Ray Spectrometer). The Suzaku XRS operates at 60mK; this low temperature is provided by a single-stage ADR using a salt pill consisting of 920g of FAA [(60)] demagnetised from 2 Tesla. The Suzaku XRS ADR is precooled by a pumped liquid Helium bath (nominally ~1.3K) to which it is connected by a gas-gap heat switch. The ADR was designed to hold 60mK for 24 hours with a 5µW total heat load. This hold time was exceeded significantly in orbit, where the Helium bath cooled to 1.21K, and the hold time increased to 38 hours [(60)]. Suzaku has proved that its ADR is successfully operational along with the XRS on a real space mission. However, a design flaw in the accommodation of the Helium Dewar on the spacecraft caused the Helium to completely boil off after only about a month after launch [(60)], thus rendering the ADR and XRS useless.

A mission due for launch in 2014, Astro-H, will fly a double ADR as the final stage cooler in the cryogenic cooling chain needed to support the SXS (Soft X-ray Spectrometer) instrument – a microcalorimeter array based detector [(61)]. This mission will launch before IXO, and will lay the foundations for implementing an ADR cooled microcalorimeter within an almost cryogen-free cryogenic chain, providing IXO designers with valuable insight into any unforeseen issues that may arise.

3.3 ADR SOLUTIONS FOR IXO

There are currently 4 cryogenics research groups working on ADR systems targeting the IXO XMS. ESA specifications require that the IXO XMS cooler must operate from a heat bath temperature of 2.5K – 4K, to be provided by a Joule-Thomson cooler (see chapter 6 for details of the IXO cooling chain). The cooler must hold 50mK for >31 hours with a 1.5 heat load from the detector and recycle in less than 10 hours [(62)]. Each of the ADR systems being considered is briefly described in this section.

3.3.1 MSSL DADR

MSSL is building on its knowledge and experience gained from developing the ESA ADR, and developing a modified system suitable for the IXO XMS. This modified system does not require such strict magnetic shielding due a change in requirements from the original XEUS mission requirements (for which the ESA ADR was developed) to the IXO mission requirements [(63)]. This allows for a smaller mass system, which combined with a revised salt pill geometry (shown below in Figure 48), means the mass is reduced significantly below the ESA ADR at 45kg (32kg without sheilding) to ~10 kg [(63)].

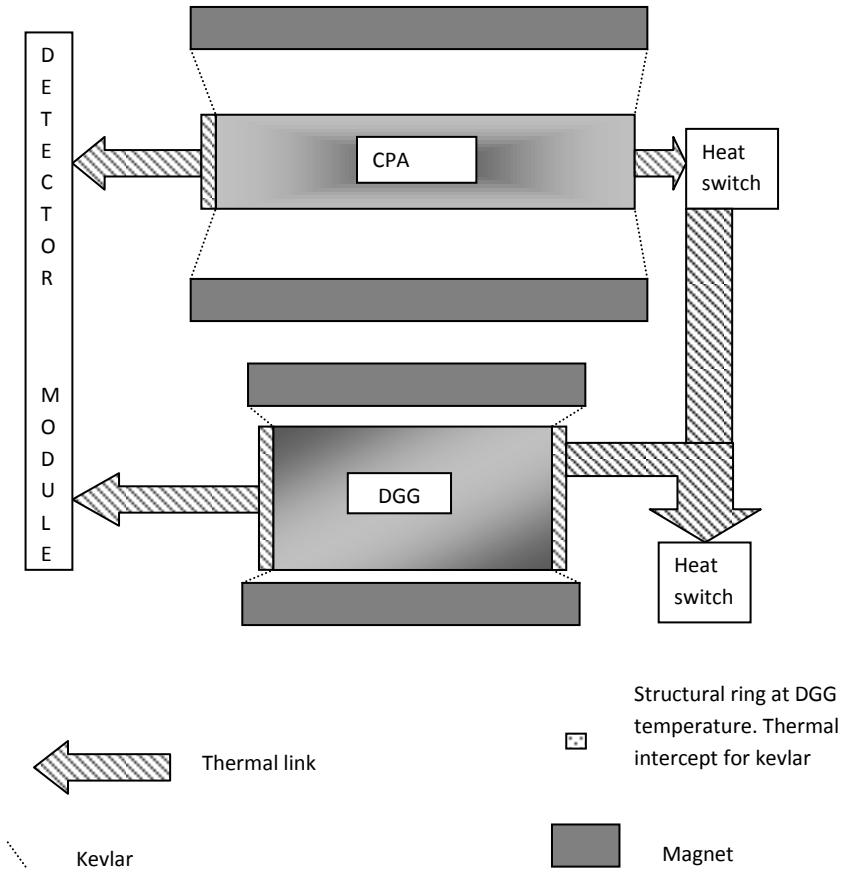

Figure 48: Revised salt pill layout and schematic representation of the MSSL IXO dADR. After (62).

The separation distance between the two salt pill magnets is designed to be greater than the minimum separation the mechanical structure can support (140mm centre of bore – centre of bore [63]), in addition to maintaining a suitably low 'stray' magnetic field on the DGG due to the fully magnetised CPA. These dimensions are detailed in Figure 49.

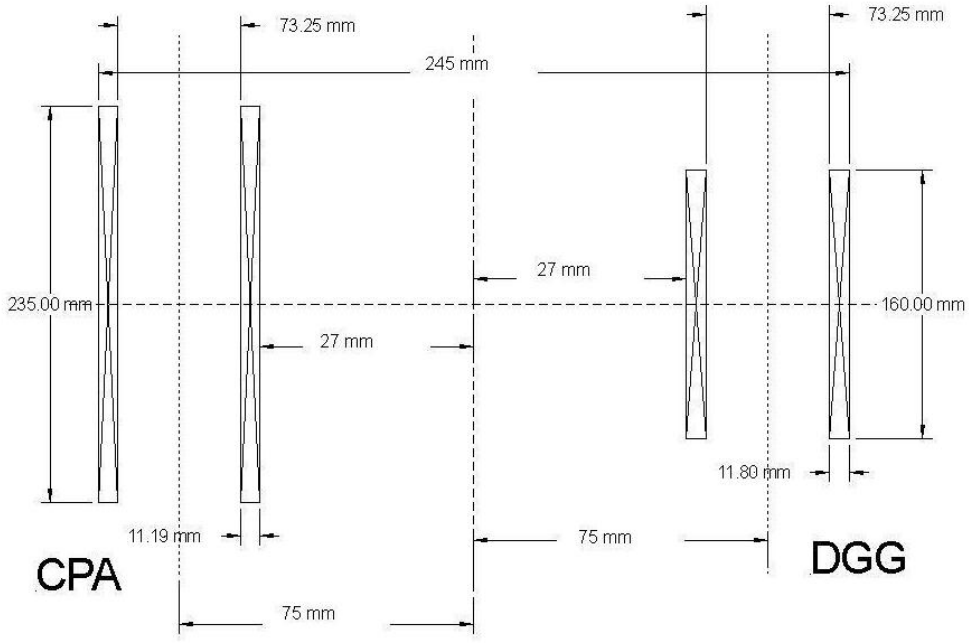

Figure 49: Dimensions of magnets and their geometrical separaton. After (63).

The selected bore separation results in the magnetic field of the CPA increasing the final demagnetisation temperature by <0.1K which is acceptably low [(63)].

The MSSL dADR uses a gas gap heat switch to interface to the heat bath (the same switch as the ESA ADR), but two solutions are proposed for the inter-salt pill heat switch:

1. A Tungsten magnetoresistive heat switch – preferred from a performance perspective for its significant reduction in recycle time as well as improvement in hold time.

2. A modified superconducting Lead heat switch based on the ESA ADR heat switch but with a fourfold increase in cross sectional area (hence conductivity) – A more developed technology (hence more cost effective and lower technical risk).

The theoretical system performance and mass breakdown of both options are presented in Table 8.

	S/C Switch + Gas Switch	MR Switch + Gas Switch
CPA mass	750 grams	500 grams
CPA 50 mK hold time	31 hours with 2 μW load (+parasitic)	32 hours with 2 μW load (+parasitic)
DGG mass	1000 grams	900 grams
DGG stabilised temperature (ADR 1st stage temperature)	0.6 K with 7μW load (+parasitic)	0.6 K with 7 μW load (+parasitic)
Re-cycle time	9 hours	<6 hours
Pill stage mass (including structure)	**2 350 grams**	**2000 grams**
Magnet mass	**7094 grams**	**7094 grams***
Heat switch mass	**~250 grams**	**~500 grams**
Total mass	**9694 grams**	**9594 grams**

Table 8: Summary of MSSL IXO ADR properties for both heat switch options. After (63).

In addition, a separate 2.7kg permendur magnetic shield is required to ensure the focal plane (IXO XMS instrument) is reduced sufficiently to below the required level during ADR operation [(63)].

Full details of the proposed MSSL dADR may be found in Hepburn (63), however, at this stage this document is not yet publically available.

3.3.2 CEA-SBT Hybrid Sorption Cooler/ADR

CEA-SBT, based in France, is developing an ADR system based on a modified double ADR. The modification is significant – a sorption cooler replaces the first (higher) temperature stage/salt pill to provide the pre-cooling for the final stage salt pill. Full details of this cooler may be found in Luchier et al. (39); however, a general overview follows here. A schematic of the proposed IXO cooler is provided in Figure 50 below.

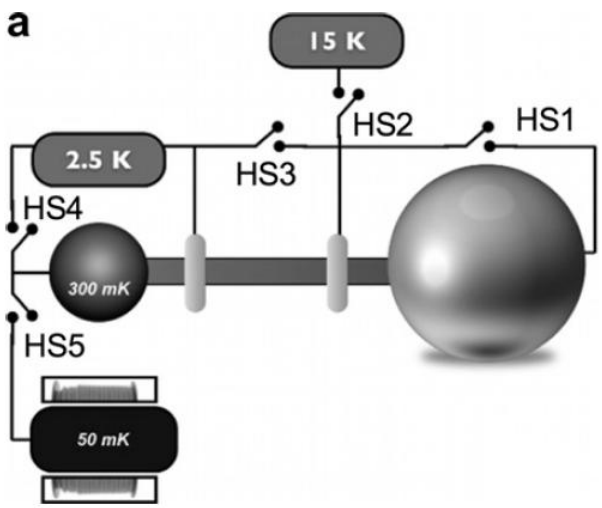

Figure 50: Schematic of CEA-SBT Hybrid sorption/ADR cooler. After (39).

The ADR stage consists of a 460g CPA salt pill and cools to 50mK. It is connected to a 300mK sorption stage via a gas-gap heat switch to provide precooling prior to demagnetisation. The 300mK stage itself is a Helium-3 sorption stage, based on Herschel heritage (39). The sorption cooler requires 4 further gas-gap heat switches to manage the heat flow throughout its cooling and recycling phases. The sorption stage requires a further heat rejection temperature at 15K (in addition to the 2.5K – 4K heat bath, which is provided by stirling cryocoolers in the IXO cooling chain (see chapter 6). This is because the heat loads that are produced during the Helium-3 condensation phase are high as the sorption pump is heated up to 45K, and during rapid recycling, heat loads can reach >2W at the heat bath temperature. The higher available cooling power at 15K means the initial cooldown can be performed faster, and the heat bath only has to cool from 15K down to 2.5K – 4K.

Thus far the design concept has been validated using a laboratory set up (to test the combination of an ADR with a sorption cooler, however is not representative of the proposed IXO cooler design), and an Engineering Model (EM) IXO cooler is under development. CAD views of the proposed EM design are provided in Figure 51.

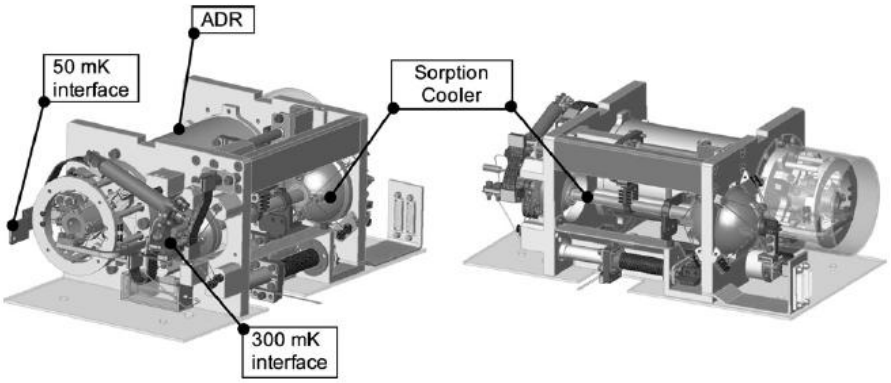

Figure 51: CAD views of proposed IXO hybrid ADR/sorption cooler. After (39).

The estimated cooler mass breakdown is given in Table 9 below, and it can be seen that the hybrid cooler has an estimated mass saving over the MSSL dADR.

Unit	Mass (g)
Sorption	270
ADR stage, of which	3550
CPA pill	770
Coil	780
Magnetic shield	1620
Superconducting shield (Nb case)	200
Various (pulleys,…)	180
Heat switches	420
Hoods	550
Structure	800
Straps	260
Various	450
Total	6300

Table 9: Summary of CEA-SBT hybrid ADR/Sorption cooler mass properties. After (39).

This system is notably more complex than a conventional double ADR such as the MSSL dADR, with a greater number of potential single point failure modes due to the greater number of heat switches required for operation.

3.3.3 JAXA ADR

JAXA have proved ADRs can successfully operate in space via Suzaku (using a NASA designed ADR), and NASA are developing an ADR for Astro-H based on this heritage. The IXO Payload Definition Document (64) states that an Astro-H based design is being

considered for IXO, under development by the NASA Astro-H team. The details of the Astro-H ADR design may be found in Shirron et al. (65), however, no details of the specific IXO ADR design have yet been published. NASA are developing a continuous ADR targeting the IXO XMS, as described subsequently.

3.3.4 NASA CADR

NASA's Goddard Space Flight Center (GSFC) is developing a continuous ADR for consideration of the IXO mission (originally for the constellation-X) [(53)]. The current design uses a 5 stage arrangement to cascade heat from the cold detector stage, up to a mechanical cooler. A schematic is given in Figure 52.

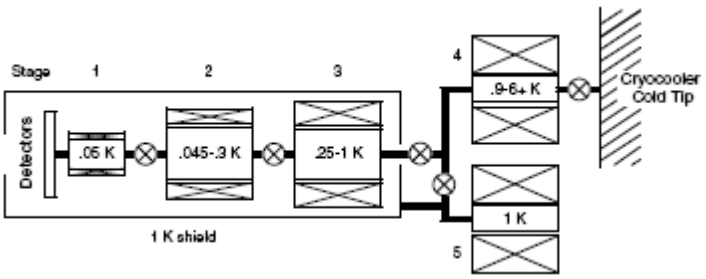

Figure 52: NASA GSFC's CADR design for Constellation-X. X-ray TES microcalorimeter spectroscopy detectors are continuously cooled to 50mK by stage 1. Heat is cascaded up the chain to be rejected at the mechanical cryocooler. An additional continuous 1K stage (stage 5) is present for cooling the SQUID arrays. ⊗ Symbols represent heat switches. Image after (53).

The principle of operation of the Goddard CADR uses salt pills designed to demagnetise to a temperature lower than the previous stage, in order to allow heat to cascade up through the chain of stages. The first stage offers continuous cooling at 50mK. Once the first stage magnets have reached zero field, the magnetisation is carried out whilst the second stage is demagnetised to below 50mK. The heat of magnetisation is thus transferred from stage 1 to stage 2, and stage 1 remains at 50mK. The heat is cascaded up through the stages one by one in a similar fashion, until it is rejected at the cold tip of a mechanical cryocooler. A separate continuous 1K stage (stage 5) exists to cool the secondary SQUID (Superconducting Quantum Interference Device) array used to

measure the output from the TES detector array. The 4-stage prototype CADR based on this design is successful in achieving continuous 50mK cooling according to published results [53]. It is shown to currently have a cooling power of 6µW at 50mK [53]. Figure 53 shows a photograph of the prototype CADR and a plot illustrating the measured temperature profiles of each stage during continuous cooling at 60mK.

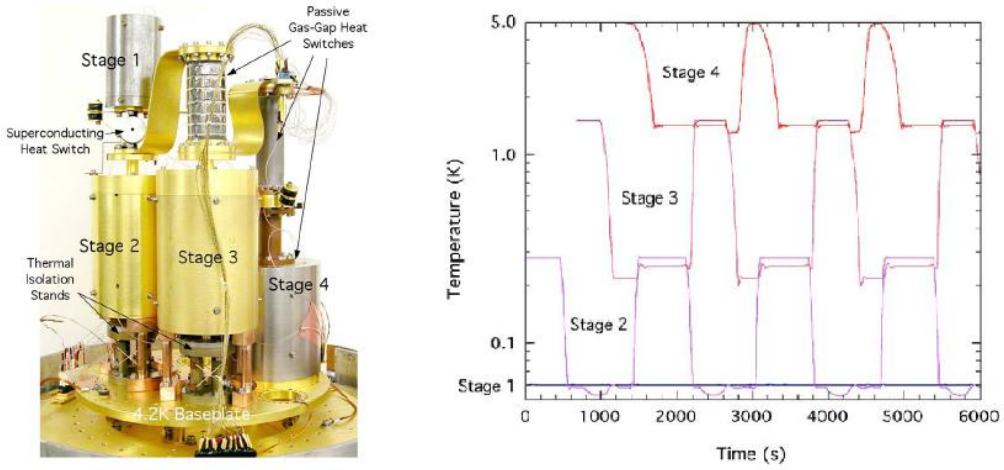

Figure 53: (Left) Photograph of prototype NASA GSFC CADR. (Right) Temperature profiles during operation holding a continuous temperature of 60mK. Images after (53).

Stage 1 is clearly stable at 60mK whilst the other stages undergo various cycling phases. Despite the demonstrated continuous cooling, the complexity of such a system means it is less attractive than it appears. Additionally, continuous cooling it not necessarily required if a single shot system can meet the observation duration and frequency requirements with higher reliability due to less complexity.

3.4 CHAPTER SUMMARY

This chapter has explained how ADR coolers work based on the magnetocaloric effect observable in certain paramagnetic materials. The key components of ADRs have been discussed, namely salt pills and common cryogenic heat switches, where paramagnetic materials suitable for cryogenic cooling and suitable space ADR heat switches have been identified. Of these, a new magnetoresistive ('MR'/Tungsten) heat switch technology has been briefly introduced.

The main types of ADR were described, including basic single ADRs, double ADRs and Continuous ADRs. An engineering model space ADR developed at MSSL, the ESA ADR, was introduced. The ESA ADR was shown to be underperforming in terms of its hold time and recycle time (with respect to the original design requirements). It was shown that replacing the ESA ADR superconducting Lead heat switch with a magnetoresistive heat switch would be expected to lead to a significant performance increase.

Finally, ADR solutions for cooling the IXO XMS were presented. Of these, the designs being considered by the European design team are the MSSL dADR, a modified version of the ESA ADR, and the CEA-SBT hybrid sorption/ADR cooler. The IXO MSSL dADR has two heat switch options; a higher performance, slightly higher technical risk magnetoresistive heat switch or a modified superconducting heat switch which would provide adequate performance with a slightly lower technical risk.

It is clear that the magnetoresistive heat switch offers potential performance advantages for space ADR systems, and potentially other space cryogenics systems. Hence, the development of this technology is the focus of chapters 4 and 5 of this thesis.

The supporting cryogenic environment for the MSSL dADR is detailed in chapter 6.

Chapter 4:

METALS AND MAGNETORESISTANCE

In the previous chapter, the need for a new heat switch in the ESA ADR was identified. The type of heat switch to replace the Lead superconducting heat switch was stated to be a Tungsten magnetoresistive heat switch. The benefits of implementing this type of heat switch were outlined, namely, the ability to switch almost instantaneously between 'on' and 'off states, and the potential for an unparalleled conductivity switching ratio, contained in a high-reliability solid-state heat switch with no moving parts.

This chapter introduces the theory of heat transport in metals, exploring the contributions from the two carrier types, electrons and phonons. The electronic contribution is shown to be dominant. The phenomenon of magnetoresistance is introduced, and it is discussed within the context of how it can be used to control the dominant electronic contribution to the thermal conductivity of a metal in order to form a heat switch. The criteria for the optimum magnetoresistive effect are discussed, and metals satisfying these criteria are identified. The choice of Tungsten as a suitable material is justified given the operating temperature requirements of the ESA/IXO ADR. The temperature and magnetic field dependence of the thermal conductivity of Tungsten are presented for the case where the metal is in the high field regime (as is defined in this chapter).

4.1 THERMAL CONDUCTIVITY OF METALS

The thermal conductivity of metals arises from a combination of two different mechanisms of heat conduction. These are the contribution from the crystal lattice itself, and the contribution from the conduction electrons. The total thermal conductivity, $\kappa(T)$, is a sum of the respective contributions of the lattice, $\kappa_{Lat}(T)$, and the electrons, $\kappa_e(T)$ (equation (17)) [66].

$$\kappa(T) = \kappa_{Lat}(T) + \kappa_e(T) \tag{17}$$

The two mechanisms of heat conduction arise from the two types of heat carriers present in metals, namely the phonons of the lattice and the conduction electrons. These carriers diffuse through the metal and transport thermal energy. Both carriers are subject to scattering interactions which limit their respective mean free paths, the average distance travelled by the carriers between collisions. These limiting interactions determine the form of the thermal conductivity.

4.1.1 LATTICE THERMAL CONDUCTIVITY

The crystal lattice of a metal conducts heat by means of the oscillations of its constituent atoms. This is the primary mechanism of heat conduction which occurs in crystalline dielectric (insulating) materials, as there are no conduction electrons acting as additional carriers for thermal energy.

The atoms of a crystalline lattice may be thought of as masses elastically coupled to one another via ‘springs’, where the springs represent the force due to the inter-atomic bonds. These bonds are assumed to have a quantum harmonic potential, of the same form as typically used to model two atoms coupled together in a diatomic molecule. The general form of such a potential is given by equation (18) [67] for a simple diatomic molecule:

$$V(x) = \frac{1}{2} m\omega^2 x^2 \tag{18}$$

This equation describes the quantum harmonic potential $V(x)$ of a diatomic molecule of reduced mass m. The reduced mass is given by the product of the masses of the 2 constituent atoms divided by their sum, i.e. $m = \frac{m_1 m_2}{(m_1+m_2)}$ [67]. The atoms oscillate at frequency ω for a given extension x from the equilibrium separation. Solving the Schrödinger equation for such a potential results in allowed energy eigenvalues, E_n , of:

$$E_n = \left(n + \frac{1}{2}\right)\hbar\omega \tag{19}$$

Where n is the quantum number of the energy state (0 or a positive integer) and $\hbar$ is the reduced Planck constant. This well known equation shows that energy can only be accepted or rejected in discrete units of $\hbar\omega$.

At any finite temperature, the atoms of a crystal lattice naturally oscillate about their equilibrium (mean) positions. The harmonic assumption is valid for small oscillation amplitudes, such as would be present at temperatures of the order of and lower than liquid Helium temperature. Such an arrangement of coupled oscillators results in the oscillator system (the entire lattice) containing a range of characteristic normal modes of vibration.

Heat introduced to one side of the lattice will impart additional energy to the local atoms, causing them to oscillate more vigorously than the average atom in the lattice. This in turn causes neighbouring atoms to oscillate with increased amplitude as the oscillatory energy transfers from atom to atom. A wavefront is effectively set up in the lattice, propagating atomic oscillation energy away from the side of the initial thermal excitation and down the thermal gradient.

The coupling of the oscillator atoms results in collective modes of their oscillations being manifested as elastic waves, which are planes of atoms moving in phase and propagating energy through the crystal lattice [(68)]. These collective modes are superpositions of the normal modes of the lattice. Thermal excitation and de-excitation of these collective modes can only occur in quantum units of $\hbar\omega$, where $\hbar$ is the reduced Planck's constant and ω is the frequency of the mode. This is a consequence of the innate quantum nature of the quantum harmonic oscillator energy spectrum, as indicated by equation (19). These quanta of energy of the collective modes may be attributed properties such as crystal momentum and velocity, and may be described by a collective distribution function. Essentially, these quanta of lattice vibration energy behave as boson particles, hence are ascribed the name *phonons*. Thermal excitation of the lattice therefore generates thermal phonons which carry heat through the lattice structure [(68)].

The theoretical phonon component of thermal conductivity for a crystal lattice shall now be calculated by considering the heat capacity of the lattice due to the thermal phonons constituting the collective modes. At a temperature T, the total energy of the phonons, U, is proportional to the total number of phonons within each mode and the total number of modes per unit energy range. This is expressed mathematically by equation (20) [(68)].

$$U = \sum_{p} \int d\omega \, D_p(\omega) \frac{\hbar\omega}{\exp\left(\frac{\hbar\omega}{k_B T}\right) - 1} \tag{20}$$

The p denotes the polarisation index which specifies the polarisation of the mode, where there are 2 possible transverse polarisations and 1 possible longitudinal polarisation, corresponding to displacements in the two planes orthogonal to the direction of propagation and displacements in the plane parallel to the direction of

propagation respectively. The number of modes per unit energy range is expressed in the slightly modified form $D_p(\omega)\, d\omega$, which is strictly the number of modes of polarisation p in the **frequency** range ω to $\omega + d\omega$ [68]. The average number of phonons in each mode is given by the Bose Distribution [68], which is a function of the ratio of the energy of the mode to the thermal energy $\hbar\omega/k_B T$, where k_B is the Boltzmann constant.

There are two established quantum models for describing the properties of phonons in a lattice; the Einstein model and the Debye model. The Einstein model is typically used for optical branches of the phonon spectrum, whereas the Debye model is better suited to describing acoustic modes (such as are thermally excitable in a monatomic lattice). The Debye model works exceptionally well at low temperatures, where the Einstein model fails due to its assumption that all atoms oscillate at the same frequency. Here, 'low' temperature means small in comparison to the material-specific Debye temperature, θ_D, which is typically of the order of a few hundred Kelvin for metals [68]. Thus, since the temperatures of interest to the work presented in this thesis are of the order of 4K and below, the determination of the theoretical form of the phonon contribution to thermal conductivity is calculated according to the Debye model, following the treatment outlined in Kittel (68).

The allowed phonon modes have corresponding wavevectors (K vectors), which correspond to points on a periodic lattice in K space. This lattice is the reciprocal lattice, and is the most useful arena for calculations involving phonon modes and their interactions.

For a specimen of volume V, there are $V/8\pi^3$ possible modes for each polarisation of a three dimensional lattice in one unit volume of reciprocal (K) space [68]. For each

polarisation, the total number of possible modes enclosed within a spherical volume of Kspace with wavevector less than the radius K is given by [(68)]:

$$N = \left(\frac{V}{8\pi^3}\right)\frac{4\pi K^3}{3} \tag{21}$$

The density of modes for each polarisation of a three dimensional cubic lattice is given by [(68)]:

$$D(\omega) = \frac{dN}{d\omega} = \left(\frac{VK^2}{2\pi^2}\right)\frac{dK}{d\omega} \tag{22}$$

In the Debye model, the dispersion relation is assumed linear, so that all modes travel at the same velocity, v, within the lattice. Thus [(68)]:

$$\omega = vK \tag{23}$$

The total number of acoustic modes of the lattice is N, which equals the number of primitive cells (smallest repeating unit) in the specimen lattice, and the number of atoms. The highest frequency mode possible is then given by the frequency ω_D, which from equation (20) is [(68)]:

$$\omega_D^3 = \frac{6\pi^3 v^3 N}{V} \tag{24}$$

Since there are no modes with frequency greater than ω_D, the expression for the total energy of the phonons becomes [(68)]:

$$U = \frac{3V\hbar}{2\pi^2 v^3}\int_0^{\omega_D} d\omega \, \frac{\omega^3}{\exp\left(\frac{\hbar\omega}{k_B T}\right) - 1} \tag{25}$$

Where the factor of 3 appears from the simplifying assumption that all three polarisations travel at the same velocity v. The integral may be simplified by making the substitution $x = \hbar\omega/k_B T$, so that the upper limit of integration due to the frequency cut-off becomes $x_D = \hbar\omega_D/k_B T \equiv \theta_D/T$.

The total phonon energy is then:

$$U = 9Nk_B T\left(\frac{T}{\theta_D}\right)^3 \int_0^{x_D} dx\ \frac{x^3}{\exp(x) - 1} \tag{26}$$

At very low temperatures, of the order and below $T \approx \theta_D/50$, the upper limit may be allowed to run to infinity as only the low frequency modes are thermally excited [(68)], since the thermal energy exciting the modes is small and modes may only be excited in quanta of $\hbar\omega$. This allows use of the relation $\int_0^\infty dx\ \frac{x^3}{\exp(x)-1} = \frac{\pi^4}{15}$. The heat capacity is then simply the temperature differential of the total phonon energy, U. After the low temperature approximation has been used to simplify the integral in equation (26), the heat capacity (at constant volume) of the lattice due to thermal phonons is [(68)]:

$$C_{Lat} = \frac{12\pi^4}{5} Nk_B \left(\frac{T}{\theta_D}\right)^3 \tag{27}$$

The system of phonons in a lattice may be treated in analogy with a gas of particles in a box, since phonons conduct heat by their diffusion through the lattice. In thermal equilibrium, there is zero net particle flux in any of the three Cartesian directions. In the $+x$ direction, for example, the particle flux is $\frac{1}{2}n\langle|v_x|\rangle$, with an equal flux travelling in the opposite direction. Here, n is the concentration of particles and $\langle|v_x|\rangle$ the average value of the modulus of the x component of the particle velocity v [(68)].

Under the influence of a temperature gradient applied in the x direction, a phonon of heat capacity c moving from a lattice region of temperature $T + \Delta T$ to a lattice region of

temperature T loses an energy amount $c\Delta T$ as it cools. The temperature difference between the two free ends of a phonon's path is [68]:

$$\Delta T = \frac{dT}{dx} l_x = \frac{dT}{dx} v_x \tau \tag{28}$$

Where l_x is the x component of the free path and τ is the average time between collisions. The net flux of energy, from consideration of the net particle flux, is then [68]:

$$q = -n\langle v_x^2 \rangle c\tau \frac{dT}{dx} = -\frac{1}{3} n\langle v^2 \rangle c\tau \frac{dT}{dx} \tag{29}$$

By definition, $l = v\tau$ and $C_{Lat} = nc$. The Debye model used for determining C_{Lat} made the assumption that v is constant, thus the heat flux may be expressed as [68]:

$$q = -\frac{1}{3} C_{Lat} v l \frac{dT}{dx} \tag{30}$$

The definition for the thermal conductivity is $q = -\kappa \frac{dT}{dx}$, so the thermal conductivity of the lattice due to phonons may be expressed as [68]:

$$\kappa_{Lat} = \frac{1}{3} C_{Lat} v l = \frac{12\pi^4}{15} N k_B v l \left(\frac{T}{\theta_D}\right)^3 \tag{31}$$

The temperature dependence of the lattice thermal conductivity is dependent on the temperature dependence of the phonon mean free path, l. This in turn depends on the dominant scattering process that is limiting the mean free path. The figure below (Figure 54) illustrates the processes which limit the phonon mean free path in metals over a range of temperatures.

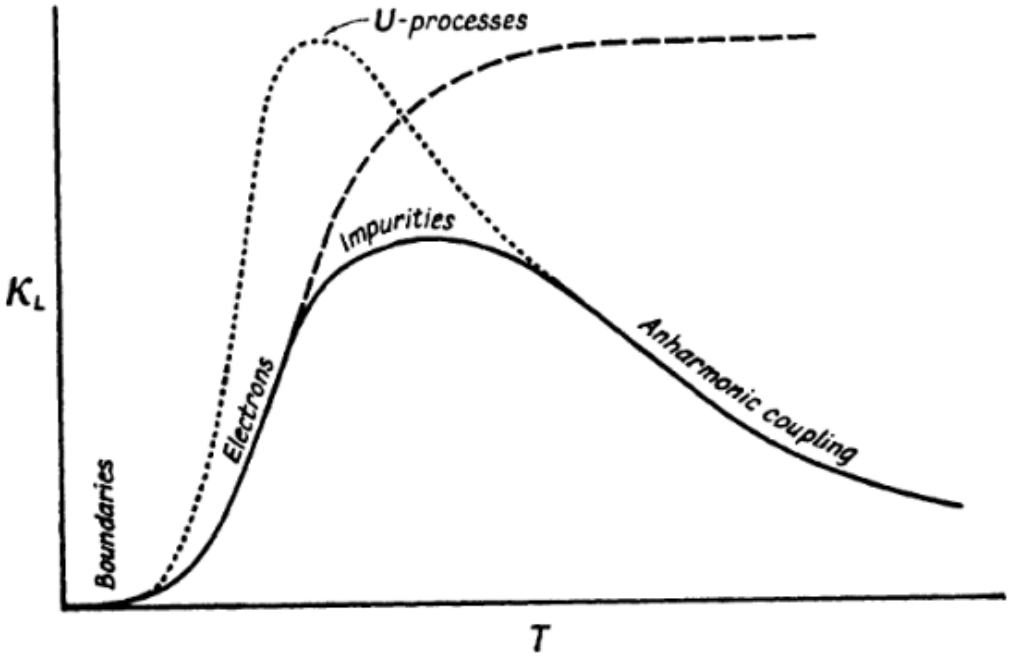

Figure 54: Typical form of Lattice thermal conductivity of metals, showing dominant scattering processes throughout the temperature range. The low temperature region (<4K) of interest is limited by electron and boundary scattering. Boundary scattering is scattering at the physical boundaries of the specimen (surfaces) and structural boundaries such as grain boundaries. Electron scattering is where phonons are scattered by conduction electrons. Impurity scattering is phonons being scattered by the presence of foreign atoms in the lattice. Anharmonic coupling occurs when the temperature is sufficient such that the anharmonic terms in the phonon potential are no longer negligible, and the phonon modes begin to affect each other. U-Processes are Umklapp processes, which are phonon scattering events where a phonon is scattered such that its position in K-Space translates by a reciprocal lattice vector. After (69).

The scattering devices may be other phonons, lattice imperfections or in the temperature range of interest (4K and below), boundaries and conduction electrons [(69), (70)]. Phonon-Phonon scattering only occurs at high temperatures ($T > \theta_D$), where the anharmonic coupling terms in the lattice potential are no longer negligible, and their effect causes the modes to affect one another. At low temperatures ($T \ll \theta_D$), the only phonon modes that are excited are the low energy long wavelength modes. Such modes have a wavelength on the same scale as the crystal dimensions, hence the point dimensionality of impurities is very small in comparison, and impurity scattering is negligible.

At liquid Helium temperature and below, a metal is approaching the boundary scattering temperature region. Boundary scattering is caused by the phonons scattering at the

sample's physical boundaries (surfaces) and at boundaries within the crystal where the crystal lattice may be aligned along a different direction either side (i.e. The *grain* is different, in analogy with wood grain). These are grain boundaries. Boundaries are geometric features, thus the impedance they cause to phonon flow do not change with temperature, as they are fixed physical properties. Thus, the mean free path, l, as limited by this type of scattering, is independent of temperature, thus the lattice thermal conductivity will be cubic in temperature as shown by equation (31).

In a conductive metal, the presence of conduction electrons can cause limitation of the mean free path proportional to $1/T$ in the temperatures of interest to the work of this thesis. This is shown in the results of Long (70) and Wagner (71), whom find experimentally that Tungsten (the metal of interest to the work in this thesis) has a lattice conductivity that is quadratic in temperature due to the scattering of phonons by conduction electrons.

The dominating scattering mechanism at the liquid Helium temperature and below is important, as it determines the overall temperature dependence of the lattice thermal conductivity. For dielectrics the limiting mechanism is certainly boundary scattering, resulting in cubic temperature dependence. In metals, the temperature at which boundary scattering begins to dominate will be different for each metal, even between samples of differing quality in crystal homogeneity. Hence, it is necessary to inspect the thermal conductivity measurements for a particular sample and deduce which mechanism dominates in order to know the correct temperature dependence of the lattice term.

4.1.2 Electron Thermal Conductivity

In a metal, the crystal binding mechanism allows for some of the electrons to move effectively as if free when under the influence of an external electric field or

temperature gradient, imparting upon them the ability to transport both heat and charge.

Valence electrons in metals are delocalised from the atoms of the crystal lattice, such that the lattice is in fact a periodic array of positive ionic cores. An oft quoted description of a metal is of 'positive ionic cores in a sea of negative electrons' [(68)]. The free valence electrons of a metal transport heat rapidly along a thermal gradient by diffusion, i.e. 'hot' electrons (those with a high kinetic energy) move to regions of 'cold' electrons, in analogy with a gas of free particles. This allows the thermal conductivity to be determined from the heat capacity of the conduction electrons using the same kinetic relation as was used for the lattice thermal conductivity.

The Pauli Exclusion Principle states that no two electrons can occupy the same quantum state, as is true for all Fermions. As a consequence, only electrons of a specific narrow range of energy may contribute to the heat capacity of a metal, and accordingly, the thermal conductivity. Electrons are governed by Fermi-Dirac statistics, which incorporates the exclusion principle. Examination of the Fermi-dirac distribution illustrates the small proportion of electrons that contribute to thermal processes. The Fermi-dirac distribution is given by equation (32) [(68)]:

$$f(E) = \frac{1}{\exp\left(\frac{E-\mu}{k_B T}\right) + 1} \tag{32}$$

The Fermi-dirac distribution gives $f(E)$, the probability of an energy state of energy E being occupied at temperature T. μ is the chemical potential, which is equal to the Fermi energy at absolute zero. This distribution function is plotted in Figure 55 for several values of temperature, expressed in terms of μ.

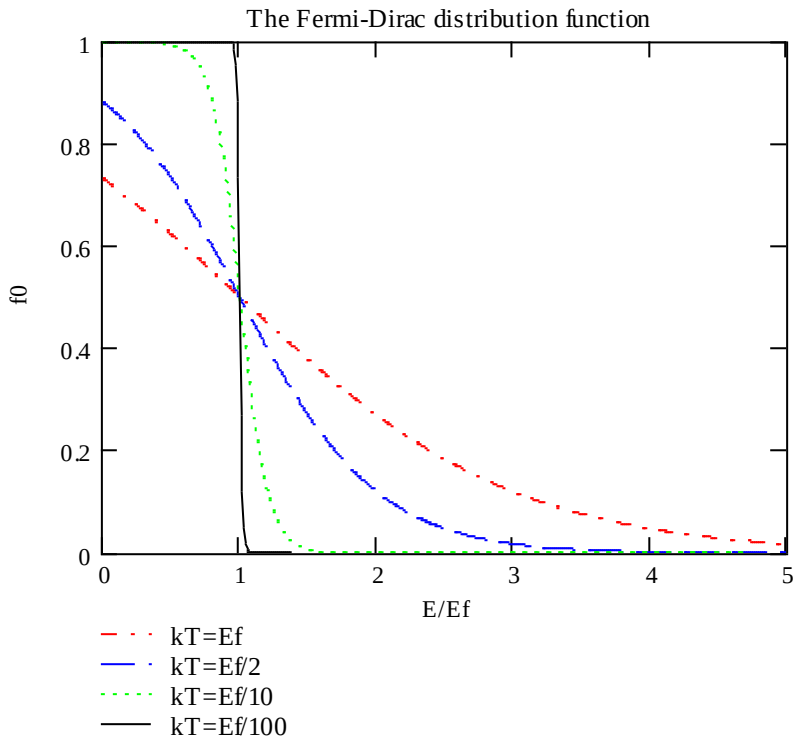

Figure 55: The Fermi-Dirac distribution function plotted for several ratios of thermal energy/Fermi energy. As the temperature is decreased towards absolute zero, the function approaches a step function.

As can be seen from Figure 55, as the temperature tends to zero the Fermi-dirac function approaches the form of a step function. Indeed, at absolute zero all states up to (and including) E_F (The Fermi energy) are filled and all above it are empty. The distribution function is a perfect step function. At any finite temperature T, electrons in the energy states within $\sim k_B T/2$ below E_F may be thermally excited to states within $\sim k_B T/2$ above E_F. These electrons are the only electrons that contribute to the heat capacity of a metal. All other electrons are in energy states too low for thermal excitation, which imparts an energy of the order $\sim k_B T$ to an electron. There are no free states for these electrons to be excited into.

The electrons that are able to transport heat and thus contribute to thermal conductivity of a metal are those valence electrons whose energies are typically within

an energy range $\sim k_B T$ of the energy of the Fermi Surface, in the so-called 'thermal layer' [(69)]. The Fermi surface is the constant energy surface in reciprocal space (momentum space or wavevector space) which at absolute zero divides the filled and unfilled energy states. In conductive metals, the Fermi surface resides in the conduction band. Electrons at the Fermi surface have energy E_F (The Fermi energy). In the free electron theory, the Fermi surface is a sphere, but for real metals is usually some more complicated shape.

The free electron theory can be used to determine the heat capacity of the conduction electrons if the temperature is sufficiently low such that $k_B T \ll E_F$ (Typically at least a few hundred Kelvin). If N electrons are heated from absolute zero to temperature T, the total energy increase is [(68)]:

$$\Delta U = \int_0^{\infty} dE\, E D(E) f(E) - \int_0^{E_F} dE\, E\, D(E) \tag{33}$$

Where $D(E)$ is the number of accessible electron states per unit energy range. This expression may be re-written [(68)]:

$$\Delta U = \int_{E_F}^{\infty} dE(E - E_F) f(E) D(E) + \int_0^{E_F} dE(E_F - E)\,[1 - f(E)]D(E) \tag{34}$$

The heat capacity is the differential of the total energy with respect to temperature, hence [(68)]:

$$C_e = \frac{dU}{dT} = \int_0^{\infty} dE(E - E_F)\frac{df}{dT} D(E) \tag{35}$$

In the regime where $k_B T \ll E_F$, the density of electron states does not change appreciably, as the energy range of accessible states remains very close to E_F. It is valid

to approximate the density of states by taking its value at E_F as a constant, such that $D(E) \approx D(E_F)$. The chemical potential, μ, remains extremely close to its value at absolute zero, E_F, hence it is reasonable to assume $\mu = E_F$. After making these approximations, the heat capacity expression becomes [(68)]:

$$C_e = D(E_F) \int_0^\infty dE \, \frac{(E - E_F)^2}{k_B T^2} \frac{\exp(E - E_F/k_B T)}{(\exp(E - E_F/k_B T) + 1)^2} \tag{36}$$

The integral can be evaluated by making the substitution $x = (E - E_F)/k_B T$, so that the heat capacity simplifies to [(68)]:

$$C_e = k_B^2 T D(E_F) \int_{-E_F/k_B T}^\infty dx \, x^2 \frac{\exp(x)}{(\exp(x) + 1)^2} \tag{37}$$

Since the temperatures being considered within the scope of this thesis are sufficiently low such that $k_B T \ll E_F$, the exponential terms are negligible at the lower limit of integration. Hence it is possible to extend the range of integration beyond the lower limit to $-\infty$. This allows the integral to be replaced by $\frac{\pi^2}{3}$ by use of an algebraic identity which proves $\int_{-\infty}^{\infty} dx \, x^2 \frac{\exp(x)}{(\exp(x)+1)^2} = \frac{\pi^2}{3}$ [(68)].

The density of energy states at the Fermi energy is [(68)]:

$$D(E_F) = \frac{3N}{2E_F} = \frac{3N}{2k_B T_F} \tag{38}$$

Where T_F has been introduced as a conventional reference temperature, which is termed the Fermi temperature as it corresponds to the Fermi energy. Using these results, the final heat capacity of a free electron gas is [(68)]:

$$C_e = \frac{1}{2} \pi^2 N k_B \frac{T}{T_F} \tag{39}$$

From this expression, the thermal conductivity due to the free conduction electrons can be found by the same kinetic expression used to calculate the lattice thermal conductivity from the phonon heat capacity [(68)]. All electrons have energy close to the Fermi energy, thus all move with a velocity close to the corresponding Fermi velocity, v_F, which allows the velocity of all thermally active electrons to be approximated by v_F. Thus, the electron contribution to the thermal conductivity may be written:

$$\kappa_e = \frac{1}{3} C_e v_F l_e = \frac{\pi^2 n k_B^2 l_e}{3 m v_F} T \tag{40}$$

Where v_F and l_e are the average electron velocity at the Fermi energy and electron mean free path respectively, n is the electron concentration and $k_B T_F = \frac{1}{2} m v_F^2$ with m as the free electron mass. The electron concentration replaces the electron number so that the heat capacity is per unit volume. The mean free path of the electrons is the only temperature dependent term. This term's temperature dependence relies on what dominant scattering mechanism is limiting the electron mean free path.

The scattering devices may be other electrons, phonons, or lattice imperfections and boundaries. Since the adopted model for the electrons is the free electron model, there are, by definition, no electron-electron interactions to consider in this case.

The electrons interact infrequently with the phonons of the lattice at liquid Helium temperature and below, due to the excited phonon modes having long wavelengths (on the scale of the sample size). These are very large in comparison to the electron wavelength, which is of the same order of magnitude as the atomic spacing. As the temperature approaches zero, the effect of phonon scattering on the electronic thermal conductivity decreases as the number of phonons decreases and their wavelengths increase.

At liquid Helium temperatures the dominant scattering mechanism of the conduction electrons is due to static inhomogeneities of the lattice, which are on the same scale as the electron wavelength. Static inhomogeneities of the lattice are lattice imperfections on the scale of the atomic spacing, and are present in several manifestations. In general, they may be characterised by their dimensionality: Point defects, line imperfections, and planar imperfections.

- **Point defects** are lattice defects at a point on the crystal lattice, typically a lattice site. These could be lattice vacancies (empty lattice sites), isotope atoms at lattice sites, and chemical impurity atoms at lattice sites. There are also interstitial defects, where an atom/impurity is situated in an interstitial location on the lattice, i.e. between lattice sites. All serve to disrupt the homogeneity of the crystal lattice in the vicinity of the point defect.

- **Line imperfections** are typically dislocations, which are where a plane of atoms within the lattice ends prematurely (in the case of edge dislocations), or where one plane of atoms in the lattice has slipped over another along a line parallel to the slip direction (as in the case of screw dislocations). These line imperfections affect the shape and regularity of the lattice in the vicinity of the dislocation line.

- **Planar imperfections** may be grain boundaries, where the grain of the crystal differs on each side of the boundary. Low-angle grain boundaries are caused by an array of dislocations [(68)]. Other planar imperfections are stacking faults, which are caused by slip (the movement of dislocations under an applied shear stress) which changes the stacking sequence of the lattice in the region. The actual surfaces of the crystal itself may be regarded as planar imperfections, as at the surface the lattice structure is different to within the bulk.

Another form of electron scattering occurs in metals with magnetic impurities at low temperatures – *Kondo* scattering. Kondo scattering is a phenomenon where the electrical resistivity increases with decreasing temperature (resulting in an overall resistance minima when combined with the scattering mechanisms considered thus far) due to the local magnetic moment present in the crystal lattice at the sites where magnetic impurities reside. This was first observed in 1934 by Kondo in Gold with Iron impurities [(72)], and is shown below in Figure 56.

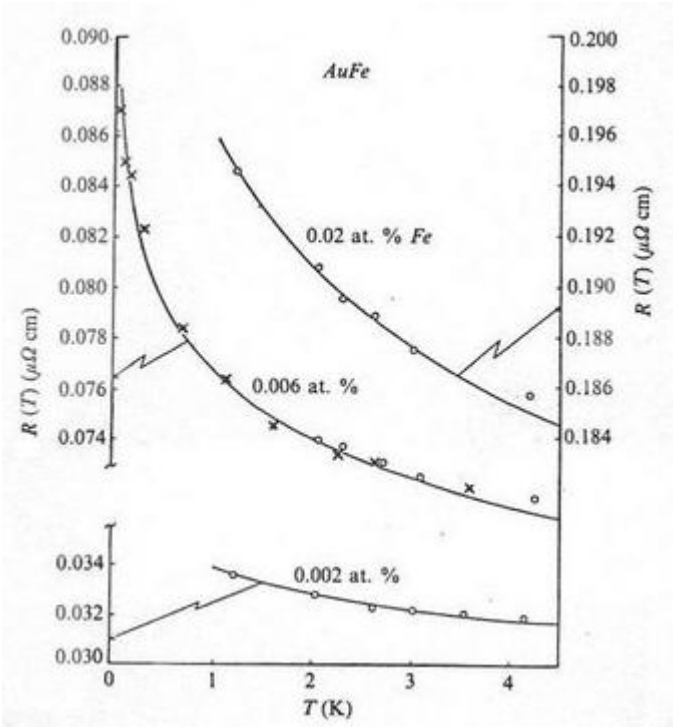

Figure 56: A comparison of Kondo's experimental results (points) for the electrical resistivity of iron impurities in gold at very low temperatures with theoretical predictions (lines) that include logarithmic term representing the Kondo effect. After (72).

No such behaviour was observed in any of the experimental measurements of thermal conductivity of Tungsten during the research published in this thesis; hence Kondo scattering shall not be discussed further.

The electronic thermal conductivity, κ_e, is related to the electrical conductivity, as in both cases the same electrons are transporting either the heat or the charge. Therefore,

in both cases, the electrons are subject to the same scattering processes. The relationship between the thermal conductivity and the electrical conductivity is given by the Wiedemann-Franz law [(68)]:

$$\kappa_e = \sigma_0 LT \tag{41}$$

Where σ_0 is the electrical conductivity and L is the Lorenz number, which for free electrons takes the value $L_0 = \frac{\pi^2}{3}\left(\frac{k_B}{e}\right)^2 = 2.45 \times 10^{-8}\ \mathrm{W\Omega\ K^{-2}}$.

The reciprocal of the electrical conductivity, the electrical resistivity, may be used to determine the quality of the lattice. At the low temperatures of interest to this thesis (4K and below), the metal is in the residual resistance region, where the resistivity is constant and is owed to the scattering of electrons by the imperfections of the lattice. This residual component is constant over all temperatures, but at high temperatures (such as ~300K) the resistivity will have dominant components from other scattering mechanisms, such as phonon scattering. The resistance at 273K divided by the resistance at 4K provides a measure of the quality/homogeneity of the crystal lattice. This quantity is termed the residual resistance ratio, or RRR. The relative resistance (inverse of the RRR) of a metal will follow the same form regardless of the quality of its lattice, but for crystals with more lattice imperfections, the residual resistance is higher, leading to a uniformly higher resistivity in comparison to a crystal with fewer lattice imperfections. This is illustrated in Figure 57 where the relative resistance (in this case, measured resistance below 20K divided by measured resistance at 290K) of potassium is plotted for two samples.

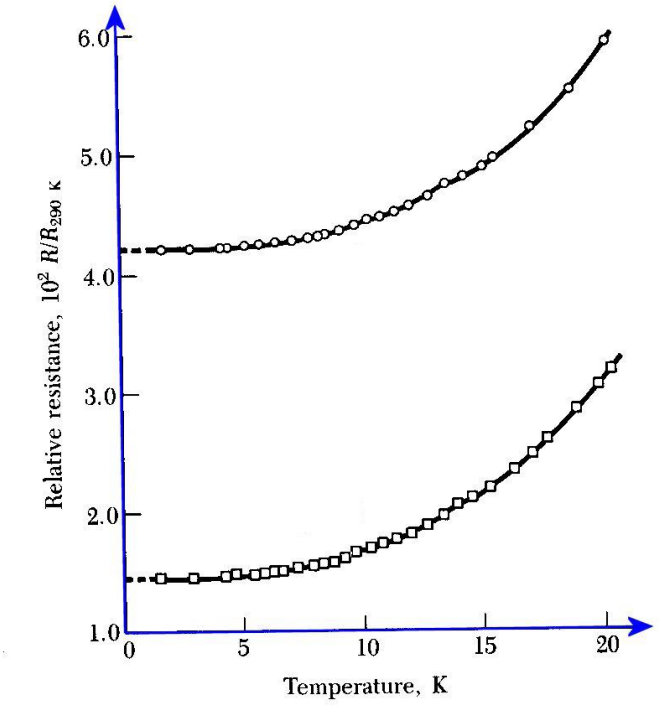

Figure 57: Relative resistance (inverse of RRR, so smaller is more pure) of Potassium for 2 samples measured below 20K. Upper curve is for a sample with more lattice imperfections (less pure). Lower curve is for sample with fewer lattice imperfections (more pure). Taken from (68).

Figure 57 clearly shows the effects of greater concentrations of lattice imperfections on the resistivity of a metal. The upper curve represents a sample with a greater concentration of lattice imperfections, causing it to have high residual resistance, hence higher relative resistance (and lower RRR value) in comparison to the sample with a lower imperfection concentration (lower curve).

The imperfections of the lattice, by their static nature, do not change with temperature, thus the limitation of the electron mean free path due to such features is constant in temperature. The resulting temperature dependence of the electronic thermal conductivity is therefore the same as for the electronic heat capacity, i.e. a linear relationship.

In such cases where the smallest dimensions of a metallic sample is of similar scale to the mean free path, the contribution to the resistivity due to boundary scattering at the sample's surfaces begins to dominate.

This situation occurs at low temperatures where the electron mean free path is limited by the scattering mechanisms due to lattice defects in the bulk metal, as has been described. In pure, high quality samples, the lattice defects are few and the mean free path may have a length of the order of a few millimetres. If a sample has any of its dimensions smaller than the mean free path, boundary scattering will be the dominant scattering mechanism. This is exemplified by the figure below, which shows the resistivity of thin tin foil as a function of thickness at 3.8K (in the residual resistance region).

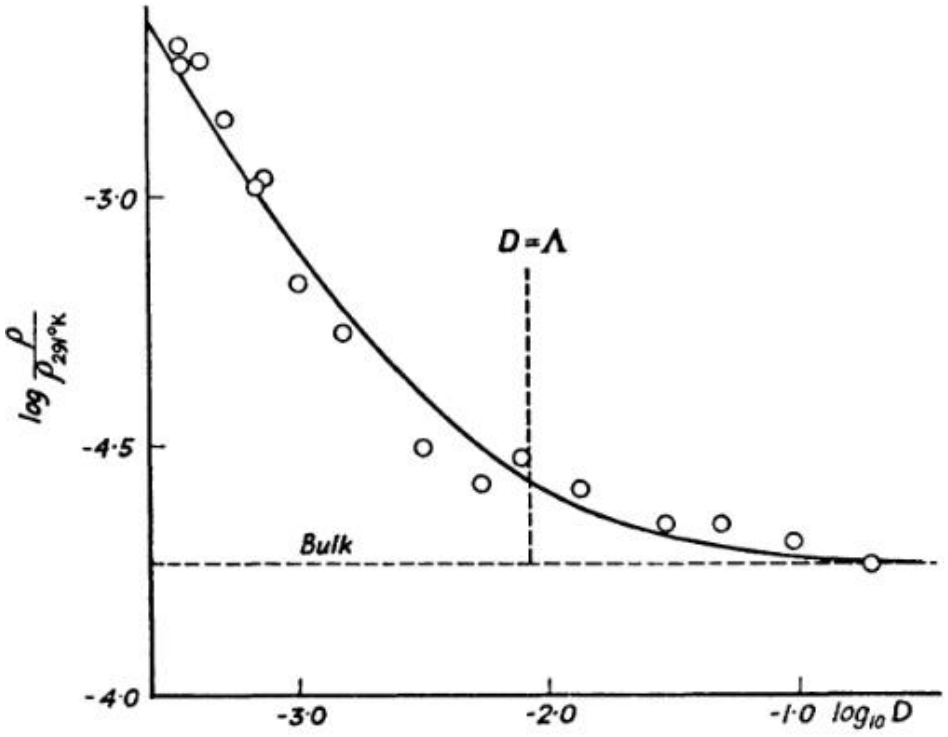

Figure 58: Resistivity of thin Sn foil at 3.8K. Bulk resistivity is shown for comparison. Situation where sample dimension D is equal to the mean free path Λ is also shown. After Andrew (73).

As Figure 58 shows, the electrical resistivity increases as the foil thickness is decreased towards approaching the mean free path (in this case labelled as Λ on the figure). This graph was originally produced by Andrew (73), whom fit his experimental results to a theoretical curve derived from scattering theory in order to deduce the mean free path. His findings agreed with other published data on the mean free path [(73)]. The graph shows how resistivity continues to increase as the thickness of the foil is decreased beyond the mean free path. The figure also shows the constant resistivity expected from a bulk sample in the residual resistance region. Since the electrical resistivity increases, the electrical conductivity and thus the thermal conductivity also decrease below the bulk value. The mean free path remains independent of temperature.

4.1.3 Relative Contributions to the Total Thermal Conductivity

The respective contributions to the thermal conductivity of a metal arising from the lattice and the electrons may be calculated theoretically for the liquid Helium temperature regime using equations (31) and (40).

The respective theoretical components of the thermal conductivity for Copper are calculated hence:

The lattice conductivity is given by equation (31). The phonon velocity is simply the velocity of sound in Copper, 4759 m s^{-1} [(74)]. The phonon mean free path of Copper, in the liquid Helium regime, is limited by the physical boundaries of the sample, as discussed in 4.1.1. For simplicity, one mole of Copper is assumed, which may be shaped into a cube of approximately 2 cm side. Thus, the phonon mean free path is taken to be 2 cm and the number of atoms is Avagadro's number. The Debye temperature of Copper is 343K [(68)]. Putting these values into equation (31) yields the following contribution to the thermal conductivity:

$$\kappa_{Lat} \approx (1.53 \times 10^{-3})\, T^3 \ \mathrm{W\,m^{-1}\,K^{-1}} \tag{42}$$

The electronic contribution is given by equation (40). Each atom of Copper provides one conduction electron. Thus, the electron concentration is found to be 8.47×10^{28} m^{-3}. The Fermi velocity is 1.57×10^{6} m s^{-1} [75], and the mean free path may be calculated from the definition of the electrical conductivity thus:

$$l_e = \frac{\sigma_0 m v_F}{n e^2} \tag{43}$$

For a Copper of RRR of 1530, the electrical conductivity at 4K is ~7.7×10^{10} Ω^{-1} m^{-1} [76]; giving a mean free path of ~0.05mm. With these values, the electronic contribution to the thermal conductivity is:

$$\kappa_e \approx (1.86 \times 10^{3}) T \ \mathrm{W\,m^{-1}\,K^{-1}} \tag{44}$$

Clearly, the coefficient for the electronic contribution is far larger than the coefficient for the lattice contribution to the thermal conductivity. At 4K the electronic contribution to the thermal conductivity is a factor ~76,000 larger than that of the lattice. In addition, the lattice contribution has a sharper decrease with decreasing temperature due to the cubic dependence. The lattice contribution to thermal conductivity in the liquid Helium regime is so small in comparison to the electron contribution that it is often neglected.

The mechanisms contributing to thermal conductivity of metals may be exploited to form a heat switch for the liquid Helium temperature regime. It is possible, for some metals, to apply an external magnetic field in order to suppress the electron contribution to the thermal conductivity to such a degree that the lattice contribution becomes dominant. This allows for the possibility of turning a lump of metal into a device that can switch between an extremely highly thermally conductive state to an

orders of magnitude lower thermally conductive state simply by switching on the external magnetic field. The phenomenon that allows this to be possible is *Magnetoresistance.*

4.2 MAGNETORESISTANCE

In metals, heat is transported by two carrier types; electrons and phonons. Phonon heat conduction arises from the thermal vibrations of the crystal lattice, and can be approximated by use of the Debye T^3 law at low temperatures. The lattice conductivity is thus seen to drop significantly with decreasing Temperature (as either T^2 or T^3 depending on the dominant scattering mechanism) in the liquid Helium temperature range. The conduction electrons in a metal are able to transport heat far more effectively than phonons, typically carrying several orders of magnitude more heat power in the liquid Helium temperature regime, as has been demonstrated in the previous section.

The phenomenon of Magnetoresistance allows the electronic heat transport process to be suppressed in a controlled manner by application of an external magnetic field. Magnetoresistance is the term generally used to describe the change in electrical resistance under application of an external magnetic field. However, since the same electrons conduct heat as well as charge, and the thermal conductivity is proportionally related to the electrical conductivity, there is inevitably a corresponding change in the thermal conductivity. Magnetoresistance therefore will refer only to the thermal magnetoresistive effect in this thesis, whereby application of an external magnetic field serves to decrease the thermal conductivity of a metal.

Phonons are unaffected by external magnetic fields, since phonons are simply relative atomic displacements and any practically achievable external field is always negligibly weak compared to the local fields arising from the atomic lattice (effectively of the order of 10^4 Tesla) [77]. Thus, the lattice contribution to the thermal conductivity at a given temperature remains constant under all applied external magnetic fields. The basis of a high switching ratio heat switch that exploits Magnetoresistance relies on the weak,

rapidly decreasing (with temperature) lattice conductivity combined with the controllability of the dominant electronic conductivity.

The origin of the magnetoresistive effect arises from the action of the Lorentz force upon the electrons within the metal when an external magnetic field is applied. The electrons describe curved paths under such conditions, manifested as helical orbits in the plane normal to the applied magnetic field, and centred on magnetic field lines. All metals exhibit some degree of magnetoresistance. If the magnetic field is strong enough to appreciably curve an electron's trajectory within a mean free path, it is likely that considerable magnetoresistance will be observed [(78)].

Under the influence of an external magnetic field, electrons describe orbits on surfaces of constant energy in momentum-space, e.g. on sheets of the Fermi surface, which correspond to the real space helical orbits [(78)]. These reciprocal space orbits are also in the plane perpendicular to the magnetic field axis. The frequency of the orbits is the cyclotron frequency, given by equation [(78)]:

$$\omega_c = eB/m^* \tag{45}$$

Where *e* is the electronic charge, *B* is the applied magnetic field, and *m** is the effective electron mass. This effective mass is a quantity which can vary between different orbits in the same sample of metal. Since the electrons are locked into these orbits, they diffuse through the metal along a temperature gradient at a greatly reduced rate than if the magnetic field were not present. The time between scattering events is increased as the magnetic field increases and forces the electrons into tighter orbits. As electron

diffusion is the dominant process contributing to thermal conductivity, the total thermal conductivity is significantly reduced.

4.2.1 MAGNETORESISTIVE METALS

The type of Fermi surface of a metal dictates the intensity of the magnetoresistive effect. This is because only the electrons close to the Fermi surface are able contribute to the conduction of heat; thus, the constant energy orbits which conduction electrons follow exist on or very close to the Fermi surface. Some metals allow for conduction electrons to traverse open orbits in reciprocal space. Typically open orbits will be present most significantly in metals with an open Fermi surface. Open orbits extend throughout the reciprocal lattice, so that electrons on such trajectories are not confined into corresponding helical real space orbits. Instead, the corresponding real-space orbits for such open orbits are sinuous paths along a straight line [(78)]. The result is that the magnetoresistive effect in these metals is not as strong as for metals that only allow closed orbits. Metals with a closed Fermi surface will have the majority of the conduction electrons locked into closed orbits, thus they cannot diffuse through the metal as readily as for the open Fermi surface case.

In order to reduce the electronic contribution to the thermal conductivity to such an extent that the lattice contribution becomes dominant, it is necessary to use a magnetic field that is strong enough to force the conduction electrons of a metal with a closed Fermi surface into such tight orbits such that the orbit radius, r_H, is much smaller than the electron mean free path, l_e [(77)]. The metal is then said to be in its high-field regime. The criterion for the high field regime is:

$$\frac{l_e}{r_H} \equiv \omega_c \tau \gg 1 \tag{46}$$

Where ω_c is the cyclotron frequency of orbit as defined previously, and τ is the electronic relaxation time $\tau = l_e / v_F$. The quantity $\omega_c \tau$ is therefore the mean angle an electron turns through between collisions. $\omega_c \tau$ depends on the effective electron mass, *m**, which is extremely difficult to calculate, especially since it varies between different orbits in the same metal. An estimate of $\omega_c \tau$ can be made by considering the definition of the cyclotron frequency and the easily measured electrical conductivity in zero applied magnetic field, which is defined by [78]:

$$\sigma_0 = \frac{ne^2 \tau}{m^*} \tag{47}$$

The quantities on which σ_0 depend are invariant under application of a magnetic field, allowing this non magnetic property to be used to eliminate *m**. Combining equation (45) with equation (47) yields the following relation:

$$\omega_c \tau = \frac{B \sigma_0}{ne} \equiv \frac{l_e}{r_H} \tag{48}$$

This allows determination of the magnetic field required to push a metal into its high field regime if the zero field electrical conductivity is known.

The application of an external magnetic field causes electrons to orbit around the lines of magnetic field. In a cubic crystal, which would otherwise have an isotropic thermal

conductivity (under zero applied magnetic field), a special direction is set by the orientation of the magnetic field. By convention, this defines the *z* direction. The nature of the curved electron trajectories, as they are bent around magnetic field lines, serves to slow down electron flow in the *x*-*y* plane. This results in the thermal conductivity no longer being isotropic, but variant in different directions relative to the magnetic field axis (*z*). The consequence of this is that the complete electronic contribution to the thermal conductivity must now be represented by a tensor containing directional components.

To construct a magnetoresistive heat switch, the magnetic field is applied orthogonally to the direction of the temperature gradient, which is directed in the *x*-*y* plane. For metals in the high field region, the general form of the electronic thermal conductivity is represented by the tensor [(79)]:

$$\kappa_e(T,B) = \begin{pmatrix} \frac{a_{xx}}{B^2} & \frac{1}{3}\left(\frac{\pi k_B}{e}\right)^2 T\frac{e(n_1-n_2)}{B} & \frac{a_{xz}}{B} \\ -\frac{1}{3}\left(\frac{\pi k_B}{e}\right)^2 T\frac{e(n_1-n_2)}{B} & \frac{a_{yy}}{B^2} & \frac{a_{yz}}{B} \\ \frac{a_{zx}}{B} & \frac{a_{zy}}{B} & a_{zz} \end{pmatrix} \quad (49)$$

Where the a_{ij} terms are functions of the temperature, $n_1$is the concentration of electrons and n_2 is the concentration of holes (vacant electron states). The derivation of this tensor is long and complex (see Lifshits et al. (77) and Azbel et al. (79) for full derivation), but the only important information to note is that each of the tensor components originates from the expansion of each a_{ij} as a power series in $1/B$ beginning from the zero term, whence the lowest order terms are kept. It is important to see that for the tensor components contributing to the thermal conductivity in the *x*-*y* plane, the *xy* and *yx* components depend on the difference between the number of

electrons and the number of holes. Thus, it is clear that if the metal is compensated ($n_1 = n_2$), these terms vanish, and these components are replaced with the next term in the expansion, such that they now depend on B as $1/B^2$. This stronger dependence on magnetic field shows that compensated metals display a stronger magnetoresistive effect than uncompensated metals.

The preceding arguments have demonstrated that the metals which exhibit the strongest magnetoresistance as a function of the applied magnetic field are those which are compensated (have equal numbers of electrons and holes) and have a closed Fermi surface [(77), (78), (79), (80)]. It is found that the transverse components of the thermal magnetoconductivity tensor for such metals have an inverse quadratic dependence on the applied magnetic field that tends to infinity [(77), (78)].

Metals that meet the criteria of compensation and a closed Fermi surface include Beryllium, Cadmium, Gallium, Molybdenum, Tungsten and Zinc. Magnetoresistive heat switch applications have been investigated for Gallium [(81)], Cadmium [(82)], Beryllium [(66)] and Tungsten [(80), (83)]. Many of these metals have their superconducting transition temperature, T_c, in the desired operating temperature range (50mK – 4K) of the heat switch for the IXO ADR (see Table 10). When a metal is in a superconducting state, its thermal conductivity (under zero magnetic field) is comparatively far lower than in the normal state (which is how superconducting heat switches work, see chapter 3). This greatly reduces the achievable switching ratio for operating temperatures below T_c. Therefore, in order to maintain maximum switching ratio the switch must be operated above its T_c, which means only metals with $T_c < 50\mathrm{mK}$ are suitable for an ADR designed to hold at 50mK.

A comparison of the key properties of the metals that meet the criteria of both compensation and a closed Fermi surface is given in Table 10.

Metal	Transition Temperature T_c [K]	Debye Temperature θ_D [K]
Beryllium	0.026	1440
Cadmium	0.56	209
Gallium	1.083	320
Molybdenum	0.92	450
Tungsten	0.015	400
Zinc	0.85	327

Table 10: Comparison of magnetoresistive materials. After (55).

For applications involving milli-Kelvin temperatures, such as the IXO ADR, only Beryllium and Tungsten have a sufficiently low T_c, at 0.026K and 0.015K respectively. It is worthwhile to recognise that during the cooling phase (holding at ~50mK) of the IXO ADR cycle the magnetoresistive heat switch will be under a magnetic field that prevents the transition to superconductivity. However, during the early stages of recycling the CPA will still be around 50mK as the magnetisation process begins and the magnetic field applied to the magnetoresistive heat switch is removed. Thus, the onset of superconductivity would impede the recycling process, and lead to a longer overall recycle time.

To ensure minimal heat conduction in the thermal 'off' state (i.e. the low thermally conducting state achieved with a magnetic field), a metal with a low phonon contribution to the thermal conductivity must be chosen. A higher Debye temperature, θ_D, implies a lower phonon thermal conductivity (see equation (31)). Beryllium has a θ_D of 1440K, whereas Tungsten has a θ_D of 400K. Beryllium is clearly an excellent

candidate, as Radebaugh's results indicate [66]; however, large single crystals are difficult to obtain and Beryllium is highly toxic, and is therefore difficult to work with. In addition to the problems in obtaining and working with Beryllium, published data [59] illustrates Tungsten has the capability to out-perform Beryllium, with the measured sample of Tungsten having a far higher thermal conductivity in the zero magnetic field case, and similar thermal conductivity when under a similar magnetic field when compared to the measured sample of Beryllium (Figure 59).

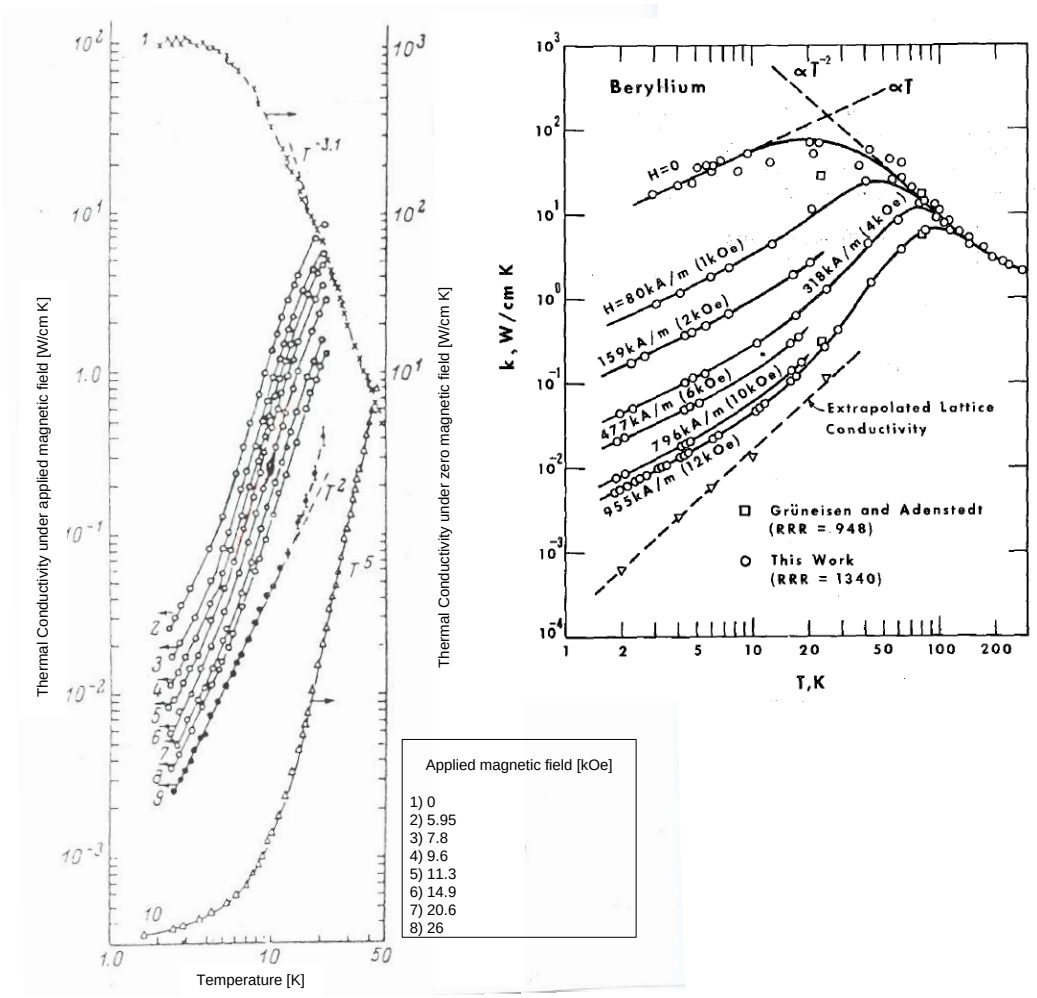

Figure 59: Left: Measured thermal conductivity of Tungsten under several applied magnetic fields. Adapted from Batdalov and Red'ko (59). Right: Measured thermal conductivity of Beryllium under several magnetic fields. After Radebaugh (66).

The published data illustrated in Figure 59 shows, along with the previous arguments, that Tungsten is the best practical metal from which to build a heat switch for cryogenic systems operating in the tens of milliKelvin to a few Kelvin temperature range.

4.2.2 TUNGSTEN

Tungsten has a body-centred cubic lattice structure, and if the magnetic field is aligned along a direction of high symmetry (e.g. a crystal axes), the *x*-*y* plane is constructed from the remaining two crystal axes and the thermal conductivity is the same in both the *x* and *y* directions. Symmetry requirements simplify the thermal conductivity tensor further as the matrix elements $a_{xz} = a_{yz} = a_{zx} = a_{zy} = 0$, as there is no longitudinal-transverse coupling [(77), (78), (79)]. Thus, the thermal conductivity tensor of Tungsten in this case has the form:

$$\kappa_e(T,B) = \begin{pmatrix} \frac{a_{xx}}{B^2} & \frac{a_{xy}}{B^2} & 0 \\ \frac{a_{yx}}{B^2} & \frac{a_{yy}}{B^2} & 0 \\ 0 & 0 & a_{zz} \end{pmatrix} \tag{50}$$

Where the applied magnetic field is aligned in the *z* direction and the thermal gradient is along the *x* direction. The *z* component of the thermal conductivity does not contribute to heat flow in the orthogonal *x*-*y* plane, which reduces the effective tensor to a 2 × 2 for a temperature gradient within the x-y plane. The transverse thermal conductivity κ_{xy} has been determined by Long [(84)] to be only a few percent of κ_{xx} in the investigated range of temperatures and fields. Thus, it is reasonable to neglect the effects of κ_{xy} and assume the thermal conductivity is isotropic within the *x*-*y* plane.

The temperature gradient for experimental measurements acts in the *x* direction. Wagner (71), Long (84), and Batdalov (59) find that for high magnetic fields, κ_{xx} has the form:

$$\kappa_{xx}(T,B) = \kappa_{Lat}(T) + \frac{a_{xx}}{B^2} \tag{51}$$

Where the lattice conductivity $\kappa_{Lat}(T)$ is completely independent of magnetic field and a_{xx} represents the magnetoresistive electronic thermal conductivity. For high fields, Wagner (71) found a_{xx} to be of the form $\frac{a_{xx}}{T} = \alpha_0 + \alpha_3 T^3$, where α_0 is the magnetoresistive electron coefficient due to impurity and boundary scattering (residual resistance processes), and α_3 is the magnetoresistive electron coefficient due to other (temperature dependent) scattering processes. As can be seen from equation (51), the form of the thermal conductivity of a metal as the sum of the lattice and electronic contributions (equation (17)) is preserved. The electron contribution has changed from the zero field linear temperature dependence of equation (40) to the high field inverse quadratic dependence on applied magnetic field with an additional term representing the weaker scattering mechanisms, which appear to have a more significant effect than for the zero field case based on Wagner's findings.

From consideration of equation (51) and the form of the lattice thermal conductivity as outlined in 4.1.1, the high field thermal conductivity $\kappa_{xx}(T,B)$ may be written:

$$\kappa_{xx}(T,B) = PT^u + \frac{\alpha_0 T + \alpha_3 T^4}{B^2} \tag{52}$$

Where P is the phonon conductivity coefficient, $T$is the temperature, u the index of phonon conductivity temperature dependence, and $B$is the magnetic field strength. The index of phonon conductivity temperature dependence may be either 2 or 3 depending on if the phonons are scattered chiefly by electrons or boundaries respectively.

Long (70) and Wagner (71) show that Tungsten in fact has a quadratic lattice term, at least in the temperature range of investigation (0.3K - 4.5K). This is shown to be because of the extensive presence of conduction electrons in the metal, which for a pure metal may scatter phonons more than boundaries in the investigated temperature range [(70), (71)].

Chapter 5 details the thermal conductivity measurements of several samples of Tungsten under both zero and 1.8 Tesla applied magnetic field, where Equation (52) is the theoretical basis on which the experimental magnetoresistive heat switch development is built.

4.2.3 Tungsten as a Magnetoresistive heat switch for Space Cryogenics

There has been considerable interest in the development of a Tungsten magnetoresistive heat switch for use in space-flight ADRs [(80), (83), (55)].

The extremely high performance (switching ratio of the order 10^5) potentially obtainable with a Tungsten magnetoresistive heat switch is abundantly evident from measurements published by Batdalov and Red'ko (59) (Figure 59 Left graph). Indeed, this paper is cited by all authors that have studied Tungsten as a thermal switch for space cryogenic applications, and is almost certainly the motivation for investigating this material for such a purpose.

The key findings of Batdalov and Red'ko's investigations are the measured low temperature (2K-20K) thermal conductivities of Tungsten under several applied magnetic fields (0 kOe – 26kOe = 0 Tesla – 2.6 Tesla, where the magnetic field strength, Oe, has been converted into an effective magnetic flux density, Tesla assuming zero magnetisation) (Figure 59 Left graph). These measurements were taken for a cylindrical single crystal Tungsten sample, with a diameter of 4.3mm (limiting dimension, length not given) and a measured RRR of 1.55×10^5. This high RRR implies this particular sample

has exceptionally low scattering due to lattice imperfections and boundary size effects. As considered earlier in this chapter, it is known that the mean free path of electrons at such low temperatures is limited by the imperfections of the lattice, and as such is temperature independent and related to the purity and quality of the crystal lattice itself. For this sample, Batdalov and Red'ko state the electron mean free path at 4K to be 1.4mm. Batdalov and Red'ko determine their sample to be in the high-field regime for all of the non-zero applied fields investigated in the liquid Helium region of temperature [(59)].

In the next chapter, the findings of Batdalov and Red'ko are compared to the findings of other authors who have performed similar measurements, alongside the experimental findings of this thesis. The results are used to determine how a Tungsten magnetoresistive heat switch might perform in a real space cryogenics application, namely the ESA ADR, and to aim to quantify the properties a Tungsten sample must possess in order to perform well as a magnetoresistive heat switch.

4.3 SUMMARY OF CHAPTER 4

The mechanisms of heat transport in metals have been described; the lattice conductivity and in particular, the conduction electrons which dominate the zero field thermal conductivity. The limitations to the conductivity and the mean free path, in the temperature range of interest, are caused mainly by scattering by lattice imperfections. The types of lattice imperfections have been described, along with a measurable parameter (the RRR) which indicates the degree of the presence of such imperfections. The effects of size on mean free path has been briefly described, such that when the mean free path approaches the sample dimensions, the primary scattering mechanism is scattering at the sample boundaries.

The phenomenon of magnetoresistance has been introduced, and the criteria for the strongest magnetoresistance stated as compensated metals with closed Fermi surfaces. In order to suppress electron conduction to such an extent that the lattice conduction becomes the dominant mechanism, a metal must be in the high magnetic field regime. The high field criterion has been introduced as the strength of the magnetic field must be sufficient enough so that the mean angle turned between collisions is much greater than 1 (radian). The mean angle turned between collisions may be estimated from the zero field electrical conductivity and the applied magnetic field.

The metals satisfying the criteria for strongest susceptibility to the magnetoresistive effect have been identified, and the choice of Tungsten as the most suitable material from which to develop a magnetoresistive heat switch has been justified given the operating temperature requirements, accessibility and workability of the material. The theoretical high field transverse magnetoresistive thermal conductivity of Tungsten is found to vary proportionally to the inverse square of the applied magnetic field. This is corroborated by the experimental work of other authors [(80), (59), (84)].

Chapter 5:

DEVELOPMENT OF A TUNGSTEN MAGNETORESISTIVE HEAT SWITCH.

The previous chapter introduced and described the theory of thermal conduction in metals, and discussed the phenomenon of magnetoresistance and how it may be exploited to control the electronic mechanism of thermal conduction in metals to form a heat switch. Tungsten was shown to be the best metal from which to construct a milliKelvin – Helium temperature magnetoresistive heat switch.

This chapter uses the theory developed in chapter 4 in order to interpret measured results of the thermal conductivity of Tungsten under an applied magnetic field. The results of other authors that have investigated Tungsten as magnetoresistive heat switch are discussed and compared to the experimental findings.

Properties determining how effective a sample will be as a heat switch are deduced from the results and published findings. Limitations of 'on' conductance due to pressed contacts where a magnetoresistive heat switch interfaces with other system components (ADR structural interface) are investigated.

The ESA ADR hold time with the original Lead superconducting heat switch is compared to the hold time obtainable when this heat switch is replaced with a Tungsten magnetoresistive heat switch, providing clear evidence of the advantages of such a switch.

5.1 INTRODUCTION

The development of the Tungsten magnetoresistive heat switch has been achieved through direct experimental investigation and comparison to published results. This chapter details the investigations that constitute the development process, by describing each experimental investigation that has been conducted and the results that have been obtained.

1. **Measurements of the thermal conductivity of Tungsten (section 5.2).**

   Measurements of the thermal conductivity of Tungsten have been made for 3 samples of Tungsten of varying purity and dimensions in the temperature range 0.3K - 4.5K under an applied magnetic field of 1.8 Tesla. The thermal conductivity in the absence of a magnetic field has been measured where possible. Results are compared to published data.

2. **Measurements of the thermal conductance of the pressed contact interface between a Tungsten heat switch and a gold-plated Copper thermal bus/mounting structure (section 5.3).**

   The thermal conductance of a typical interface between the thermal bus/mounting structure (gold-plated high-purity Copper) for the heat switch (e.g. like for the ESA ADR) and the Tungsten heat switch has been characterised in the region 4K - 8K. Three types of interface configuration have been investigated, and the results used to justify the selection of the optimal interface type.

3. **Comparison of the ESA dADR hold time with a superconducting and a magnetoresistive heat switch (section 5.4).**

The ESA dADR hold time is investigated using both experimental and modelling results for the superconducting heat switch and the replacement of this heat switch with a Tungsten magnetoresistive switch. This shows the benefit and performance enhancement that can be achieved in a real millikelvin ADR system designed for space cryogenic applications.

5.2 THERMAL CONDUCTIVITY MEASUREMENTS

5.2.1 EXPERIMENTAL METHOD

Thermal conductivity measurements have been made for three Tungsten samples in the temperature range 0.3K - 4.5K, under an applied magnetic field of 1.8 Tesla (which defines the condition of the '**off**' state) and in the absence of a magnetic field (which defines the condition of the '**on**' state). The Tungsten samples were based on the design as published in Canavan et al. (80).

5.2.1.1 INVESTIGATED TUNGSTEN SAMPLES

All Tungsten samples were grown and wire-electronic discharge machined by Mateck GmbH [10]. Purity analyses were performed by the manufacturer for two of the samples using GDMS (Glow Discharge mass-spectrometry), and the full results are presented in Table 11.

Sample 1

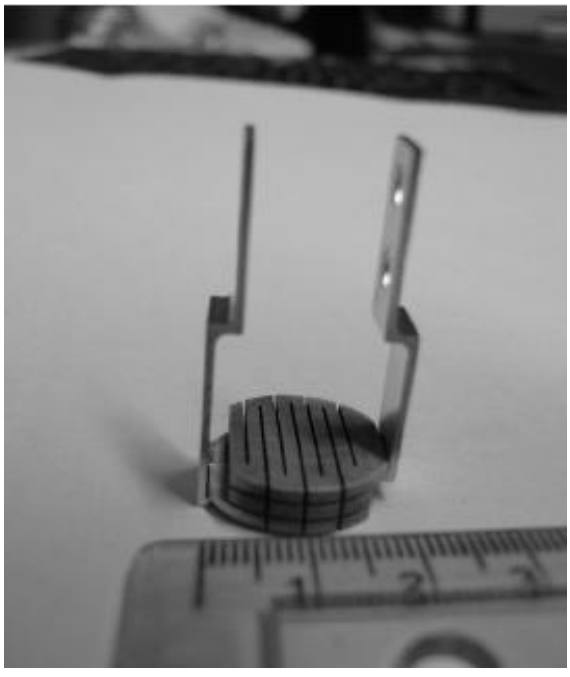

Figure 60: Tungsten crystal Sample 1

[10] Mateck GmbH. Im Langenbroich 20, D-52428 Juelich, Germany.

Sample 1 has a square cross section *A* of 1.5mm × 1.5mm and an effective path length of *L* = 24.9cm. GDMS analyses measure the purity of this sample to be 99.999%. The RRR has not been measured, as the electrical resistivity at temperatures ~4K was found to be too low to be measured by the available equipment. However, the RRR may be inferred to be >7000, since this is the lower bound on the 99.995% pure sample of identical geometry as measured by Canavan et al (80). At each end of the thermal path ('hot' and 'cold' ends of the crystal) were vacuum brazed a high-purity (99.998%) Copper arm, in order to be able to mount the sample for testing.

	Concentration **µg/g**			Concentration **µg/g**	
Element	Sample 1	Sample 2	Element	Sample 1	Sample 2
Ag	< 0.004	< 0.005	**N**	< 0.01	< 0.01
Al	0.02	0.05	**Na**	0.10	0.06
As	< 0.004	< 0.008	**Nb**	0.04	0.2
Au	< 0.009	< 0.009	**Nd**	< 0.002	< 0.002
B	< 0.001	< 0.002	**Ni**	< 0.006	< 0.009
Ba	< 0.002	< 0.002	**O**	< 0.7	< 0.5
Be	< 0.0006	< 0.0008	**Os**	< 0.07	< 0.07
Bi	< 0.004	< 0.005	**P**	< 0.003	< 0.004
Br	< 0.005	< 0.004	**Pb**	< 0.006	0.03
C	< 2.7	< 3.7	**Pd**	< 0.002	< 0.002
Ca	0.04	< 0.01	**Pr**	< 0.0003	< 0.0004
Cd	< 0.02	< 0.03	**Pt**	< 0.003	< 0.003
Ce	< 0.0008	< 0.001	**Rb**	< 0.0005	< 0.0007
Cl	≤ 0.009	≤ 0.004	**Re**	< 0.08	< 0.09
Co	< 0.001	0.01	**Rh**	< 0.0009	< 0.003
Cr	0.02	0.05	**Ru**	0.00	< 0.004
Cs	≤ 0.06	≤ 0.03	**S**	0.06	0.04
Cu	6.10	2.7	**Sb**	< 0.009	< 0.01
Dy	< 0.001	< 0.002	**Sc**	< 0.0001	< 0.0002
Er	< 0.0009	< 0.001	**Se**	< 0.02	< 0.02
Eu	0.08	0.1	**Si**	0.20	0.08
F	< 0.003	≤ 0.01	**Sm**	0.00	0.01
Fe	0.04	0.2	**Sn**	< 0.03	< 0.04
Ga	0.01	< 0.009	**Sr**	0.00	< 0.0004
Gd	< 0.002	< 0.002	**Ta**	≤ 1.8	≤ 22
Ge	< 0.08	< 0.09	**Tb**	< 0.0003	< 0.0004
Hf	< 0.01	< 0.01	**Te**	< 0.009	< 0.01
Hg	< 0.05	0.9	**Th**	< 0.0004	< 0.0002
Ho	< 0.0003	< 0.0005	**Ti**	< 0.0006	0.01
I	< 0.0004	< 0.0005	**Tl**	< 0.0005	< 0.0008
In	0.01	< 0.005	**Tm**	< 0.0004	< 0.0005
Ir	<0.0007	0.02	**U**	< 0.0003	< 0.0004
K	≤ 0.03	≤ 0.09	**V**	< 0.0005	0.01
La	< 0.0007	< 0.0009	**W**	Matrix	Matrix
Li	0.00	< 0.001	**Y**	< 0.0002	0.001
Lu	< 0.0003	< 0.0005	**Yb**	< 0.001	< 0.002
Mg	0.01	0.08	**Zn**	0.06	0.5
Mn	0.00	< 0.002	**Zr**	< 0.002	< 0.002
Mo	0.60	50			
			Total	**9.3 µg/g**	**77.2 µg/g**

Table 11: Measured GDMS Purity for samples 1 and 2

Sample 2

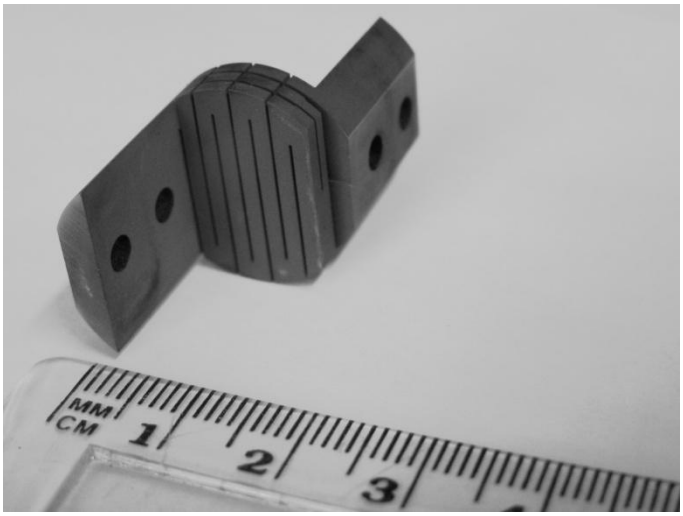

Figure 61: Tungsten crystal Sample 2

Sample 2 has a thermal path of the exact same geometry as sample 1, i.e. a square cross section *A* of 1.5mm × 1.5mm and an effective thermal path length of *L* = 24.9cm. Sample 2 has a GDMS measured purity of 99.992% (Table 11). The RRR has been measured to be 1600. The mounting flanges of sample 2 are an integral part of the crystal, precisely machined by the manufacturer. This eliminates extra contact resistance present between the Copper mounting flange and the Tungsten sample.

Sample 3

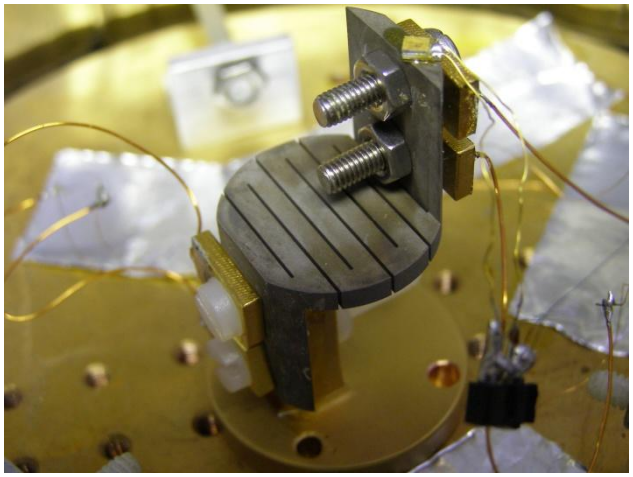

Figure 62: Tunsten crystal Sample 3

Sample 3 has a cross section *A* of 2mm × 2mm and consists of only one layer, giving an effective thermal path length of *L* = 8.5cm. The purity of this sample was not measured by GDMS, but the RRR was measured and found to be 580 ±11%. Sample 3 has integral mounting arms machined in the same way as sample 2.

A summary of the properties of all three samples is provided in Table 12.

	Sample 1	Sample 2	Sample 3
RRR	>7000 (Inferred)	1600	580 (±11%)
Purity [%]	99.999	99.992	Not measured
L [cm]	24.9 (9.4 tested)	24.9	8.5
A [mm × mm]	1.5 × 1.5	1.5 × 1.5	2 × 2

Table 12: Summary of properties of the MSSL Tungsten samples.

The RRR values were obtained using a 4-wire method to obtain accurate measurements of the sample's electrical resistance at 293K and 4.2K. The sample was enclosed by a Copper radiation shield housed within a liquid Helium cryostat. The shield was employed to minimise the influence of any higher temperature radiation on the measurements. The resistance was measured using an Agilent 34470A 7½ digit nanoVolt/microOhm meter, capable of measuring resistances as low as 100 nΩ.

5.2.1.2 'OFF' STATE THERMAL CONDUCTIVITY MEASUREMENT METHOD

The 'off' state (1.8 Tesla applied magnetic field) thermal conductivity measurement experiments were carried out in an evacuated laboratory cryostat containing an ADR, pre-cooled by a liquid Helium bath within a liquid nitrogen outer chamber. A schematic and photo of the experimental set up is shown in Figure 63, in this case showing sample 2, though the set up is equivalent for all samples (aside from the aforementioned differences for sample 1).

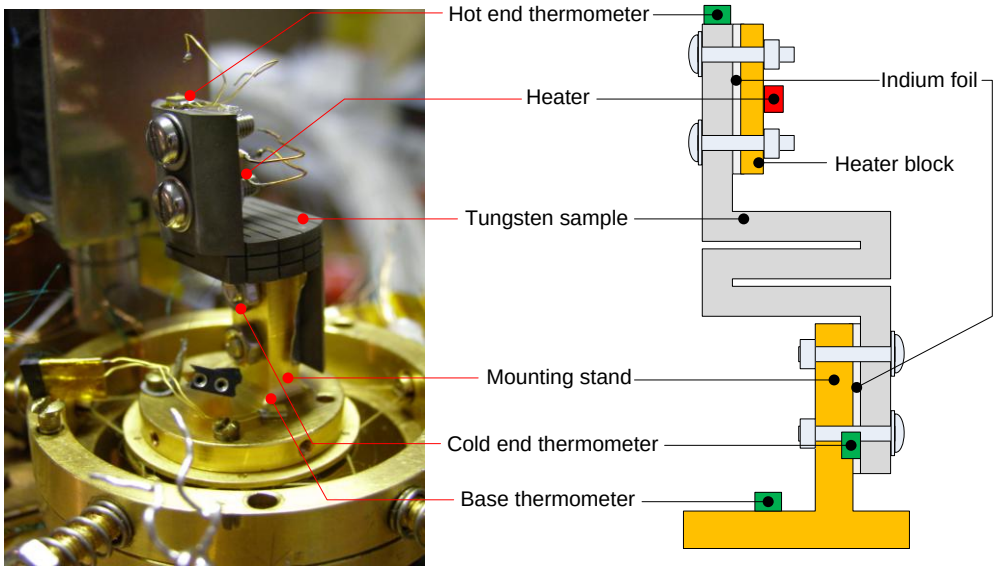

Figure 63: MSSL Tungsten heat switch thermal conductivity experimental set-up (showing sample 2).

In order to measure the thermal conductivity, one of the sample mounting arms was bolted to the cold finger of the ADR while the other was left free. The magnetic field for the Tungsten samples was generated by a magnet surrounding the cold finger of the ADR, capable of providing a stable magnetic field of up to 1.8 Tesla, homogeneous in the region of the Tungsten samples. In order for the vacuum brazed joint of sample 1 to not influence the measurements the thermometers and heater were mounted on one layer of the Tungsten giving an effective path length of L = 9.4cm.

To minimise any radiation heat load from higher temperature stages (4K), a Copper radiation shield was implemented in order to enclose the crystal and its support structure. This was necessary because in the low temperature range (<1K), radiation effects were seen to skew the measurements by keeping the crystal from attaining isothermal thermal equilibrium between the ends of the thermal path.

Direct current power, in the range of microwatts (a few tenths of a microwatt to of the order of 10 microwatts), was applied to a heater (10kΩ metal film resistor) located on

the free end (‘hot’ end) of the sample’s thermal path. The heater for sample 2 and 3 was mounted on a gold plated Copper block with a conforming layer of Indium foil between the block and the Tungsten (see section 5.3). The associated boundary would not interfere with the measurements as it is only the difference in temperature of the hot and cold end of the Tungsten that is relevant. All power dissipated by the heater can be assumed to be conducted into the Tungsten, as the only other potential loss mechanisms are by radiation and conduction down the wires, both of which are easily negligible.

The heater, with such small applied power, allowed for controlled creation of a small but confidently-measureable temperature difference (ΔT) of ~0.1K between the two ends of thermal path, for different base temperatures set by the ADR. For each measurement, the base temperature (‘cold’ end) was set by manually magnetising/demagnetising the ADR until the desired temperature was achieved. Once the cold end was at the desired temperature, the system was left to achieve thermal equilibrium, so as to ensure that the initial conditions saw the two ends of the crystal at the same temperature, i.e. no temperature gradient with zero applied power. Current was then supplied to the heater. The input power was measured by monitoring the supplied current and the voltage across the 10kΩ resistor. The applied heater power is then simply equal to the product of these quantities. For each measurement, the power was gradually increased by increasing supply current, until a sufficient temperature gradient was achieved between the two crystal ends. Once such a temperature gradient was established, the equilibrium temperatures were recorded. The applied power was then removed and the thermometer resistances recorded as the Tungsten cooled back down to the base temperature, thus ensuring that the previous initial conditions were still valid and no change had occurred.

5.2.1.3 'ON' STATE THERMAL CONDUCTIVITY MEASUREMENT METHOD

The thermal conductivity of Tungsten in the absence of a magnetic field ('on' state) is high in comparison to its thermal conductivity under a 1.8 Tesla magnetic field. Thus, a relatively large amount of input heat power (of the order of a few milliWatts) is required to induce a temperature difference between the two ends of the thermal path that is large enough to measure confidently (at least ~0.1K). In order maintain a stable measurement temperature, the 'on' state thermal conductivity was measured in a liquid Helium cryostat at two base temperatures, the liquid Helium boiling point (4.2K) and the temperature of boiling liquid Helium after the vapour pressure had been reduced (~1.5K). The Helium bath was required to provide a stable base temperature for the measurements as the high input heat powers required caused the ADR salt pill to warm up, and a stable temperature measurement was not possible. The method of measurement was the same as for the 'off' state, except that instead of using the ADR to control the temperature of measurement, the temperatures were dictated by the temperature of the liquid Helium that was providing the cooling for the samples.

5.2.1.4 EXTRACTION OF THERMAL CONDUCTIVITY DATA FROM MEASUREMENTS

All temperature measurements were performed using Cernox resistance thermometers (which have a negligible magnetoresistance which has negligible effect on temperature measurements) connected in a 4-wire configuration to an AVS 47 resistance bridge. For each measurement, the raw data consists of the supplied heater power $\dot{Q}$ and the equilibrium resistances of the hot and cold end thermometers. The resistances are converted to temperature using the thermometer manufacturer's supplied calibration data and a polynomial fit to this calibration data. The thermal conductivity is then simply calculated using equation (53):

$$k(T) = \frac{L}{A}\left(\frac{\dot{Q}}{\Delta T}\right) \tag{53}$$

Where T is the average temperature between the hot and cold thermometers; *L* is the path length of the sample and *A* is the cross sectional area of the sample.

5.2.2 Results

5.2.2.1 'Off' State Thermal Conductivity

The thermal conductivity of the Tungsten in its thermal 'off' state, i.e. under an applied magnetic field of 1.8 Tesla, is shown in Figure 64 and Figure 65 for all three samples. The same data is plotted firstly on a linear scale showing estimations of the uncertainty in each measurement as error bars (Figure 64) and secondly showing only the measured points on a logarithmic scale (Figure 65).

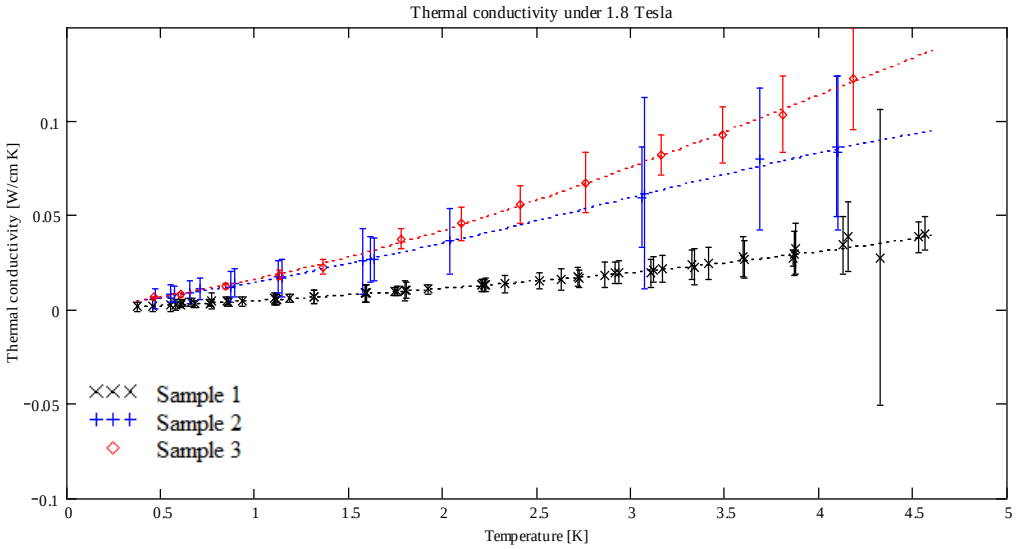

Figure 64: (Above) Measured thermal conductivity under an applied magnetic field of 1.8 Tesla for all 3 samples (linear scale).

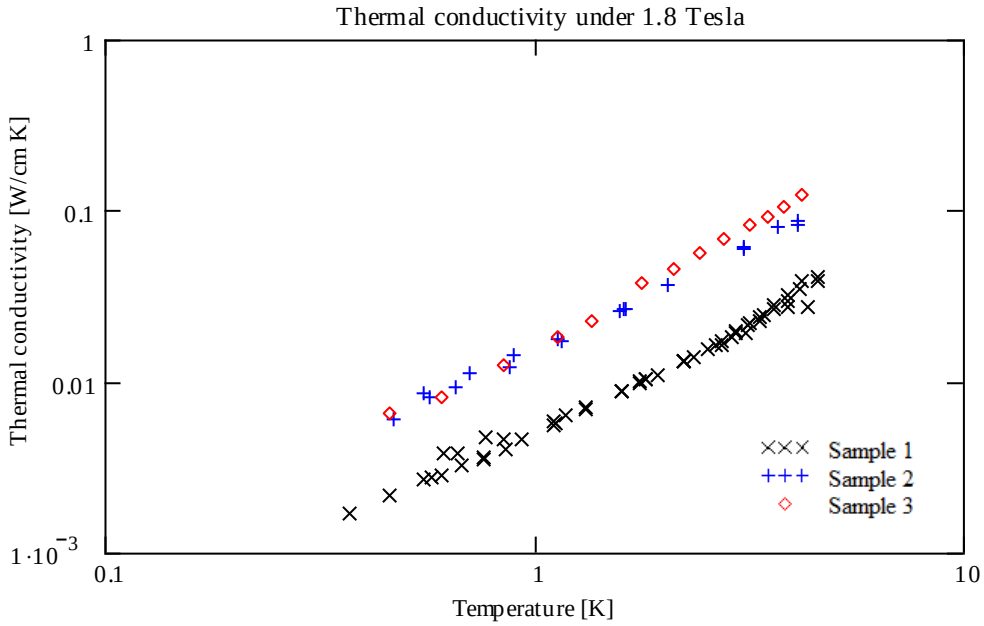

Figure 65: (Above) Measured thermal conductivity under an applied magnetic field of 1.8 Tesla for all 3 samples (log scale).

Sample 1 clearly shows the lowest thermal conductivity under 1.8 Tesla applied field. At 4.31K, the measurement uncertainty in the thermal conductivity of sample 1 is significantly greater than for any other measurement of this sample, as can be seen from the exceptionally large error bar magnitude. This is because an extremely low applied heater power (~1 microwatt) was used for this measurement. The resulting difference in temperature between the two crystal ends was very small, ~0.02K. The fractional uncertainty in both the applied power and temperature difference were thus much higher than for the rest of the measurements.

Sample 2 and 3 have very similar measured thermal conductivity values across the investigated temperature range. The measurements of sample 3 fall within the estimated uncertainty of the measurements for sample 2. The measurement uncertainty for sample 2's thermal conductivity is consistently larger than for the other two samples. This was found to be because consistently smaller applied heat powers were used for sample 2 in comparison to samples 1 and 3, leading to a larger fractional uncertainty in

the heat power used in the calculation of the thermal conductivity, hence greater uncertainty in the calculated thermal conductivity.

The logarithmic plot illustrates the similar temperature dependencies of all 3 samples, implying that the same thermal transport mechanism dominates the thermal conductivity for all three samples when under an applied magnetic field of 1.8 Tesla.

5.2.2.2 'ON' STATE THERMAL CONDUCTIVITY

Figure 66 shows the measured 'on' state (zero applied magnetic field) thermal conductivities for all three samples. Each data point is a mean value calculated from several measurements of the temperature difference for different input powers. The error in these measurements has been estimated by calculating the standard deviation, σ, with the error bar magnitude set to ± 1σ. For visual clarity, dotted lines join the data points for each sample.

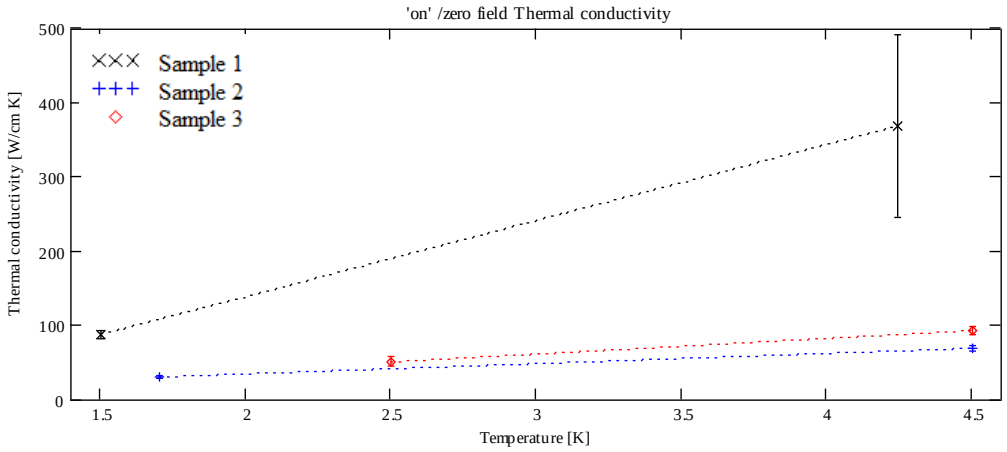

Figure 66: Measured thermal conductivity in the absence of an applied magnetic field for all 3 samples (Upper chart is linear scale, lower chart is log scale). Data points for each sample are joined by a dotted line which acts purely as a visual aid.

Clearly, sample 1 has the highest 'on' state thermal conductivity at both temperatures of measurement, at 368 ±123 W cm^{-1} K^{-1} at 4.23K, and 87.6 ±5.9 W cm^{-1} K^{-1} at 1.50 K. The thermal conductivity of sample 1 is so high that it is difficult to achieve a steady state

situation where a constant applied power generates a constant measureable temperature difference between the two ends of the sample. Thus, it was only possible to obtain 2 useable measurements for the 1.50K thermal conductivity, resulting in the associated statistical uncertainty having less credence than desired. The higher thermal conductivity at 4.23K resulted in a large uncertainty due to the large variation in the measurements obtained.

Sample 3 displays the second highest 'on' state thermal conductivity, at 93.0 ±5.6 W cm^{-1} K^{-1} at 4.50K and 51.3 ±6.2 W cm^{-1} K^{-1} at 2.50K. Sample 2 has 'on' conductivities very close but not within the stated error, with measured values of 69.0 ±4.0 W cm^{-1} K^{-1} at 4.50K and 29.6 ±2.0 W cm^{-1} K^{-1} at 1.70K.

5.2.2.3 Switching Ratio

A comparison of the 'on' and 'off' state measurements of thermal conductivity for all three samples is shown in Figure 67 on semi-logarithmic axes.

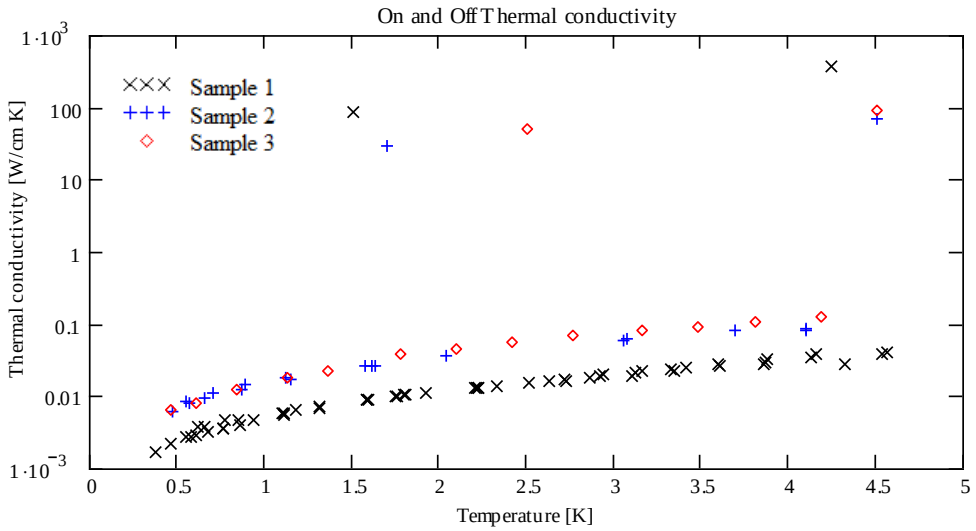

Figure 67: Measured 'on' and 'off' state thermal conductivity values for all three samples.

Figure 67 effectively shows the measured performance as a heat switch for each sample – The switching ratio. The switching ratio of a heat switch is the ratio of its 'on' state

thermal conductivity to its ‘off’ state thermal conductivity. The numerical values of the switching ratio measured for each sample are shown in Table 13.

Sample	T [K]	Switching ratio
1	1.5	10770
	4.23	10670
2	1.7	600
	4.5	437
3	2.5	890
	4.5	707

Table 13: Switching ratios determined at the temperatures of measurement of the 'on' state thermal conductivity for all three samples.

It is clear that sample 1 has the highest switching ratio and offers the best performance as a heat switch. Sample 3 appears to have a very similar switching ratio to sample 2, but with slightly higher thermal conductivity in the ‘off’ state above ~2K.

5.2.3 Analysis and Discussion of Results

5.2.3.1 Estimation of $\omega_c\tau$ – A Measure of Magnetoresistive Effect

The suitability of fitting the results obtained to the high field equation for the thermal conductivity of Tungsten in a magnetic field (as described in chapter 4, equation (52)) may be justified by considering the mean angle turned between collisions by the conduction electrons, $\omega_c\tau$. As described in chapter 4, $\omega_c\tau$ may be estimated by equation (48), and is equivalent to the ratio of the orbit radius to the electron mean free path. Where it cannot be measured directly, the electrical conductivity in the absence of a magnetic field, σ_0, may be estimated using the Wiedemann-Franz law (equation (41)) in conjunction with the measured thermal conductivities under zero applied magnetic field. The use of the free-electron Lorenz number as the constant of proportionality between the electrical and thermal conductivities is justified based on the findings of Wagner et al. (85), which are reproduced in Figure 68.

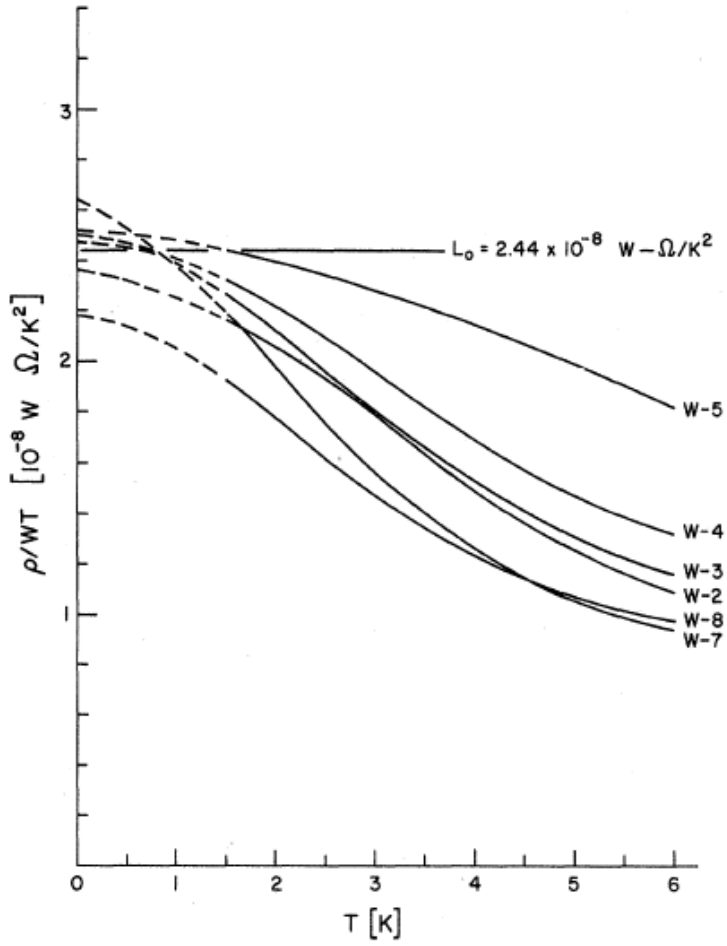

Figure 68: Variation of Lorenz number with temperature for 6 single-crystal Tungsten samples. After Wagner (85).

Figure 68 shows the variation of the Lorenz number for six single crystal Tungsten samples of differing RRR and size, as measured by Wagner et al. (85) in the temperature range 1.5K to 6K. The published RRR and diameter values of each of these samples is reproduced in Table 14.

Sample Label	Diameter [mm]	RRR
W-2 (Mirror finish)	1.5	59,000
W-3 (Mirror finish)	1.5	43,000
W-4 (Matt finish)	1.0	30,000
W-5 (Matt finish)	1.5	9,400
W-7 (Mirror finish)	3.0	95,000
W-8 (Mirror finish)	1.5	75,000

Table 14: RRR and size specifications for Wagner's samples of Tungsten. Data from Wagner (85).

Inspection of Table 14 and Figure 68 indicates that for a fixed crystal diameter of 1.5mm, the measured Lorenz number in the 4K region generally decreases with increasing RRR.

All samples investigated by Wagner et al. (85) have a Lorenz number within approximately a factor of 2 below the free electron value, which is marked on the figure. This implies Tungsten single crystal samples generally have Lorenz numbers close to, but within a factor of 2 below the free electron value, thus the resulting estimation of $\omega_c\tau$ will be conservative if the free electron Lorenz number is used in the calculation of the electrical conductivity. A conservative estimate is favourable because it acts almost as a lower bound on $\omega_c\tau$, a quantity which determines if a sample is in its high field region if it is much greater than unity. Thus, if a conservative estimate indicates a sample is in its high field region, it provides greater confidence that the sample *is* actually in its high field region. For consistency (because the electrical measurement of σ_0 was not possible for sample 1) and for the inherent conservatism, this method of determining $\sigma_0$has been used for all samples in this investigation.

The estimated $\omega_c\tau$ values for each sample at the temperatures at which the 'on' state thermal conductivity has been measured are presented in Table 15. Also shown are the measured switching ratios for each sample (ratio of 'on' state thermal conductivity to 'off' state thermal conductivity) and the estimated electrical conductivity (obtained via the Wiedemann-Franz law as described previously), σ_0.

Sample	T [K]	Switching ratio	σ_0 [Ω^{-1} m^{-1}]	$\omega_c\tau$
1	1.5	10770	2.39E+11	**21.4**
	4.23	10670	3.57E+11	**31.8**
2	1.7	600	7.14E+10	**6.4**
	4.5	437	6.28E+10	**5.6**
3	2.5	890	8.41E+10	**7.5**
	4.5	707	8.47E+10	**7.6**

Table 15: Estimated mean angle turned between collisions ($\omega_c\tau$) for each sample at the temperatures at which the 'on' conductivity was measured.

Table 15 shows that sample 1 has the highest $\omega_c\tau$ values, which means electrons in this sample, on average, undergo the most turns between collisions when exposed to a 1.8 Tesla magnetic field. Sample 1 has $\omega_c\tau = 31.8$ which means the electron mean free path is of the order 30 times greater than the orbit radius of the electrons at ~4.2K, in comparison to ~6 and ~8 for samples 2 and 3 respectively.

The switching ratios are also highest in sample 1, because this sample's conduction electrons undergo fewer scattering processes in both the 'on' state and the 'off' state due to higher 'on' conductivity and $\omega_c\tau$ respectively. The obvious explanation of this is the comparatively high purity of sample 1, which means it has far less lattice defects and distortions due to impurity atoms. Chapter 4 described how the mean free path of electrons was limited by lattice defects and impurities in the temperatures of interest to this work, thus higher purity implies a longer mean free path and a lower magnetic field is required to put the sample into the high field region.

Samples 2 and 3 have similar switching ratios and $\omega_c\tau$ values to one another, but they differ both in purity and crystal width. This implies size also has an effect on the performance as a magnetoresistive heat switch. This will be discussed later in 5.2.4.

5.2.3.2 High Field Magnetoresistance Theoretical Description of Results

The high field criterion is given by $\omega_c\tau \gg 1$. From inspection of the calculated $\omega_c\tau$ values, it appears that sample 1 is the most likely of the three to be in the high field regime with an applied magnetic field of 1.8 Tesla. Samples 2 and 3 both have $\omega_c\tau$ values a factor of ~6 - ~8 greater than unity at both temperatures of measurement, which may not be sufficient to satisfy the high field criterion.

It was shown in chapter 4 that the thermal conductivity of Tungsten in a high field, $\kappa_{xx}(T, B)$, has the form:

$$\kappa_{xx}(T,B) = PT^{u} + \frac{\alpha_0 T + \alpha_3 T^4}{B^2} \quad (54)$$

Where P is the phonon conductivity coefficient, $T$is the temperature, u the index of temperature dependence of the lattice conductivity, α_0 is the magnetoresistive electron coefficient due to impurity and boundary scattering, α_3 is the magnetoresistive electron coefficient due to other scattering processes and $B$is the magnetic field strength.

Expectation Values

Expectation values for the parameters P, α_0 and α_3 may be obtained from consideration of the findings of Canavan (80), Wagner (71), Long (70) and Batdalov and Red'ko (59). All of these authors report a lattice conductivity with a quadratic dependence on temperature. The values for these parameters derived from the published results of the aforementioned authors are presented in Table 16.

Source	Crystal Width [mm]	P [W cm^{-1} K^{-3}]	α_0 [W Tesla^2 cm^{-1} K^{-2}]	α_3 [W Tesla^2 cm^{-1} K^{-5}]	RRR
Wagner (71) [Fit published by Canavan et al. (80)]	3	5×10^{-4}	4.2×10^{-3}	6.3×10^{-5}	63,000
Long [70]	2	3.7×10^{-4}	Not specified	Not specified	30000
Canavan et al. [80]	1.5	Not specified	13.7×10^{-3} [W Tesla$^{1.7}$ cm^{-1} K^{-2}][11]	6.1×10^{-5}	>7000
Batdalov and Red'Ko [59] [Fit performed by the author of this thesis]	4.3	1.937×10^{-4}	4.563×10^{-3}	6.593×10^{-5}	1.55×10^{5}

Table 16: Expectation values of fitting parameters for the high magnetic field thermal conductivity as derived from published works of other authors

The estimation of the phonon conductivity coefficient, P, for a **cubic** lattice temperature dependence is made possible by the equation for the lattice conductivity given in chapter 4 (equation (31) [70]. For Tungsten at 4K, the atomic density is 6.37×10^{28} m^{-3} assuming a lattice constant of 3.15×10^{-10} m based on a lattice constant of 3.16×10^{-10} m at 293K [86] and a thermal expansion coefficient of 4.30×10^{-6} K^{-1} [87] (assumed constant 293K value – in actual fact it drops sharply below around ~250K). This atomic density yields a Debye approximation to the specific heat of 206 J K^{-1} m^{-3} (equation (27)). The phonon velocity is the velocity of sound in annealed Tungsten, 5221 m s^{-1} (74) and the phonon mean free path is the limiting sample width 1.5mm (because at 4K phonon mean free path is limited by boundaries), the lattice contribution to the thermal conductivity at 4K comes out at 5.37 W cm^{-1} K^{-1}. The theoretical estimate of the phonon conductivity coefficient for a cubic temperature dependence is thus 5.37 W cm^{-1} K^{-1} divided by (4K)^3, giving P = 0.084 W cm^{-1} K^{-4}.

[11] Note different Tesla exponent in units due to fit published by Canavan et al (79).

Fitting to the high field equation

Fits of the measured data to equation (52) were performed for each sample for the case of both a quadratic temperature dependent lattice contribution, PT^2, and a cubic lattice contribution, PT^3. The resulting fits are presented in Figure 69.

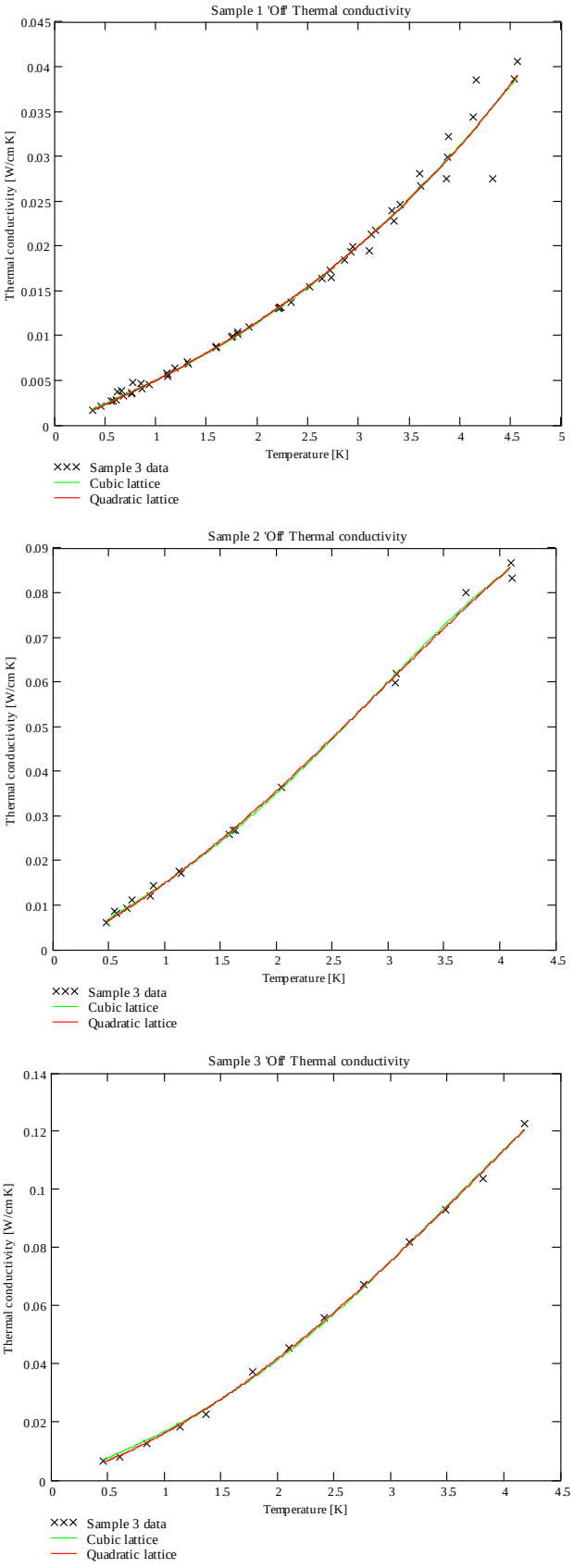

Figure 69: Fits to high-field magnetoresistive thermal conductivity equation for each sample 1, 2, and 3. Fits have been performed assuming both a quadratic lattice term (RED LINE) and a cubic lattice term (GREEN LINE).

The fitting parameters of equation (52) for each scenario are presented in Table 17.

		Fitting Parameters			
Sample	Lattice term	P [W cm^{-1} K^{-3}] (T^2) [W cm^{-1} K^{-4}] (T^3)	α_0 [W Tesla^2 cm^{-1} K^{-2}]	α_3 [W Tesla^2 cm^{-1} K^{-5}]	R^2 value
1	T^2	6.635×10^{-4}	0.014	3.993×10^{-5}	0.981
	T^3	2.645×10^{-4}	0.016	-6.218×10^{-5}	0.981
2	T^2	3.319×10^{-3}	0.038	-2.081×10^{-4}	0.998
	T^3	1.433×10^{-3}	0.045	-8.033×10^{-4}	0.998
3	T^2	5.104×10^{-3}	0.037	-1.64×10^{-4}	0.999
	T^3	1.937×10^{-3}	0.05	-9×10^{-4}	0.998

Table 17: Fitting parameters for fitting high field magnetoresistive thermal conductivity equation to each samples data. Shown for both a quadratic and a cubic in temperature lattice term.

The quality of how well the curves fit the data has been estimated by calculating the R^2 value (a standard statistical quantity). The closer the R^2 value is to one, the better the fit. The R^2values show no difference between the goodness of fit of either quadratic or cubic lattice temperature dependence. However, inspection of the calculated P values for each sample where a cubic dependence has been assumed shows that it always comes out smaller (by a minimal factor of ~43 for sample 3) than the theoretical value calculated previously (P = 0.084 W cm^{-1} K^{-4}). This significant difference indicates that the lattice conductivity is limited not by boundary scattering, but by electron scattering as was found by Canavan et al. (80), Wagner (71), Long (70) and Batdalov and Red'ko (59).

Further inspection shows that for each sample with a cubic dependence, the α_3 term is negative, which is not possible for a physical scattering process. This further indicates this form of the thermal conductivity does not correctly represent the data. The α_3 term

is positive only for sample 1 with a quadratic lattice temperature dependence, indicating only sample 1 under 1.8 Tesla is described well by the high field equation. This implies samples 2 and 3 are not in the high field region, as their comparatively low $\omega_c\tau$ values corroborate.

It is possible that fitting with 3 parameters for the high field equation may yield any mathematically valid values that provide a good fit, yet such values are not necessarily physically valid, as is seen from the generation of unphysical negative values for α_3. Comparison of the expectation values of the fitting parameters in Table 16 with those obtained for sample 1 with a quadratic lattice term (Table **17**) shows reasonable (order of magnitude) agreement, providing credence to these numbers. The similarity of sample 1's α_0 to that found by Canavan et al. implies a similar degree of impurity and boundary scattering. The lower α_0 (by a factor of ~3-4) for the samples of other authors implies these samples have a lower degree of these types of scattering, as would be expected from their higher RRR values.

Significance of α_3

In order to investigate the significance of the α_3 term, and to see if samples 2 and 3 have a thermal conductivity under an applied field of 1.8 Tesla that may be represented by a form of the high field thermal conductivity equation, the high field equation (equation (52)) was investigated without the scattering parameter α_3 present. The reason for this is that although previous investigations find evidence for α_3 [(71)], the dominant electron scattering mechanisms in the investigated samples are likely to be due to lattice defects such as static impurities as well as boundary scattering due to the small cross sectional areas involved, as described in chapter 4. The resulting fits are presented in Figure 70.

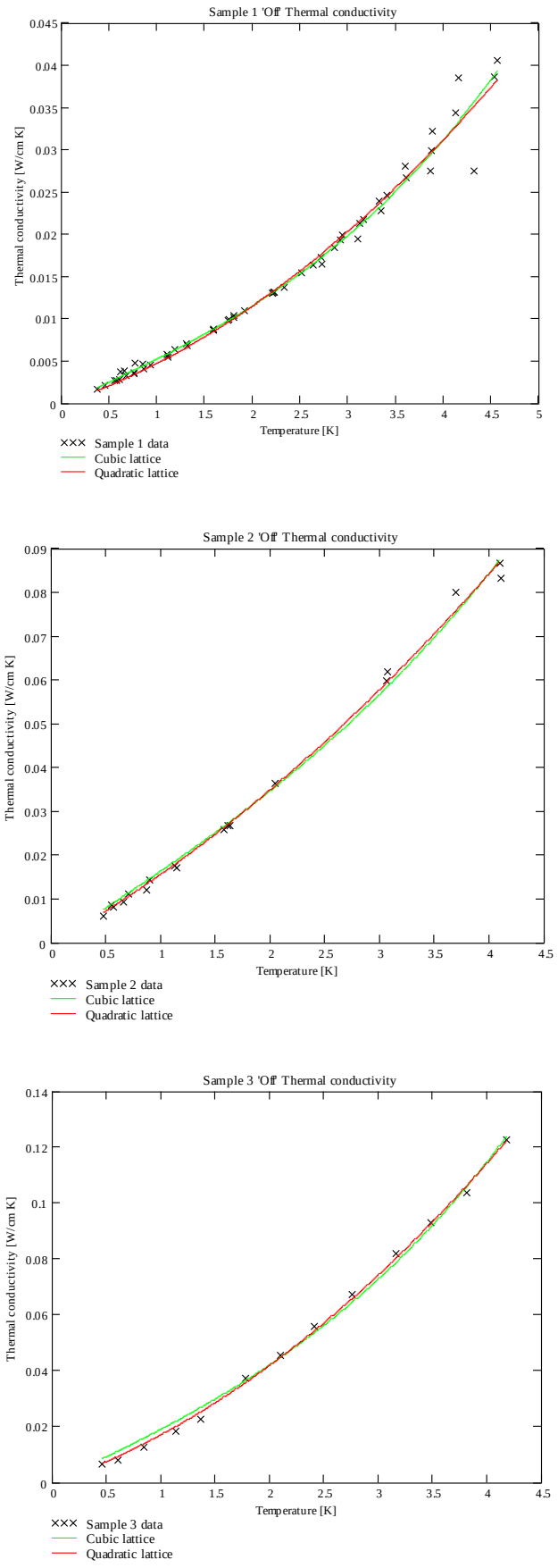

Figure 70: Fits of high field thermal conductivity equation without α_3 for samples 1, 2 and 3 with a cubic (Green line) and a quadratic (Red line) lattice term.

The fitting parameter values are presented in Table 18 in the same format as for the previous fits.

Sample	Lattice term	P [W cm^{-1} K^{-3}] (T^2) [W cm^{-1} K^{-4}] (T^3)	α_0 [W Tesla^2 cm^{-1} K^{-2}]	R^2 value
1	T^2	1.019E-3	0.012	0.98
	T^3	1.691E-4	0.017	0.981
2	T^2	1.788E-3	0.045	0.997
	T^3	3.106E-4	0.052	0.995
3	T^2	3.787E-3	0.044	0.999
	T^3	6.344E-4	0.06	0.996

Table 18: Fitting parameters for the high field thermal conductivity equation without α_3 for the measured 1.8 Tesla thermal conductivity data of Samples 1, 2 and 3.

Initial inspection reveals that the T^3 form of the lattice conductivity again yields P values much smaller than the expected theoretical value for boundary scattering (P = 0.084 W cm^{-1} K^{-4}). Using the same arguments as for the previous fitting case, T^3 form of the lattice conductivity shall not be considered further. Considering only the quadratic lattice fits for each sample, the values of P for samples 2 and 3 are an order of magnitude larger than the expectation values derived from Table 16. Additionally, α_0 for each sample is reasonably similar to the equivalent fit with the $\alpha_3$term included. The α_0 term for samples 2 and 3 is ~3 times larger than the largest value reported by other authors [Table 16]. For sample 1, the P value is large in comparison to the case where α_3 is included (by ~1.5) which is sufficient enough to make it less comparable to the expectation values in Table 16. This suggests that although α_3 is typically small in

comparison to the other parameters, it is still required to represent the complete high field thermal conductivity of Tungsten.

The results of fitting to the high field equation with and without α_3 present indicate that sample 1 is in the high field region under 1.8 Tesla applied magnetic field, and samples 2 and 3 are not. This is because the high field equation does not provide a physically meaningful fit to the measured 1.8 Tesla thermal conductivity of these samples. This is further substantiated by their low estimated $\omega_c\tau$ values, which indicates that they are unlikely to be in the high field region.

5.2.3.3 NON HIGH FIELD SAMPLES

There is no physically justifiable theory for a metal in a magnetic field that is not sufficiently strong enough to push it into its high field region (80). Canavan et al. (80) take the approach of assuming that in this 'low field' region, the zero field and high field mechanisms act together in parallel. Given such assumptions, the thermal conductivity may be represented by:

$$\kappa_{xx}(T,B) = PT^2 + \frac{1}{\frac{B^2}{\alpha_0 T+\alpha_3 T^4}+\frac{w_0+\alpha T^2}{T}} \tag{55}$$

Where a quadratic lattice conductivity has been assumed based on the findings so far, and the additional terms arise from the form of the thermal resistivity in zero magnetic field, *w* (80):

$$wT = w_0 + \alpha T^2 \tag{56}$$

Where w_0 is the thermal resistivity at $T = 0$ and α is the coefficient of the temperature dependent part of the thermal resistivity.

Using this 'low field' equation to fit to the measured 1.8 Tesla thermal conductivities of samples 2 and 3 results in the curves shown in Figure 71 and the parameters summarised in Table 19.

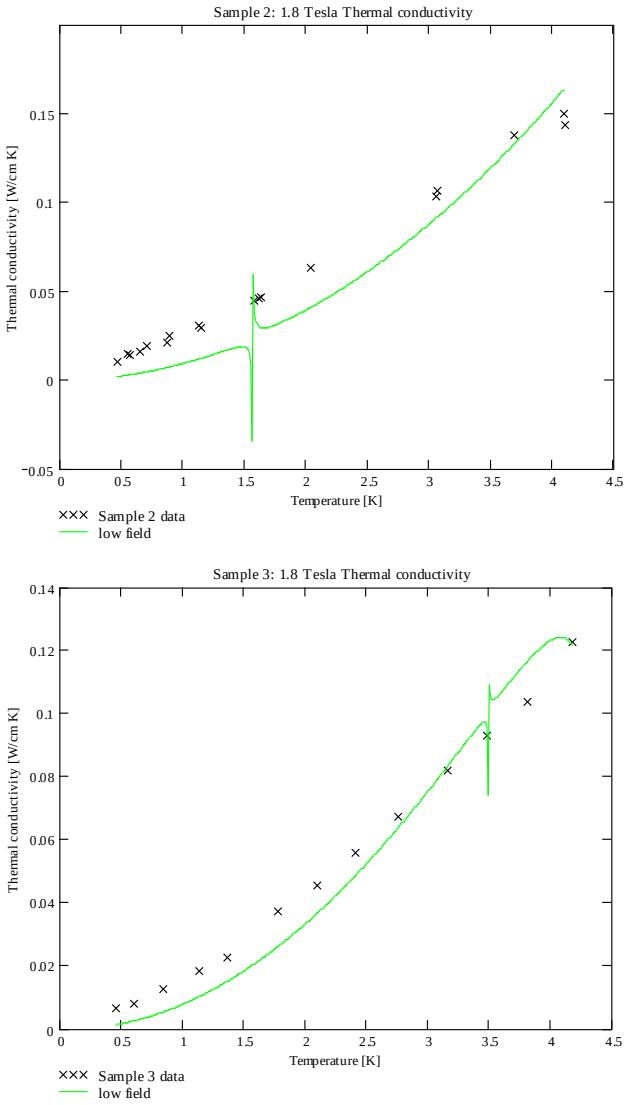

Figure 71: Fits of equation (55) to the 1.8 Tesla measured thermal conductivity data of sample 2 (Upper plot) and sample 3 (lower plot).

Sample	P [W cm^{-1} K^{-3}]	α_0 [W Tesla^2 cm^{-1} K^{-2}]	α_3 [W Tesla^2 cm^{-1} K^{-5}]	w_0	α	R^2 value
2	9.78×10^{-3}	-5.86×10^{47}	4.25×10^{46}	-5.53×10^{3}	2.27×10^{3}	0.977
3	9.03×10^{-3}	1.53	-0.036	-996	50.7	0.989

Table 19: Fitting parameters of equation (55) for the 1.8 Tesla thermal conductivity of samples 2 and 3.

Clearly, this equation fits the data far worse than any of the high field equations used thus far, with discontinuities appearing in the curves and unphysical large and negative values for the fitting parameters. This could be because of the large number of fitting parameters, however the parameter values are vastly different to the expectation values (which were used as guess values for performing the fits). This equation is clearly not suitable for describing the magnetoresistive thermal conductivity of samples 2 and 3 under 1.8 Tesla applied field.

5.2.3.4 Interpretation of High Field Magnetoresistive Description of Sample 1

Since the high magnetic field thermal conductivity equation is only valid for sample 1 in these investigations, it is only this sample that can reliably be investigated in terms of its lattice and electronic contributions based on the theory of high field magnetoresistive thermal conductivity as outlined in chapter 4. Figure 72 shows the sample 1 measured thermal conductivity under an applied field of 1.8 Tesla plotted alongside the fit to the high field equation for the thermal conductivity. The high field fit has been broken down into its constituent lattice and electron contributions, which are shown on the figure for comparison.

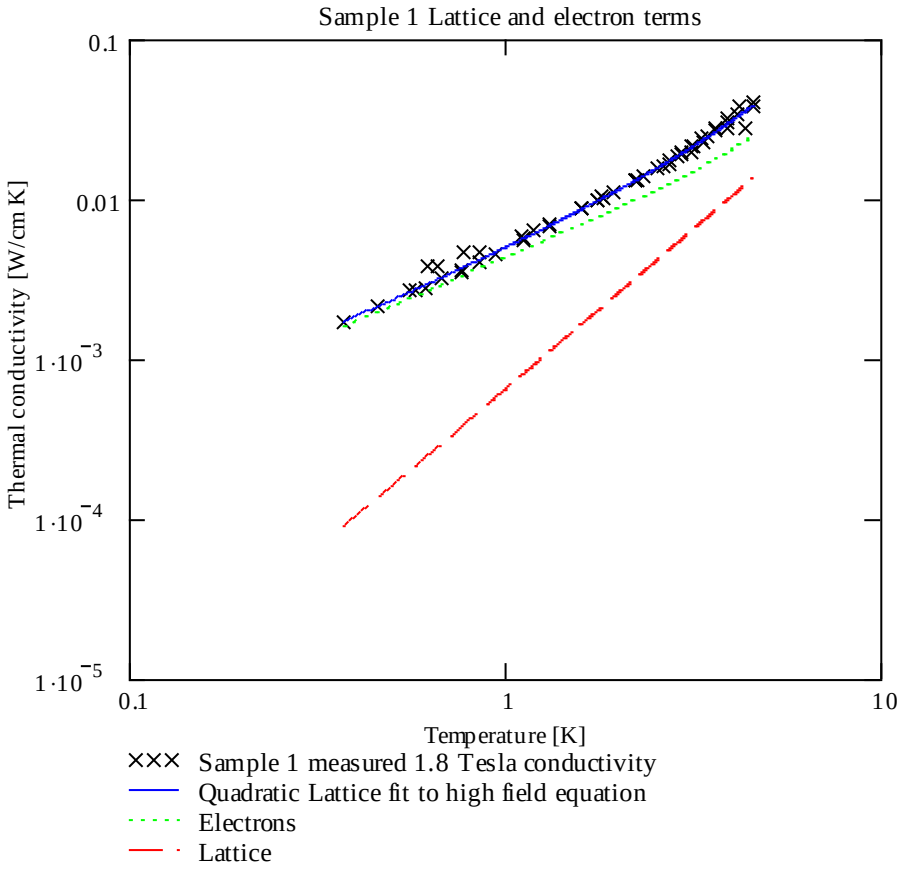

Figure 72: Sample 1 thermal conductivity under 1.8 Tesla applied magnetic field. The fit to the high field magnetoresistive thermal conductivity equation is shown (SOLID BLUE LINE) along side the respective contributions from the lattice (DASHED RED LINE) and the electrons (DOTTED GREEN LINE).

The fit to the high field thermal conductivity equation (52), with the parameters specified on the first row of Table 17 shows that the thermal conductivity of sample 1 under 1.8 Tesla applied field is dominated by electrons across the investigated temperature range. The lattice contribution becomes less significant as the temperature decreases, as expected from its strong temperature dependence. This analysis shows that despite sample 1 being in the high field region, it is clearly not in a magnetic field strong enough to suppress its electrons so that the dominant contribution to the thermal conductivity comes from the lattice. As electrons are contributing the most to the thermal conductivity of sample 1 in its high field region, it may be easily inferred

that the other samples which are not in their high field region suffer even stronger electronic contributions to their thermal conductivity under 1.8 Tesla.

5.2.4 Comparison of Measured Data to Published Results

Finite Applied Magnetic Field

Measurements of the total thermal conductivity of Tungsten under an applied magnetic field have been made by Batdalov and Red'ko (59), Duval et al. (83) and Canavan et al. (80). Figure 73 shows the measured data for the thermal conductivity of samples 1, 2 and 3 under 1.8 Tesla applied field in comparison to the published results of these authors measured under similar experimental conditions.

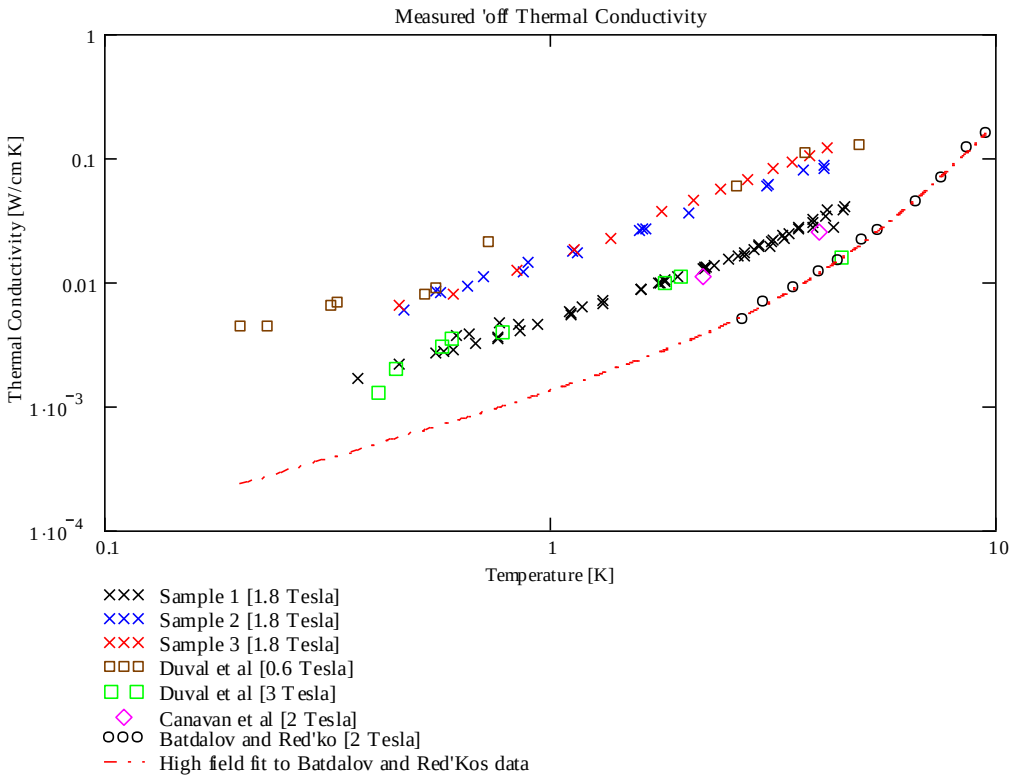

Figure 73: Comparison of 'off' state thermal conductivity measurements to published data measured under similar conditions.

It appears that the sample 1 measured thermal conductivity under an applied field of 1.8 Tesla correlates well with Duval et al.'s [83] measured thermal conductivity under an applied field of 3 Tesla. Duval et al. point out the 3 Tesla magnetic field was

inhomogeneous along the length of their sample; hence the effective field may have been lower [83].

Canavan et al.'s (80) data provides only two data points at 2 Tesla applied field, which agree well with both the measured sample 1 1.8 Tesla data and Duval et al.'s 3 Tesla data. Duval et al.'s data have similar temperature dependence for 0.6 Tesla and 3 Tesla, and agrees with the general temperature dependence of samples 1, 2 and 3. The measured data for sample 2 and sample 3 under an applied field of 1.8 Tesla correlates well with Duval et al.'s measured data under an applied field of 0.6 Tesla.

Batdalov and Red'Ko [59] have measured down to about 2.7K under an applied field of 2 Tesla, and their data has been plotted up to 9.5K in Figure 73. Their data in this temperature range has been fit to the high field magnetoresistive thermal conductivity equation, and this fit used to extrapolate down to 0.2K in order to better compare to the other samples. The temperature dependence appears slightly stronger for this sample from the measured data in the range 2.7K - 9.5K, but the measured data for the other samples does not go beyond ~4.5K so it is difficult to compare directly. The extrapolation from the high field fit indicates the thermal conductivity is lower than all other samples investigated.

Canavan et al. have fit the data obtained by Wagner (71) aswell as their own measured data to the high field magnetoresistive thermal conductivity equation (80). The parameters of the fit of the high field magnetoresistive thermal conductivity equation for sample 1 and the samples investigated by Canavan et al. and Batdalov and Red'Ko are compared in Table 20.

Sample	Fitting Parameters			
	Crystal Width	P [W cm^{-1} K^{-3}]	α_0 [W Tesla^2 cm^{-1} K^{-2}]	α_3 [W Tesla^2 cm^{-1} K^{-5}]
1	1.5mm	6.635×10^{-4}	14×10^{-3}	3.993×10^{-5}
Wagner (published values from fit performed by Canavan et al.)	3mm	5×10^{-4}	4.2×10^{-3}	6.3×10^{-5}
Canavan et al.	1.5mm	Not specified	13.7×10^{-3} [W Tesla$^{1.7}$ cm^{-1} K^{-2}][12]	6.1×10^{-5}
Batdalov and Red'Ko	4.3mm	1.937×10^{-4}	4.563×10^{-3}	6.593×10^{-5}

Table 20: High field magnetoresistive thermal conductivity equation fitting Parameters for sample 1, Canavan et al.'s published values for their sample and Wagner's sample, and Batdalov and Red'Ko's sample.

The fitting parameters show that sample 1 has the strongest lattice contribution to the thermal conductivity, and Batdalov and Red'Ko's sample has the smallest. The lattice contribution would be expected to be higher in smaller samples due to more boundary scattering of the phonons occurring at the sample surfaces. This fits with the calculated P values, which decrease as the crystal width increases.

As described in chapter 4, the $\alpha_0$term is related to electron-impurity and electron-boundary scattering, thus is expected to be higher in samples with a higher degree of these processes. Sample 1 and the sample measured by Canavan et al. have the same crystal width and similar measured purities, which explains the close $\alpha_0$values. Batdalov and Red'Ko's sample has an extremely high measured RRR, at 1.55×10^5, and a large crystal diameter of 4.3mm, implying high purity and a lower degree of boundary scattering. This explains why this sample has a much lower α_0 than sample 1 and Canavan et al.'s sample. The fit to Wagner's data performed by Canavan et al. yields a

[12] Note different Tesla exponent in units due to fit published by Canavan et al (79).

comparably low α_0, lower in fact that Batdalov and Red'Kos, which would not be expected due to its smaller size and lower RRR. However, the difference is minor, and essentially these two values are the same. All samples have comparably similar $\alpha_3$values, indicating similar levels of electron-phonon interactions. As described in chapter 4, the $\alpha_3$term is thought to arise from electron-phonon scattering processes [71].

Zero Applied Magnetic Field

The thermal conductivity under zero applied magnetic field has been measured by Duval et al. (83) and Batdalov and Red'Ko (59). These measurements are shown alongside the equivalent measurements for samples 1, 2 and 3 in Figure 74. Dotted lines joining the points of each data set are shown for visual clarity.

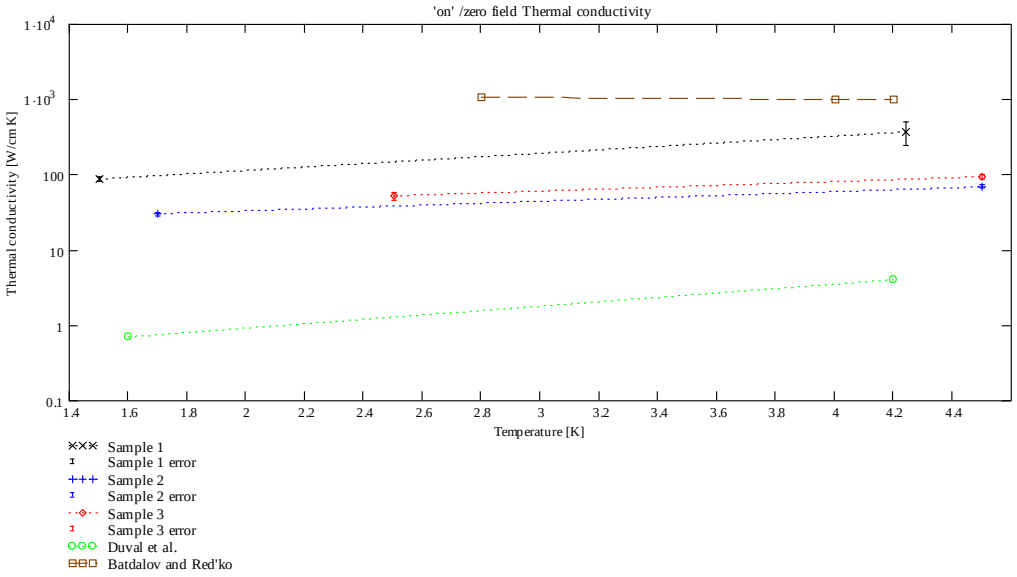

Figure 74: Comparison of 'on' state thermal conductivity measurements to published data measured under similar conditions. Dotted lines join measured points of each sample purely for visual clarity.

Batdalov and Red'Ko clearly measure the highest 'on' state thermal conductivity, at 1000 W cm^{-1} K^{-1} at 4.2 K [59] and increasing with decreasing temperature. Duval et al. measure the equivalent quantity to be 4 W cm^{-1} K^{-1} at 4.2 K [83], where sample 1 has 368

±123 W cm^{-1} K^{-1} at 4.23K, sample 2 has 69.0 ±4.0 W cm^{-1} K^{-1} at 4.50K, and sample 3 has 93.0 ±5.6 W cm^{-1} K^{-1} at 4.50K, all decreasing with temperature.

Summary of Key Characterising Parameters

Clearly, Batdalov and Red'Ko's sample demonstrates by far the best measured switching ratio, at 1.83×10^5 at 2.8K and 7.50×10^4 at 4.2K. A comparison of switching ratios and all characterising properties for each sample investigated is given in Table 21.

Crystal	RRR	Purity [%]	Crystal width [mm]	Switching ratio (Calculated for this thesis at temperature T[K] and applied field B[Tesla])	$\omega_c\tau$ (Calculated for this thesis at temperature T[K] and applied field B[Tesla])
Sample 1	>7000 (Inferred)	99.999	1.5	10670 (4.23K, 1.8 Tesla)	**31.8** (4.23K, 1.8 Tesla)
Sample 2	1600	99.992	1.5	437 (4.5K, 1.8 Tesla)	**5.6** (4.5K, 1.8 Tesla)
Sample 3	580 (±11%)	Not measured	2	707 (4.5K, 1.8 Tesla)	**7. 6** (4.5K, 1.8 Tesla)
Duval et al.	100-200	Not measured	0.5	230 (4.2K, 3 Tesla) 34 (4.2K, 0.6 Tesla)	**5.80** (4.2K, 3 Tesla) **1.16** (4.2K, 0.6 Tesla)
Canavan et al.	>7000 (measured lower bound)	99.995	1.5	No measured 'on' thermal conductivity	No measured σ_0 from which to calculate $\omega_c\tau$
Batdalov and Red'Ko	1.55×10^5	Not measured	4.3	7.50×10^4 (4.2K, 2 Tesla)	**96.8** (4.2K, 2 Tesla)

Table 21: Comparison of parameters characterising each sample, including samples investigated by other published authors.

5.2.4.1 INTERPRETATION OF FINDINGS

The measurements of thermal conductivity in 5.2.2 and the comparison to published data in 5.2.4 show that the performance of Tungsten as a magnetoresistive heat switch is extremely variable, and dependent on a combination of crystal width and purity.

Larger crystal widths mean a lower degree of electron-boundary scattering, and higher purity means a lower degree of electron-impurity scattering. Lower degrees of electron scattering means the electron mean free path is longer. A good heat switch has a high switching ratio, which is due to a large change in thermal conductivity when under an applied magnetic field, typically due to a high 'on' state conductivity and a low 'off' state conductivity. The results show that longer electron mean free paths lead to better heat switch performance.

On state conductivity

In the 'on' state, a longer electron mean free path means thermal electrons may travel further before dissipating their heat, thus resulting in a higher thermal conductivity. This is shown by the following results:

- Batdalov and Red'ko measure the highest 'on' state thermal conductivity of any investigated author, at 1000W cm^{-1} K^{-1} at 4.2K (59). Their sample had the highest purity, indicated by an RRR of 1.55×10^5 and a large crystal width of 4.3mm. The electron mean free path is quoted by Batdalov and Red'Ko to be 1.4mm for their sample (59) (at 4K), which is approximately ⅓ of the crystal width.

- Sample 1 has the next highest 'on' conductivity, 368 ± 123 W cm^{-1} K^{-1} at 4.23K. It also has the next highest purity. The stated purity is 99.999% with an inferred RRR of >7000. The crystal width is 1.5mm.

- Samples 2 and 3 have reasonably similar 'on' state conductivities to one another; at 69.0 ± 4.0 W cm^{-1} K^{-1} at 4.50K, and 93.0 ± 5.6 W cm^{-1} K^{-1} at 4.50K respectively. These are significantly below sample 1. The purity of these samples is lower than sample 1, with respective RRR values of 1600 and 580. Sample 2 has a measured purity of 99.992%. Sample 3 has a slightly higher 'on' conductivity (by ~1/3) than sample 2, despite its lower measured RRR (hence inferred lower purity). However, sample 3 has a larger cross section of 2mm as opposed to 1.5mm for sample 2. This implies that in this case the reduction in boundary scattering of the electrons by increasing the crystal width by ~1/3 is more significant than the increase of impurity scattering associated with a ~2/3 decrease in RRR.

- The 'on' conductivities are much higher in samples 2 and 3 than for Duval et al.'s sample, which is measured at 4W cm^{-1} K^{-1} at 4.2K (83). The low RRR of 100-200 implies low purity; however, this could be misleading as the crystal width is only 0.5mm. In chapter 4, it was shown how the residual resistance of a metal increases if the crystal width is of the order of the electron mean free path, and increases with decreasing crystal width. Hence, a crystal with a small width will have a lower RRR than a larger width crystal of equal purity, giving a potentially misleading indication of purity if a sample's purity is inferred based on RRR alone. Thus, the low 'on' conductivity of this sample is most likely due to a comparatively high degree of boundary scattering.

The collective data indicates that 'on' conductivity is limited primarily by boundary scattering (i.e. sample width), as the larger diameter sample 3 is more conductive in the absence of a magnetic field than sample 2 despite its lower purity. In addition, Duval et al. measured the lowest value, on the sample with the smallest crystal width of 0.5mm

which is approximately ⅓ of the mean free path determined by Batdalov and Red'Ko for their sample.

OFF state conductivity

In the 'off' state, the longer mean free path means for a given magnetic field strength, the thermal electrons complete more turns between scattering events. The rate at which electrons move along a temperature gradient is reduced as the rate of scattering is reduced since the conduction electrons are locked into helical orbits around the magnetic field lines. The 'off' state thermal conductivity therefore decreases with decreasing scattering rates.

The strength of the magnetoresistive effect in a sample dictates how much the electronic component of thermal conductivity may be reduced by a magnetic field. This may be considered by using $\omega_c\tau$ as a proxy for the magnetoresistive effect. Larger $\omega_c\tau$ values result in better 'off' state performance (lower thermal conductivity). This is shown by:

- Batdalov and Red'ko measure an extremely low 'off' conductivity due to the high $\omega_c\tau$ of 96.8 at 4.2K for a 2 Tesla field. This means the electrons, on average, perform 15 turns between collisions, which is far greater than for any other sample investigated. The magnetoresistive effect is strongest in this sample due to the least degree of scattering of the electrons.

- Sample 1 achieves the next best 'off' conductivity with an $\omega_c\tau$ of 31.8, higher than any other sample for which $\omega_c\tau$ could be estimated (excluding Batdalov and Red'ko).

- Samples 2 and 3 achieve similar 'off' state conductivities to one another, and comparable $\omega_c\tau$ values.

It is recognised that $\omega_c\tau$ does not always represent the strength of the magnetoresistive effect in a sample. This is because $\omega_c\tau$ (in this work) is estimated using the electrical conductivity (which is proportional to thermal conductivity) in the absence of a magnetic field. This means that for samples with a low 'on' conductivity due to excessive boundary scattering, an artificially low $\omega_c\tau$ value would be obtained, just as for the measured RRR. This is indicated by:

- Duval et al.'s sample under 0.6 Tesla applied field achieves similar off state performance to samples 2 and 3 under an applied field of 1.8 Tesla. At 0.6 Tesla, Duval et al.'s sample has a smaller calculated $\omega_c\tau$ value and would therefore be expected to achieve a worse 'off' state performance (higher thermal conductivity). The cross section is only 0.5mm, hence the 'on' conductivity is limited by boundary scattering and $\omega_c\tau$ is deceptively low.

It is expected that the significance of boundary scattering will decrease as magnetic field increases [(78)], as the electrons are locked into tighter orbits and boundary scattering becomes increasingly rare. Hence, it is reasonable to assume that purity is the dominant contributor to the 'off' state performance. Higher purity means less electron-impurity scattering and a higher magnetoresistive effect. This is supported by:

- The lowest 'off' state thermal conductivity measured for the highest purity sample – Batdalov and Red'ko, with exceptional purity inferred from its high RRR of 1.55×10^5.

- The next best 'off' state performance is shown equivalently by sample 1 under 1.8 Tesla, Canavan et al. under 2 Tesla and Duval et al. under 3 Tesla (all these 'off' state conductivities are close). Sample 1 has a purity of 99.999%. The purity of Canavan et al.'s sample is stated as 99.995%, whereas Duval et al have not

measured the purity of their sample, but state an extremely low RRR of 100-200. This implies low purity, but as previously pointed out, may be misleading as the crystal width is only 0.5mm. From inspection of the RRR and purity of Canavan et al.'s sample and the measured purity of sample 1, Duval et al.'s sample most likely has the lowest purity. Hence, it would be expected that a higher field would be required to decrease the thermal conductivity to the same levels as sample 1 and Canavan et al's sample, as is observed. However, Duval et al. state the actual field experienced by the sample could be lower than the 3 Tesla specified, but also point out they did not understand why their sample had such low purity (as the assumption of low purity was based on the measured low RRR) [(83)].

- The worst 'off' state performances were demonstrated by the least pure samples. Samples 2 and 3 under an applied field of 1.8 Tesla have similar 'off' state measured thermal conductivities, which are close to Duval et al.'s sample under 0.6 Tesla applied field. The purity of sample 2 is known to be 99.992%, and it's RRR to be 1600. The low RRR of sample 3 (RRR = 580) together with its larger crystal width indicates this sample must have poor purity in comparison to sample 2. From observations of the magnetoresistive effect, if it is assumed purity alone drives the degree to which a given magnetic field decreases the thermal conductivity, it may be inferred that the purity of Duval et al.'s sample is likely to be lower than that of Canavan et al. or sample 1, yet higher than sample 2.

Switching Ratio

Naturally, a high switching ratio is achieved by a high 'on' state conductivity and a low 'off' state conductivity. Based on the observations as discussed so far, 'on' state

performance is predominantly dependant on crystal width. For the best 'on' state performance, a crystal width of significantly larger than the electron mean free path is required (~3× for Batdalov and Red'Kos sample). 'Off' state performance is governed by a high purity, with the best performance being achieved with purity >99.999% (Batdalov and Red'ko's sample and sample 1).

A lattice dominated 'off' state thermal conductivity

Figure 73 shows that under the investigated range of temperature and applied magnetic fields, the 'off' state conductivity follows similar temperature dependence for all investigated samples, including the samples investigated by other published authors. Fitting the high field magnetoresistive thermal conductivity equation to the measured 'off' state data for sample 1 indicates that the electron contribution to the thermal conductivity is still dominant despite 1.8 Tesla being strong enough to put this sample into its high field regime. The higher 'off' state thermal conductivities of the other samples (except Batdalov and Red'Kos' data), the similarity of temperature dependence between samples, and the lower estimated $\omega_c\tau$ values show that the electron contribution to the thermal conductivity is even more strongly dominant in samples 2 and 3, as well as in Duval et al's sample. Clearly the magnetoresistive effect is not as strong in these samples, due to a greater degree of scattering of the electrons.

A comparison of the sample 1 1.8 Tesla data and Batdalov and Red'Ko's 2 Tesla data together with the corresponding fits to the high field magnetoresistive equation is shown in Figure 75, with the separate contributions from the lattice and the electrons identified. The fit has been extended to beyond the temperatures of measurement for both samples.

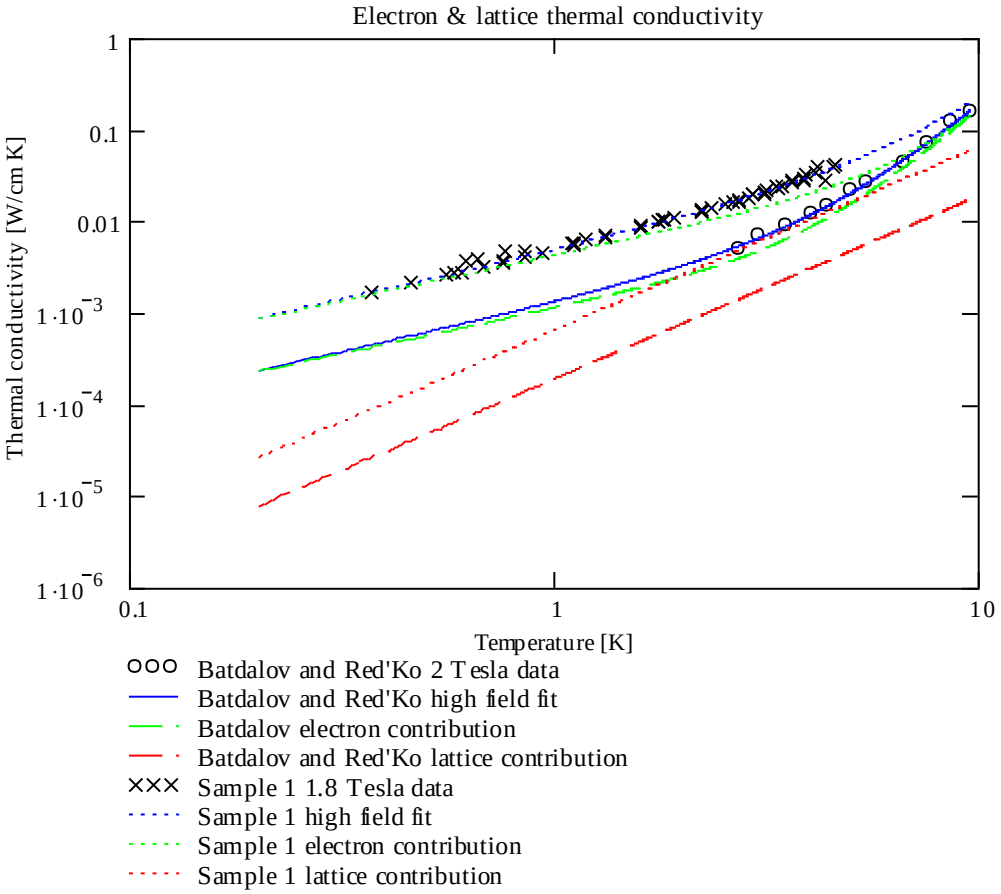

Figure 75: High field thermal conductivity of Batdalov and Red'Ko's sample compared to sample 1. In each case, the electronic and lattice contribution to the thermal conductivity are shown.

Figure 75 shows that in Batdalov and Red'Ko's extremely high switching ratio sample, the slope of the measured data is the same as the lattice contribution, indicating the lattice contribution could indeed be dominant. The fit using the high field equation does not show this, however, as the fit shows the electron contribution to dominate. The electronic and lattice components of sample 1 are both larger than the equivalents in Batdalov and Red'Ko's sample. The high field fit in the form presented does not seem to fit Batdalov and Red'Ko's data as expected, as the lattice conductivity appears dominant from the slope of the measured data. This could be because the form of the magnetoresistive electronic thermal conductivity, $\frac{\alpha_{xx}}{T} = \alpha_0 + \alpha_3 T^3$, that was assumed

for the fit is not valid for a Batdalov-type sample, as it was deduced by Wagner for a sample of RRR 63,000 where the electron contribution remains dominant.

The extrapolation of the sample 1 high field fit line up to around 10K gives the impression sample 1's conductivity crosses that of Batdalov and Red'Ko's sample, such that above 10K Batdalov and Red'ko's sample with 2 Tesla applied field has a higher thermal conductivity than sample 1 with 1.8 Tesla applied field. This does not fit with the results obtained for the 3 samples in this investigation, although no investigation has been made above ~5K. Clearly, higher temperature data for sample 1 and sub 2K data for a Batdalov-type crystal are required in order to investigate this further.

5.2.5 Summary Of Findings

Samples with higher purity demonstrate a stronger magnetoresistive effect, hence have lower 'off' state conductivities for the same applied field, as is evident from the high performance of sample 1 (99.999% pure) compared to sample 2 (99.992% pure) and 3 (≤ 99.992% pure by comparison of performance to sample 2). This is backed up by the findings of Batdalov and Red'Ko [(59)]. The dominant scattering process affecting electrons in the 'off' state is impurity scattering. Higher purity means longer mean free path, thus a given orbit radius for a given magnetic field will lead to a higher $\omega_c\tau$.The electrons on average complete more turns between collisions in purer samples, thus heat is not propagated as quickly, hence the electronic contribution to the thermal conductivity is lower.

The highest switching ratio samples are those which have the highest purity and the largest crystal widths. There is not enough data to determine the relationships between purity, crystal width and switching ratio/heat switch performance. It is evident from comparison of Duval et al.'s 'on' thermal conductivity with other samples that this quantity is detrimentally affected for crystal widths below the electron mean free path.

Based on the investigated samples, it is not clear what purity and crystal width is necessary for a sample to exhibit a magnetoresistive effect that is strong enough to allow the lattice contribution to dominate, as in all samples electron conduction remains dominant. However, the gradient of Batdalov and Red'ko's 'off'' conductivity data implies a dominant lattice conductivity has been achieved.

5.3 INTERFACING TO THE TUNGSTEN HEAT SWITCH

If the heat switch in an ADR is a Tungsten magnetoresistive heat switch, the ADR recycle time may minimised by having as high as possible thermal conductance through the heat switch when in its thermal 'on' (zero applied field) state. The conductance of the Tungsten itself may be engineered to be extremely high by selection of an appropriate sample with high purity and a sufficient crystal width to keep boundary scattering to a minimum; however, thermal resistance bottlenecks at the interface between the Tungsten and its mountings within the ADR are inevitable. This is because of the thermal resistance that occurs between any two materials arranged in a pressed contact configuration, such as would likely be present where the Tungsten crystal is bolted to the internal architecture of the ADR.

At any boundary between two materials pressed together, a degree of thermal resistance is inevitable due to the extreme decrease in effective area at the boundary. This is because the actual contact area between two materials depends on the surfaces of the materials at the contact location, which at the microscopic level is far from smooth even for highly polished metals. This concept is illustrated in Figure 76.The surfaces actually only contact at a few, effectively point-like locations. The number of these locations could be as few as three, regardless of the apparent surface area [(88)].

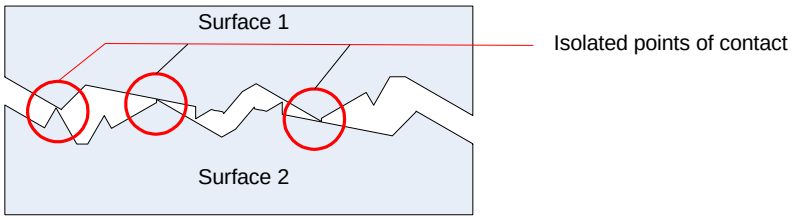

Figure 76: Contact between two surfaces at a pressed contact boundary

Thus, when implementing a Tungsten magnetoresistive heat switch into an ADR system, it is important to consider the thermal performance of the interface between the Tungsten and the mounting structure that provides the thermal connection to the salt pills.

If the Tungsten crystal itself has its own integral mounting arms, such as samples 2 and 3, there are only the two mounting contact boundaries to consider, where each arm bolts to its mounting at either end of the crystal length. A Tungsten switch with external mounting connections, such as sample 1, has additional thermally resistive boundaries at the vacuum brazed joints between the Copper and the Tungsten. For a minimal ADR recycle time and maximal hold time, a maximal thermal conductance through the Tungsten heat switch structure is required. It is essential to minimise the number of thermal boundaries and maximise the conductance of each individual boundary. For this reason, it is considered the design of Tungsten heat switch mounting structure will be based on a design with a Tungsten sample having integral mounting arms.

A review of inter-metallic pressed-contact conductances is given by Salerno and Kittel (88). Salerno and Kittel cite that the conductance across press contacts is a function of the applied force, not the apparent area of the contact [(88)]. As the pressing force is increased, the contact surfaces are deformed, increasing the contact area. Further surface deformation leads to contact at new locations. It is the narrow nature of the contact locations that is the major cause of the contact boundary resistance [(88)].

Additional contributions to thermal resistance at pressed contacts may come from oxide layers that have formed on the surfaces, the oxide compounds generally having a high resistance due to phonon conduction being the only mechanism of heat transport. The effect of oxide layers is worsened by acoustic mismatches between the non-oxidised and

oxidised layers [88], where phonons propagate at different speeds in the different materials.

From the review of experimental data by Salerno and Kittel, the thermal conductance across pressed contacts was found to obey a simple power law function of temperature, equation (57) [88].

$$k(T) = \alpha T^n \tag{57}$$

Where n typically ranges from 0.75 – 2.5 [88]. In addition, the thermal conductance increases asymptotically with applied force as the actual contact area approaches the apparent surface area.

Since the most significant factor in pressed contact resistance is the actual area of contact, the best way to minimise the resistance is to maximise the area of contact. This can be done using what Salerno and Kittel denote 'conforming coatings' – a coating on the surfaces that allows maximal contact between the surfaces by 'conforming' to the contours of each surface. Such a coating is required to be pliable enough to match the contours of both surfaces at low temperatures (<4K). In their review, Salerno and Kittel find Apiezon-N™ grease is the best conforming coating [88]. Since grease based solutions are not viable for space applications due to outgassing, the next best solution was found to be a layer of 0.13mm thick Indium foil placed between the contact surfaces [88]. This foil thickness should be thick enough to match the contours of both surfaces yet thin enough to not introduce too much extra resistance due to bulk Indium, which would have a significant effect at temperatures below 3.41K, where Indium becomes superconductive.

5.3.1 EXPERIMENTAL METHODS

In order to ascertain the optimal thermal configuration for the mounting assembly of a Tungsten magnetoresistive heat switch, a single-crystal Tungsten disc was obtained, again grown and machined by Mateck GmbH. In an attempt to replicate mounting a sample based on the design of sample 1, the disc was sized at 20mm diameter and 1.5mm thickness. The disc had a highly polished surface, and had four 2.5mm holes drilled though in order to mount it within a pressed contact configuration. Figure 77 shows a drawing of the disc.

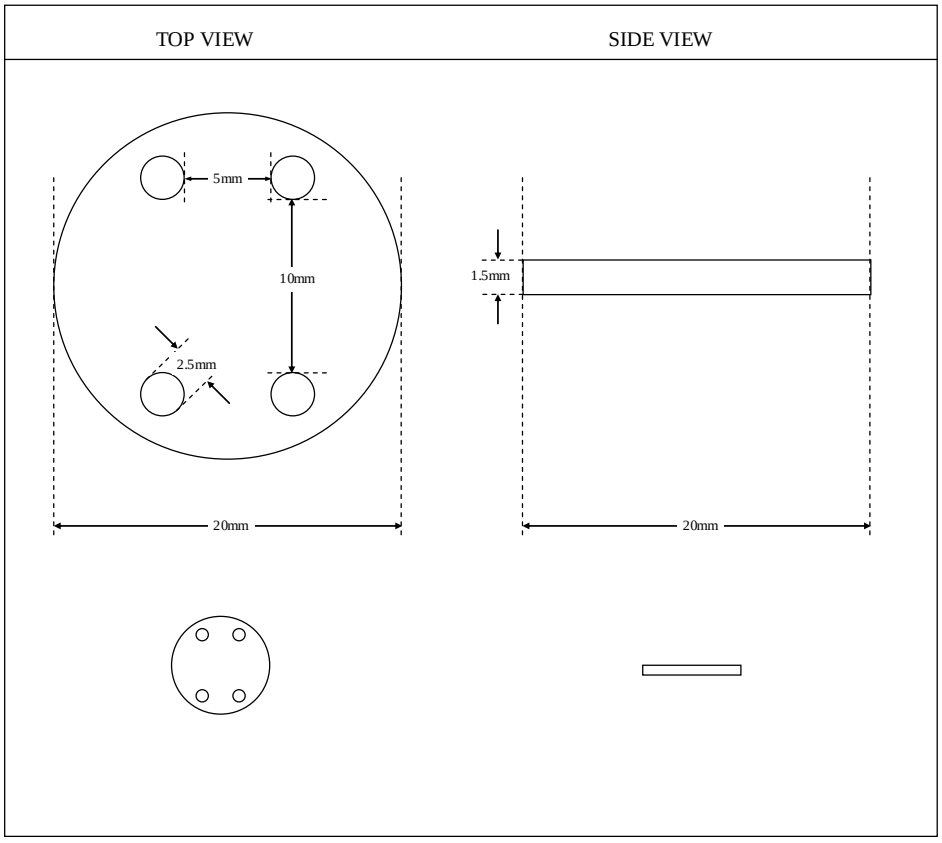

Figure 77: Tungsten disc sample specification for boundary characterisation experiments.

The Tungsten disc was mounted on a gold-plated high purity Copper mounting stand, held in place by a gold plated high-purity Copper clamping block. The block-disc-stand fixtures were M2.5 screws passing straight through holes in the clamping block and

Tungsten disc, and screwing into tapped holes in the stand. The experimental set up is shown in Figure 78:

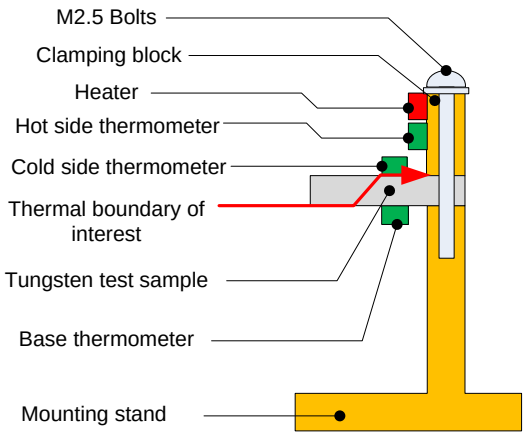

Figure 78: Diagram of experimental set-up for determining the boundary conductance between Tungsten and gold plated high purity Copper.

The thermal boundary of interest was the boundary between the Tungsten disc and the clamping block. Thus, a heater (10k metal film resistor) was mounted on the clamping block, close to the edge in contact with the Tungsten disc. A Cernox resistance thermometer was placed next to the heater. A second Cernox resistance thermometer was placed on the Tungsten disc as close to the clamping block as possible. The stand was attached to the 4K plate of a liquid Helium cryostat, thus maintaining a stable stand base temperature of 4.2K during experiments.

The degree of compressive force was characterised by measuring the torque applied to the screws. In order to ensure the clamping force remained constant for each experiment, the screws were each tightened to 60N cm torque for each experiment.

Once the experiment was cooled to liquid Helium temperature, the heater was supplied with current in order to generate heat power at the clamping block. The thermometers either side of the boundary were monitored, and the equilibrium temperatures for a given applied power were noted. The difference of these temperatures was plotted

against the applied power, and the gradient of the resulting line used to determine the conductance of the boundary as a function of average temperature (averaged over the hot and cold sides of the boundary). After each measurement, the experiment was allowed to cool back down to 4.2K. Measurements were made for several values of increasing average boundary temperatures, which were controlled by increasing the heater power.

The experiment was conducted in identical conditions for three types of boundary:

1. Tungsten with surface as finished by manufacturer and no conforming coating (Untreated).

2. Tungsten with no oxide layer on surface (visible outer oxidised layer removed by fine grade emery paper), and no conforming coating (No oxide).

3. Tungsten with surface as finished by manufacturer with a single layer of 0.13mm thick Indium foil acting as a conforming coating (Untreated + Indium).

In each case, the surfaces were thoroughly cleaned using acetone in order to remove any grease and dirt.

5.3.2 Results and Analysis

The boundary conductance was determined as a function of average boundary temperature for three boundary types as detailed above. The results as measured (raw data) are presented in Table 5.12.

.

Interface Type	Heater power [W]	Tungsten Temp. [K]	Copper Temp. [K]	Delta T [K]	Av. T [K]	Conductance [W/K]
Untreated	0.0029733	4.370845556	4.443818875	0.07297332	4.407332216	0.040745029
	0.01085	4.473489727	4.717432694	0.243942967	4.59546121	0.044477609
	0.023625	4.624600237	5.095881873	0.471281636	4.860241055	0.050129261
	0.0415266	4.831989769	5.553480216	0.721490447	5.192734992	0.057556687
	0.0640552	5.074060415	6.046348454	0.972288039	5.560204435	0.065880889
	0.0914137	5.346487504	6.560758602	1.214271097	5.953623053	0.075282777
	0.1038435	5.469108265	6.778137003	1.309028738	6.123622634	0.079328663
	0.129852	5.697283635	7.18329818	1.486014545	6.440290908	0.087382725
	0.2475	6.610509016	8.670833071	2.060324055	7.640671044	0.120126734
	0.432276	7.759624671	10.41553327	2.655908596	9.087578969	0.162760119
No Oxide	0.0108024	4.706597815	4.790388166	0.083790351	4.748492991	0.128921765
	0.0236916	4.873506726	5.045576511	0.172069784	4.959541618	0.137685998
	0.0416271	5.088072705	5.362762783	0.274690078	5.225417744	0.151542059
	0.06411795	5.338896434	5.720712346	0.381815912	5.52980439	0.167928963
	0.091026	5.617508692	6.108010046	0.490501354	5.862759369	0.185577469
	0.10133856	5.715522549	6.243382378	0.527859828	5.979452463	0.191980057
	0.1602	6.244858045	6.950475208	0.705617164	6.597666626	0.227035294
	0.24902706	6.924733035	7.832015587	0.907282552	7.378374311	0.274475751
	0.355788	7.628724379	8.723678838	1.094954459	8.176201609	0.324934062
	0.41427288	7.970521176	9.155644114	1.185122938	8.563082645	0.349561102
Untreated + Indium	0.0109786	4.798200805	4.801083107	0.002882302	4.799641956	3.808970018
	0.041526	5.180604967	5.190184721	0.009579755	5.185394844	4.33476656
	0.091203	5.719594874	5.736700989	0.017106116	5.728147932	5.331601934
	0.16024	6.361024658	6.384807561	0.023782903	6.37291611	6.737613194
	0.201888	6.702808559	6.730935327	0.028126768	6.716871943	7.177788788
	0.248325	7.055532832	7.085553582	0.03002075	7.070543207	8.271778739
	0.2996565	7.416976516	7.45181167	0.034835154	7.434394093	8.602129252
	0.3571743	7.795441933	7.834051819	0.038609886	7.814746876	9.250851028
	0.41451264	8.146260565	8.189401345	0.04314078	8.167830955	9.608371493

Table 22: Raw data results of interface characterisation experiments. Applied heater power, temperature of Copper block, temperature of Tungsten are all measured quantities. Delta T is the difference in temperature each side of the interface (Copper Temp – Tungsten Temp). Av. T is the average temperature of the interface (Copper Temp + Tungsten Temp/2).

The results were fit to an equation of the form of equation (57) and are presented in Figure 79.

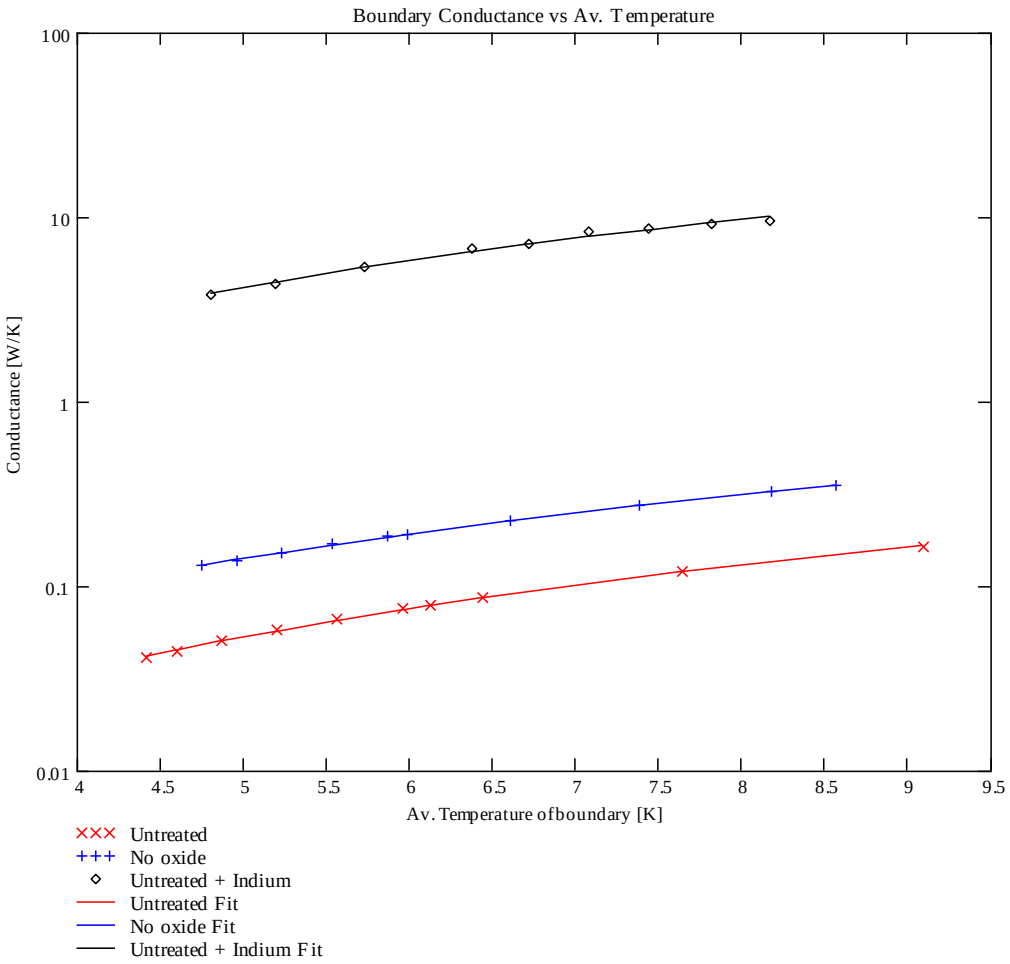

Figure 79: Thermal conductance of Tungsten-Copper boundary under a screw-torque of 60N cm for 3 cases: Untreated, No oxide layer (oxide layer removed) and Indium conforming layer.

The fitting parameters of equation (57), α and n, are summarised below in Table 23.

Boundary Type	Fitting Parameter	
	α	n
Untreated	2.416×10^{-3}	1.919
No oxide	9.096×10^{-3}	1.703
Untreated + Indium	0.223	1.817

Table 23: Summary of fitting parameters for equation (57) for 3 boundary cases.

All 3 boundary types have a similar temperature dependence, with n ~1.8, which falls neatly within the expected range according to Salerno and Kittel's review. For the investigated clamping force, it is apparent that removal of the top oxide layer improves boundary conductance noticeably, by approximately a factor of 4 upon inspection of α values. Most strikingly, the boundary conductance is increased by addition of a conforming layer of Indium foil, in this case by almost two orders of magnitude compared to the untreated boundary. This is in agreement with the findings of Salerno and Kittel (although they investigated different metals), in that Indium foil greatly increases boundary conductance. The results are as expected from the theory that a conforming layer maximises actual contact area between two surfaces, and removal of the oxide layers eliminates the associated resistance. It is reasonable to assume from the data obtained and from consideration of the effects of an oxide layer, that the best conductance for a given clamping force would likely be achieved by removal of the oxide layer and addition of a conforming layer of Indium foil.

The presence of a pressed contact interface between a Tungsten heat switch and its mounting within the ADR will inevitably affect the performance of the heat switch, most notably in the 'on' state when high conductance is desired. The thermal boundary at either end of the heat switch provides additional thermal resistances in a serial arrangement, such that the overall thermal resistance through the boundaries and the heat switch, W_{Total}, is given by:

$$W_{Total} = W_{hb} + W_s + W_{cb} \tag{58}$$

Where $W_{hb}$is the thermal resistance of the 'hot' boundary (boundary at the warmer end of the switch), W_s is the thermal resistance of the magnetoresistive heat switch and

$W_{cb}$is the thermal resistance of the cold boundary (boundary and the colder end of the switch).

In terms of conductance (the reciprocal of resistance), equation (58) equates to:

$$\frac{1}{k_{Total}} = \frac{1}{k_{hb}} + \frac{1}{k_s} + \frac{1}{k_{cb}} \tag{59}$$

Where each thermal resistance has been replaced by the equivalent thermal conductance. Sample 1 has a measured 'on' conductivity of 368 ±123 W cm^{-1} K^{-1} at 4.23K, equating to an 'on' conductance of ~0.33 ± 0.11 W K^{-1}. The 'on' conductance for sample 1 at 4.23K is calculated for the case of each type of boundary investigated, and presented in Table 24. It has been assumed that the heat switch is completely isothermal.

Boundary Type	'on' conductance at 4.23K [W K^{-1}]
None	0.33
Untreated	0.018
No oxide	0.046
Untreated + Indium	0.27

Table 24 : 'on' conductance of sample 1 for each type of boundary/interface at 4.23K.

From these estimations, it is seen the presence of two untreated boundaries with a conforming layer of Indium reduces the 'on' state conductance through the heat switch by around 18% in comparison to a situation where the boundaries are not present (which is of course not possible in a real system). The lack of an Indium conforming layer would result in a conductance decrease of 95% for an untreated boundary, which could

have serious implications on the system performance increases expected based on the high ‘on’ conductance of a Tungsten magnetoresistive heat switch.

It is essential that pressed contact thermal boundaries are treated with an Indium conforming layer, and the conductance across them maximised as much as possible in order to preserve the benefits of a high ‘on’ state thermal conductivity heat switch.

5.4 EFFECTS ON ESA ADR PERFORMANCE

The ESA ADR, discussed in chapter 3, currently has a measured 50mK hold time of ~9.5 - 10 hours with the superconducting Lead head switch between the DGG and CPA stages and no applied heat load. Such performance is far below the original design requirements, where the pill was designed to hold for 24 hours with 1 microwatt heat load on top of the parasitic loads. If this system in its current state were to be used on a mission such as IXO, its low hold time would result in severe observation time constraints on the microcalorimeter instrument.

The hold time may be maximised by using a heat switch which has minimal thermal conductivity in its 'off' state, and maximal thermal conductance in its 'on' state. Figure 80 shows a comparison of the 'off' state thermal conductivity of the ESA ADR superconducting heat with the thermal conductivity potentially achievable using a magnetoresistive heat switch across the complete operating temperature range of the ESA ADR. The magnetoresistive heat switch thermal conductivity is evaluated for 2 cases: A sample 1 type switch and a Batdalov like sample. Both cases assume a 1.8 Tesla applied magnetic field is used to achieve the 'off' state. The magnetoresistive heat switch thermal conductivities are based on the high field thermal conductivity fits performed in section 5.2, where the parameters used are summarised in Table 25. The data for the superconducting heat switch is based on an experimentally verified (in the temperature range 1K-5K [55]) fit that is used in modelling the ESA ADR [55].

	P [W cm^{-1} K^{-3}]	α_0 [W Tesla^2 cm^{-1} K^{-2}]	α_3 [W Tesla^2 cm^{-1} K^{-5}]
Sample 1 Type	6.635×10^{-4}	14×10^{-3}	3.993×10^{-5}
Batdalov Type	1.937×10^{-4}	4.563×10^{-3}	6.593×10^{-5}

Table 25 : Fit parameters used for thermal conductivity of magnetoresistive heat switches.

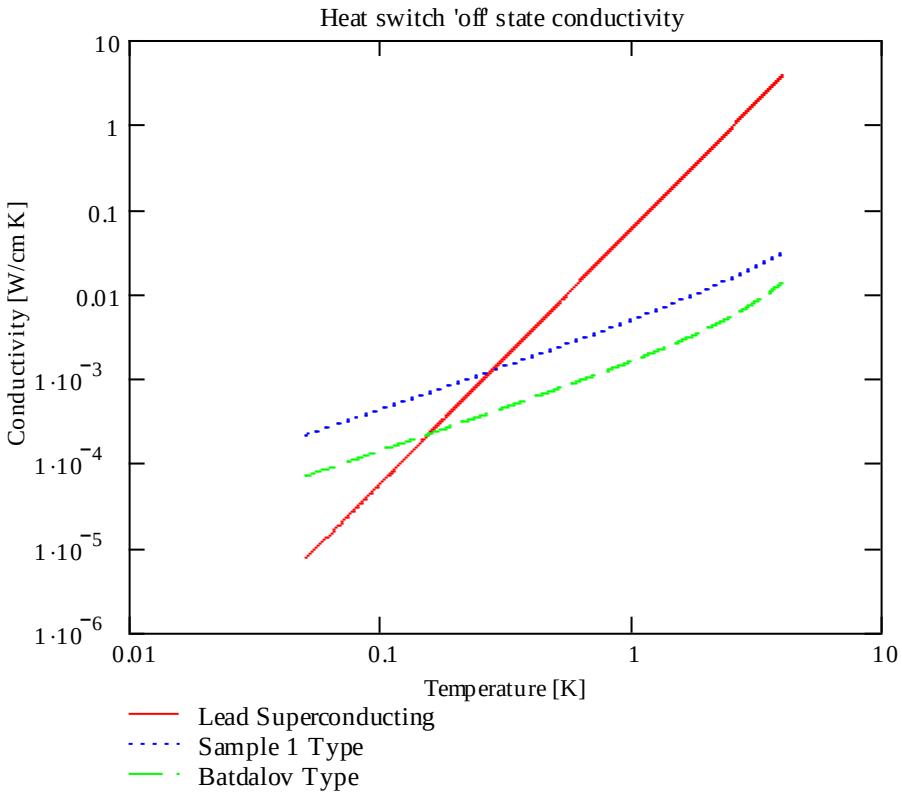

Figure 80 : Comparison of 'off' conductgivity for superconducting heat switch and 2 types of Magnetoresistive heat switch.

Figure 80 shows that for most of the operational temperature range of the ESA ADR, both magnetoresistive heat switches have a lower thermal conductivity than the superconducting heat switch. The superconducting heat switch has a lower extrapolated thermal conductivity below ~290mK than the sample 1 type MR switch, and below ~160mK for the Batdalov type. Here, it is important to realise that below 1K, the

superconducting heat switch conductivity has not been experimentally verified, nor has the MR data below ~300mK for sample 1 or 2.73K for a Batdalov type crystal. It is possible a Batdalov type crystal would have lower thermal conductivity than predicted below ~2.7K. However, the extrapolated performances represent the best possible estimates using currently available data.

Both the superconducting and magnetoresistive heat switches require a magnet to control the state of the switch. The size of this magnet must be kept small, in order to minimise the mass it contributes to the system. The heat switch when implemented in an ADR system must be small enough to fit within the bore of a small magnet coil (E.g. for the ESA ADR: diameter <20mm, overall height <70mm). Thus, several heat switch configurations are investigated in terms of their actual 'off' conductance, which is the property governing heat leak.

The superconducting heat switch conductance, including its Vespel support rod, has been compared to the conductance through magnetoresistive heat switches that fit within the specified magnet bore size. The conductances have been calculated based on the conductivities presented in Figure 80. These magnetoresistive heat switches are:

1. Sample 1 under an applied field of 1.8 Tesla, denoted 'sample 1'.

2. A theoretical sample denoted 'Batdalov 1', with identical geometry to sample 1 but with the measured 'off' state performance of Batdalov and Red'Ko's sample, where an applied field of 1.8 Tesla has been assumed.

3. A sample 1 type sample with an extended path length of 124.5 cm (a 15 layer sample), denoted '15 layer'.

The comparison of the conductance through these samples is shown in Figure 81.

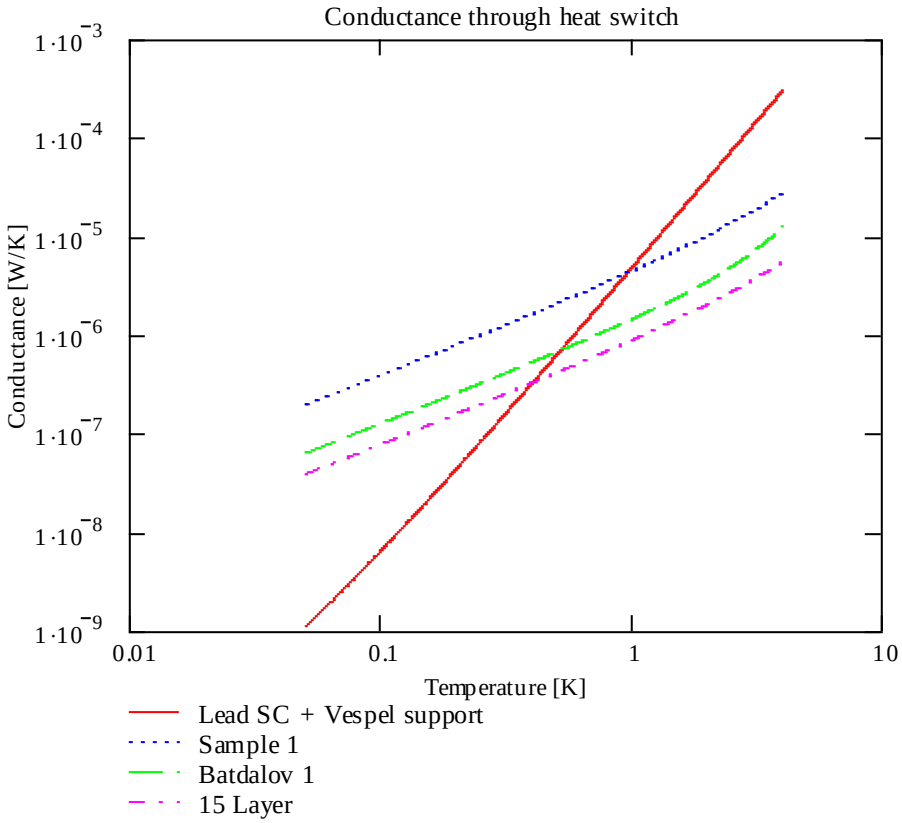

Figure 81 : Conductance through each type of heat switch.

The conductance through each heat switch follows the same pattern as the conductivities as would be expected, however the temperatures below which the superconducting heat switch offers better 'off' state performance are:

- ~1K for sample 1
- ~550mK for Batdalov 1
- ~430mK for 15 layer

Although at the holding temperature of 50mK it appears the Lead heat switch offers the lowest thermal conductance, it is important that for the majority of the temperature range the MR switches are lower. The importance is highlighted by examining the heat

load on the CPA pill (assumed to be at 50mK) due to heat conducted through the heat switch from the DGG stage as it warms up, as shown in Figure 82.

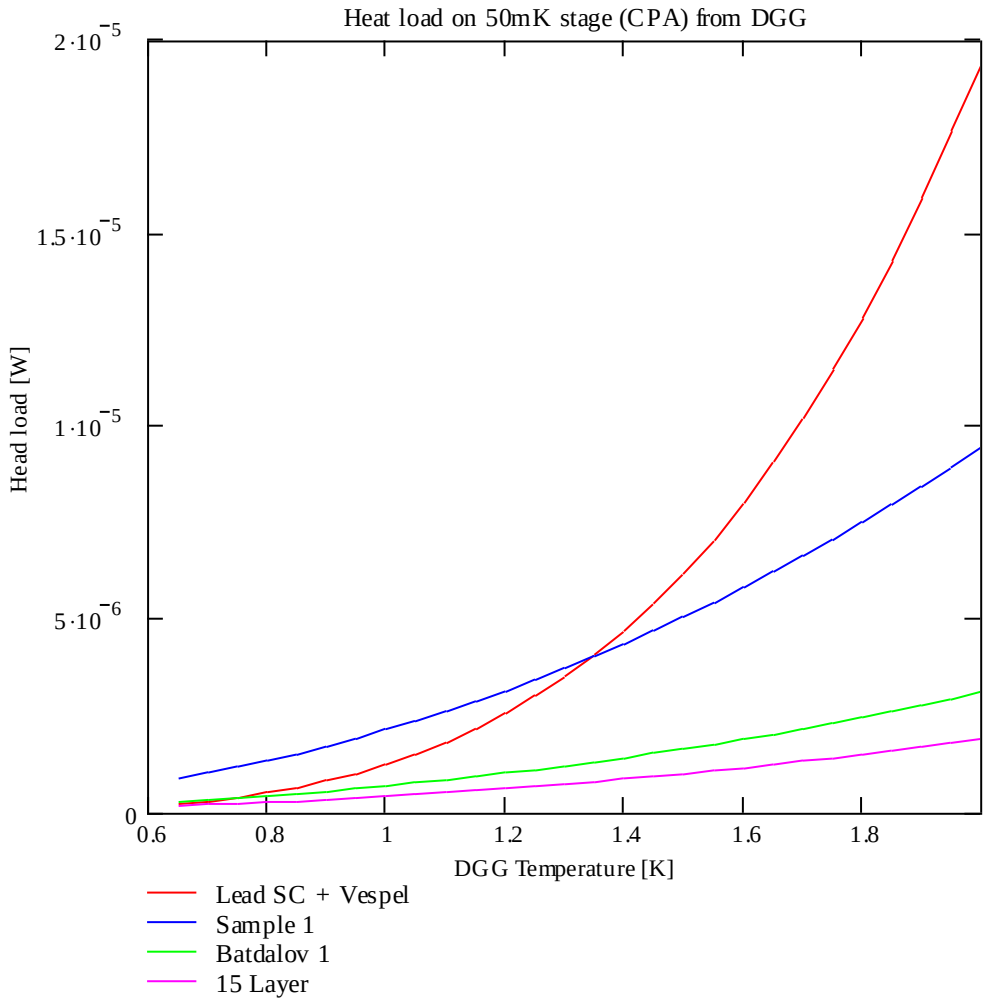

Figure 82: Heat load on 50mK CPA stage from warming DGG for each heat switch

The lower magnetoresistive switch conductance at higher DGG temperatures (>~1.3K for sample 1, >~0.8K for Batdalov 1 and >~0.7K for 15 layer) means that whilst in the final stages of CPA pill demagnetisation during holding at 50mK (servoing), the net heat leak into the CPA pill will be lower, thus the associated entropy increase will be smaller. This means it takes longer for the thermal entropy increase to overcome the magnetic entropy decrease, resulting in a longer hold time. Additionally, the magnetoresistive heat switches allow for a vastly superior thermal link between the CPA and DGG stages

due to the significantly higher 'on' state conductivity offered. The 'on' conductivity of the superconducting switch is 7.5 W cm^{-1} K^{-1} at 4K [55], compared with a measured 368 ±123 W cm^{-1} K^{-1} at 4.23K for sample 1. In terms of actual conductance, the superconducting switch has at best 6×10^{-4} W K^{-1} assuming no thermal resistances present at its interface boundaries. Section 5.3 showed how the 'on' conductance through a magnetoresistive heat switch is limited by the thermal resistance at its attachment points, however, the conductance is expected to be 0.27 W K^{-1} at 4.23K if a conforming layer of Indium is used. This means the magnetoresistive heat switch offers ~450 times greater 'on' conductance than the superconducting switch at ~4K. Thus, the CPA begins demagnetisation from a much lower initial temperature (~0.6K as opposed to ~1.8K) hence a much lower initial entropy, which results in a longer hold time.

The hold time (assuming no additional heat load beyond parasitics) has been estimated for each of these heat switches at 50mK, based on the conductances shown in Figure 81. The hold time has been calculated using the MSSL computational model for the ESA ADR hold time, as detailed in Bartlett (55). The model provides accurate prediction of the hold time when a superconducting heat switch is used. The lower initial temperature of the CPA has been taken into account in the modelling when a magnetoresistive switch is used based on the findings of Bartlett (55). The hold time for each heat switch is presented in Table 26.

Heat Switch	Modelled 50mK Hold time [Hours]
Lead superconducting plus Vespel support	9.3
Sample 1	19
Batdalov 1	33.5
15 Layer	36.5

Table 26: Comparison of modelled ESA ADR hold times at 50mK for different heat switches.

The modelling results show the vastly improved hold time expected when a magnetoresistive heat switch is used to replace the superconducting heat switch in the ESA ADR, primarily due to the benefits of having a high enough conductance to allow the CPA pill temperature to match that of the DGG stage as it is demagnetised.

There are ongoing investigations on the measured performance of the ESA ADR using a 15 layer heat switch. Unfortunately, the neither the RRR or purity of this switch have yet been measured. To date, two hold time tests at 100mK and 50mK have been conducted. At 100mK, the modelled hold time is 59.7 hours for a 15 layer switch with the 'off' state performance of sample 1 (For sample 1 itself, the hold time is calculated to be 38 hours). The 100mK hold time was measured to be just over 24 hours, where the hold time has been counted for the duration the servo controller kept the CPA pill to a temperature of 100mK to within 1mK. The 50mK hold time was measured to be just over 10 hours. This again was counted as the duration the servo held the CPA at 50mK to within 1mK.

These tests have encountered several problems with additional radiation heat loads affecting the thermometry, most notably on the 50mK tests. These radiation loads are due to the removal of the 1K radiation shield to accommodate the switch and the larger surface area of the magnetoresistive sample magnet emitting more 4K radiation than the original magnet for the superconducting heat switch.

It is not possible to draw firm conclusions from these early results, as more tests with the ESA ADR are required. The data does indicate, however, that the magnetoresistive heat switch does offer improvement over the superconducting heat switch at 50mK, where an extra hour of hold time has been experimentally achieved. The poor performance compared to the modelled expectations indicate that the 15 layer 1.5mm square cross section magnetoresistive heat switch in the ESA ADR does not have as low an 'off' state conductivity as sample 1, hence is likely a lower purity crystal.

5.5 SUMMARY OF CHAPTER 5

This chapter has described the investigations carried out using Tungsten single crystal samples as magnetoresistive heat switches. The thermal conductivity has been measured under zero magnetic field and an applied magnetic field of 1.8 Tesla, for three samples. Sample 1 and 2 have different purity, but the same crystal width. Sample 1 has a higher purity than sample 2, which resulted in it having a higher thermal conductivity in its 'on' state, and a lower thermal conductivity in its 'off' state. Sample 3 has even lower purity than sample 2, but a slightly larger crystal width. The resulting performance as a heat switch is similar to sample 2. This shows both impurity and boundary scattering play a significant role in the performance as a heat switch, and the susceptibility of a sample to the magnetoresistive effect. Higher purity samples exhibit a stronger magnetoresistive effect.

The results for sample 1, the only sample in the high field region under an applied field of 1.8 Tesla, were explained using the high field magnetoresistive thermal conductivity equation. The results were compared to other published data, and explained using the theory of the equation and scattering processes present at the investigated temperature range.

The thermal conductivity measurements were verified by comparison to published measurements, and the similarities and differences between samples regarding RRR values and crystal widths used to comparatively explain the measurements.

The implementation of a Tungsten heat switch into a cryogenic system was investigated by investigating the performance of pressed contacts between Tungsten and gold plated high purity Copper. It was found that a thin layer of Indium foil improves conductance across a pressed contact.

Practical magnetoresistive heat switches have been discussed in terms of the conductance of the switch as a whole, modelled using the theoretical fits to data obtained from investigations on the thermal conductivity. It was found that a magnetoresistive heat switch can potentially offer a vast hold time improvement within a real system (the ESA ADR) but this is yet to be experimentally confirmed.

Investigations into using a magnetoresistive heat switch within the ESA ADR are ongoing, but early results show magnetoresistive heat switch can improve hold time performance over the previous Lead superconducting heat switch.

Chapter 6:

IXO COOLING CHAIN SOLUTION DEVELOPMENT

This chapter introduces the IXO cooling chain, and briefly describes the requirements it must fulfil in order to support the MSSL dADR cooling the IXO XMS. The cooler technology employed at each temperature stage is described following selection based on available technology.

A conceptual design of a cryostat is presented at top level, followed by a detailed description of the design and thermal and mechanical analyses of the suspension system. A suspension configuration is proposed based on the analyses, with detailed descriptions and measurements of key structural and thermal components. The need for the development of a low thermal conductivity feedthrough assembly for the cryostat is highlighted, and a conceptual design is presented. The thermal modelling of the feedthrough assembly is described and used to determine the optimal design configuration.

The thermal performance of the cooling chain is analysed and the results presented for 4 cases: the dADR holding and recycling for a cooling chain operating in both warm and cold redundancy modes (the case representing a single cooler failure at both of the temperature stages offering redundancy mode operation). The analysis shows that the proposed cooling chain and cryostat can support the cooling chain for all cases considered.

6.1 REQUIREMENTS OF THE IXO CRYOGENIC COOLING SYSTEM

Chapter 3 presented the final stage (50mK) dADR cooling solution for the IXO XMS instrument under development at MSSL. The requirements necessary for the MSSL 50mK dADR to support the cooling of the IXO XMS are outlined subsequently.

This thesis focuses on one design approach for the IXO cryogenic cooling system, under development at EADS Astrium UK ("Astrium") under contract from ESA. However, alternative approaches are being developed in parallel by NASA, ESA and JAXA programmes.

6.1.1 OVERVIEW OF DADR REQUIREMENTS

In order to provide the 50mK environment necessary for the operation of the IXO XMS, the MSSL dADR requires:

- A heat bath to pre-cool to a suitable demagnetisation temperature and to reject heat produced by the magnetisation phase of the cooling cycle. The heat bath must have a temperature <4K in order to provide sufficient cooling at 50mK. A lower temperature heat bath is beneficial as it increases the performance of the dADR [63].

- Thermal isolation from the ambient spacecraft environment (At a temperature of <290K (300K during on ground testing (62)).

- A cryo-harness to electrically connect the cryogenic instrumentation to the spacecraft data handling systems.

- Current leads to supply electrical current to the dADR magnets. 2 current leads are required for each of the 2 magnets, giving a total of 4. ESA require the magnet currents to be <5A [62].

- Current leads to supply electrical current to the heat switch magnets for the magnetoresistive heat switch linking the 2 temperature stages of the dADR [(63)].

6.1.2 System Level Requirements

6.1.2.1 dADR Heat Bath

The heat bath for the dADR may be provided by either a stored cryogen (such as liquid Helium) or by a cooling chain comprised of cryogen-free cryocoolers. The planned long mission life of IXO (>5 year [(62)]) drives the requirement that the cooling solution must be cryogen-free [(62),(8)].

The cryogen free solution for providing the dADR heat bath has been specified by ESA to be <4K [(62)].

6.1.2.2 Accommodation

Thermal isolation from the ambient spacecraft environment will be provided by a cryostat which encloses the complete cryogenic cooling system.

The IXO XMS cryostat must:

- Minimise radiative heat incident on the dADR and the XMS using MLI or reflective coating [(62),(8)].

- Provide a low-thermal conductivity suspension system to structurally support the cryogenic temperature stages during all mission phases, including launch, whilst ensuring minimal heat conduction from the ambient spacecraft environment [(62)]. ESA require that this suspension system consist of CFRP, glass fibre reinforced plastic, and/or Kevlar support straps [(62)].

- Be vacuum tight for testing of the cryogenic cooling chain on the ground.

- Be as lightweight as possible [(62)].

- Have a minimum first resonance of >40Hz [62].

6.1.2.3 HARNESS AND CURRENT LEADS

The cryo-harness must impart a heat load of <140mW x2 at 20K, and <400mW x2 at 100K [62].

The current leads for the dADR pill magnets and heat switch magnets must be optimised to deliver minimal parasitic heat load due to thermal conduction both when live and when inactive, in addition joule heating when live. The current leads carry a high current (~2.4A and 1.4A respectively for the pills and switches [63]) hence must have a large enough cross section to support such currents. Hence, a trade off between conducted heat load and joule heating effects must be performed (see 6.4.8.1).

6.1.3 THE NEED FOR A COOLING CHAIN

The most efficient refrigeration cycle is the ideal theoretical reverse-Carnot cycle (see chapter 2, section 2.2.3.1), which cannot be practically achieved. Thus, if a cooling system could cool from a hot temperature (T_H) of 300K down to a cold temperature (T_C) of 4K, it would have an efficiency less than the theoretical Carnot maximum (η_{max})[25]:

$$\eta_{max} = \frac{T_C}{T_H - T_C}$$

The theoretical maximum efficiency for such a cooling cycle is $\eta_{max} < 0.014$. This means the cycle would require an input power of > 1/0.014 ~71 times the required cooling power. In order to lift parasitic conduction (~proportional to $(T_H - T_C)$) and radiation (proportional to $(T_H^4 - T_C^4)$) from 300K to 4K, the required cooling power would be large, and the power needed to drive the cycle would far exceed the spacecraft power budget.

In practice, the thermodynamic cycles utilised by cryogen-free cryocooling systems have efficiency considerably below the idealised Carnot cycle and typically operate across a specific temperature range (see chapter 2, section 2.4).

A cryogen-free heat bath for the dADR will have a limited cooling capacity based on the available power, the efficiency of the cooling cycle and the cooling method. In order to ensure as much of this cooling capacity as possible is used to provide a heat bath for the dADR, it is necessary to minimise all other (parasitic) heat loads onto the heat bath temperature stage.

In order to minimise parasitic heat load due to conduction through the suspension system, current leads and cryo-harness as well as thermal radiation, it is clearly necessary to have intermediate temperature stages extracting heat between the dADR heat bath (<4K) and the ambient spacecraft environment (the outer body of the cryostat) at <290K. These intermediate stages will be designed to be at temperatures that can be maintained by available cooling technology. The addition of intermediate temperature stages also means that the efficiency of the coolers at each stage will be higher than a hypothetical cooler that cools directly from 300K-4K, which combined with the broken down parasitic heat loads results in significantly less power consumption by the cryogenic system than if a single cooling cycle could be used.

The cooling chain configuration, under development at Astrium, is determined by the cryogen-free cooling technology that is available to the company.

6.2 AVAILABLE COOLING CHAIN TECHNOLOGY

6.2.1 INTRODUCTION

The typically available technology capable of providing cooling in space to temperatures below the cryostat external temperature (~<290K) are shown in Figure 83. Operational details of the principal types of cryogenic coolers are given in chapter 2.

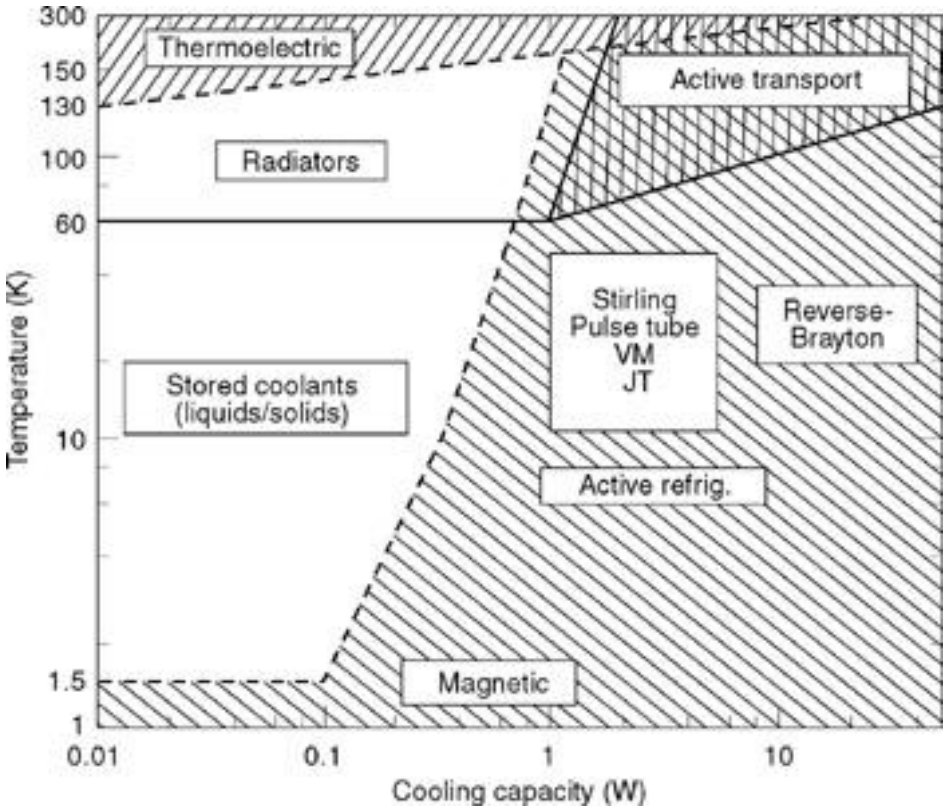

Figure 83: Typical cryocooling technology available for space use. After (38).

As Figure 83 shows, intermediate temperature stages between a 4K heat bath and a 290K cryostat may be provided by radiators and mechanical coolers such as Stirling and Pulse tube based machines. Astrium has substantial flight heritage with both Stirling coolers and radiators [28].

6.2.2 RADIATORS

Radiators are advantageous in that they are passive and have high inherent reliability, however they cannot provide useful cooling below about 60K. This is due to the cooling

capacity being proportional to the fourth power of temperature, where at lower temperatures the large radiator volume and mass that would be required to provide sufficient cooling would suffer high parasitic heat loads from the substantial structure that would be necessary to support it [38].

6.2.3 Astrium Stirling Coolers

Stirling cooler technology developed at Astrium has flight-proven excellent reliability [28] and is capable of providing cooling down to a temperature of 10K [26], [89].

The Astrium 10K Stirling cooler was developed by Astrium and RAL for the US Air Force Research Labs (AFRL) as a proof-of-concept for an AFRL technology development programme [26], [89]. It is based on a modified design of the space qualified Astrium 20K cooler, which traces its evolution back to the 80K cooler developed by Oxford (as discussed in chapter 2).

The 20K and the 10K cooler both have a mid-stage interface, providing additional cooling at an intermediate temperature (between the cold tip temperature and the compressor heat reject temperature). With no load on the mid-stage, the AFRL 10K cooler is capable of achieving a base temperature of 9.4K, and can provide 45mW of cooling power at 10.4K [89].

Stirling coolers cannot provide cooling down to 4K. In order to produce a <4K heat bath for the dADR, another cryogen-free cooling technology is required.

6.2.4 Cryogen-Free dADR Heat Bath

The heat bath for the dADR must be cryogen-free and provide a continuous stable temperature of <4K. This has been previously achieved using a Joule-Thomson closed loop system, as is currently successfully providing cooling at 4K aboard the Planck mission, acting as a 4K heat bath for the dilution cooler cooling the HFI (High Frequency

Instrument) [90]. For details of the operational principles of a closed loop JT system, refer to chapter 2 (section 2.2.3.5).

The Planck 4K JT cooler was developed by RAL and Astrium under contract from ESA. It utilises Astrium mechanical compressors to compress the ^{4}He working fluid, and is pre-cooled directly by a sorption cooler operating at 18K. Published data shows the JT cooler can achieve ~19mW of cooling power at 4K with a 18K pre-cooler temperature [37]. The Planck 4K cooler is schematically represented in Figure 84.

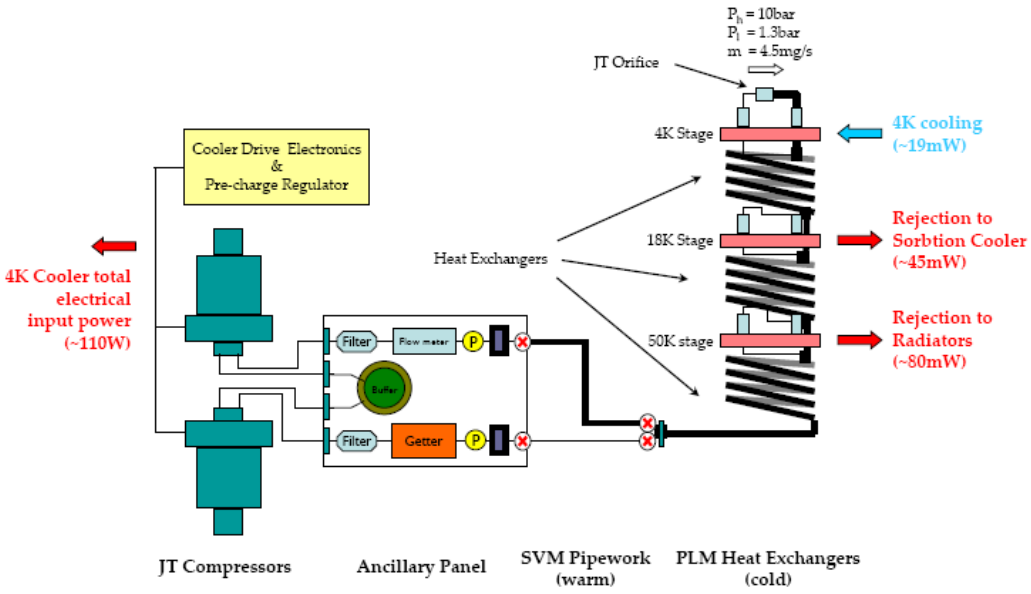

Figure 84: Schematic of Planck 4K JT cooler. After (91).

Figure 85 shows the Planck 4K cooler on test at RAL.

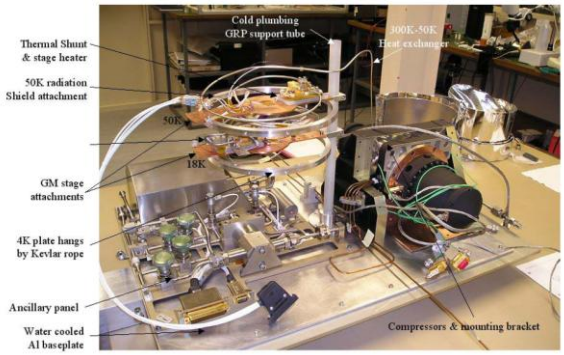

Figure 85: Planck 4K cooler on test at RAL. Courtesy of Astrium/RAL.

6.3 OVERVIEW OF PROPOSED IXO COOLING CHAIN

6.3.1 INTRODUCTION

The IXO cooling chain is the cryogenic subsystem that supports the thermal requirements of the 50mK final stage cooler. It consists of a series of coolers, each providing cooling at a given temperature. Each of these temperature stages works to reduce the parasitic heat loads to the stage below, ultimately leading to minimising the parasitic loads on the dADR and XMS.

6.3.2 COOLER SELECTION PHILOSOPHY

The cooling chain requirements are driven by the thermal requirements of the final stage (50mK) cooler, the MSSL dADR. The thermal requirements of the 50mK cooler are typically driven by the available cooling technology that can provide the necessary heat bath. Inevitably, cooling chain design is a cyclical process in which currently available cooling chain technology is developed further to match the requirements of the final stage cooler and the final stage cooler is developed to match the requirements of the heat bath interface.

The selection of coolers for the Astrium IXO cooling chain is driven by requirements set by ESA based on inputs from the XMS requirements and the developers of cryo-coolers such as MSSL, CEA, Astrium and RAL; and based on the cooling technologies available for development at Astrium. These requirements form a basis for the design, which is detailed hereafter, however full details of the ESA requirements may be found in the ESA requirements specification for the IXO XMS cooling chain (62) and the IXO Payload Definition Document (64).

6.3.3 DESIGN BASIS

The Astrium IXO cooling chain is to be based on the Astrium XEUS NFI2 (Narrow field Instrument, configuration 2) configuration, developed as part of Astrium's XEUS study (the former incarnation of IXO), and described in this extract from (64):

- *The operating temperature is achieved by a set of cryogen free cryo-coolers: the first step in the cooling train is realized by two-stage Stirling cooler providing a 150K stage and cooling the coldest shield and the JT cooler down to 15K. An additional cooling stage at 100K will be provided by either a cold radiator or a single stage Pulse Tube/Stirling cooler as a backup solution.The second step is achieved by a 3He Joule-Thomson cooler to 2K, similar to the design of the Planck 4K JT cooler taking advantage of new compressor developments currently ongoing. The JT cooler is pre-cooled by the lowest stage of the precooler (~15K). The last stage cooler is realized using a hybrid sorption cooler/ADR cooler currently under development for the SPICA/Safari mission. The system is a one shot system implying that all intermediate temperatures for anchoring the harness are stable. The typical operational time is about 30 hours with a regeneration time for the Sorption cooler/ ADR of less than 10 hour.*

- *A two stage ADR based on the previous developments will also be considered.*
- *The system includes a high degree of redundancy: A fully redundant system for the Stirling and JT cooler can be implemented. The 50mK cooler is not redundant, but some internal redundancy is implemented in the cooler itself (as implemented on Herschel).*
- *The cooling system includes 3 thermal shields (150 K, 15 K and 2 K) and the isolation between, these shields is optimized using MLI or low emissivity coating for the lowest temperatures.*
- *The system will be launched under vacuum which requires a pump down a few weeks before launch. Following launch the system will be opened to allow outgassing before it is switched on.*

6.3.4 PROPOSED COOLING CHAIN

The design of the cooling chain has evolved since the IXO Payload Definition Document (64) was written. The complete proposed IXO cooling chain from ambient temperature to 50mK is schematically represented in Figure 86.

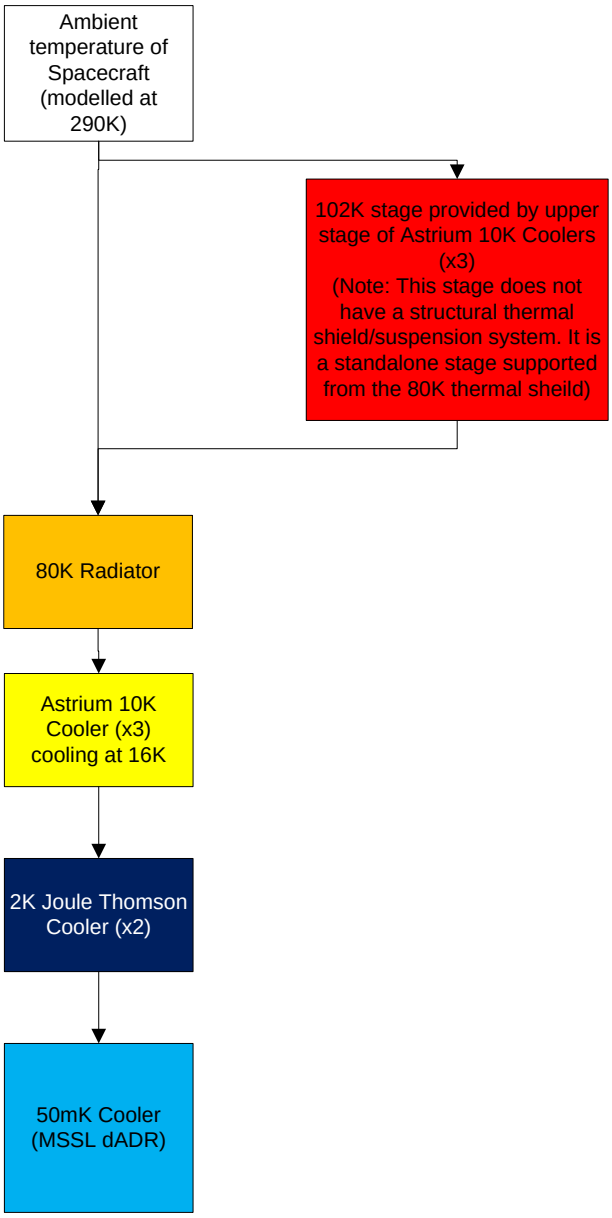

Figure 86: IXO Cooling chain schematic representation.

6.3.4.1 102K STAGE

The next temperature stage down from the ambient cryostat temperature will be actively cooled at an operating temperature of 102K. 102K is chosen as it is the optimal temperature based on a trade-off between how much heat the coolers can lift (which increases with increasing operating temperature) and the parasitic heat the stage is subjected to from the cryostat as well as the parasitic load down from the 102K stage to the 80K stage below (both of which decrease with increasing operating temperature).

The 102K temperature stage is provided by the upper temperature stages of 3 Astrium dual stage 10K Stirling cycle coolers. 3 coolers are used because a minimum of two are required to lift the heat required at the lower and upper temperature stages (see 6.8), and a third is required to meet the redundancy philosophy (see 6.3.5). Each cooler is estimated to be capable of lifting 2096.5mW at 102K when the low temperature stage is cooling at 16K [92].

The 10K dual stage Stirling cycle coolers are currently under development at Astrium, and are based on the design heritage of the 10K Stirling cycle coolers developed by Astrium for AFRL (Air Force Research Labs) described previously. Figure 87 shows a CAD drawing of the 10K Stirling cooler displacer unit. The 102K stage is the ring midway along the cold finger (shown).

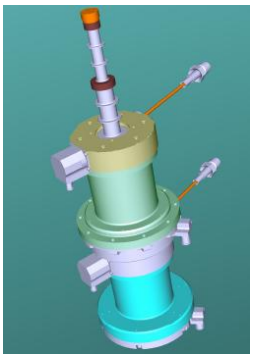

Figure 87: CAD drawing of 10K Stirling cooler displacer unit (courtesy of Astrium).

The 102K stage will be devoted purely to cooling the Joule-Thomson pipes (see 2K stage, 6.3.4.4), cryo-harness and current leads for the ADR and its heat switch. These loads mean the 102K stage does not have sufficient spare cooling power to maintain a thermal shield temperature as it would add significant radiative and conductive heat loads. Providing the thermal shield and first suspended enclosure cooling stage will be a radiator designed to radiate at ~77K, maintaining a thermal shield temperature of 80K.

6.3.4.2 80K STAGE

A thermal shield at 80K is required to provide the first stage of pre-cooling for the cooling chain that reduces radiation load on the inner stages and for cooling the first stage of the suspension system.

The 80K environment is provided by an external radiator connected to the rest of the cooling chain via a TLA (Thermal Link Assembly). The radiator itself is designed to radiate at ~77K, which is the lowest temperature at which the radiator can provide sufficient cooling whilst respecting constraints on the size of the radiator. The radiator has area $1.1m^2$ and cannot be made larger due to accommodation constraints on the spacecraft. The temperature stage is at 80K in order to allow for a 3K temperature differential across the TLA. Since the cryogenic radiator is located outside the cryostat and the 80K thermal shield is inside the cryostat, a feedthrough is required for the TLA. This feedthrough must be able to contain a vacuum for the purposes of on-ground testing, yet deliver minimal parasitic heat load from the ~300K cryostat body to the ~80K TLA. The feedthrough conceptual design and thermal analysis is presented in 6.6.

The radiator is sized according to the modelled cooling requirements for the case of maximum possible cooling requirement, and its radiating area of $1.1m^2$ provides 1460mW of cooling. The location of the radiator will be directly above the cryostat (termed CVV – Cryostat Vacuum Vessel), above a 150K radiator which is required for the thermal control of the spacecraft. This configuration is demonstrated schematically in Figure 88.

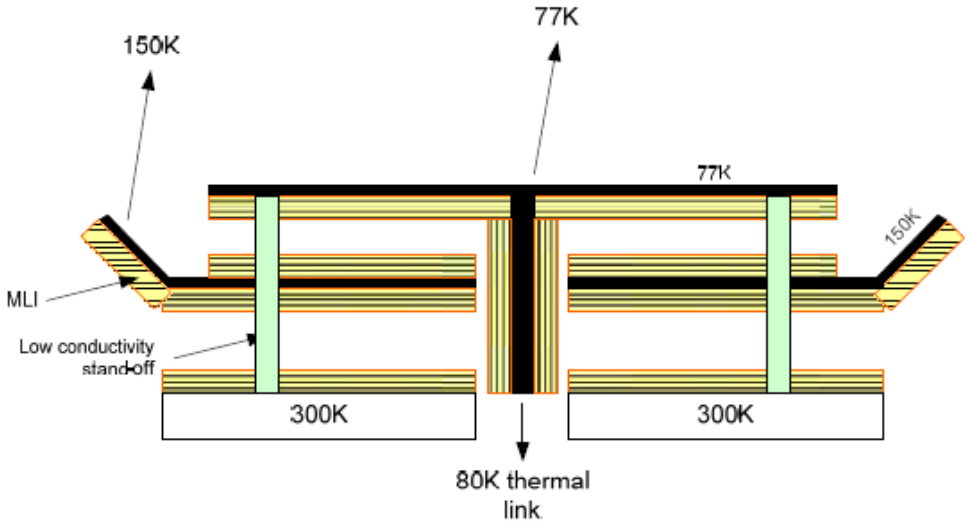

Figure 88: Dual radiator configuration. The 80K stage radiator (designed to radiate at 77k) is mounted onto the CVV (Cryostat Vacuum Vessel) via low-thermal conductivity standoffs. A 150K radiator (required for spacecraft thermal control) sits under the 80K radiator. The 80K thermal link connecting the 80K radiator to the 80K stage is partially shown. Image courtesy of Astrium.

6.3.4.3 16K STAGE

A 16K stage is required to provide the heat bath temperature necessary for a Helium based Joule Thomson loop to function, as the JT gas must be sufficiently below its inversion temperature (see 2K stage, 6.3.4.4). The 16K temperature stage is provided by 3 Astrium Dual stage 10K Stirling cycle coolers. These coolers are currently under development at Astrium, and are based on the heritage of the 10K Stirling cycle coolers developed by Astrium for AFRL (Air Force Research Labs). Each cooler is predicted to have a heat lift of 578.9mW at 16K with the mid-stage cooling at 102K. Figure 87 shows a CAD drawing of the 10K Stirling cooler displacer unit.

6.3.4.4 2K STAGE

The heat bath for the dADR will be maintained at a temperature of ~2K in order to maximise the dADR performance. The 2K stage temperature will be provided by two closed-loop Joule Thomson (JT) coolers which are currently under development at RAL, and are based on the heritage of the RAL 4K JT cooler currently flying onboard the

Planck mission (as described previously, and shown in test configuration in Figure 85). The compressors will be provided by Astrium, as was the case for the Planck JT cooler.

Each JT cooler is predicted to have a heat lift of 30mW at 2K using ^{3}He as the working fluid instead of ^{4}He as used on Planck. In order for the Joule Thomson effect to provide useful cooling at ~2K, the working fluid must be pre-cooled to 16K so that it is sufficiently below its inversion temperature 17.4K [(93)].

The working fluid is pre-cooled, and its self provides pre-cooling, via counterflow heat exchanger pipes running from the compressors located outside the cooling chain enclosure (Cryostat Vacuum Vessel, CVV) down to the 2K stage. These pipes are thermally anchored to the 16K and 102K stages to ensure the Helium is sufficiently pre-cooled for the JT cycle.

6.3.5 REDUNDANCY

6.3.5.1 REDUNDANCY MODES

The cooling chain offers redundancy mode operation at the 2K stage and the 16K/102K stages. There are 2 JT circuits at the 2K stage and 3 dual stage Stirling coolers at the 16K/100K stages. This configuration offers two modes of redundant operation: Cold redundancy and Warm redundancy.

In cold redundancy, the cooling is provided by one active JT cooler at the 2K stage, and two active 10K Stirling coolers at the 16 and 102K stages. The inactive JT loop and Stirling cooler add in additional parasitic heat leak as they do not provide any cooling and provide a conductive path between stages. The inactive coolers are there to substitute the active coolers in the event they fail.

In warm redundancy, the 2K cooling is provided by both JT loops, and the 16K/102K cooling provided by all three 10K Stirling coolers. In this configuration, each individual

cooler is working at a much lower fraction of its maximum cooling capacity, thus maximising lifetime and reliability. Should one of the 2K coolers fail, the other is able to provide sufficient cooling by working harder, as in the case for cold redundancy. If a single 10K cooler fails, the other two can provide sufficient cooling to maintain stable temperature.

It is therefore assumed that nominal operation would be warm redundancy mode, and cold redundancy is the operational case for when one JT cooler has failed and one 10K Stirling cooler has failed.

6.3.5.2 CONDUCTION THROUGH INACTIVE COOLERS

In the case of Cold redundancy operation; the failure of a single dual stage 10K stirling cooler means a loss of cooling power at the 16K and 102K stages. Further impact comes from the fact that the redundant cooler is now providing a conductive thermal path between the CVV body and the 16K stage, via the 80K stage. This extra heat load onto the 15K and the 80K stages must be accounted for. The values for the heat loads on these stages are taken from the detailed thermal analyses being used to develop the coolers.

The same holds for the failure of a single JT cooler. In this case, the redundant JT pipework provides a thermal path between temperature stages. The number used for the heatload on each stage is determined from an estimation of the pipework's length and cross sectional area (specified by RAL [(94)]).

6.3.6 CRYOSTAT LOCATION ON SPACECRAFT

The cryostat vacuum vessel which contains the complete cooling chain will be located on the MIP (Movable Instrument Platform) of the IXO spacecraft, as illustrated in Figure 89.

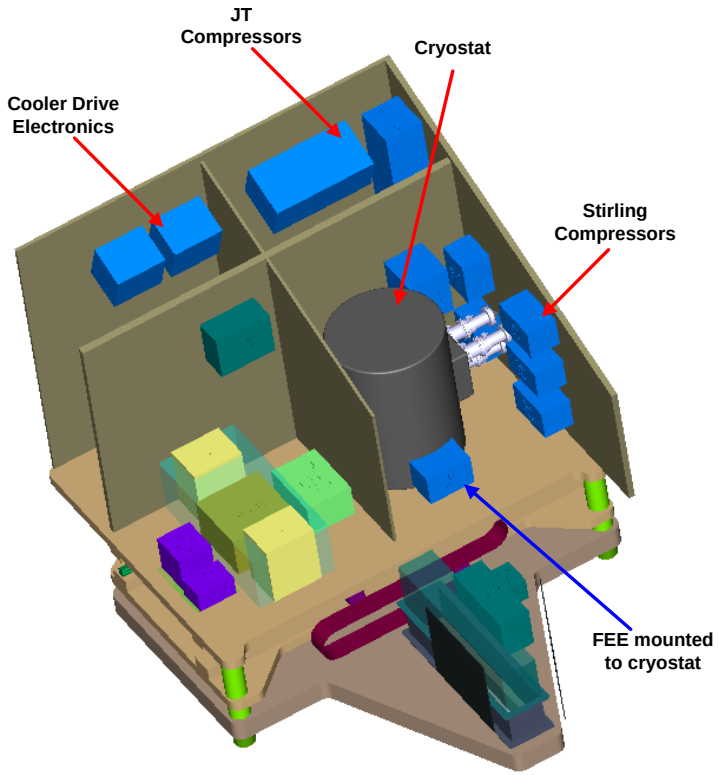

Figure 89: MIP (Movable Instrument Platform) showing location of cryostat which contains the cryogenic cooling chain (Image courtesy of Astrium).

The figure shows the location of the cryostat and Stirling cooler compressors in one of the quadrants of the MIP. The Stirling cooler displacers must be located as close as possible to the compressors in order to maintain a transfer line length below 300mm (nominal length – longer transfer lines reduce performance). The cryostat must have a diameter below 550mm to fit in the allocated space on the MIP. These two constraints require the stirling cooler displacers to be located on one side of the CVV. The Stirling cooler displacers are shown mounted on a box shaped structure on the side of the CVV (see 6.4.6). The compressors for the JT cooler are shown in another quadrant, and the cooler drive electronics in yet another. The cooler drive electronics are the electronics that control the coolers. The Front End Electronics (FEE) box contains the electronics that transfer data from the XMS instrument to the spacecraft (beyond the scope of this thesis). The FEE for the cryogenic system is mounted directly onto the cryostat.

6.4 PROPOSED DESIGN

6.4.1 OVERVIEW

The cryogenic cooling chain will be enclosed within a cryostat vacuum vessel (CVV), with each temperature stage having its own thermal shield/enclosure constructed of aluminium (except the 102K stage, as this is dedicated to pre-cooling the Joule Thomson pipework and harness which requires almost all of the available cooling capacity).

The basic CVV design is based on a 'russian doll' configuration comprising modified concentric cylinders, such that the thermal shield at each temperature stage fits inside the shield for the temperature stage above it. Each thermal enclosure is supported by a low thermal conductivity suspension system mechanically connecting it to the thermal enclosure at the next temperature stage.

The CVV has been sized based primarily on the dimensions of the final stage (50mK) cooler. The 50mK cooler is the double ADR under development at MSSL as introduced in chapter 3 (section 3.3.1); however, the CVV can also accommodate the CEA-SBT Hybrid sorption/ADR cooler (as described in 3.3.2). Both coolers are of similar maximum diametric dimensions, however, the MSSL cooler is slightly smaller across its diagonal. Sizing the cryostat for the CEA case allows the flexibility that the same CVV design can be used independently of which final stage cooler is ultimately selected. This thesis, however, details the MSSL option only.

6.4.2 CVV SIZING PHILOSOPHY

The final stage cooler dimensions have not been finalised for either the MSSL dADR or the CEA Hybrid cooler, thus an estimate made by CEA based upon the scaling up of their ESA TRP (Technology Research Programme) cooler to meet the cooling requirements for IXO has been used [(95)]. The MSSL dimensions are estimations based upon the required magnet coil dimensions and the minimum tolerable separation between them, as

detailed in Hepburn (63). CEA estimate their cooler to have the dimensions: 300mm length x 160mm width x 220mm height [(95)]. The MSSL cooler has preliminary dimensions of 235mm length x 97mm width x 245mm height [(63)], giving a maximum diagonal of 264mm. The rectangular cross section of the CEA cooler has a diagonal of ~272mm; however, the final cooler will not have a rectangular cross section as all internal components are round in shape. The cryostat is, therefore, initially sized based on a 270mm (inner) diameter innermost (2K) shield which should be more than sufficient.

The outer shields are sized to fit closely around the inner shields, taking into account the suspension system and the thickness of the MLI (Multi Layer Insulation) lining the walls (see 6.4.7). This approach minimises the volume of the cryostat, which ensures the total mass is minimised, the surface area of each shield and hence the radiation load to inner stages is minimised, and the spatial accommodation requirements are minimised. The cryostat consists of four thermal shields maintained at 2K, 16K, 80K and ~300K (the outermost, 300K shield is the CVV outer body).

If required at a later stage, the diameter of the 2K shield could be increased or decreased, and the other shields scaled accordingly without major changes to the details of the suspension system itself. It is worth noting that it is highly likely that in the final design, the 2K shield will be an integral part of the final stage cooler.

6.4.3 Components of CVV Assembly

The CVV assembly consists of:

1. CVV Outer body
2. Thermal shields at 2K, 16K and 80K
3. MLI on inside of CVV (30 layers, Herschel type – see 6.4.7.2 for details)

4. MLI on outside of 80K (30 layers, Herschel type) and 16K shields (20 layers, Herschel type - see 6.4.7.2 for details)
5. X-ray filter windows on CVV and each of the thermal shields (see 6.4.4)
6. 2K baseplate (directly interfaced to JT cold stage)
7. 16K baseplate (directly mounted onto 10K cooler cold finger)
8. 80K baseplate (With TLA to external radiator)
9. 102K baseplate (directly mounted onto 100K cooler interface) – this is used to connect the 10K cooler cold-heads to the 2 J-T cooler heat exchangers (see 6.4.5)
10. Final (50mK) stage cooler: MSSL dADR (see chapter 3)
11. Detector package (containing XMS Microcalorimeter and relevant readout electronics – see 6.4.4)
12. Suspension system 16K-2K (detailed in 6.5)
13. Suspension system 80K-16K (detailed in 6.5)
14. Suspension system at CVV(300K)-80K (detailed in 6.5)
15. 3x 10K dual stage Stirling cooler displacers
16. 2x Joule Thompson (JT) loops
17. ADR current leads (see 6.4.8.1)
18. Cryo-harness (see 6.4.8.3)
19. Thermal link assembly between final stage cooler and detector package

20. Thermal strap/TLA connecting 80K shield to 80K radiator (not yet detailed)
21. Low thermal conductance feedthrough for radiator TLA - see 6.6.
22. Required feedthroughs in the CVV body, for pipes from external cooler compressors, harnesses & current leads (not detailed)
23. Internal feedthroughs through thermal shields where required (not detailed)
24. FEE (Front End Electronics) box (not detailed)
25. Supports for cryostat (not detailed)

The detector package has its own self-contained 2K shield, thus the cryostat 2K shield does not enclose it.

6.4.4 DESIGN OF CVV

The design of the cryostat is shown in Figure 90, where it can be seen how the detector package, two-stage Stirling cooler displacers and the 50mK dADR cooler will fit into the CVV. Also shown are the MLI and the X-ray filter windows on each shield, which have been sized based upon the detector package specifications (as shown in Figure 91), the focal length and the mirror diameter.

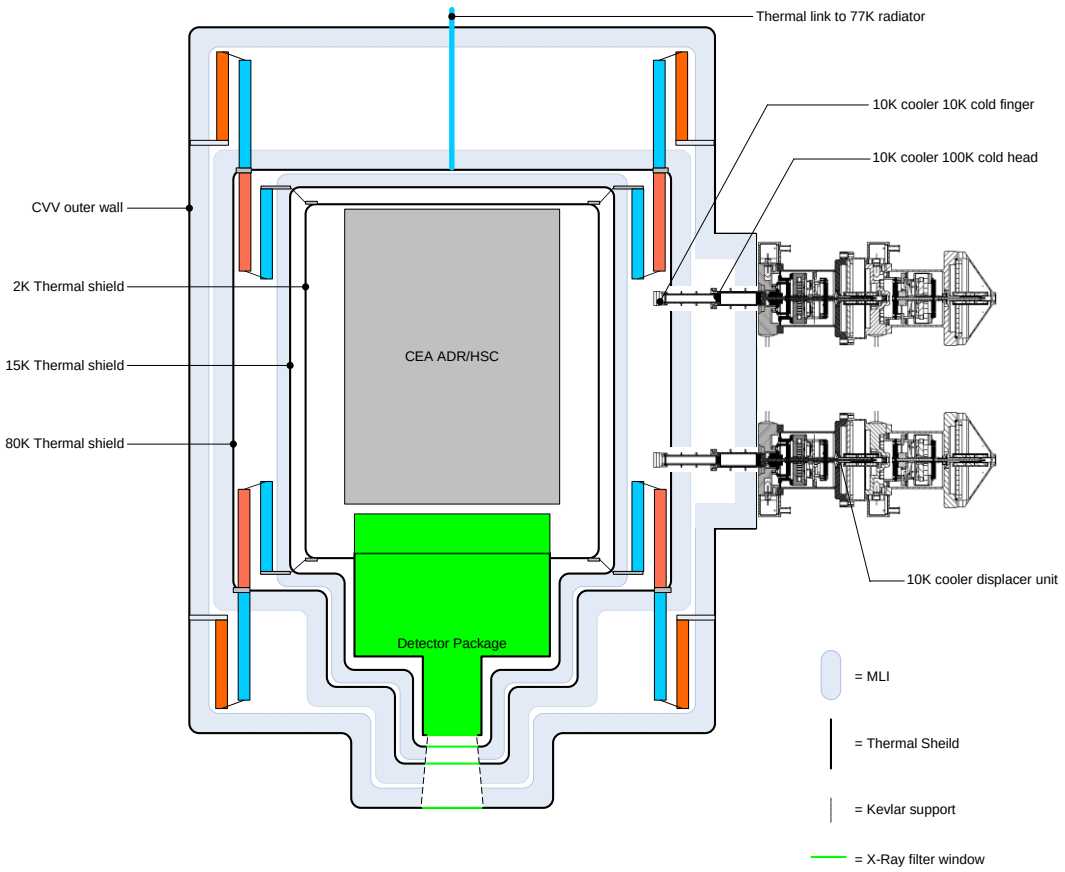

Figure 90: Cryostat design showing stirling coolers, detector package and Volume allocated for 50mK cooler (MSSL dADR or CEA ADR/HSC)

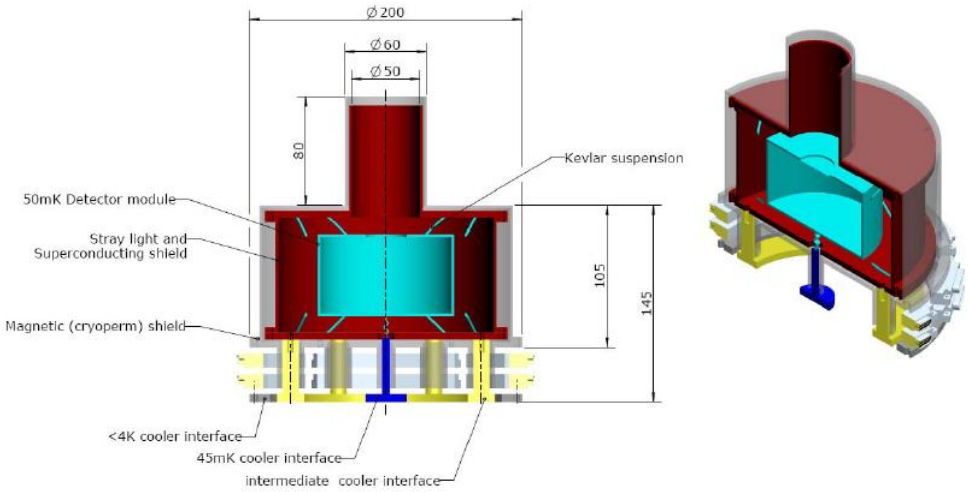

Figure 91: Detector package showing specifications. Courtesy of Astrium.

A 3D representation of the cryostat based on the design described in this section is presented in Figure 92. The figure also shows the 3 Stirling coolers, and the 'box' into which they are fixed (described in 6.4.6).

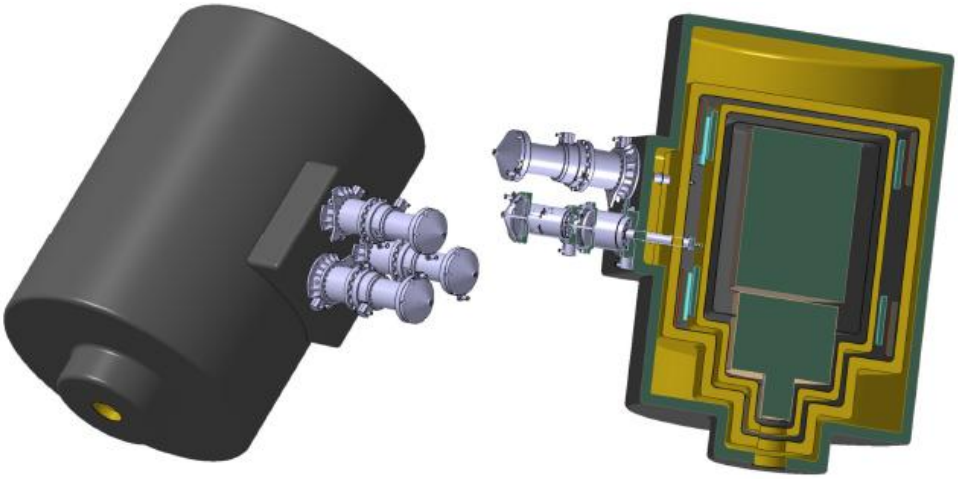

Figure 92: 3D CAD model of CVV. Position of 3 Stirling coolers is clearly shown. Image courtesy of Astrium.

6.4.5 Temperature Stage Accommodation

The 3 Stirling coolers require their cold interfaces to be thermally coupled to one another to form the 16K and 102K temperature stages. For the 16K stage this is done through the baseplate of the 16K thermal shield. However the 102K stage does not have a dedicated thermal shield in the cryostat. Therefore an additional baseplate is required for the 102K stage. This has not been designed in detail but will be supported from the 80K stage using low-conductivity stand-offs. Flexible thermal straps will link the 102K baseplate to the mid-stage of the Stirling coolers and the J-T heat exchangers will be mounted on the baseplate.

The 2K baseplate (not shown) will be located on the 2K shield, either in line with the 16K and 102K baseplates or at the 'top' of the shield ('top' is defined as the end of the cryostat furthest from the X-ray entrance filters). The JT cooler heat exchanger pipes and harness (both not shown) will be housed between the base plates within the 'box' volume occupied by the Stirling cooler cold heads, described subsequently.

6.4.6 Accommodation of Stirling Cooler Displacers

Due to accommodation constraints (previously discussed in 6.3.6) of the CVV onboard the MIP, the Stirling cooler displacers must be located on one side of the CVV outer shell. In order to comply with these constraints and align the cold stages of the displacers with the corresponding thermal baseplates, a boxed compartment on the CVV outer shell was designed.

The 10K Stirling coolers are arranged two on top, one on bottom, as shown in Figure 93. A possible arrangement for the two sets of JT pipes and the harness is shown below right (for the 300K-102K heat exchangers). The JT pipes are shown in red, the harness in green. At this stage, however, a detailed layout is not possible so this only indicates that sufficient volume exists to perform this accommodation. It also allows the potential for an easy thermal connection to the cold baseplate for a large length section of pipe/harness if required. The exact arrangement of the JT pipes is TBD depending on requirements to be specified by RAL.

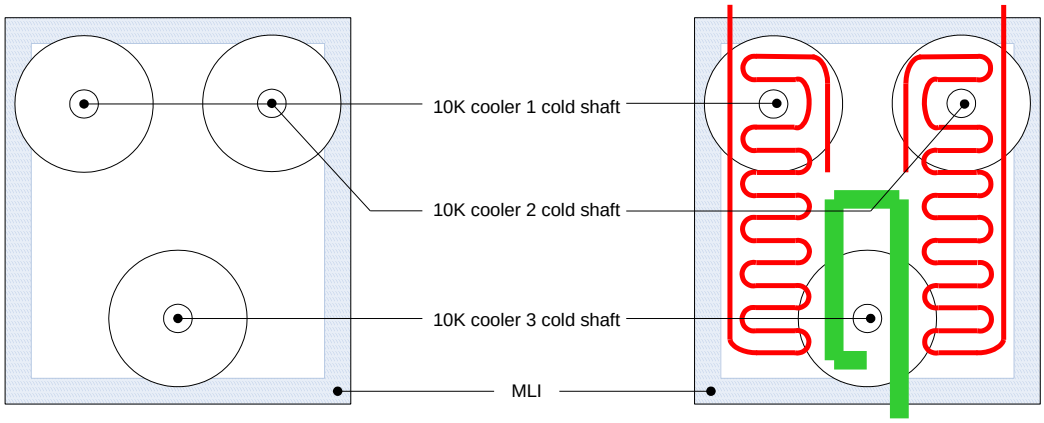

Figure 93: Arrangement of 10K cooler displacers. Possible arrangment of heat exchangers and harness is shown on right.

In particular, further attention is required to enable easy access to the thermal link assemblies between the cold-tips and the thermal shields. This will require a more detailed investigation of the assembly/integration sequence with the detector assembly.

The FEE (Front end electronics) box (not shown) will be mounted on the external cryostat wall directly below the 10K cooler displacers. The cryostat will also require a simple support structure (not shown) for mounting on the IXO MIP.

6.4.7 THERMAL SHIELDS

6.4.7.1 OVERVIEW

The thermal shields of the cooling chain are comprised of aluminium alloy as typically used for space cryogenics shields due to their affordable combination of strength, good thermal conductivity and low density [15]. The thickness of each shield has not been determined from any stress analyses at this stage, however, a CVV outer body thickness of 5mm has been chosen as this will certainly provide sufficient strength [15]. The internal shields are sized at 2mm thickness following the approach of previous analyses for the XEUS assessment study; however, the addition of titanium rings (see 6.5) at the interface between the shields and the suspension attachment ensures stresses induced by the suspension system are spread over the titanium rings, minimising strain on the shields themselves.

6.4.7.2 MLI

Each thermal enclosure (with the exception of the CVV outer body) is subject to thermal radiation emanating from the interior surface of the thermal enclosure of the temperature stage above. The exterior surfaces of all thermal enclosures are covered with several layers of MLI to minimise absorbed radiation. The interior of the CVV is also lined with MLI to minimise the heat radiating into the CVV.

The minimisation of heat transferred between thermal shields by radiation is achieved by minimising the effective emissivity of the MLI. This is performed by increasing the number of MLI layers. Figure 94 shows how the effective emissivity varies with number of layers:

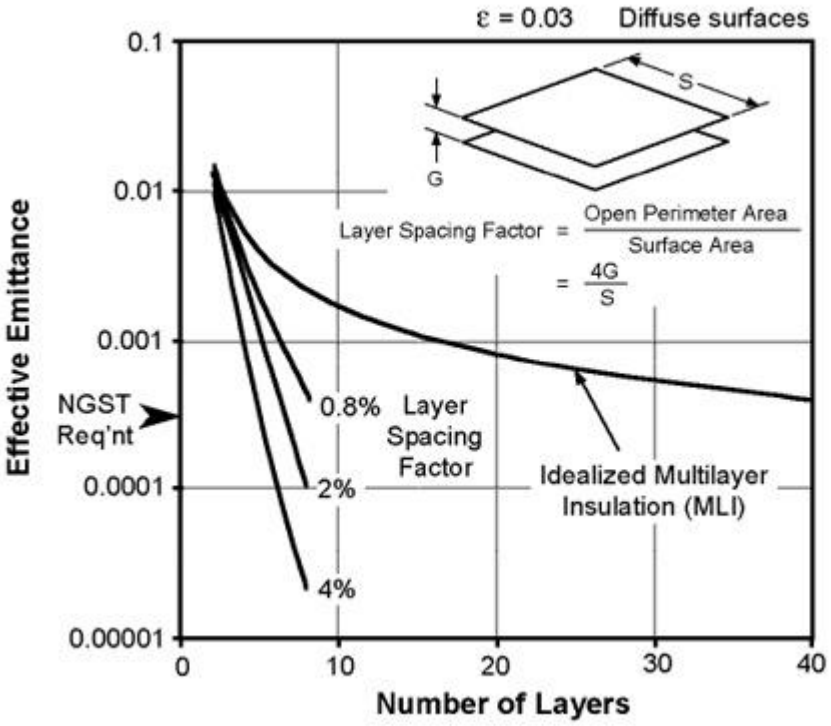

Figure 94: MLI effective emissivity as function of number of layers. After (96).

As can be seen from Figure 94, MLI emissivity does not decrease significantly with the addition of extra layers above ~20-30 layers. Additionally, larger layer numbers require more space and hence lead to larger spacing between thermal shields, resulting in larger outer stage thermal shields which present a larger radiating area, offsetting any benefit gained in reduced effective emissivity. The larger shields increase the diameter of the CVV itself as well as the mass of the complete system.

The number of layers of MLI on the inside of the CVV and outside of the 80K shield is selected to be 30, which corresponds to about 2cm blanket thickness if the MLI is Herschel-type. Herschel-type MLI (i.e. the MLI that was used on the Herschel spacecraft) has been assumed for all MLI blankets used in the cooling chain, and is detailed in an Astrium technical note (97). 20 layers of Herschel MLI surround the 15K shield, as the performance gained by adding further layers for the temperatures involved is not worth the increase in overall system volume and mass.

6.4.7.3 Radiative Heat Transfer Between Sheilds

The thermal shields have been assumed to be isothermal in this first order analysis. The situation outlined in Figure 95 represents radiative heat transfer from a warmer shield to a cooler shield for two cases: The first (upper) schematic represents the situation for the CVV – 80K stage, and the second (lower) schematic represents the situation for the 80K – 16K and 16K – 2K stages.

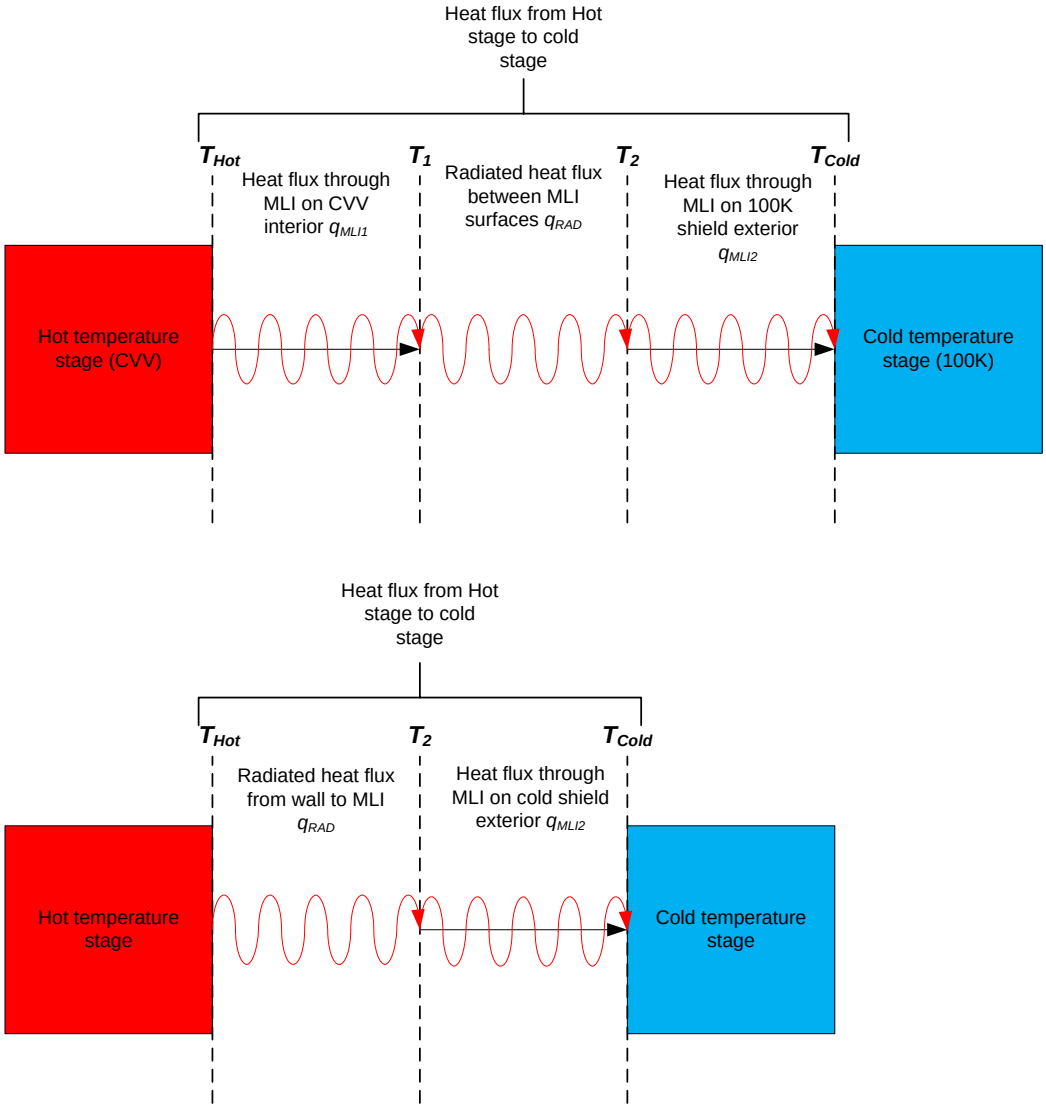

Figure 95: The treatment of radiated heat flux between hot and cold thermal enclosures as a boundary problem. Upper diagram shows situation for CVV (300K) – 80K stages. Lower diagram shows situation for 80K - 16K and 16K - 2K stages.

The temperatures of the higher (hot, T_{Hot}) and lower (cold, T_{Cold}) stages fix the boundary temperatures. In thermal equilibrium, the heat flux due to radiation from the upper stage and the heat flux through the MLI blankets must be equal. This boundary problem was solved using a computational numerical method for the equilibrium flux by varying T_1 and T_2 (the temperatures at the respective MLI blanket surfaces). The resulting flux solution is the heat load per unit area on a lower stage due to thermal radiation from the temperature stage above.

The equilibrium flux condition is given by:

$$\begin{aligned} q_{MLI1} &= q_{RAD} = q_{MLI2} \\ q_{RAD} &= q_{MLI2} \end{aligned} \tag{60}$$

Where the first equation represents the situation for the CVV – 80K stage, and the second equation represents the situation for the 80K – 16K and 16K – 2K stages.

The individual heat fluxes were calculated using fits to measurements performed on Herschel type MLI, as detailed in the technical note [97]:

$$\begin{aligned} q_{MLI1} &= \left(a\frac{(T_{Hot}+T_1)}{2}+b\right)(T_{Hot}+T_1)+\varepsilon_{MLI}\sigma(T_{Hot}^4-T_1^4)\frac{\rho_{MLI}}{n_{MLI1}} \\ q_{RAD} &= \sigma\varepsilon(T_1^4-T_2^4) \text{ (For CVV body – 80K stage)} \\ q_{RAD} &= \sigma\varepsilon(T_{Hot}^4-T_2^4) \text{ (For 80K – 16K/16K – 2K)} \\ q_{MLI2} &= \left(a\frac{(T_2+T_{Cold})}{2}+b\right)(T_2+T_{Cold})+\varepsilon_{MLI}\sigma(T_2^4-T_{Cold}^4)\frac{\rho_{MLI}}{n_{MLI2}} \end{aligned} \tag{61}$$

Where q_{MLI1} is the heat flux from the CVV body to the innermost interior MLI sheet (on the CVV interior wall), $q_{RAD}$is the heat flux radiated from the higher temperature stage (if higher stage is CVV body, q_{RAD} is the heat flux radiated from the interior CVV MLI),

q_{MLI2} is the heat flux from the outermost layer of the MLI to the lower temperature stage. The other quantities in the equations are the parameters governing the heat flow through the layers of the MLI blanket, a and b, the sheet layer density or number of sheets per unit length (ρ_{MLI}), the number of MLI sheet layers on the CVV interior (n_{MLI1}), the number of MLI sheet layers on the exterior of the cold stage enclosure (n_{MLI2}), the Stefan-Boltzmann constant (σ) and the emissivity of the MLI (ε_{MLI}) and the effective emissivity ε.

6.4.7.4 SHIELD PROPERTIES

The external dimensions, separation distances and MLI thicknesses are given in Table 27 for each temperature stage thermal shield.

Shield	Main body		Mid section		Top section		Total height (cm)	Thickness (cm)	Max. Radial Separation dist. To next shield (cm)	Min. Radial Separation dist. To next shield (cm)	MLI thickness (cm)	Min. clearance gap to lower stage (cm)
	Diameter (cm)	Height (cm)	Diameter (cm)	Height (cm)	Diameter (cm)	Height (cm)						
2K	27.4	36.4	20.0	10.0	6.0	8.0	54.4	0.2	1.6	1.0	N/A	N/A
15K	31.0	40.1	22.4	9.8	8.4	7.8	57.7	0.2	5.8	2.3	1.3	1.0
80K	43.0	45.0	27.5	9.8	13.5	7.8	62.6	0.2	5.0	5.0	2.0	1.0
Outer body	54.0	72.0	N/A	N/A	24.5	7.1	79.1	0.5	N/A	N/A	2.0	1.0

Table 27: Table of thermal enclosure properties for each temperature stage.

6.4.8 ELECTRICAL INTERFACING

6.4.8.1 ADR CURRENT LEADS

(a) HEAT CONDUCTION

The current leads for the final stage cooler run from the outer CVV body to the 2K stage. As this is the case, heat will inevitably be conducted by each wire. The heat conduction will be minimised by thermally anchoring the wires at each temperature stage. The amount of heat conducted by a wire is given by:

$$Q_{Cond} = \frac{A_{wire}}{L_{wire}} \int_{T_2}^{T_1} k_{wire}(T) dT \qquad (62)$$

Where $k_{wire}(T)$ is the thermal conductivity of the material from which the wire is made, A_{wire} is the cross sectional area of the wire and L_{wire} is the length of the wire and T_1 and T_2 denote the upper and lower temperatures (respectively) at which the wire is thermally anchored.

(b) JOULE HEATING

Wires carrying electrical current introduce additional heat loads due to joule heating, where the current carrying electrons scatter off the ionic lattice imparting kinetic energy to lattice ions. This thermal agitation of the ions increases the temperature. The amount of joule heating is dependent on the resistance of the wire, such that the amount of heat generated in a wire of resistivity $\rho_{wire}(T)$ by a current I is given by:

$$Q_{Joule} = \frac{L_{wire}}{A_{wire}} \int_{T_2}^{T_1} I^2 \rho_{wire}(T) dT \qquad (63)$$

Equations (62) and (63) show the conducted heat load to be proportional to the ratio A_{wire}/L_{wire}, yet the heat load due to joule heating effects is proportional to

L_{wire}/A_{wire}. For this reason, the wires must be designed to be optimised for the current they will carry and the temperatures at each of their ends. An optimised wire will be one which has an A_{wire}/L_{wire} that provides the minimal heat load from the combined effects of conduction and joule heating for a given wire material, current and temperature range.

For the low temperature stage (16K-2K), the effect of joule heating may be removed by implementing superconducting current leads, since the temperatures involved are low enough for the practical exploitation of superconductivity. By definition, superconducting leads have zero electrical resistivity; hence only thermal conduction contributes to the heat load on the 2K stage. The superconducting current leads are sized based on assuming a maximum allowable current density of 80% of the critical current density (the maximum current density the superconducting material can support before the superconducting state collapses).

6.4.8.2 Optimised Current Leads

The optimisation of the current leads was performed using a computational model to calculate the optimal wire diameter for a given material, current, wire length and thermal anchoring temperatures.

The resulting optimised wire configurations for the dADR current leads are detailed in Table 28, alongside the heat loads incident on the cold stage during both the dADR recycling and holding phases. The equivalent information for the magnetoresistive (MR) heat switch current leads is given in Table 29.

ADR Current leads							
			Wire properties			Total heat loads [mW]	
Temperature stage	No. Leads	Required current [A]	Material	Wire length [m]	Wire diameter [mm]	MIN, dADR holding	MAX, dADR recycling
CVV-102K	4	2.4	Copper	0.3	0.52	276	478
102K-80K	4	2.4	Copper	0.3	0.6	48.4	91
80K-16K	4	2.4	Copper	0.3	0.275	88.4	114
16K-2K	4	2.4	Magnesium Diboride	1	0.5	0.015	0.015

Table 28: dADR current leads at each temperature stage

MR heat switch current leads							
			Wire properties			Total heat loads [mW]	
Temperature stage	No. Leads	Required current [A]	Material	Wire length [m]	Wire diameter [mm]	MAX, dADR holding	MIN, dADR recycling
CVV-102K	2	1.4	Copper	0.3	0.4	139	81.6
102K-80K	2	1.4	Copper	0.3	0.45	26.5	13.5
80K-16K	2	1.4	Copper	0.3	0.2	33.8	23.4
16K-2K	2	1.4	Magnesium Diboride	1	0.5	0.015	0.015

Table 29: Magnetoresistive heat switch current leads at each temperature stage

6.4.8.3 HARNESS

The same considerations of conduction and joule heating apply to the wires of the harness, however joule heating would be less significant due to the smaller currents involved.

An existing 'off the shelf' Astrium Cryo-Harness has been considered. This harness consists of 3 sub harnesses of differing line impedances. The baseline properties of this harness are outlined in Table 30.

Line impedance	2K-15K stage	15K-80K stage	80K-300K stage	Total round-trip resistance [ohms]
2R	150 x 28AWG phosphor bronze x 0.3m	150 x 28AWG phosphor bronze x 0.3m	150 x 28AWG phosphor bronze x 0.3m	2.04R
10R	150 x 26AWG stainless steel x 0.3m	150 x 26AWG stainless steel x 0.3m	150 x 26AWG stainless steel x 0.3m	9.98R
100R	800 x 30AWG stainless steel x 1.0m	800 x 30AWG stainless steel x 1.0m	800 x 30AWG stainless steel x 1.0m	89.5R
Total thermal load	3.0mW	70mW	537mW	

Table 30: Baseline cryo-harness thermal properties.

6.5 CVV SUSPENSION SYSTEM DESIGN

6.5.1 SIMPLE MECHANICAL ANALYSIS FOR SUSPENSION DESIGN

For a first order analysis to determine the required configuration of the suspension system (to determine the natural mode frequencies of the suspension during design); the CVV, thermal shields and the 50mK cooler were modelled as masses connected via springs, in a coupled oscillator arrangement. The mass-spring allocations are specified in Table 31.

Mass allocation	Components	Spring allocation	Components
M1	T7 – 280K stage (CVV body)	K1	CVV mounting to spacecraft (MIP). Considered to be effectively hard mounted
M2	T5 – 80K stage	K2	Suspension system between CVV body and 80K Shield
M3	T4 – 16K stage	K3	Suspension system between 80K shield and 15K shield
M4	T3 – 2K stage	K4	Suspension system between 15K and 2K shield
M5	T1 – 0.05K stage	K5	Internal suspension system of the dADR. Spring constant derived from quoted dADR resonance.

Table 31: Mass and spring allocations for suspension modal analysis

A detailed mass breakdown each of the allocated masses detailed in Table 31 is provided in Table 32.

Mass Data									
Description	Number	Unit mass [kg]	Calculated [kg]	Margin [%]	Margin [kg]	Total [kg]	Low T [K]	High T [K]	Source
T1 - 0.05K stage							0.05	2	
Detector assy			0.70	20%	0.14	0.84			Allocated (ESA)
Intermediate shield			0.20	20%	0.04	0.24			Allocated (ESA)
Outer shield			0.50	20%	0.10	0.60			Allocated (ESA)
0.05K Strap			0.10	20%	0.02	0.12			Allocated (ESA)
Temperature sensor			0.02	20%	0.00	0.02			Allocated (ESA)
ADR suspended components (overestimated)			2.00	20%	0.40	2.40			Added for mechanical
(pills + some structure 1 mole CPA, 0.9 mole DGG)									
Sub-total, m0 [kg]			3.52		0.70	4.22			
T3 - 2K stage									Inc. margin
							2	16	
ADR fixed components (overestimated)			7.95	20%	1.59	9.54			CEA IXO subkelvin coo
Detector 2-4K electronics			0.50	20%	0.10	0.60			Ref fig 2, XMS spec
Magnetic shield - MSSL version [as in technote v1]			2.70	50%	1.35	4.05			From MSSL technote
			0.00	20%	0.00	0.00			Aluminium Cylinder x 1
Ancilliaries			0.25	20%	0.05	0.30			Allocated (ESA)
Harness (50mK- J-T temp)			0.50	100%	0.50	1.00			Allocated (Astrium)
Baseplate - bottom (rings)			0.07	20%	0.01	0.08			Aluminium Tube x 1
Baseplate - top (rings)			0.07	20%	0.01	0.08			Aluminium Tube x 1
2K shield			2.30	20%	0.46	2.76			Aluminium Cylinder x 1
FPA supports			0.00	20%	0.00	0.00			NONE
FPA support tube			0.00	20%	0.00	0.00			NONE
Tensioning equipment			0.50	50%	0.25	0.75			Allocated (Astrium)
ADR Current Leads + heat switch leads			0.00	100%	0.00	0.01			0.5mm dia s/c w ire x 1
J-T orifice assy #1			0.10	20%	0.02	0.12			Est from Ast 4K
J-T orifice assy #1			0.10	20%	0.02	0.12			Est from Ast 4K
Thermometer	2	0.05	0.10	20%	0.02	0.12			Allocated (Astrium)
Sub-total, m1 [kg]			15.14		4.39	19.53			Inc. margin
T4 - 16K stage							16	80	
J-T heat exchanger #1			0.70	20%	0.14	0.84			Est from Ast 4K
Heat switch			0.00	20%	0.00	0.00			NOT USED
10K harness section			0.50	100%	0.50	1.00			Allocated (Astrium)
10K thermal strap	3	0.1	0.30	20%	0.06	0.36			Allocated (Astrium)
10K shield			3.80	20%	0.76	4.56			Aluminium Cylinder x 1
10K main ring(s)			1.80	20%	0.36	2.16			Titanium Tube x 2
10K support tubes - inner			0.10	20%	0.02	0.12			CFRP Tube x 10
10K support tubes - outer			0.11	20%	0.02	0.13			CFRP Tube x 10
10K support rings - inner			0.38	20%	0.08	0.46			Titanium Tube x 2
10K support rings - outer			0.80	20%	0.16	0.96			Titanium Tube x 4
MLI			0.10	20%	0.02	0.12			Allocated estimate
ADR Current Leads + Heat Switch leads			0.00	100%	0.00	0.00			0.275mm/0.25 dia cop
Tensioning equipment			0.50	50%	0.25	0.75			Allocated (Astrium)
J-T heat exchanger #2			0.50	20%	0.10	0.60			Est from Ast 4K
Thermometer	2	0.05	0.10	20%	0.02	0.12			Allocated (Astrium)
Sub-total, m2 [kg]			9.70		2.49	12.20			Inc. margin
T5 - 80K stage							80	280	
J-T heat exchanger #1			0.70	20%	0.14	0.84			Allocated (Astrium)
thermal strap	3	0.05	0.15	20%	0.03	0.18			Allocated (Astrium)
harness section			1.00	100%	1.00	2.00			Allocated (Astrium)
enclosure - top/bottom			1.55	20%	0.31	1.86			Aluminium Cylinder x 1
shield			6.08	20%	1.22	7.30			Aluminium Cylinder x 1
Tensioning equipment			0.50	20%	0.10	0.60			Allocated (Astrium)
main ring(s)			1.04	20%	0.21	1.24			Titanium Tube x 2
MLI			0.20	20%	0.04	0.24			Allocated (Astrium)
ADR Current Leads + Heat switch leads			0.00	100%	0.00	0.01			0.6mm/0.45mm dia cop
support tubes - inner			0.28	20%	0.06	0.34			CFRP Tube x 24
support tubes - outer			0.23	20%	0.05	0.28			CFRP Tube x 24
support rings - inner			0.63	20%	0.13	0.75			Titanium Tube x 3
support rings - outer			0.89	20%	0.18	1.07			Titanium Tube x 4
J-T heat exchanger #2			0.50	20%	0.10	0.60			Est. from Ast 4K
Thermometer	2	0.05	0.10	20%	0.02	0.12			Allocated (Astrium)
Sub-total, m3 [kg]			13.86		3.57	17.43			Inc. margin
T7 - 280K stage									
10K Cold heads - nom	2	3.3	6.60	20%	1.32	7.92			Assume similar to 20K
10K Cold head - red	1	3.3	3.30	20%	0.66	3.96			
80K cryo-radiator	1	0.0	0.00	20%	0.00	0.00			Scaled area = 0.7m^2
ADR Current Leads + Heat switch leads			0.00	20%	0.00	0.00			0.52mm/0.4mm dia cop
main ring(s)			2.86	20%	0.32	1.93			Aluminium Tube x 2
Venting valve	2	1	0.50	20%	0.10	0.60			
Enclosure			24.81	20%	4.96	29.77			Aluminium Cylinder x 1
Support structure	1	10	10.00	20%	2.00	12.00			Allocated for cryostat
Compressors - JT - nom	1	18	18.00	20%	3.60	21.60			Base on Planck compr
Compressors - JT - red	1	18	18.00	20%	3.60	21.60			Base on Planck compr
Compressors - 10K - nom	2	8.64	17.28	20%	3.46	20.74			Assume Maxi compres
Compressors - 10K - red	1	8.64	8.64	20%	1.73	10.37			Assume Maxi compres
J-T switch assy	1	2	2.00	20%	0.40	2.40			
Pre-cooler switch asy	1	2	2.00	20%	0.40	2.40			
CDE - JT - nom	1	8	8.00	20%	1.60	9.60			Cf. SEA Planck unit = 6
CDE - JT - red	1	8	8.00	20%	1.60	9.60			Cf. SEA Planck unit = 6
CDE - 10K - nom	2	8	16.00	20%	3.20	19.20			Scale up from FIRST, a
CDE - 10K - red	1	8	8.00	20%	1.60	9.60			Scale up from FIRST, a
J-T nom warm pipe-work	1	1.5	1.50	20%	0.30	1.80			
J-T red warm pipe-work	1	1.5	1.50	20%	0.30	1.80			
Final stage cooler electronics	1	5	5.00	20%	1.00	6.00			Electronics are relative
Ancillaries - JT - nom	1	7	7.00	20%	1.40	8.40			Astrium 4K cooler
Ancillaries - JT - red	1	7	7.00	20%	1.40	8.40			Astrium 4K cooler
Electrical harnesses	1	10	10.00	20%	2.00	12.00			Allocated (Astrium)
Sub-total, m4 [kg]			185.99		36.95	222.93			Inc. margin
			Calculated	Calc. margin	Margin	Prediction			
CRYOGENICS TOTAL [kg]			228.20	21%	48.11	276.31			

Table 32: Detailed mass breakdown of complete cryogenic system.

A schematic of the 5 mass model is shown in Figure 96, showing the labelling of each mass and spring.

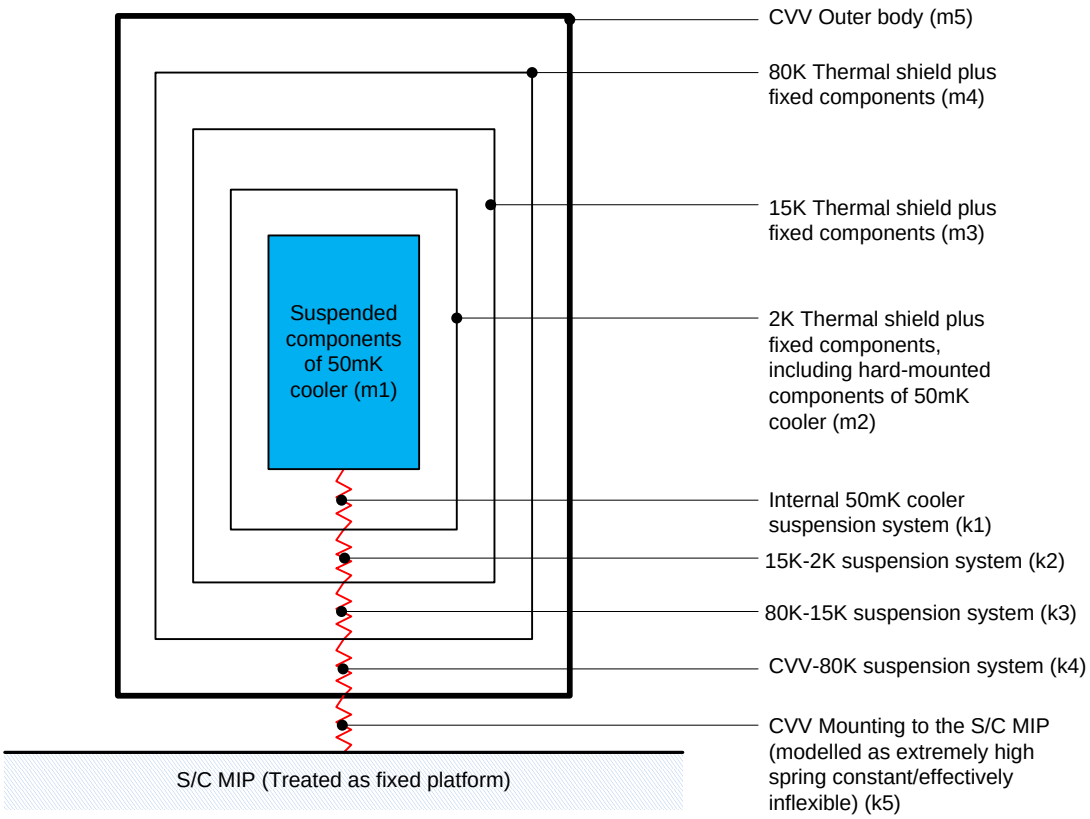

Figure 96: Mechanical model schematic showing labels of each mass (thermal enclosure) and spring constant (inter-stage suspension)

Each thermal enclosure, together with each component structurally attached to it, is modelled collectively as a mass m_n (where n = 1, 2..5). Each individual component has a margin added to its mass, typically 20%, however full details are given in Table 32.

Each suspension stage is modelled as a spring. In all analyses, no damping effects have been considered. The attachment to the spacecraft (S/C) Moving Instrument Panel (MIP) on which the CVV will be mounted is assumed to be effectively rigid, thus k1 is set to an impractically high value of 1×10^{16} N/m.

The final stage cooler is hard-mounted onto the 2K base-plate, and the detector package is hard-mounted onto the 2K shield. The cooler and detector package contain their own internal suspension systems which have not been detailed in this analysis, however the stated resonance frequencies [63), (98)] have been taken into account alongside the masses of the suspended components (m_1 in model) to determine an estimate of the spring constant k_1.

The equations of motion for the simple 5 mass, 5 spring system are:

$$\begin{aligned} m_1\ddot{x}_1 &= -k_1x_1 + k_2(x_2 - x_1) \\ m_2\ddot{x}_2 &= -k_2(x_2 - x_1) + k_3(x_3 - x_2) \\ m_3\ddot{x}_3 &= -k_3(x_3 - x_2) + k_4(x_4 - x_3) \\ m_4\ddot{x}_4 &= -k_4(x_4 - x_3) + k_5(x_5 - x_4) \\ m_5\ddot{x}_5 &= -k_5(x_5 - x_4) \end{aligned} \tag{64}$$

Where the mass and spring constant numerical index labels are subscripted. The spring extensions for each of the springs are denoted x_n, and the acceleration of each mass due to displacement from its equilibrium position are the second time derivative of the spring extensions, denoted by $\ddot{x}_n$.

The assumption of harmonic oscillatory solutions, x_n, implies $x_n(t) = A_n e^{i\omega t}$, such that $\ddot{x}_n = -\omega^2 x_n$ where ω are the natural mode frequencies to be determined.

Rearranging the equations of motion, taking into account the form of the harmonic solutions and expressing in matrix form yields:

$$\omega^2 \begin{pmatrix} A_1 \\ A_2 \\ A_3 \\ A_4 \\ A_5 \end{pmatrix} = \begin{pmatrix} \frac{(k_1+k_2)}{m_1} & \frac{-k_2}{m_1} & 0 & 0 & 0 \\ \frac{-k_2}{m_2} & \frac{(k_2+k_3)}{m_2} & \frac{-k_3}{m_2} & 0 & 0 \\ 0 & \frac{-k_3}{m_3} & \frac{(k_3+k_4)}{m_3} & \frac{-k_4}{m_3} & 0 \\ 0 & 0 & \frac{-k_4}{m_4} & \frac{(k_4+k_5)}{m_3} & \frac{-k_5}{m_4} \\ 0 & 0 & 0 & \frac{-k_5}{m_5} & \frac{k_5}{m_5} \end{pmatrix} \begin{pmatrix} A_1 \\ A_2 \\ A_3 \\ A_4 \\ A_5 \end{pmatrix} \quad (65)$$

The eigenvalues of the 5×5 matrix on the right hand side of (65) are the squared natural mode frequencies. From these values, the modal table of predicted natural frequencies is deduced for a particular suspension configuration.

6.5.2 Suspension Design Philosophy

The stiffness at each stage, k_n, has been tuned to keep the first natural mode of the system above the specified minimum requirement of 40Hz. The modal analysis includes the mass maturity margin, which is typically ~20%. It is clear that during further design refinements a more detailed analysis will have to be undertaken including strength and micro-vibration response aspects.

Typical space cryogenic suspension systems utilise low thermal conductivity straps comprised of strong, flexible materials such as Kevlar and struts made out of CFRP or G10.

The figure below shows the thermal conductivity of a number of unidirectional composites which have space cryogenics heritage, including Kevlar (labelled aramid in Figure 97), S-Glass and G10.

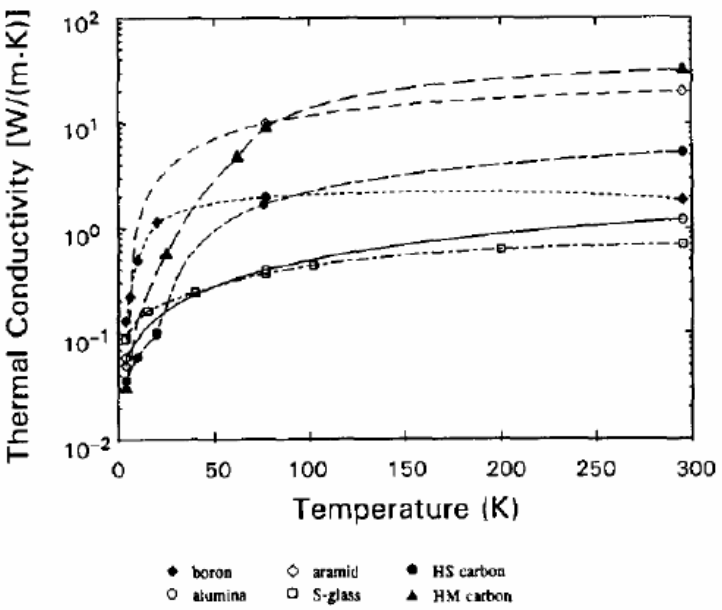

Figure 97: Thermal conductivity of unidirectional composites (aramid is Kevlar), after (99).

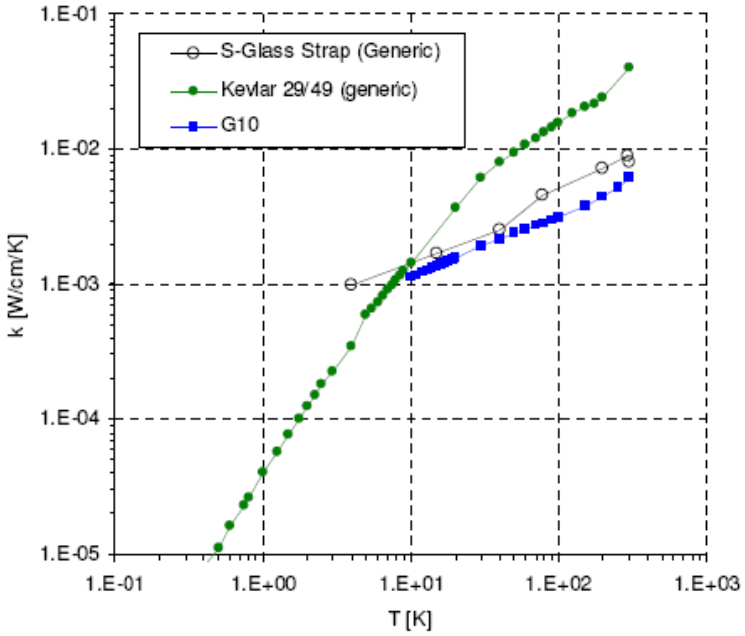

Figure 98: Thermal conductivity of S-glass, Kevlar, and G10 (99).

It can be seen that the conductivity of Kevlar is higher than S-glass above about 10K. Although the stiffness of Kevlar at room temperature is higher than for S-glass (about 80 GPa versus about 60 GPa), so that less material is required to support the same mass during launch, it is clear that Kevlar is the best choice below about 10K, and S-glass is the

best choice above this temperature. Hence in the suspension design, Kevlar suspension straps are used below 10K and S-glass is used above 10K [13].

Kevlar is well known for cryogenic space applications, having been used in a number of missions (e.g.Herschel sorption coolers). It can be purchased in either braided or single-fibre form. Single fibre form has been assumed, as it has a much higher strength to conductivity ratio (because the braided fibres are not in the direction of the force). In the past the braided fibre has been used because the supported masses are small and the equivalent diameter required to support the mass is very small and difficult to work with. For IXO it is envisaged that the supported mass could be quite high and therefore this problem is unlikely to be encountered, as the string diameter should be large enough to easily work with [(99)].

S-glass fibre is commonly used for cryogenic space applications for composite structures or in tape form. For cryogenic applications NASA has used it for several space shuttle borne experiments (99).

The suspension system is currently designed only in the lateral and longitudinal axes. The strap design is performed to achieve identical lateral and longitudinal frequencies, for simplicity at this stage.

Thermal analysis (following the thermal analysis detailed in 6.5.4) showed that straps alone could not provide a sufficiently long thermal path between the CVV-80K and 80K-16K temperature stages to maintain the conducted parasitic heat to sufficiently low

13 It should be noted that when calculating the stiffness of the suspension system it has been assumed that these materials can be obtained in any required diameter. In practice this is clearly not the case, and therefore some small differences might be expected when the detailed design is completed.

levels whilst respecting the requirement of a CVV outer diameter of <550mm. Hence, a stiff, low thermal conductivity structure is required to support the straps connecting each stage. The proposed structure concept is shown schematically in Figure 99.

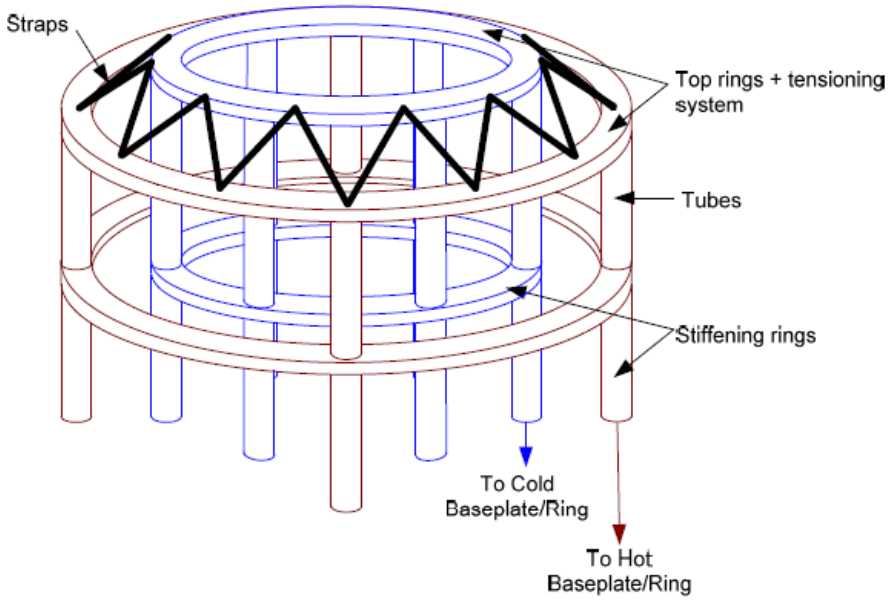

Figure 99: Suspension system design. Low thermal conductivity straps connect the top rings of the hot and cold temperature stages. For the outermost 2 suspension stages, the top rings are supported by a system of tubes and stiffening rings. After (99).

The complete suspension system consists of the typical strap system mounted on a pair of stiff rings (labelled top rings on figure) supported by G10 tubes mounted on stiff rings attached to the thermal shields being suspended (labelled cold/hot baseplate/ring in figure). Further stiff rings are added along the tubes in order to provide increased rigidity of the suspension system. The presence of the tubes increases the path length parasitic heat must travel between temperature stages, decreasing the heat load to sufficiently low levels.

The suspension at each stage is identical for the top and bottom ends of the cryostat, such that each thermal shield is suspended symmetrically.

6.5.3 Suspension Stiffness Analysis

6.5.3.1 Overview

The suspension system at each stage is modelled as a ring of identical low thermal conductivity straps, which interconnect rigid metal rings located at the top and bottom of each thermal enclosure. To enable the suspension system to provide a sufficiently long thermal path between temperature stages, the metal rings at the CVV body, 80K and 16K stages are supported by a system of low thermal conductivity tubes stiffened by metal stiffening rings. (note: The 16K-2K suspension system consists of only the straps connecting the 16K and 2K rings - there are no tubes).

6.5.3.2 Suspension Stage Spring Constant

The total collective spring constant for a given suspension stage (k_T) is a combination of the effective spring constants of the individual components of the suspension system; i.e. the tubes and the straps (the metal suspension and stiffening rings are both assumed to be rigid). The suspension system may be represented in the simplified manner as shown in Figure 100.

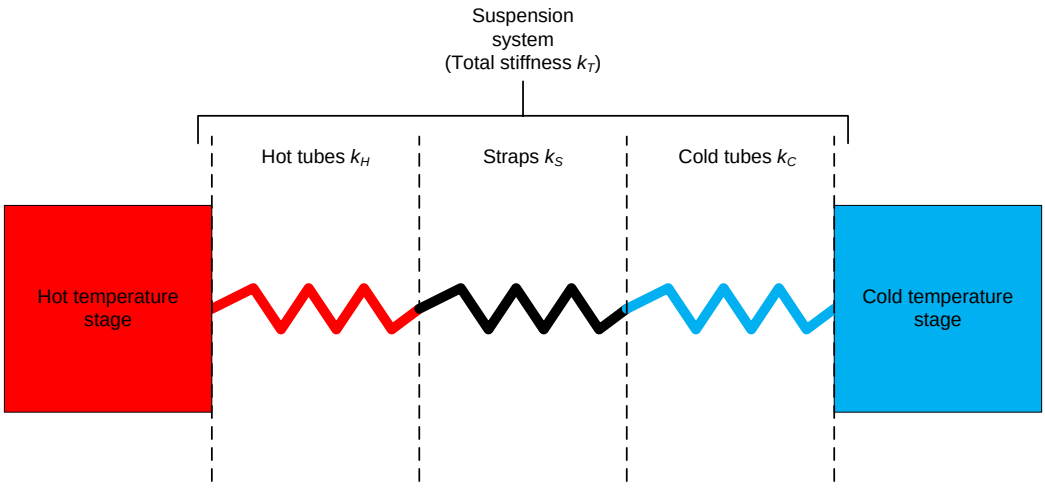

Figure 100: Simplified representation of suspension system. Each component group has a collective stiffness constant

The total spring constant (k_T) (stiffness) of a given suspension stage is obtained by:

$$\frac{1}{k_T} = \frac{1}{k_H} + \frac{1}{k_S} + \frac{1}{k_C} \quad (66)$$

Where k_H is the total spring constant of the system of Hot tubes, k_S is the total spring constant of the strap system and k_C is the total spring constant of the system of Cold tubes.

The properties of the tubes that determine their individual stiffness, the number of tubes and the strap properties are tuned to give the required stiffness performance of the whole suspension stage.

The resulting suspension configurations are then fed into a thermal analysis model in order to determine the heat conducted through each stage (see 6.5.4).

6.5.3.3 TUBE STIFFNESS

The spring constant for each individual tube of the hot and cold tube systems is determined from the modulus of elasticity of the tube material E_r, the tube moment of intertia I_x (which is a function of tube inner and outer tube diameter), height L, the distance of the load from the tube end a (set to zero in all cases), and number of sections the tube is divided by the addition of stiffening rings $n_{sections}$ (assuming the stiffening rings are equally spaced along tube). Treating the tubes as straight bars modified by tube formulae, this is represented mathematically as [100]:

$$k_{tube} = \frac{12E_r I_x}{\left((L-a)^2(L+2a)\right)} n_{sections}^2 \quad (67)$$

The total spring constant of the hot tubes (k_H) is then the sum of the individual spring constants of the individual hot tubes, as is the case for the cold tubes (k_C).

6.5.3.4 STRAP STIFFNESS

The straps connecting the suspension rings are arranged as in Figure 101 (left):

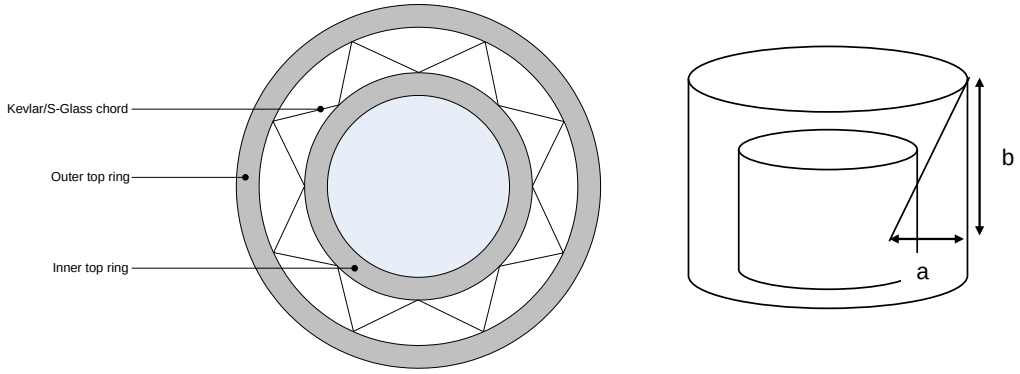

Figure 101: Suspension system. Left graphic shows inner and outer rings interconnected by straps. Right graphic shows strap arrangment in terms of radial projection (a) and axial projection (b).

The properties that determine the spring constant of each individual strap are the strap length, thickness and the axial (b) and radial (a) projections of the straps (as shown in Figure 101 (right).

The total spring constant for the straps (k_S) is calculated as the sum of the spring constants of the individual straps supporting the stage. The straps are assumed to be single fibres of either S-Glass or Kevlar, dependent on the temperature at which they will operate (see section 6.5.2).

6.5.4 Thermal Conduction Through the Suspension System

6.5.4.1 Overview

The suspension system configuration is driven by the stiffness requirements detailed previously. The suspension system has been designed to be of low thermal conductance by the choice of materials and the creation of the ring/tube system which allows for a much longer thermal path than if the suspension simply consisted of straps. Having straps only would result in too much heat being conducted through the suspension system unless the straps were made significantly longer, which would require a larger diameter CVV and hence higher radiation loads between stages and a higher mass for the cooling chain subsystem.

The calculation of the heat load due to conduction through the suspension system is performed by modelling the situation as a boundary equilibrium problem, as represented in Figure 102:

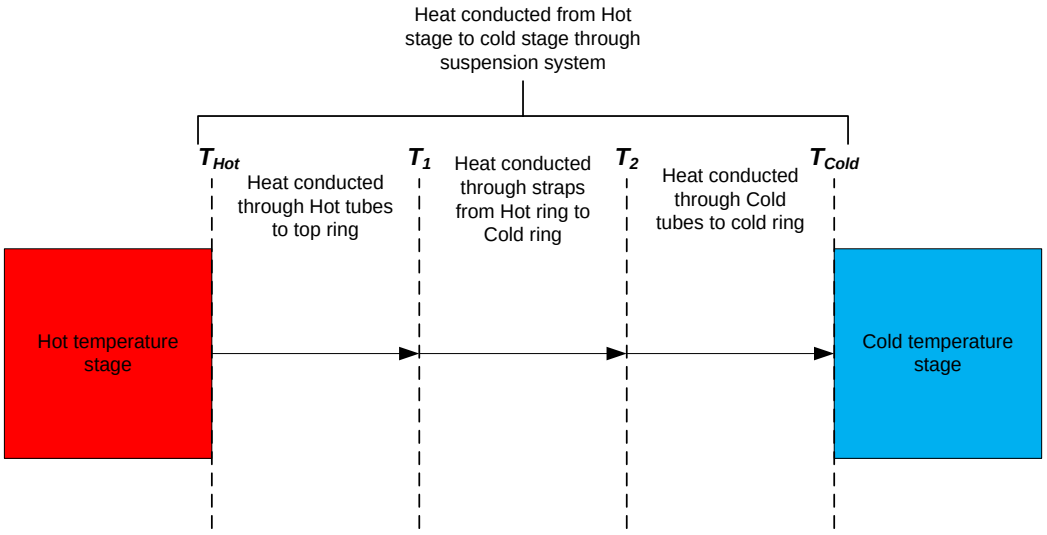

Figure 102: Heat conduction through suspension systems as an equilibrium boundary problem.

Such that the heat conducted through each part of the suspension (hot tubes, straps, cold tubes) is equal.

6.5.4.2 HEAT CONDUCTED THROUGH TUBES

The heat conducted through the Hot tubes is given by:

$$Q_{tube} = N_{Hottubes} \frac{A_{tube}}{L_{tube}} \int_{T_1}^{T_{Hot}} k_{tube}(T) dT \tag{68}$$

Where $N_{Hottubes}$ is the number of hot tubes, A_{tube} is the cross sectional area of one tube, L_{tube} the length of one tube and $k_{tube}(T)$ the thermal conductivity of the material from which the tubes are made. T_{Hot} is the temperature of the Hot stage, T_1 is the temperature at the top ring (the boundary between the hot tubes and the straps).

The exact same equation is used for the cold tubes, only with the number of cold tubes $N_{Coldtubes}$ instead of $N_{Hottubes}$ and the temperature of the cold top ring (boundary between the cold tubes and the straps) T_2 in place of T_{Hot} and the temperature of the cold stage T_{Cold} in place of T_1.

6.5.4.3 CONDUCTION THROUGH STRAPS

For the straps, the heat conduction equation is of the same form as for the tubes, only it uses the number of straps as the numerical multiplier and the relevant cross-sectional area, length and thermal conductivity of the straps. The temperature range is between T_1 and T_2.

The equilibrium heat conduction occurs when the temperatures T_1 and T_2 are such that the heat conducted through each part of the suspension system is the same. This equilibrium heat load is the heat load due to conduction through the suspension system.

6.5.5 PROPOSED SUSPENSION SYSTEM CONFIGURATION

The sizing of the suspension is based on the first order analysis described in 6.5.1, assuming the suspension can be represented by a system of un-damped coupled harmonic oscillators. At present the amount of damping is unknown, however a value of 0.5% critical viscous damping (typical for lowly damping structural systems) yields no significant impact on the predicted modes.

6.5.5.1 - 16K-2K SUSPENSION

The 2K shield is suspended by Kevlar straps held in tension. The straps have been sized to be short enough that the 16K shield is not too much larger than the 2K shield, yet long enough to provide an adequately long thermal path in order to keep the heat load sufficiently low. At the top and bottom of the 2K shield, there is an aluminium alloy ring to which the Kevlar straps attach via the tensioning mechanism (see 6.5.6). The tensioning mechanism connects the Kevlar straps to corresponding titanium alloy rings

on the 16K shield. The Kevlar and rings arrangement is illustrated schematically in Figure 101, as seen from above (number of straps shown is not representative of actual number of straps required).

The key properties of the straps are outlined below in Table 33. The strap positions are defined by their lateral (a) and axial (b) projections (see 6.5.6). These are the projections in the plane of the support rings and CVV axial direction respectively.

Strap property	
Strap material	Kevlar 29
Strap diameter [mm]	0.45
Strap length [cm] (pre-tension)	2.00
Axial projection (b) [cm]	1.2
Lateral projection (a) [cm]	1.6
Number of straps	72

Table 33: Details of the straps constituting the 2K - 16K suspension system

The outer titanium rings, attached to the 16K shield, are wide enough to anchor the Kevlar straps to the 16K stage and support the 80K-16K suspension system. The ring specifications are given below in Table 34. Note: sizes are rounded up to nearest mm.

Parameter	2K Rings	16 K Rings
Material	Aluminium alloy	Titanium alloy
Diameter (outer) [mm]	274	341
Width [mm]	10	31
Thickness [mm]	3	3

Table 34: 16K and 2K Ring specifications.

6.5.5.2 - 80K-16K SUSPENSION

The suspension system between the 80K-16K stages is slightly more complex than the previous case. In order to achieve the required stiffness, yet keep the thermal load on the colder stage down, a rigid tube and ring support system has been combined with the rings and straps suspension system. This has the effect of significantly increasing the length of the thermal path between the 80K shield and the 16K shield. This design concept is shown in Figure 103 corresponding to the orientation of the bottom (in CVV diagram) 80K-16K suspension system:

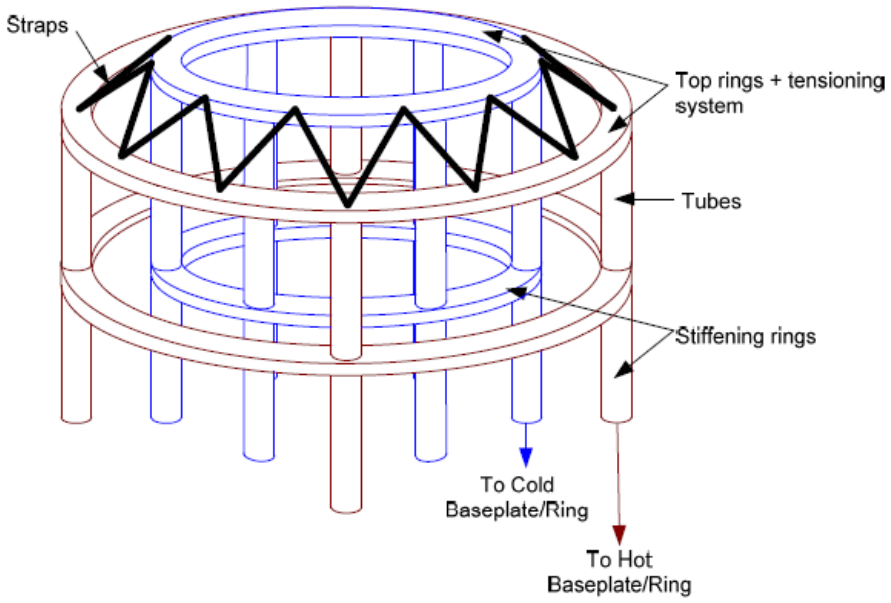

Figure 103: Tube and ring suspension system. Diagram shows straps interconnecting the top rings of the Hot (80K) and Cold (16K) stages.

The 16K titanium rings (cold rings) have G10CR tubes attached, orthogonal to the ring plane, with a number of titanium stiffening rings positioned at intervals along the height of the tubes. At the ends of the tubes, another titanium ring is attached (top ring). This ring is the anchoring ring for the straps via the tensioning system. The tensioning system is identical in concept to the 16K-2K mechanism. The straps connect this ring to another, larger diameter ring (outer top ring) in exactly the same way as for the 16K-2K

suspension straps and rings system. This larger diameter outer ring is then attached to a similar tube/ring support system which is attached to the 80K titanium ring (hot ring).

The G10CR tubes are attached to the titanium (alloy) rings by means of bonding to a titanium double-flange which is designed to ensure that the joint is as secure as possible. A diagram of the tube-flange joint is shown in Figure 104:

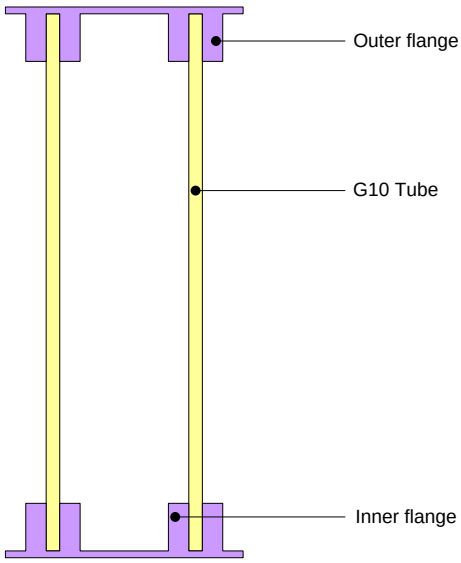

Figure 104: Option 1 for the tube-flange attachment (cross section of tube/flange shown).

Alternatively, the tubes could be joined in this manner to the base ring and top ring only, with the intermediate stiffening rings modified to have holes through which the tubes pass, with bonding flanges for attachment, as in Figure 105:

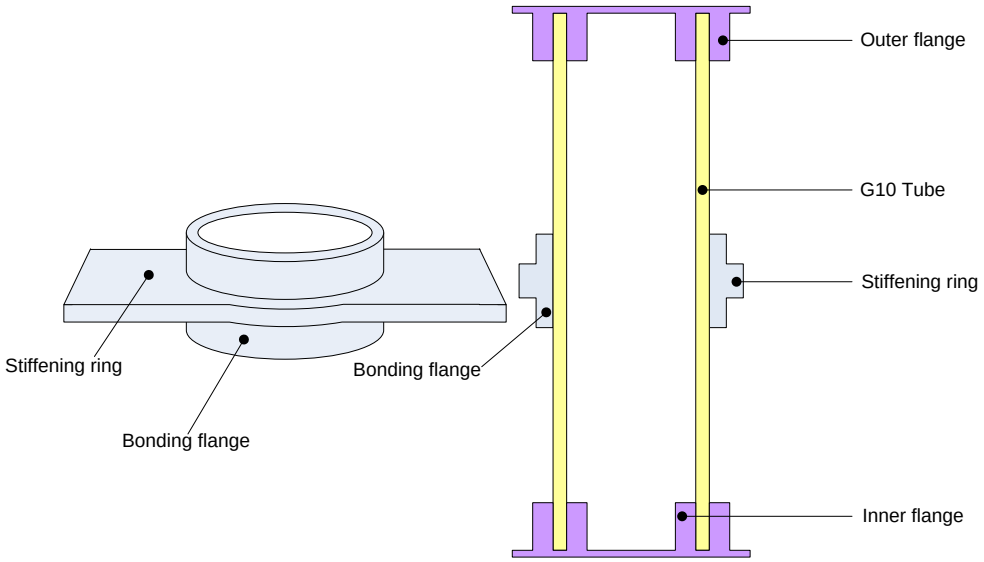

Figure 105: Option 2 for the tube-flange attachment.

This approach would probably be less complex and stronger than having separate shorter tubes bonded to each stiffening ring. It also minimizes the stiffness lost by multiple bolted joints.

The properties of the rings are given in Table 35 (Note: Titanium alloy is Ti-6Al-4V in all cases).

Parameter	16K Rings	80K Rings	Hot / cold top rings	Hot / cold stiffening rings
Material	Titanium alloy	Titanium alloy	Titanium alloy	Titanium alloy
Diameter (outer) [mm]	341	430	430 / 406	430 / 406
Width [mm]	31	17	12 / 12	12 / 12
Thickness [mm]	3	5	3 /3	3 /3

Table 35: 16K - 80K ring specifications.

The tube properties are given in Table 36:

Parameter	Cold tubes	Hot tubes
Tube material	G10CR	G10CR
Tube diameter [mm]	12	12
Tube length [mm]	92	105
Wall thickness [mm]	4	4
Number of stiffening rings (inc. top ring)	2	4
Total Number of tubes (top + bottom)	10	10

Table 36: 16K - 80K tube properties.

Strap properties are given in Table 37:

Strap Property	
Strap material	S-Glass
Strap diameter [mm]	0.33
Strap length (pre-tension) [cm]	1.36
Axial projection (b) [cm]	0.8
Lateral projection (a) [cm]	1.1
Number of straps	96

Table 37: 16K - 80K Strap properties.

The 80K titanium rings are the same rings upon which the 300K-80K suspension system is mounted.

6.5.5.3 - 300K-80K SUSPENSION

The outermost suspension system is identical in design to the previously described 80K-16K suspension system. The only differences being the numbers and dimensions of the components.

The properties of the rings are given in Table 38:

Parameter	80K Rings	300K Rings	Hot / cold top rings	Hot / cold stiffening rings
Material	Titanium alloy	Titanium alloy	Titanium alloy	Titanium alloy
Diameter (outer) [mm]	430	525	430 / 406	430 / 406
Width [mm]	17	40	12 / 12	12 / 12
Thickness [mm]	5	5	3 /3	3 / 3

Table 38: 80K- 300K Ring properties

The tube properties are given in Table 39:

Parameter	Cold tubes	Hot tubes
Tube material	G10CR	G10CR
Tube diameter [mm]	12	12
Tube length [mm]	110	90
Wall thickness [mm]	4	4
Number of stiffening rings	3	4
Total Number of tubes (top + bottom)	24	24

Table 39: 80K - 300K Tube properties.

The strap properties are given in Table 40:

Strap property	
Strap material	S-Glass
Strap diameter [mm]	0.22
Strap length [cm]	1.36
Axial projection [cm]	0.8
Lateral projection [cm]	1.1
Number of straps	192

Table 40: 80K - 300K suspension strap properties.

6.5.6 SUSPENSION TENSIONING SYSTEM

The tensioning system for the Kevlar/S-Glass straps uses the same design concept for all three suspension stages. The design consists of a pair of capstans, and an array of small pulleys. The two capstans are located beside each other on the outer ring to enable the easiest and most accessible adjustment of the tension. Two are used to enable the easiest possible distribution of even tension around the circumference of the rings. The location of the capstans is shown Figure 106.

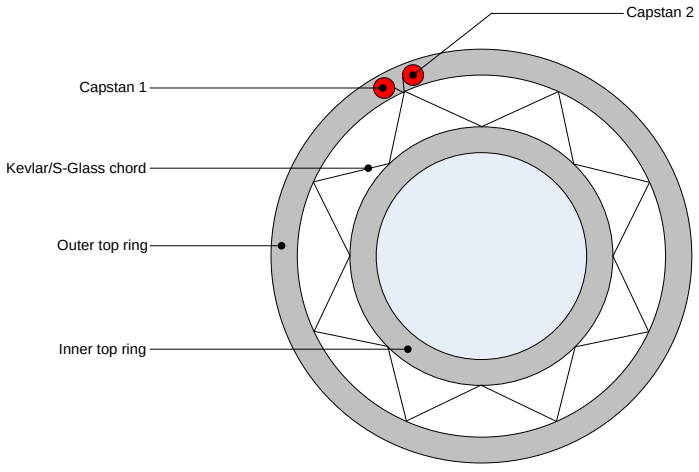

Figure 106: Tensioning system layout. Pulleys (not shown) are located at points where the straps meet the rings.

A pulley is situated at each anchoring point on the inner and outer ring. The pulleys will have inner diameter of 2.5mm, as they must remain small in order to keep the mass and

spatial accommodation requirements to a minimum, yet they must be large enough to keep the Kevlar/S-glass from being bent beyond their respective minimum bend radii. The pulley configuration is shown in Figure 107.

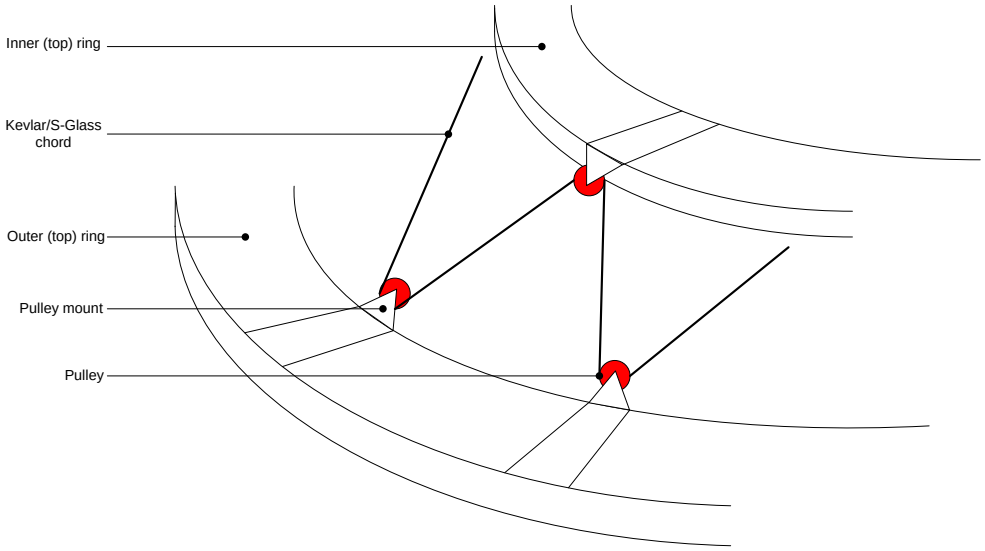

Figure 107: Pulley system layout. Schematic shows a section of the suspension system top rings and how the straps are supported by the pulley system.

The pulleys could either be actual pulley wheels, made of titanium, G10CR or Torlon, attached to a titanium mounting, or simply polished titanium pegs or holes which are either integral parts of the top rings or integral parts of the mounting. The proposed pulley options are illustrated in Figure 108.

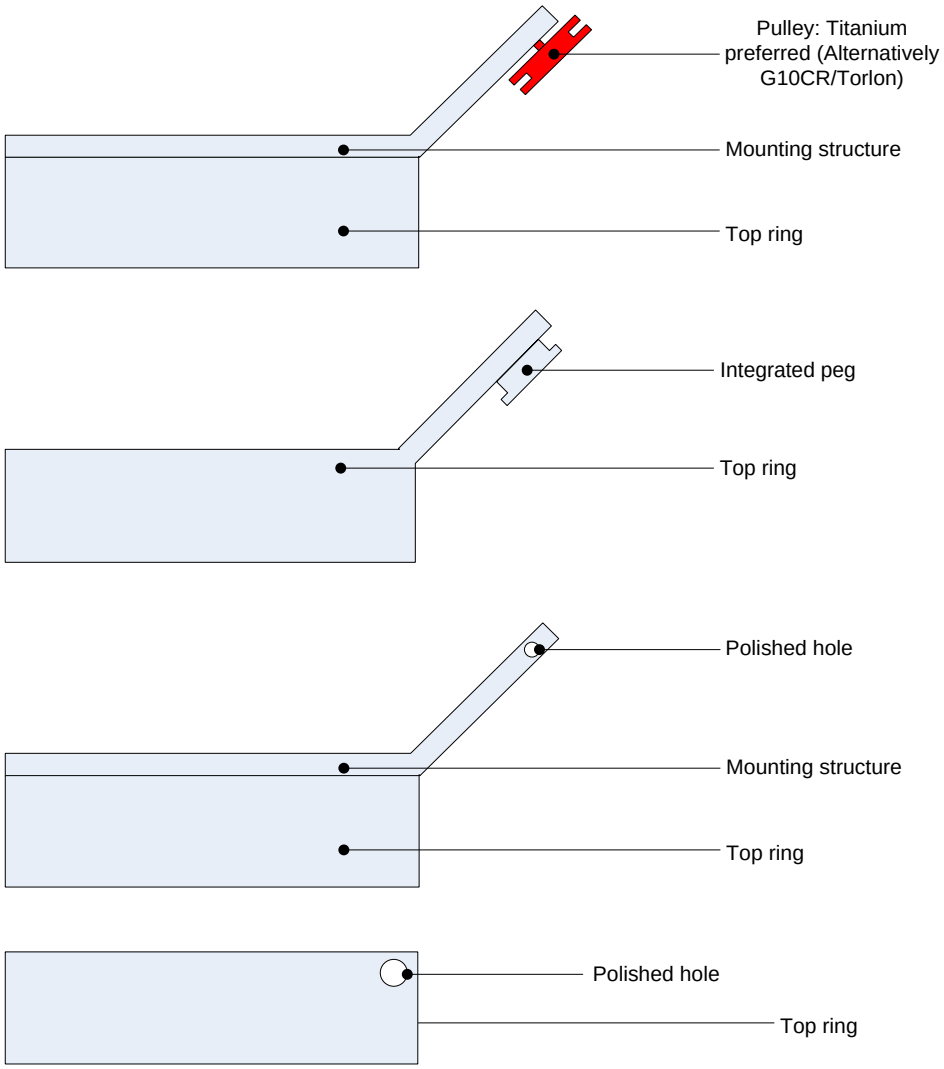

Figure 108: Possible options for pulley types

The pulley wheel design would allow a lower heat transfer and allow easier even distribution of tension, but would be more difficult to initially string up and assemble.

This type of tensioning system has been used by MSSL [63] and CEA [95] in their cooler developments, as well as at Astrium during the development of the Planck 4K cooler programme.

An alternative approach is to use a dedicated tensioning tool, with a fitting bonded to the Kevlar, but this is less reliable to assemble.

If it turns out the second design is too difficult to manufacture, it could use a separate mounting structure as for the first design. Friction between the Kevlar and pulley peg/hole could be minimised by using a low-friction coating.

6.5.7 Suspension Modes

The modes predicted for the CVV assembly based on the suspension system design and analysis presented thus far are summarised below in Table 41.

Mode	Frequency [Hz]
1	41.6
2	121.6
3	166.5
4	216.6
5	1065937.2

Table 41: Predicted CVV modes based on suspension design.

As can be seen, the first mode is above the required 40Hz. Thus, the design fulfils the requirements considered and indicates that the presented suspension design is suitable for purpose. However, as indicated in 6.5.2, no strength or microvibration analyses have yet been undertaken, hence a more detailed analysis will be required for the final suspension design.

6.6 80K RADIATOR TLA FEEDTHROUGH

6.6.1 OVERVIEW

The presence of the external radiator providing the cooling for the 80K temperature stage requires overcoming the design challenges presented as a vacuum-tight high thermal conductivity link must pass through the CVV wall (at ambient spacecraft temperature) yet remain at 80K. For this purpose, a special low thermal conductivity feed-through assembly has been conceptually designed based on thermal considerations.

The situation leading to the requirement of a special feedthrough is illustrated in Figure 109:

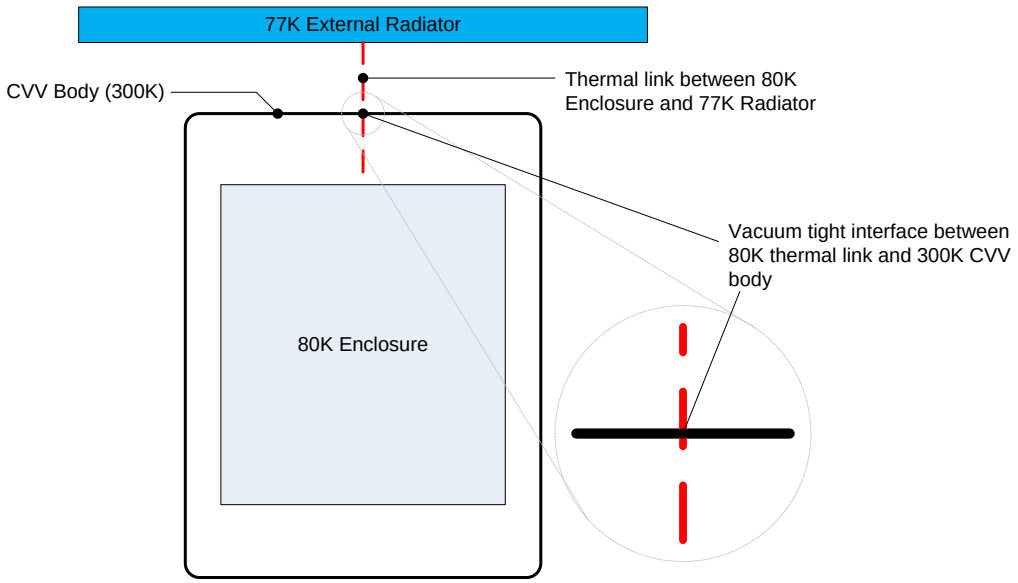

Figure 109: Reason for the requirement of a specially designed low thermal conductivity feedthrough for the link between the 80K temperature stage and the external radiator.

The CVV body has been assumed to be at 300K in these analyses. It is assumed that the Thermal link will be at 80K at the point it passes through the CVV wall. The heat load from the 300K CVV body onto the 80K thermal link must be minimised as far as practically possible. This means the feedthrough assembly must provide a long thermal

path from the 300K interface to the 80K interface whilst preserving a small diameter (several cm). This is because a larger diameter feedthrough assembly could provide additional complications in terms of the strength and stiffness of the CVV body, and is more likely to have a vacuum failure during launch (recall cryostat will be launched under vacuum, 6.3.3). Additionally, a large diameter feedthrough assembly will have more significant thermal contraction differences relative to the CVV body, and could also provide extra complications during assembly, integration and verification (AIV).

6.6.2 Design Concept

The design concept of the feedthrough assembly is shown schematically in Figure 110.

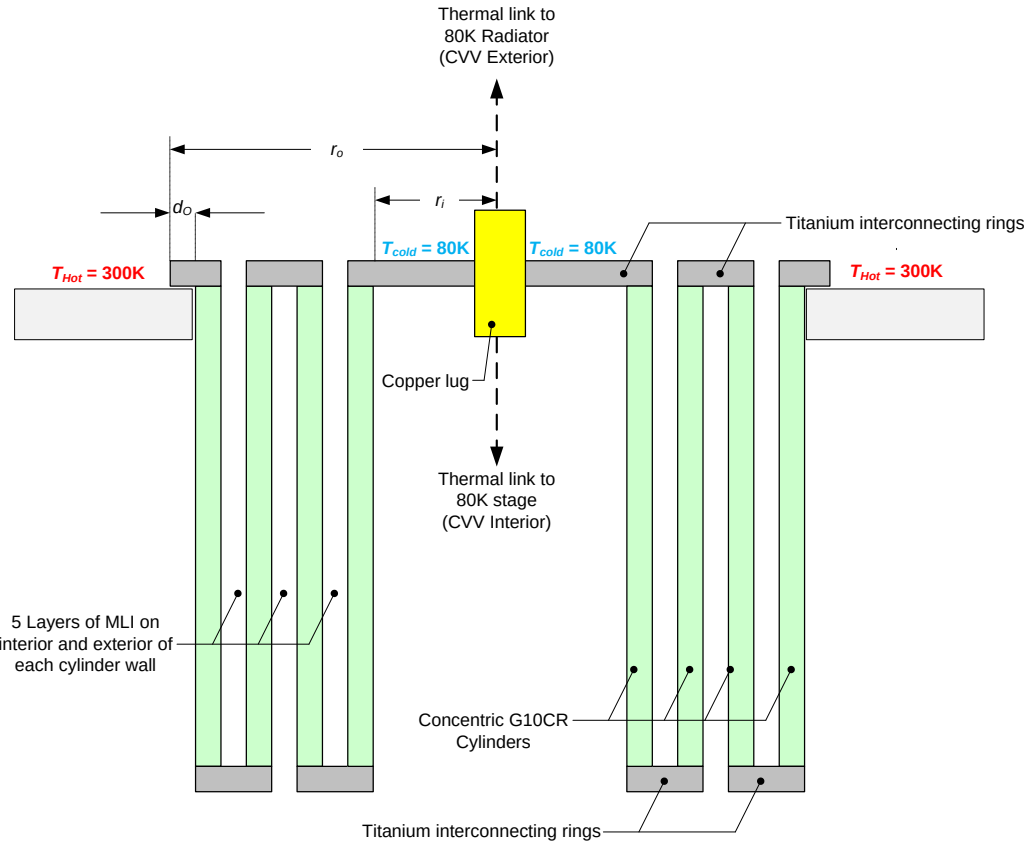

Figure 110: Schematic representation of feedthough design (shown as a slice through the diameter). At the centre is an 80K high purity Copper lug which connects the internal part of the thermal link to the external part.

The feedthrough assembly consists of a number (n_c) of concentric G10CR cylinders, interconnected at alternate ends by titanium rings. Titanium is chosen for its relatively low thermal contraction properties and high strength. G10CR is the best option for the low thermal conductivity cylinders as it meets outgassing requirements and is high strength across the temperature range of operation.

At the centre of the innermost titanium ring of the feedthrough assembly is a high purity gold plated Copper lug which connects the internal part of the thermal link assembly to the external part. It has been assumed that there are 10 layers of Hershel-type MLI (see 6.4.7.2) in the gaps between the cylinders, with 5 sheets on the interior and exterior of each cylinder, giving a blanket thickness of 0.34cm on each side of every cylinder wall.

In order to analyse the performance of the feedthrough assembly, a thermal model was constructed.

6.6.3 Thermal Model of Feedthrough Assembly

The optimal configuration of the design concept is proposed based on purely thermal considerations. Radiative and conductive heat transfer through the assembly were considered. Model input parameters are defined subsequently.

Boundary temperatures at the hot and cold interfaces:

- T_{Hot} = 300K At the interface with the CVV body.
- T_{Cold} = 80K At the interface with the central Copper lug.

Feedthrough assembly footprint properties:

- r_{outer}, the outer radius of the feedthrough assembly.
- r_{inner}, the inner radius of the feedthrough assembly (accommodation radius for the central Copper lug).

- d_O, the overlap of the outermost titanium ring with the hole in the CVV body. This quantity is required to specify the outer radius thermal boundary position with respect to r_{outer}.

Cylinder properties:

- n_c, the number of cylinders (in multiples of 2 (*i*) between 2 and 10).
- t_c, the wall thickeness of each cylinder.
- h_c, the height of each cylinder.

The treatment of the heat flow problem is based on several simplifying assumptions, illustrated for clarity in Figure 111 and described subsequently.

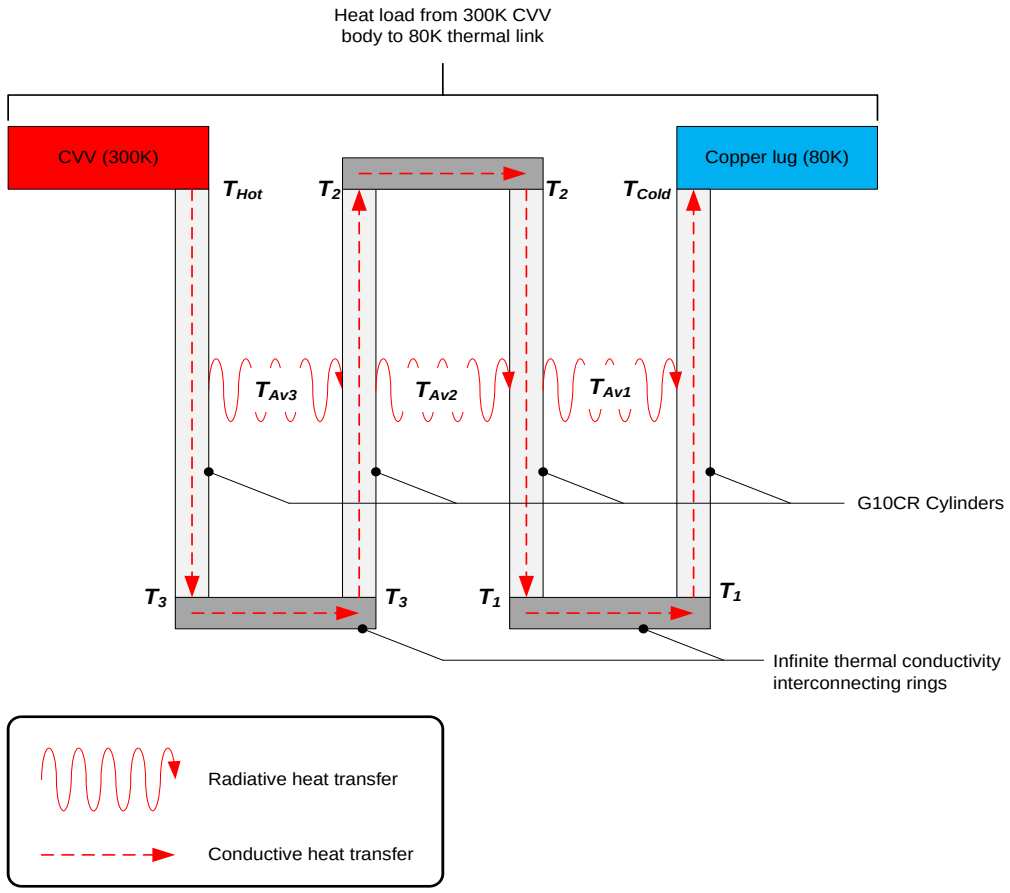

Figure 111: Treatment of the heatflow problem from the 300K CVV body to the 80K thermal link (shown for 4 cylinders). Shows how conductive and radiative processes are accounted for. The interconnecting rings are assumed infinitely thermally conducting so that there is no temperature drop between the two connected ends of any two cylinders.

The model assumes that the presence of the titanium rings, and the interfaces between the G10CR cylinders and the titanium rings have negligible effect on the heat flow. The outermost cylinder therefore is assumed to have a temperature of 300K at the end that interfaces to the CVV body, and the innermost cylinder is assumed to have a temperature of 80K at the end that interfaces to the innermost titanium ring that holds the Copper lug. The temperatures of the intermediate cylinders are assumed to be the same at the ends where two cylinders are connected by a titanium ring.

6.6.4 CONDUCTIVE HEAT TRANSFER

The treatment of the conductive contribution to the heat load is of a thermal path, with the amount of conducted heat governed by the temperatures of the ends of the cylinders, the length and cross sectional area of each cylinder, and the thermal conductivity of the G10 in the range between the end temperatures of each cylinder. For the i^{th} cylinder, the conductive heat load is given by:

$$Q_{c(i)} = \frac{A_i}{L_i} \int_{T_{L_i}}^{T_{U_i}} k_{G10CR}(T)dT \tag{69}$$

Where A_i is the cross sectional area of the cylinder, L_i is the length of the cylinder, T_{U_i} and T_{L_i} are the upper and lower temperatures at each end of the cylinder (respectively) and $k_{G10CR}(T)$ is the thermal conductivity of G10CR (the cylinder material).

6.6.5 RADIATIVE HEAT TRANSFER

The radiative contribution to the heat load involves further simplifications, as each cylinder is treated as emitting radiation at a single temperature along its entire length. This temperature is simply the average of the temperatures of the cylinder ends, T_{Av_i}:

$$T_{Av_i} = \sqrt{\frac{(T_{U_i} + T_{L_i})}{2}} \tag{70}$$

It is recognised that averaging in this way may underestimate the radiated heat if there is a large temperature gradient across a cylinder, since radiated heat is proportional to the fourth power of temperature. However, initially the average was taken to be the fourth root of the average of the temperature to the fourth power between the two ends of the cylinder, $T^*_{Av_i}$:

$$T^*_{Av_i} = \sqrt[4]{\frac{\left(T^4_{U_i} + T^4_{L_i}\right)}{2}} \quad (71)$$

Using $T^*_{Av_i}$ always resulted in lower total heat load onto the TLA in comparison to using T_{Av_i}. Hence, in order to allow for contingency, the 'worst case' method was selected.

The radiated heat flux between any two cylinders is treated in the exact same way as the radiated heat flux between any two thermal enclosures within the CVV in the thermal analysis described in 6.4.7.3. The situation for radiative heat exchange between any two cylinders is treated according to Figure 112:

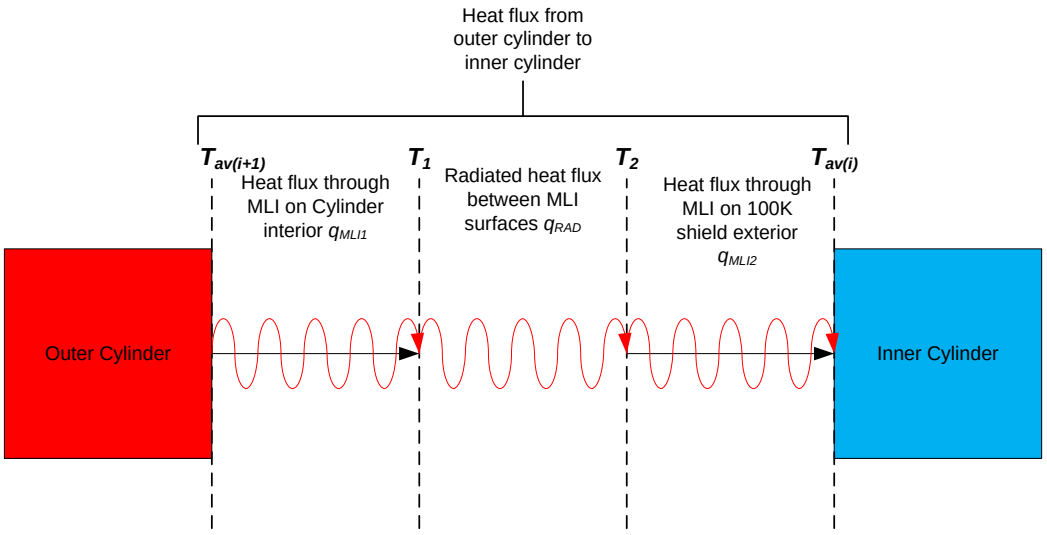

Figure 112: Treatment of radiative heat flow between the i^{th} and $(i+1)^{th}$ cylinders.

Hence, the radiated heat flux onto the i^{th} cylinder, $Q_{r(i)}$, from the $(i+1)^{th}$ cylinder is found by the convergent solution where:

$$Q_{r(i)} \equiv q_{MLI1} = q_{RAD} = q_{MLI2} \quad (72)$$

And the individual heat fluxes are defined in Figure 112. These heat fluxes are found using [97]:

$$q_{MLI1} = \left(a\frac{(T_{Hot}+T_1)}{2}+b\right)(T_{Hot}+T_1)+\varepsilon_{MLI}\sigma(T_{Hot}^4-T_1^4)\frac{\rho_{MLI}}{n_{MLI1}}$$

$$q_{RAD} = \sigma\varepsilon(T_1^4-T_2^4) \text{ (For CVV body – 100K stage)} \quad (73)$$

$$q_{MLI2} = \left(a\frac{(T_2+T_{Cold})}{2}+b\right)(T_2+T_{Cold})+\varepsilon_{MLI}\sigma(T_2^4-T_{Cold}^4)\frac{\rho_{MLI}}{n_{MLI2}}$$

The radiation heat flux is determined iteratively by varying T_1 and T_2 for a given set of hot and cold boundary temperatures.

6.6.6 Total Heat Through Each Cylinder

The total heat flowing into any given cylinder is the sum of the conducted and radiated heat loads onto it:

$$Q_{(i)} = Q_{c(i)} + Q_{r(i)} \quad (74)$$

The total heat flowing out of any cylinder is the sum of the conducted and radiated heat leaving the cylinder. In the steady-state, the total heat flowing into and out of each cylinder should be equal.

Firstly, the conducted and radiated heat from the outer to the inner cylinder is calculated. The conducted heat loads are evaluated based on the temperatures of the ends of each cylinder (as per (69) beginning from guess values which are automatically set at intermediate temperatures equally spaced between the boundary temperatures. The radiated heat is calculated at each iterative stage based on the average temperature of each cylinder, as previously described in 6.6.5. The intermediate cylinder end temperatures are then adjusted until a convergent solution for the heat flowing through the feedthrough assembly is found, by which the total steady-state heat energy entering and leaving each cylinder is equal. The solution condition is given by:

$$Q_{(i)} = Q_{(i+1)} = Q_{n_c} \tag{75}$$

Once the solution is found, the output is the solution value (the heatload onto the 80K thermal link, in mW), the breakdown into radiated and conducted heat at each cylinder and the temperature profile of the complete feedthrough mechanism, i.e. the temperatures at the ends of each cylinder.

6.6.7 RESULTS OF THERMAL MODELLING INVESTIGATION

The model described previously has been used to simulate differing configurations of the feedthrough assembly, in order to determine the effects of several geometric properties on the heat load such that an optimal configuration may be determined.

The variables tested are the number of cylinders n_c, the cylinder length/height h_c and the feedthrough outer diameter r_{outer}. The cylinder wall thickness t_c must be kept as small as possible based on thermal considerations, yet must be thick enough to be mechanically strong enough to support the thermal link, especially during the launch phase. At present, all analyses have assumed that a 2mm wall thickness would be adequate.

In all analyses, the inner radius r_{inner} has been kept at a constant value of $r_{inner} = 1$cm, and the overlap with the CVV $d_O$has been held constant at $d_O = 0.5$cm (its value does not have any significance other than to determine the radial position of the outer thermal boundary with respect to r_{outer}, so could be set to any geometrically suitable value), so that varying r_{outer} gives the dependence on the radius of the outer thermal boundary radial position.

6.6.7.1 NUMBER OF CYLINDERS

The feedthrough assembly has been assumed to have the geometrically suitable properties presented in Table 42.

Feedthrough size		Cylinder properties				MLI	heat load to TLA
Inner radius [cm]	Outer radius [cm]	Number	height [cm]	thickness [mm]	gap [cm]	gap [cm]	[mW]
1.00	6.50	2	4.00	2.00	4.80	4.13	**6.31**
1.00	6.50	4	4.00	2.00	1.47	0.80	**4.77**
1.00	6.50	6	4.00	2.00	0.80	0.13	**3.61**

Table 42: Feedthrough properties during variation of number of cylinders

The table above shows how adding in more cylinders changes the heat load onto the TLA and the sizes of the gaps between the MLI blankets on any two opposing cylinders when everything else remains constant. Figure 113 shows the variation of total heat load with number of cylinders.

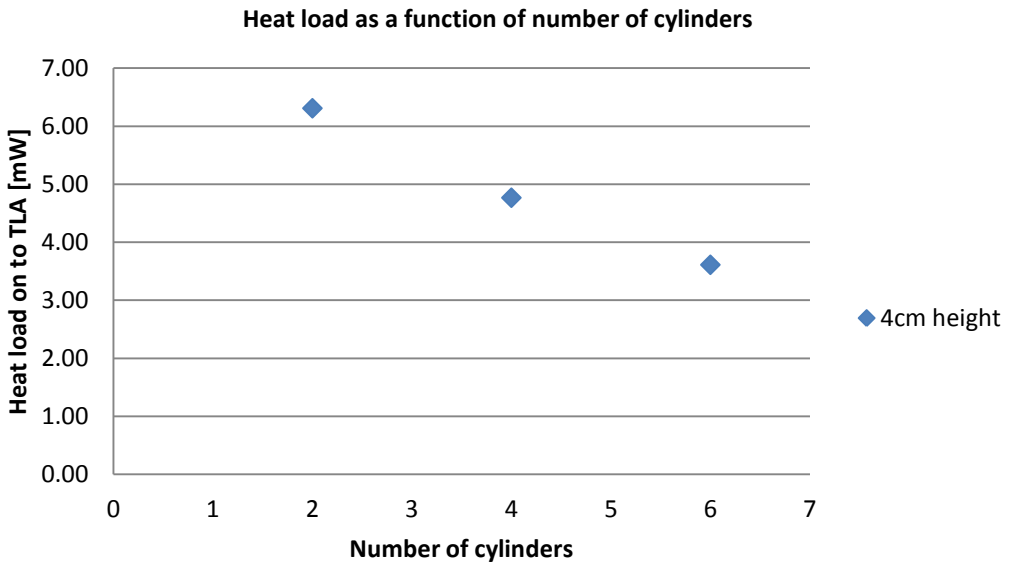

Figure 113: Heat load as a function of number of cylinders for a cylinder height of 4cm. All other variable properties are held constant, as in Table 42.

As expected, the longer thermal path length introduced by adding in more cylinders reduces the heat load onto the TLA in linear proportionality. However, for a feedthough assembly with the geometric properties listed in Table 42, the MLI-MLI gap on opposing cylinders is only 0.13cm with 6 cylinders. This gap is too small, as if the MLI becomes loose it could provide a thermal short circuit between the cylinders. It is possible to make the feedthrough assembly larger in diameter, but this would serve to increase the

heat load as larger cylinders radiate more heat and the cross sectional area of each cylinder would increase, thus increasing conducted heat.

6.6.7.2 CYLINDER HEIGHT

The cylinder height has been varied, assuming the same geometric properties as in the previous analysis, for a case of 4 cylinders. The geometric properties are detailed in Table 43.

Feedthrough size		Cylinder properties				MLI	heat load to TLA
Inner radius [cm]	Outer radius [cm]	Number	height [cm]	thickness [mm]	gap [cm]	gap [cm]	[mW]
1.00	6.50	4.00	1.00	2.00	1.47	0.80	**8.35**
1.00	6.50	4.00	2.00	2.00	1.47	0.80	**5.16**
1.00	6.50	4.00	4.00	2.00	1.47	0.80	**4.77**
1.00	6.50	4.00	6.00	2.00	1.47	0.80	**5.38**
1.00	6.50	4.00	8.00	2.00	1.47	0.80	**6.32**

Table 43: Feedthrough properties during variation of cylinder height.

The variation of heat load with cylinder height for a feedthrough assembly with the geometric properties as listed above is plotted in Figure 114.

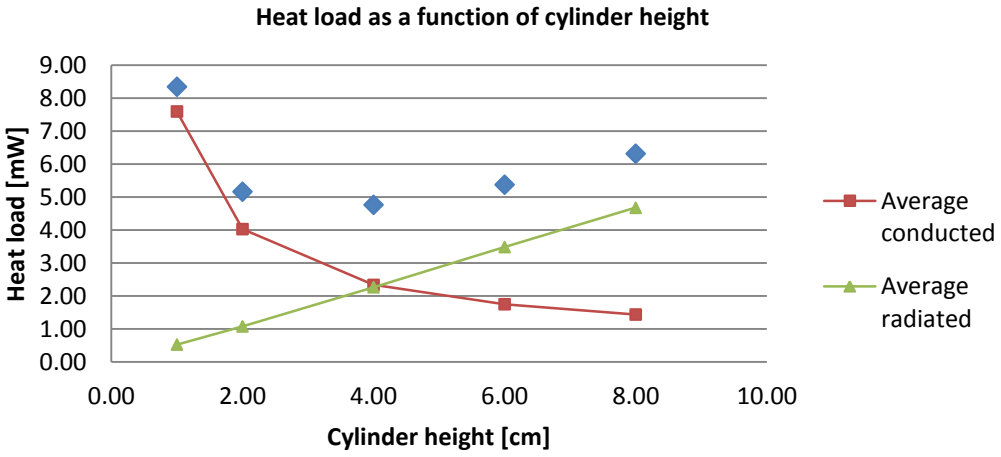

Figure 114: Variation of heatload on TLA with cylinder height for 4 cylinder case

As the height is low (2cm), the heat load is high. The heat load decreases with increasing cylinder height as a longer thermal path is present. This trend breaks around a cylinder

height of 4cm, and the heat load begins to increase with increasing cylinder height. This is because as the cylinder height increases, not only does the thermal path length increase thus reducing conduction, but the surface area of each cylinder wall increases which serves to increase radiation. This indicates for a given feedthrough assembly geometry and configuration, there will be an optimal cylinder height that exists at the turning point when the height is large enough to allow the increase in radiation to dominate over the decrease in conduction.

6.6.7.3 FEEDTHROUGH OUTER RADIUS

The outer radius of the feedthrough has been varied, for a 4 cylinder configuration with heights of 4cm. The properties of the feedthrough are detailed in Table 44.

Feedthrough size		Cylinder properties				MLI	heat load to TLA
Inner radius [cm]	Outer radius [cm]	Number	height [cm]	thickness [mm]	gap [cm]	gap [cm]	[mW]
1.00	5.50	4	4.00	2.00	1.13	0.47	**4.34**
1.00	6.00	4	4.00	2.00	1.30	0.63	**4.56**
1.00	6.50	4	4.00	2.00	1.47	0.80	**4.77**

Table 44: Feedthrough properties during variation of feedthrough outer radius.

The outer radius has been varied for 3 geometrically practical values, where practicality has been determined concerning the MLI-MLI gap between opposing cylinders and maintaining a physically ‘small’ footprint with respect to the diameter of the CVV. The variation of heat load with feedthrough size is plotted in Figure 115.

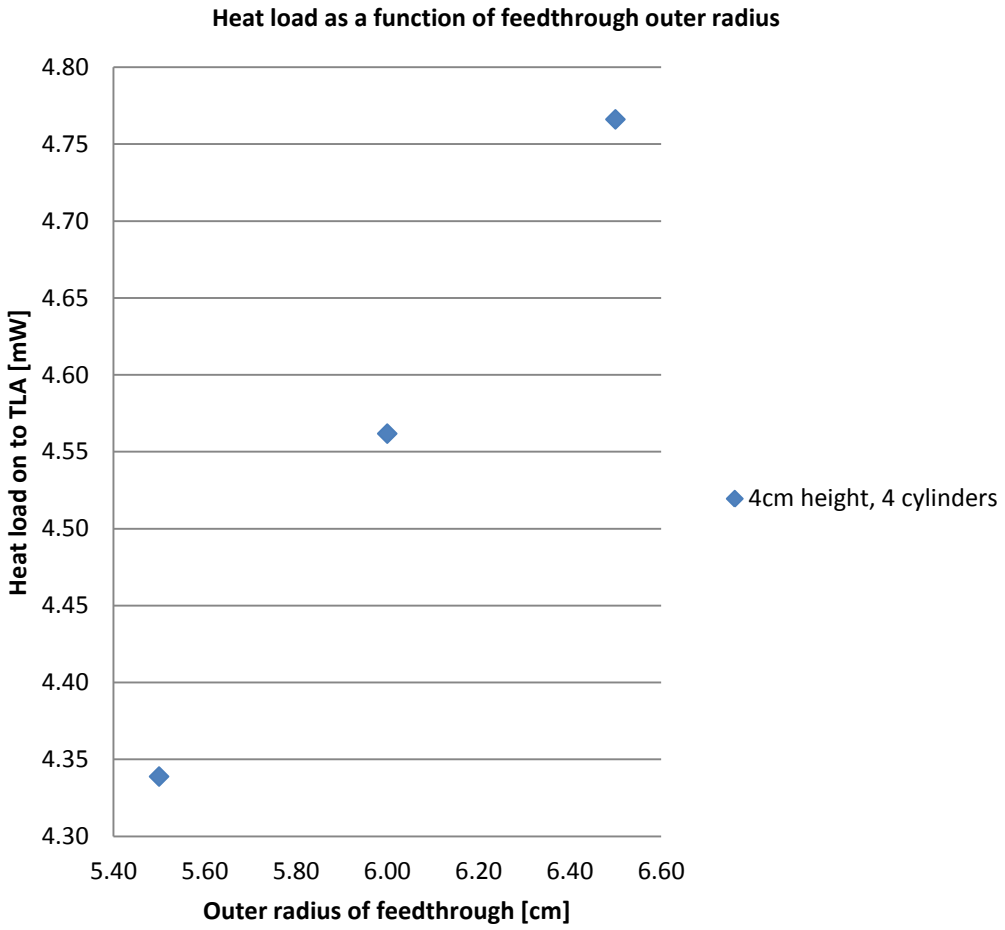

Figure 115: Variation of heat load on to TLA with feedthrough size (outer radius) for a 4 cylinder of height 4cm configuration.

As expected, a linear dependence is observed as outer radius has a strong effect on the heat load due to the larger cross sectional area associated with larger diameter cylinders as well as the increase in radiation due to increasing cylinder wall surface area. The outer radius must be kept as small as possible whilst maintaining sufficient distance between the MLI blankets on opposing cylinder walls in order to minimise the heat load onto the TLA.

6.6.8 DESIGN IMPLICATIONS

The heat loads have been calculated for several geometrically practical configurations of the feedthrough assembly, and it has been shown that in order to minimise the heat load onto the 80K TLA, the following design measures must be taken:

- The number of cylinders must be maximised for a given feedthrough size (outer radius) and tube thickness.
- The height of the cylinders must be set to an optimal value, whereby the heat load onto the TLA (for a given number of cylinders of a set wall thickness accommodated within a given feedthrough radius) is minimised with respect to the conducted heat (which decreases with height) and the radiated heat (which increases with height).
- The outer radius should be as small as is practically possible concerning the number of cylinders, the cylinder thickness and the gap between the MLI blankets on opposing cylinder walls.

There will be an optimal configuration trading off between adding more cylinders and minimising the overall feedthrough size (outer radius) whilst maintaining a sufficient gap between MLI blankets on opposing cylinder walls. This trade-off is shown below, where the outer radius has been increased from the geometrically practical minimum value for an inner radius of 1cm and the lowest possible number of cylinders, 2, assuming a minimal allowable gap of ~0.5cm between the MLI blankets on opposing cylinder walls. At each increase of the outer radius, the increment of increase is the minimal increase required to support an extra 2 cylinders. A constant cylinder height of 4cm has been maintained.

The feedthrough properties are detailed in Table 45.

Feedthrough size			Cylinder properties			MLI	heat load to TLA
Inner radius [cm]	Outer radius [cm]	Number	height [cm]	thickness [mm]	gap [cm]	gap [cm]	[mW]
1.00	2.90	2	4.00	2.00	1.20	0.53	5.12
1.00	5.60	4	4.00	2.00	1.17	0.50	4.43
1.00	8.40	6	4.00	2.00	1.18	0.51	4.26

Table 45: Feedthrough properties whilst varying number of cylinders and minimising outer radius whilst keeping an MLI-MLI gap of ~0.5cm.

The cylinder number has only been taken up to 6, because beyond this value the outer radius gets too large (>8.4cm) and results in a feedthrough assembly that takes up too much volume in the CVV. Additionally, the results as plotted in Figure 116 show that there is little decrease in heat load for larger radius (more complicated, higher number of cylinder) feedthrough assemblies.

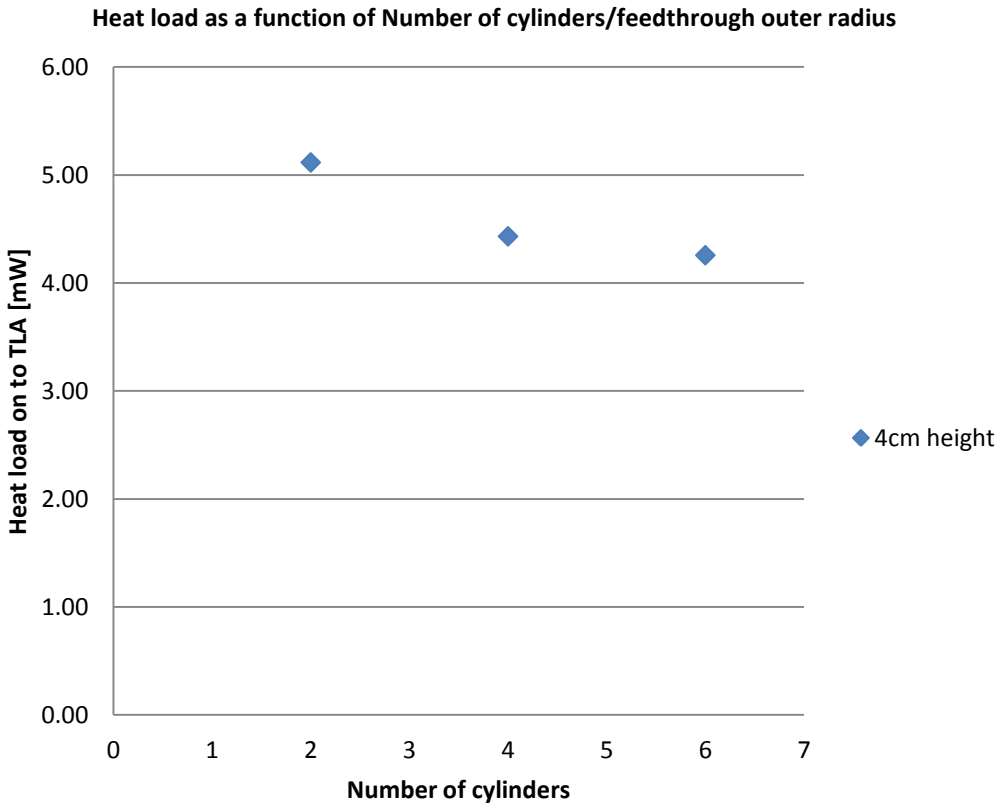

Figure 116: Heat load as number of cylinders is increased whilst maintaining a minimal outer radius and an MLI-MLI gap of ~0.5cm.

This analysis shows the optimal number of cylinders, maintaining practical considerations, is 4, with a minimal outer radius of 5.6cm (with an overlap of 0.5cm) for an MLI-MLI gap of 0.5cm. The cylinder height may be optimised for this design by considering the variation of heat load with cylinder height:

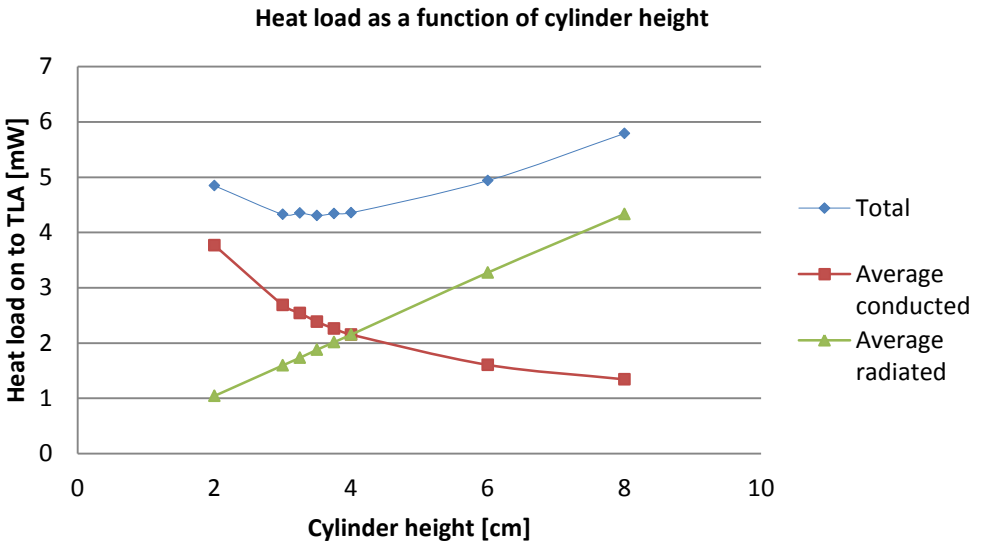

Figure 117: Variation of heat load with cylinder height for a 4 cylinder, 0.56mm outer radius feedthrough assembly.

Figure 117 clearly shows an optimal cylinder height of around 3.5cm.

6.6.9 Optimal Design

The results presented previously show that using this model and feedthrough assembly design, the best configuration for minimal heat load on the 80K thermal link would be as detailed in Table 46:

Footprint properties		
Inner radius	1	cm
Outer radius	5.6	cm
Mounting overlap	0.5	cm

Cylinder properties		
Number of cylinders	4	
Cylinder height	3.5	cm
cyclinder thickness	2	mm
Inter-cylinder Gap	1.1666667	cm
MLI thickness	0.6666667	cm
MLI-MLI gap	0.5	cm

Table 46: Geometric and cylinder properties of best configuration for feedthrough assembly.

Of course, the difference between the outer radius and the mounting overlap (d_O) is the optimised radial position of the hot temperature boundary; the same thermal performance could be achieved with a larger outer radius and correspondingly larger d_O.

With this design, the model predicts a heat load of 4.31mW onto the thermal link. The temperature profile across the cylinders is shown in Figure 118, and the heat transfer breakdown for each cylinder in Figure 119. Full details of the temperature profile and heat load breakdown are summarised in Table 47.

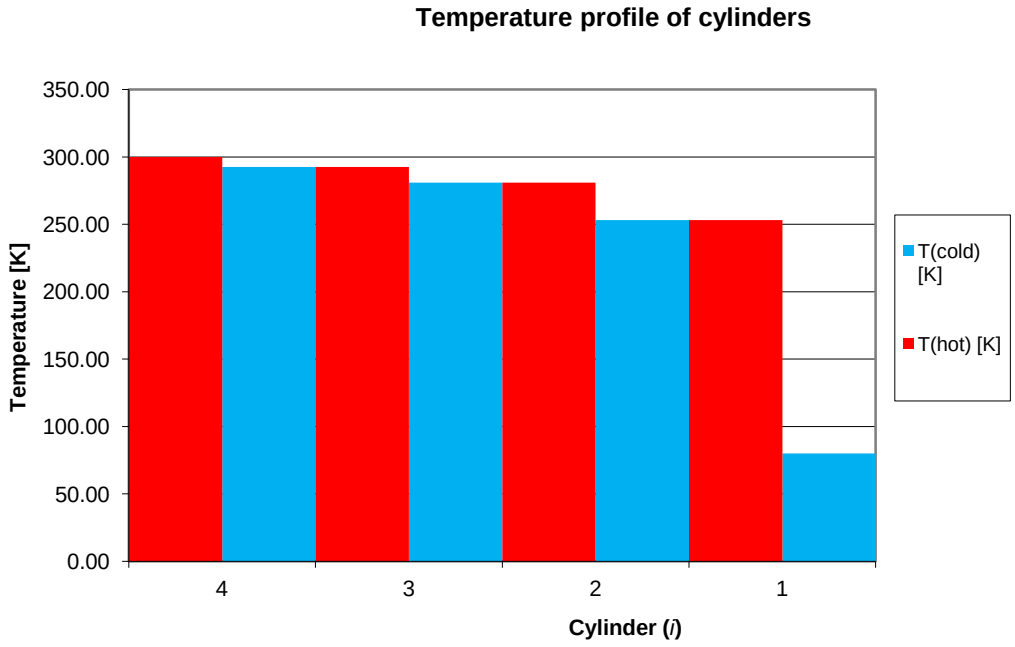

Figure 118: Temperature profile across feedthrough assembly (cylinders). Red columns show the warm end temperatures of each cylinder (i) and blue shows the cold end temperatures. Indexing begins at the 80K end.

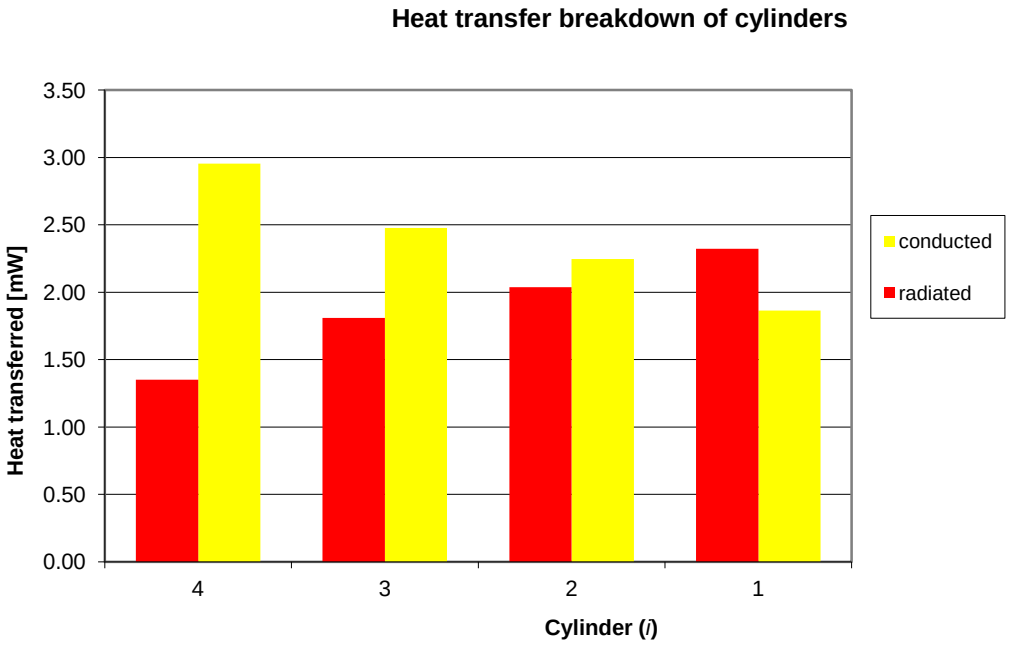

Figure 119: Heat transfer breakdown by cylinder

Cylinder	Radius [cm]	A [cm^2]	L [cm]	T(hot) [K]	T(cold) [K]	Q [mW]	Conducted [mW]	Radiated [mW]
1	1.00	6.28×10^{-3}	3.5	253.00	80.00	4.18	1.86	2.32
2	2.37	3.52×10^{-2}	3.5	280.80	253.00	4.28	2.25	2.04
3	3.73	8.76×10^{-2}	3.5	292.60	280.80	4.28	2.48	1.81
4	5.10	1.63×10^{-1}	3.5	300.00	292.60	4.31	2.95	1.35

Table 47: Table showing cylinder geometric properties, temperature distributions and breakdown of heat flow into radiated and conducted contributions.

The temperature profile clearly shows that the cylinders near the cold end have a greater thermal gradient. This is because of the lower thermal conductivity in the lower end of the temperature range. The heat load breakdown shows a clear trend of increasing radiation and decreasing conduction for cylinders positioned radially closer to the central 80K Copper lug. This is again because of the decreasing thermal conductivity at the lower end of the temperature range limiting the heat conduction.

The assumption of modelling each cylinder as an isothermal average of its temperature extremes for radiative calculations would be reasonable for cylinders 2, 3, and 4,

however may not be ideal for cylinder 1. However, the radiation model assumes all radiation absorbed by cylinder 1 goes to the 80K stage, and its radiation emissions are not relevant, thus the assumption based on the isothermal average is reasonable.

It may be noticed from the heat loads presented in Table 47 that they are not exactly equal as per the solution condition. The reason for this is the model may not be able to find exact solutions, and in order to generate results in a reasonable time scale the tolerance has been set to 0.1mW difference between cylinders.

This optimal design is geometrically and thermally suitable for the implementation on the CVV, however, a detailed strength and stress analysis should be undertaken for the next stage of development.

6.8 COOLING CHAIN THERMAL ANALYSIS

6.8.1 OVERVIEW

The thermal analysis of the cryogenic cooling chain was performed using a simple heat flow model, taking into account all thermal loads and available cooling power at each temperature stage. For each temperature stage, the incident thermal loads are calculated. The thermal loads are a combination of thermal radiation emitted from the outer thermal enclosure (where the effect of MLI is taken into account by an iterative boundary solver, as described in 6.4.7.2), thermal loads conducted through the suspension system (described in 6.5.4) and thermal loads conducted through the harness and through any current leads running between stages (described in 6.4.8). Joule heating effects from any active current leads are also taken into account (described in 6.4.8). Each heat load is calculated and augmented with a contingency margin of typically 30%, or 50 % for cases where heat load calculations are based on less mature designs.

The total heat load on each stage is used to determine the percentage capacity at which the coolers must work to maintain the stage temperature. If the coolers at one temperature stage are working at 100% capacity, all the available cooling power offered by the coolers is being used to maintain the temperature. If the coolers work at above 100% capacity, the cryogenic chain will fail as the temperature cannot be maintained. Typically, each cooler will be working at some fraction of its total cooling capacity. The lower the fraction, the more reliable the cooler's lifetime will be, as it is stressed to a lower degree.

Performance analysis of the cooling chain was modelled for 4 cases; Recycling or cooling 50mK cooler for the case of running in warm or cold redundancy mode. The cooling budget and heat flow maps for each case are presented subsequently.

6.8.2 dADR HOLDING

Nominal cooling chain operation occurs during the phase where the dADR is holding at 50mK, cooling the detectors and allowing for XMS observations to be performed. Cooling chain performance has been analysed for both warm redundancy and cold redundancy cases.

6.8.2.1 WARM REDUNDANCY MODE

Warm redundancy mode provides cooling using all available coolers, i.e. 2 active JT coolers and 3 active 10K Stirling coolers. Table 48 details the cooling budget for when the dADR is cooling at 50mK and the cooling chain is operating in warm redundancy.

CASE:	(8) Holding, 15K warm, JT warm			POWER INC MARGIN		431 W								
		Required heat lift,	Required heat lift,	Available heat lift, per cooler		T. link conductance	# operational	Temp drop [K]	Cooler temp [K]	Est heat lift req, per		Duty, per cooler %	Electrical input, per cooler [W]	Total heat heat lift
Stage	Temp [K]	no sys	inc. sys	µW	mW	µW					Notes			
TFPA	0.05	1.60E-03	1.60E-03	1.60		1	0.1	1	1.60E-05	0.050	1.60E-03	Set by ESA for 0.3K mid-stage			
T3	2	7.0	9.2		30.0		0.5	2	0.02	1.98	4.6	30 mW maximum continuous heat-lift	15%	46	60
T4	16	330	429		578.9		0.6	3	0.24	15.76	143	Updated from TNO-MAX-AST-0007-02	25%	55	1737
T5	80	974	1266		1460.00		0.52	1	2.43	77.57	1266		87%		1460
T6	102	1080	1404		2096.5		0.8	3	0.58	101.42	468	Updated from TNO-MAX-AST-0007-02	22%	55	6290
T7	280														

Table 48: Cooling budget for dADR holding with cooling chain operating in warm redundancy mode

The heat flow along the cooling chain is shown in Figure 120.

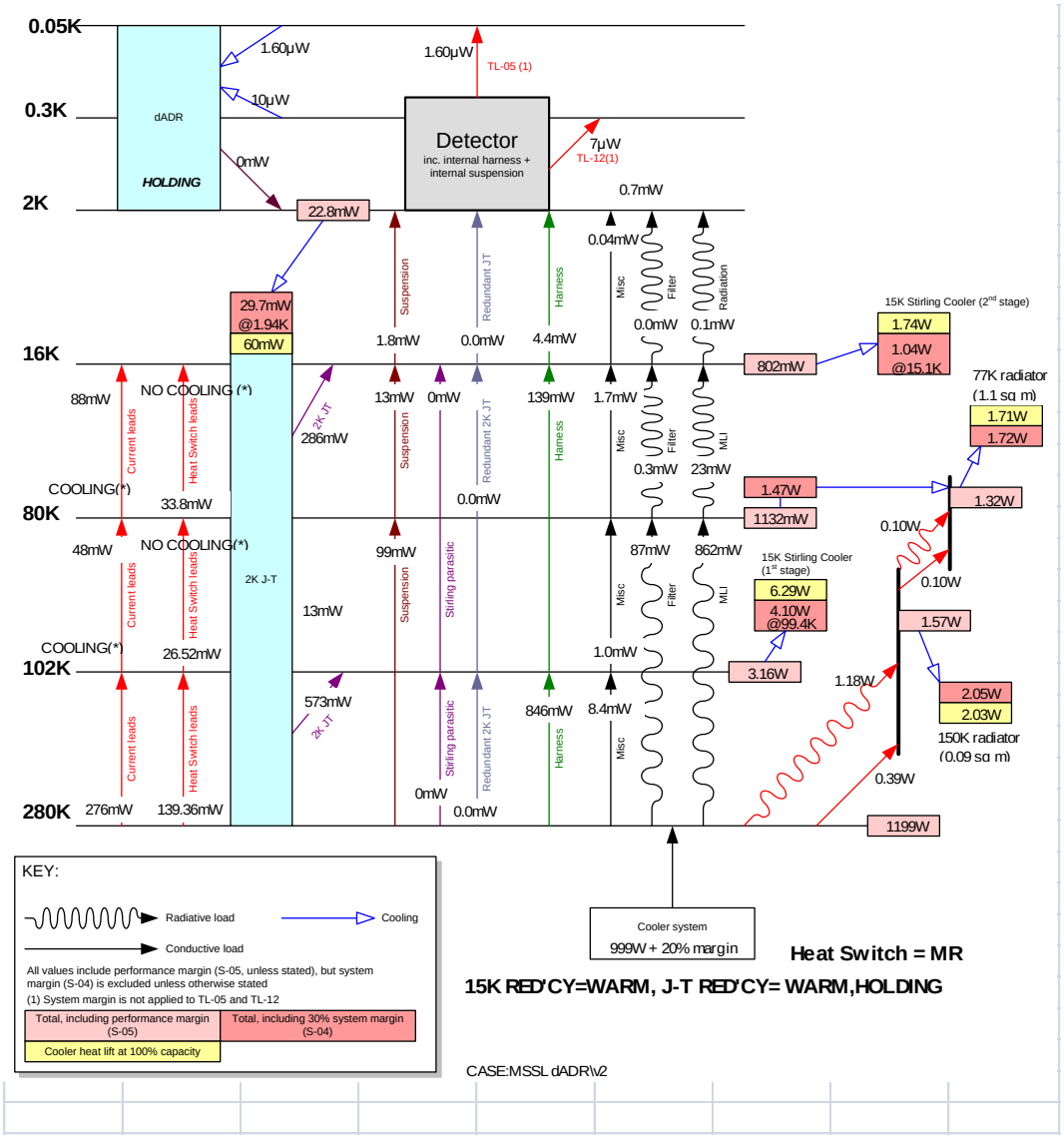

Figure 120: Heat flow through cooling chain when dADR is holding and cooling chain is operating in warm redundancy mode

6.8.2.2 Cold Redundancy Mode

Cold redundancy mode marks the case where 1 JT cooler and 1 10K Stirling cooler has failed, or are dormant awaiting activation upon failure of a working cooler. The cooling budget for when the dADR is cooling at 50mK and the cooling chain is operating in cold redundancy is given in Table 49.

CASE:	(2) Holding, 15K cold, JT cold			POWER INC MARGIN			790 W								
Stage	, 15K war	Required heat lift, no sys	Required heat lift, inc. sys		Available heat lift, per cooler		T. link conducta nce	# operatio nal	Temp drop [K]	Cooler temp [K]	Est heat lift req, per	Notes	Duty, per cooler %	Electrical input, per cooler [W]	Total heat heat lift
				µW	mW	µW									
TFPA	0.05	1.60E-03	1.60E-03	1.60		1	0.1	1	1.60E-05	0.050	1.60E-03	Set by ESA for 0.3K mid-stage			
T3	2	9.8	12.8		30.0		0.5	1	0.03	1.97	12.8	30 mW maximum continuous heat-lift	43%	130	30
T4	16	614	798		578.9		0.6	2	0.66	15.34	399	Updated from TNO-MAX-AST-0007-02	69%	176	1158
T5	80	974	1266		1460.00		0.52	1	2.43	77.57	1266		87%		1460
T6	102	2548	3312		2096.5		0.8	2	2.07	99.93	1656	Updated from TNO-MAX-AST-0007-02	79%	176	4193
T7	280														

Table 49: Cooling budget for dADR holding with cooling chain operating in cold redundancy mode (i.e. 1 JT failure, 1 Stirling failure)

The heat flow along the cooling chain is shown in Figure 121.

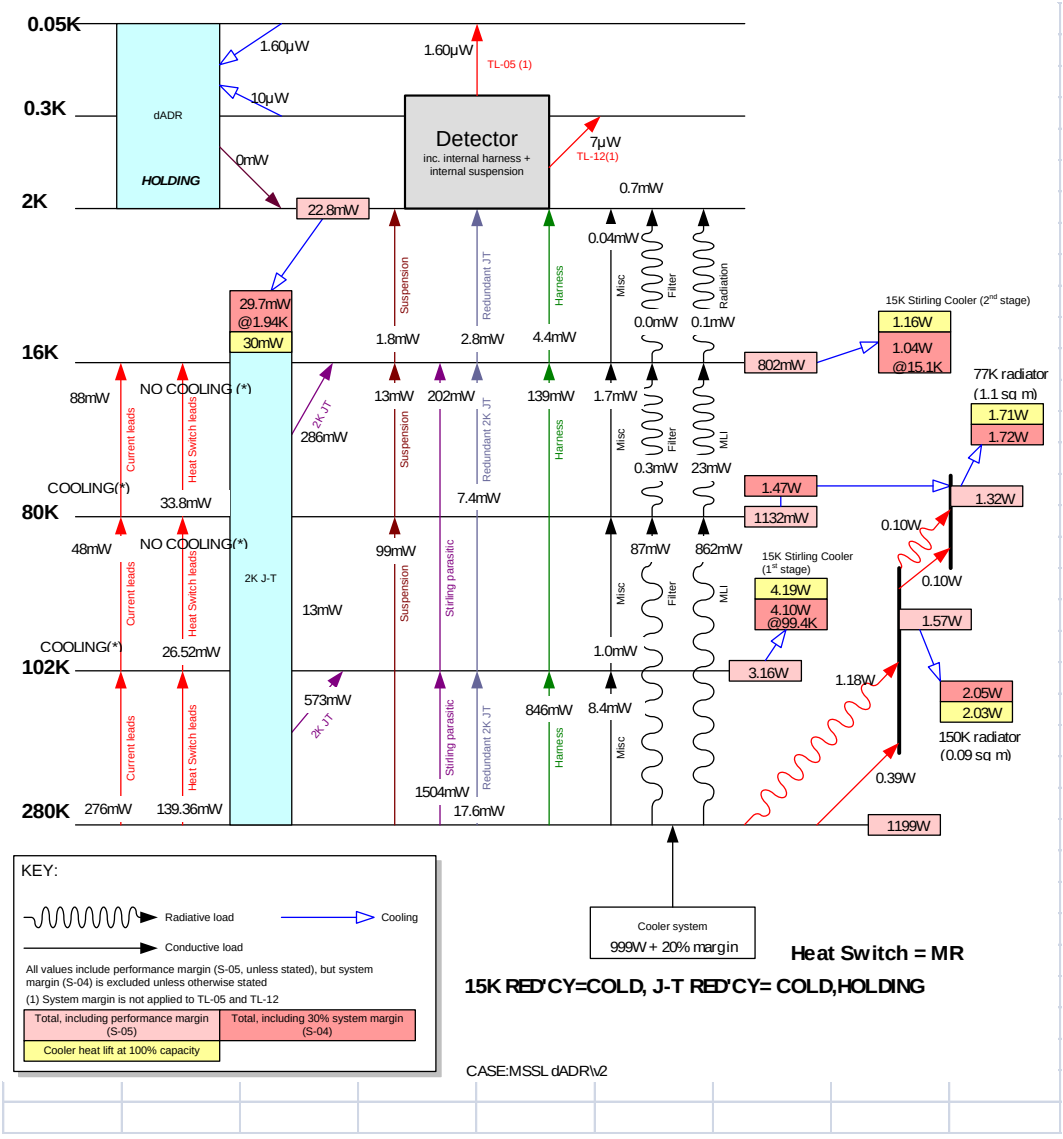

Figure 121: Heat flow map of cooling chain when dADR is holding and cooling chain is operating in cold redundancy mode

6.8.3 dADR Recycling

Whilst the dADR is recycling, heat is produced during the magnetisation of the salt pills. Hence, this heat must be extracted at the 2K heat bath, provided by the JT coolers. The cooling chain must work harder to absorb this additional heat as well as to provide the nominal cooling required during holding mode.

6.8.3.1 Warm Redundancy Mode

Warm redundancy mode provides cooling using all available coolers, i.e. 2 active JT coolers and 3 active 10K Stirling coolers. The cooling budget for the case of the dADR recycling with the cooling chain operating in warm redundancy is given in Table 50.

CASE:	(7) Recycling, 15K warm, JT warm			POWER INC MARGIN			793 W							
Stage	Temp [K]	Required heat lift, no sys	Required heat lift, inc. sys	Available heat lift, per cooler µW	Available heat lift, per cooler mW	Available heat lift, per cooler µW	T. link conductance	# operational	Temp drop [K]	Cooler temp [K]	Est heat lift req, per	Notes	Duty, per cooler %	Electrical input, per cooler [W]	Total heat heat lift
TFPA	0.05	1.60E-03	1.60E-03	1.60		1	0.1	1	1.60E-05	0.050	1.60E-03	Set by ESA for 0.3K mid-stage			
T3	2	20.0	26.1		30.0		0.5	2	0.05	1.95	13.0	30 mW maximum continuous heat-lift	43%	132	60
T4	16	439	571		578.9		0.6	3	0.32	15.68	190	Updated from TNO-MAX-AST-0007-02	33%	73	1737
T5	80	1132	1472		1460.00		0.52	1	2.83	77.17	1472		101%		1460
T6	102	1529	1987		2096.5		0.8	3	0.83	101.17	662	Updated from TNO-MAX-AST-0007-02	32%	73	6290
T7	280														

Table 50: Cooling budget for dADR recycling with cooling chain operating in warm redundancy mode

The heat flow along the cooling chain is shown in Figure 122.

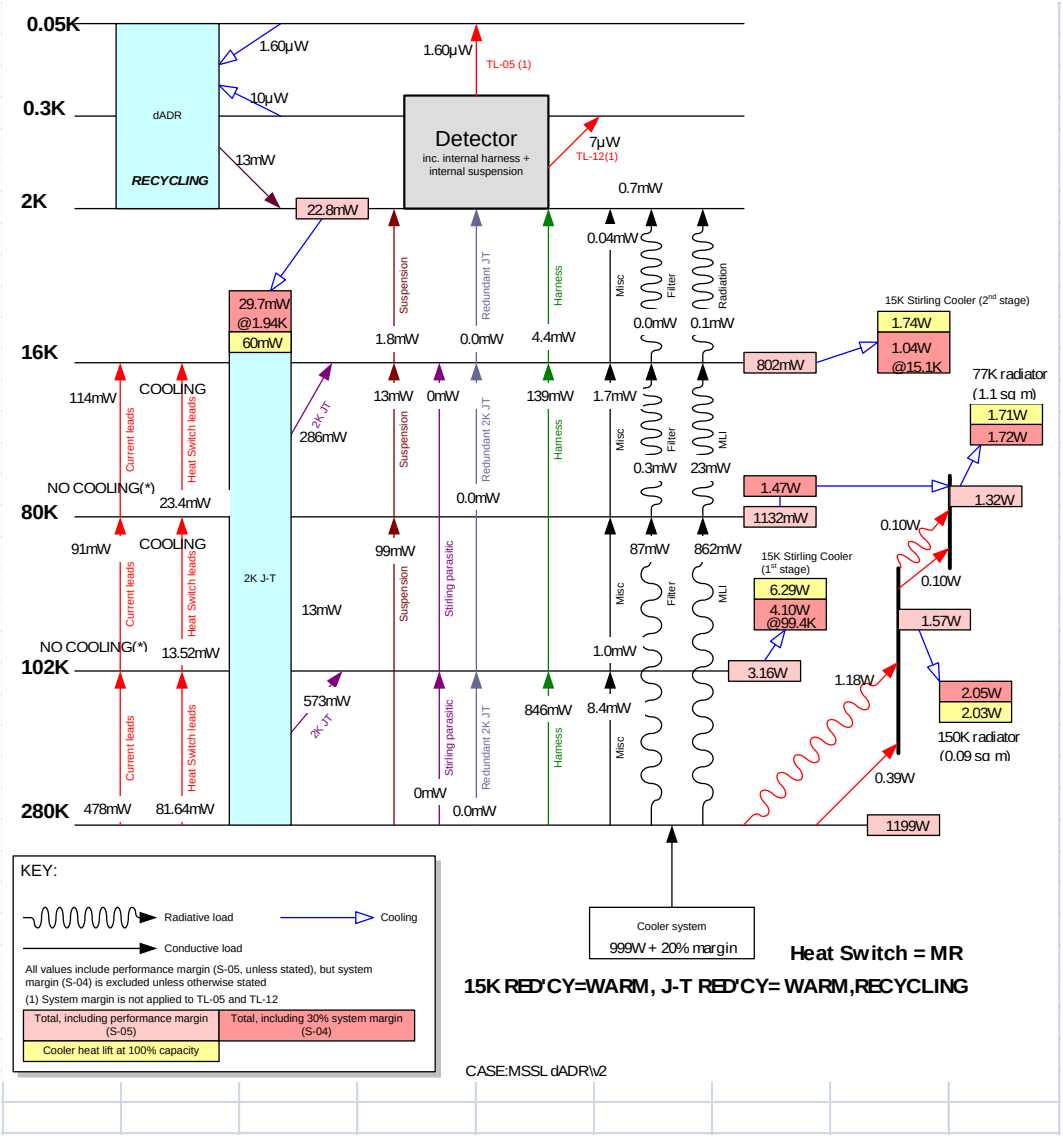

Figure 122: Heat flow map of cooling chain operating in warm redundancy with dADR recycling

6.8.3.2 COLD REDUNDANCY MODE

Cold redundancy mode marks the case where 1 JT cooler and 1 10K Stirling cooler has failed, or are dormant awaiting activation upon failure of a working cooler. The cooling budget for a recycling dADR and the cooling chain operating in cold redundancy is given in Table 51.

CASE:	(1) Recycling, 15K cold, JT cold			POWER INC MARGIN		1199 W								
Stage	Temp [K]	Required heat lift, no sys	Required heat lift, inc. sys	Available heat lift, per cooler µW	Available heat lift, per cooler mW	Available heat lift, per cooler µW	T. link conductance	# operational	Temp drop [K]	Cooler temp [K]	Est heat lift req, per	Notes	Duty, per cooler %	Electrical input, per cooler [W]	Total heat heat lift
TFPA	0.05	1.60E-03	1.60E-03	1.60		1	0.1	1	1.60E-05	0.050	1.60E-03	Set by ESA for 0.3K mid-stage			
T3	2	22.8	29.7		30.0		0.5	1	0.06	1.94	29.7	30 mW maximum continuous heat-lift	99%	301	30
T4	16	802	1043		578.9		0.6	2	0.87	15.13	521	Updated from TNO-MAX-AST-0007-02	90%	218	1158
T5	80	1132	1472		1460.00		0.52	1	2.83	77.17	1472		101%		1460
T6	102	3156	4102		2096.5		0.8	2	2.56	99.44	2051	Updated from TNO-MAX-AST-0007-02	98%	218	4193
T7	280														

Table 51: Cooling budget for cooling chain operating in cold redundancy with dADR recycling

The heat flow along the cooling chain is shown in Figure 123.

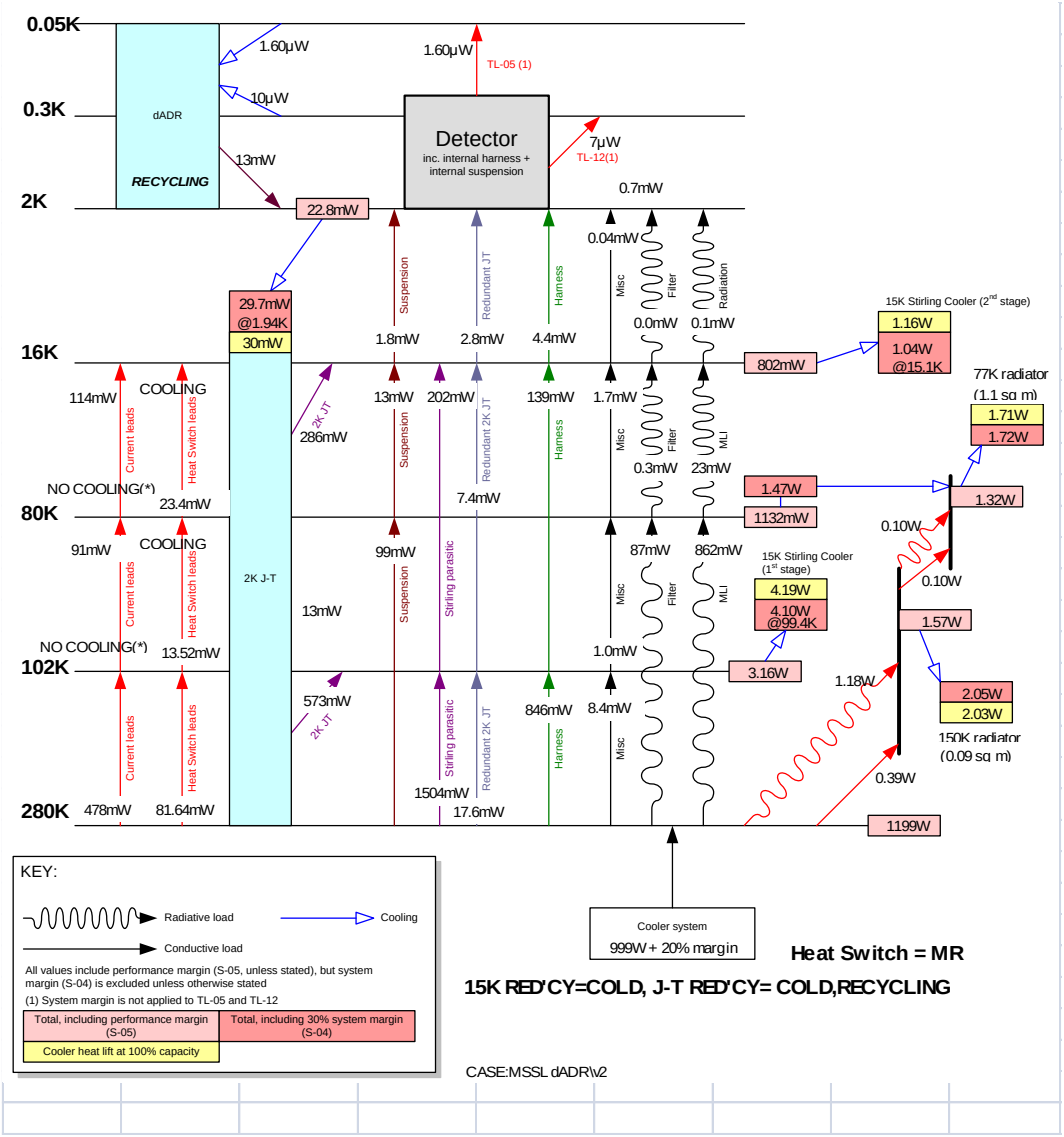

Figure 123: Heat flow map of cooling chain operating in cold redundancy with dADR recycling

6.8.4 SUMMARY

The cooler duty cycle (% of maximum cooling capacity) for each temperature stage for each of the cases presented above is shown in Figure 124.

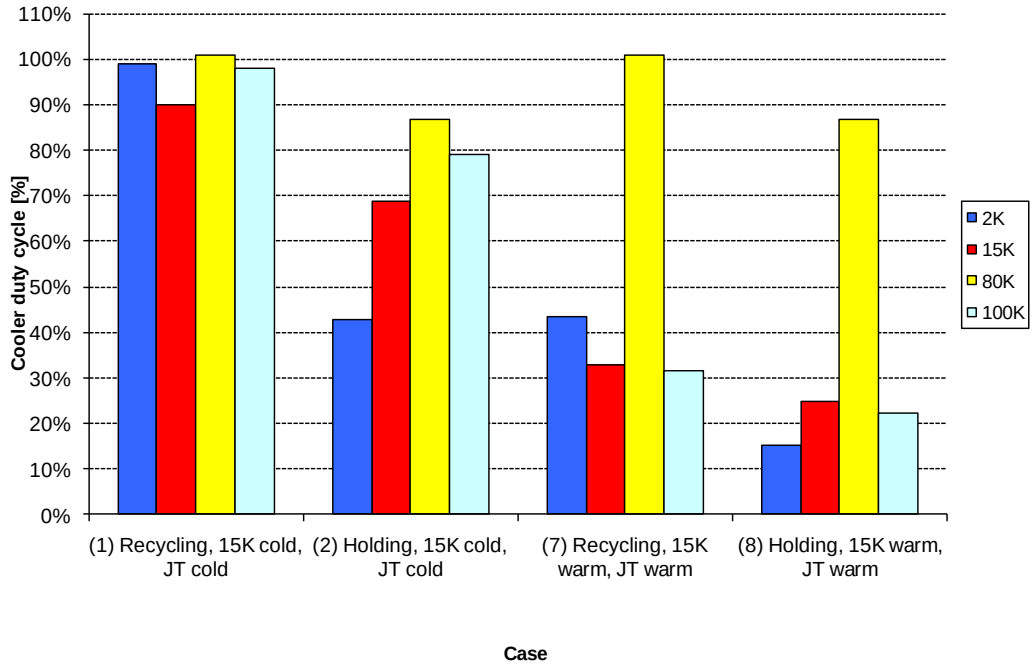

Figure 124: Cooler duty cycle for each operational case presented. Worst possible case is Recycling in cold redundancy

The thermal analyses show that the cooling chain can support the IXO XMS instrument during all required cases. It should be noted that the radiator is shown to operate at 101% capacity during the dADR recycling phase. Clearly, this is not possible; however, all heat loads include a contingency margin, so in reality the radiator will be operating at below 100%.

In the case of a single cooler failure, or equivalently if cold redundancy is implemented, the coolers at each stage have to work much harder to account for the deficit in cooling power at the 2K and 16K stages and to lift the extra parasitic heat conducted by the

inactive coolers. The worst case performance occurs in cold redundancy mode during recycling of the dADR, where each cooler is working close to 100% capacity. Though this is maintainable, it results in increased operational stresses on the coolers, thus reduces their lifetime reliability. It is therefore recommended that cold redundancy only be implemented upon a cooler failure.

For warm redundancy cooling chain operation, the coolers clearly work at a lower capacity than in cold redundancy, hence maximising their operational lifetime due to lower operational stresses. The most demanding cooling case occurs during recycling of the dADR, where the increase in cooler duty cycle is apparent at each temperature stage. Even during this most demanding case, in warm redundancy all active cooling stages operate at below 50% capacity. In order to maximise reliability of the cooling chain lifetime, it is therefore recommended that warm redundancy be the nominal operational mode of the cooling chain.

6.9 CHAPTER SUMMARY

The IXO cooling chain has been described in terms of the cooler technology present at each temperature stage. The mechanical and thermal analyses of the cryogenic cooling chain have been described, and used to design a CVV that can support the cooling chain structurally and thermally.

The design of the CVV has been presented in detail, including the details of the suspension systems that support the individual thermal enclosures. The suspension system has been designed from stiffness requirements dictated by the minimum allowed value of the first resonance. The suspension system combines low thermal conductivity tensionable straps supported by a system of low thermally conducting tubes and stiffening rings at the CVV-80K stage and 80K-16K stage. The 16K-2K suspension system consists of straps only. Accommodation volume has been allocated for the JT pipes, harness and stirling cooler displacers within the CVV body. The predicted modes of the suspension system meet the requirement of first mode >40Hz.

The external 80K radiator requires a feedthrough assembly in order to minimise the conducted and radiated heat load from the 300K CVV body. This feedthrough assembly has been designed conceptually using 4 3.5cm long low thermal conductivity G10CR cylinders of wall thickness 2mm. The walls are covered with 5 layers of MLI on each side and the cylinders are interconnected at alternate ends with titanium rings. The feedthrough has an outer radius of 5.6cm, and gives a pre-margin heat load of 4.31mW onto the 80K thermal link.

The thermal performance of the CVV has been analysed for the MSSL dADR operating as the final stage 50mK cooler. Thermal maps have been presented for the recycling and cooling phase of the dADR, for both warm and cold redundancy (the case where 1 JT and 1 Stirling cooler has failed).

The results show that the cooling chain and CVV design can support the dADR requirements for all cases: dADR holding at 50mK and dADR recycling for both warm and cold redundancy cooling chain operation. It is clear that the case of warm redundancy offers significantly lower operational stresses on each cooler due to the lower required duty cycle of each cooler, hence is recommended as the nominal cooling chain operational mode.

Chapter 7:

SUMMARY & FURTHER DEVELOPMENT

This chapter concludes the thesis by briefly summarising the key findings presented in each chapter, and combining them to form a concise, coherent presentation of the progress in milli-Kelvin ADR technology developments for space missions that have been achieved as part of this research work.

Potential further development activities for improving upon the magnetoresistive heat switch research presented in chapter 5 are highlighted, with a focus on improving the understanding of how sample width and crystal purity dictate heat switch performance. In addition, the next stage of development leading towards a space-qualified magnetoresistive heat switch is considered, where further work is required in particular to develop a switch that can survive the vibrations associated with a spacecraft launch.

The IXO cooling chain and CVV design presented in chapter 6 are discussed in terms of potential development towards a working, space qualified, completely cryogen-free cooling chain for future missions. The CVV design and IXO cooling chain configuration will continue development at Astrium, and could be selected by ESA to be the cryogenic solution for the IXO XMS.

7.1 SUMMARY OF THESIS

7.1.1 CHAPTER 1

Chapter 1 began by introducing the field of X-ray astronomy, a comparatively recent yet extremely insightful tool to study high energy astrophysics. High energy accelerations of charged particles and atomic transitions from high energy states were shown to be the processes emitting X-rays in space that form the basis of observable phenomena at the heart of this field. The history of X-ray Astronomy was briefly described, highlighting a few of the key missions and leading up to the International X-ray Observatory (IXO) – The future mission that aims to study [(6), (7)]:

- Black holes and matter under extreme conditions
- Formation and evolution of galaxies, clusters and large scale structure
- Life cycles of matter and energy

An overview of the IXO mission was given, including the instruments constituting its payload. Of these, the X-ray Microcalorimeter Spectrometer (XMS) was emphasised, as it is the cryogenic instrument to which the technology development of this thesis focuses on. The XMS was shown to improve on previous X-ray spectrometers such as Chandra and XMM-Newton in energy resolution and sensitivity, so that the science goals listed above could be studied. The envisaged XMS science goals as detailed in the IXO Assessment Study Report (7) were outlined with some examples of how the XMS will achieve them.

The principles of operation of the XMS as a TES technology based microcalorimeter were described, and the requirement for a 50mK operating temperature was stated to be due to the need for the detector absorber to be cold enough to measurably heat up upon an incident X-ray photon. It was shown that energy resolution of TES detectors such as the

XMS improves with decreasing temperature, smaller heat capacities and larger changes in sensor resistance with temperature at the superconducting transition. This cryogenic technology forms the basis for illustrating the requirement for the production of controllable, stable cryogenic thermal environments in space.

7.1.2 CHAPTER 2

Chapter 2 introduced cryogenics, and more specifically, space cryogenics as the discipline dedicated to producing low temperature environments for space instrumentation. The common method of evaporative cryogen based cooling was discussed, including a description of Helium, the only cryogen capable of cooling to below ~4K. The requirement for longer mission durations and lower temperatures led on to a discussion of cryocoolers, which were explained beginning with the Carnot refrigeration cycle.

Some of the common cryocoolers, and those of interest to the work of this thesis, were described, including Stirling Coolers, Joule Thomson coolers and radiators. It was shown that cooling below ~1K, such as is required by the IXO XMS, requires specialised cryogenic technologies, which include:

- Sorption Coolers
- Dilution Refrigerators
- Magnetic coolers

The principles of operation of sorption and dilution coolers were described, and it is clear they are fairly complex systems. Dilution refrigerators have flown in space, but only open-cycle dilution refrigerators (Planck), since closed cycle refrigerators require gravity to operate, thus require significant engineering development for space use. Open cycle dilution coolers vent their Helium supply to space hence have a short <3 year

lifetime. Sorption coolers have been used on Herschel, however, can only cool to ~300mK. Magnetic coolers known as Adiabatic Demagnetisation Refrigerators (ADRs) were highlighted as a space demonstrated technology (Suzaku) capable of reliably providing the 50mK thermal environment for the IXO XMS.

Chapter two concluded by illustrating typical cryogenic cooling technologies have a temperature range of operation where they can provide limited useful cooling, and that available cooling power decreases with the required cryogenic temperature.

7.1.3 CHAPTER 3

Chapter 3 explored ADRs in more detail, explaining how the magnetocaloric effect that ADRs exploit was initially discovered aswell as the theory behind it. It was shown that a large change in entropy occurs in materials that are paramagenetic down to ~1K when magnetised, due to the electronic magnetic dipoles adopting a lower energy configuration (such that they align with the applied magnetic field) as the splitting of the energy levels increased with the magnetic field.

The operation of an ADR cooling cycle was described, showing how isothermal magnetisation performed by extracting the heat produced during magnetisation to a heat bath was the first step to producing cooling. The subsequent thermal isolation of the ADR from the heat bath and adiabatic demagnetisation was shown to cool the paramagnetic material due to the distribution function of the magnetic ions requiring that the temperature must decrease if the magnetic field decreases in order to maintain the ordering. Thus, cooling is produced as the ADR is demagnetised at a rate sufficient to counteract the heat load at the desired operating temperature. Cooling ceases upon reaching zero magnetic field or the ordering temperature of the paramagnetic refrigerant, at which point the cycle is repeated by magnetising again, during which there is no cooling produced (the recycle time).

The key thermodynamic components of an ADR were described, including the salt pills and the heat switches. The properties and types of paramagnetic material that exhibit a magnetocaloric effect suitable for ADR use were described, and some common refrigerant materials listed. Several common types of heat switch were described; including mechanical, gas-gap and superconducting heat switches. Finally, a top-level brief introduction to a new technology: the magnetoresistive heat switch was provided.

Different types of ADRs were described, including their operation, including the single ADR, double ADR and continuous ADR. The MSSL ESA ADR was introduced, and shown to be a part-space-qualified engineering model that does not meet its original XEUS design requirements in terms of hold time (24 hour with a 1μW applied heat load) and recycle time (<4 hour). Measured performance shows it currently achieves a 9.5 – 10 hour hold time for a 15 hour recycle time. Previous modelling and early investigations into magnetoresistive heat switch technology indicated the performance may be significantly increased by swapping the Lead superconducting heat switch that connects the two salt pills for a Tungsten magnetoresistive heat switch, and the XEUS design requirements exceeded.

Developmental ADR solutions targeting the IXO XMS were described, including a modified evolution of the MSSL ESA ADR, denoted in this thesis as the MSSL dADR. Also described were the CEA-SBT hybrid ADR/Sorption cooler, and the NASA continuous ADR. The MSSL dADR, as presented, is expected to meet the IXO XMS hold time/recycle time and cooling performance using either a modified superconducting heat switch or achieve increased performance with the slightly less technologically mature magnetoresistive heat switch.

It is clear from the discussions of chapter 3 that the magnetoresistive heat switch is a potential key technology for maximising the hold time/recycle time performance of ADR

systems, especially the MSSL ESA ADR and MSSL IXO dADR. Hence, this technology requires further study.

7.1.4 CHAPTER 4

The theory of magnetoresistivity was introduced in chapter 4, beginning with an explanation of how metals typically transport heat based on simple solid state physics theory; the free electron model and the Debye theory of phonons. It was shown that electrons and phonons of the lattice both contribute to heat conduction, and that scattering against lattice imperfections, impurities and the size of a metal sample affects the form of both the lattice and electronic contributions of thermal conductivity by limiting the mean free path. At liquid Helium temperatures and below, electron conductivity is limited by the size of the sample and scattering off impurities, and phonon conductivity is limited by only the sample size.

A case study of Copper showed that in the liquid Helium temperature regime and below, the contribution of electrons to the thermal conductivity outweighs that of phonons by 4-5 orders of magnitude. Hence, it is clear that if the electronic contribution could be controlled (switched on or off), it would be possible to construct a heat switch with an equivalent switching ratio.

Magnetoresistance was shown to be a phenomenon which potentially has the ability to control the electronic contribution to the thermal conductivity of a metal by causing the conductive electrons to move in helical orbits (in real space), thus effectively slowing the motion along the thermal gradient. The theory of ‘high field’ magnetoresistance was presented, which considers the case of a magnetic field strong enough to force the electrons into orbits with a radius significantly below the length of their mean free path. It was shown that the strongest magnetoresistive effect occurs in those metals which are compensated and have a closed Fermi surface, since compensation removes first

order terms from the magnetoresistive thermal conductivity tensor which act in the x-y plane (assuming the magnetic field is aligned along the z axis, a direction of crystal symmetry) ; and a closed Fermi surface means fewer open and extended electron orbits in reciprocal space (which translate as a sinuous sort of motion in real space – not as 'slowing' as helical orbits which arise from closed reciprocal space orbits).

Based on considerations of the phonon conductivity, superconductivity and toxicity/ease of workability, it was shown that Tungsten was the best choice of metal from which to build a magnetoresistive heat switch. As evidenced from Batdalov and Red'ko's (59) measurements of Tungsten magnetoresistive thermal conductivity, Tungsten can achieve a switching ratio (ratio of thermal conductivity in the normal and magnetoresistive state) of 7.50×10^4 at 4.2K with a ~2 Tesla applied magnetic field.

The form of the magnetoresistive thermal conductivity of Tungsten was determined, according to arguments based on the high field magnetoresistive theory as detailed in Lifshits et al. (77). This provides a basis with which to interpret thermal conductivity measurements of Tungsten samples in a magnetic field.

7.1.5 CHAPTER 5

The development of magnetoresistive technology by experimental investigation was the topic of chapter 5. Thermal conductivity measurements were made for three samples of Tungsten heat switch under a magnetic field of 1.8 Tesla in the range of ~0.3K – 4K. Measurements of thermal conductivity with zero applied magnetic field were also performed at the temperatures achievable with a liquid Helium bath.

It was shown that only sample 1 can be described satisfactorily using high-field magnetoresistive theory due to its high purity (99.999%), and that there is no effective theory for describing the magnetoresistive thermal conductivity of samples 2 (99.992% purity) and 3 (purity inferred to be ≤99.992% by comparison to sample 2). The low purity

of samples 2 and 3 evidently does not permit a sufficiently long electron mean free path for a magnetoresistive electron to complete enough turns between collisions since the mean free path is not small enough in comparison to the electron orbit radius. The results of the thermal conductivity measurements were reviewed against comparable measurements performed by other authors that have investigated the thermal magnetoresistivity of Tungsten.

It was found that both crystal purity and crystal width have an effect on the performance of a Tungsten magnetoresistive heat switch, with purer samples having a more marked magnetoresistive effect and higher 'on' conductivity; and larger samples having higher 'on' conductivity in general, thus resulting in high switching ratios. It was shown that the 'on' state conductivity is limited by crystal width as it is decreased below the electron mean free path of the sample, as is particularly evident from the results of Duval et al (83) with a 0.5mm width sample.

The 'off' state performance (thermal conductivity in a magnetic field) was found to be far worse in a sample of 99.992% (sample 2) in comparison to an otherwise identical 99.999% sample (sample 1); however, similar performance to sample 1 was observed by Canavan et al with a 99.995% pure sample (identical in geometry) (80). This indicates the third decimal point in purity is crucial to heat switch performance, and an optimal heat switch would have purity >99.995% considering only 'off' conductivity, in addition to perhaps a larger cross section/crystal width (as evidenced from Batdalov and Red'kos results with a crystal width of 4.3mm as opposed to sample 1, 2 and Canavan et al's sample that have a crystal width of 1.5mm). Hence, further investigations into purity and crystal width are required to determine the optimal properties for a milliKelvin ADR heat switch by mapping out the exact relationships between size, purity and heat switch performance.

The practical implementation of a Tungsten magnetoresistive heat switch within an ADR system means the high 'on' conductance of such a heat switch will be limited by the conductance at the points of attachment: i.e. where the heat switch interfaces with the ADR structure. This has been assumed to be a bolted, 'pressed contact' joint, as is typical for space cryogenics systems. The contact conductance at ~4K was determined for several types of 'conforming layer' at a constant bolt torque of 60 N cm. It was found that for a Tungsten-gold plated Copper pressed contact (as would be typical for an ADR structure), a layer of 0.13mm thick Indium foil would increase the contact conductance by the order of two orders of magnitude compared to the control case of having no modifications. A factor ~4 increase could be obtained simply by abrasion of the contact surfaces to remove any oxide layers. It is therefore essential to consider at least adding Indium foil into any pressed contact joint configuration to make the most of a magnetoresistive heat switch, and reduce performance limitations as far as possible.

The measured thermal conductivity data of sample 1, together with the measured Tungsten-Copper contact conductance data was used to estimate the effect on the performance of the ESA ADR that would be observed by swapping the Lead superconducting switch with a Tungsten magnetoresistive heat switch. It was shown that a switch with the properties of sample 1, with 15 layers as opposed to 3 (a factor ~5 increase in conductance path length) would increase the 50mK hold time from the current ~9.5 hours to ~36.5 hours. The expected performance of a 15 layer heat switch was compared to preliminary results obtained with a real 15 layer Tungsten heat switch that has recently been installed in the ESA ADR for developmental investigation. Despite offering a marginal performance increase of about half an hour on the 50mK hold time, the improvement was nowhere near the prediction for a sample 1 type sample, suggesting the 15 layer switch in the ESA ADR is of particularly poor purity (it had not been measured prior to installation), certainly not at the 'five nines' (99.999%) level of

sample 1. Hence, a measured 'significant improvement' in ADR performance with a Tungsten magnetoresistive heat switch is yet to be seen, however, the measured sample 1 data does strongly indicate that with a sufficiently pure sample, this will be observed in future investigations.

7.1.6 CHAPTER 6

In order to support the MSSL dADR on IXO, a cooling chain and suitable thermal environment must be engineered. This was the focus of chapter 6.

The proposed IXO cooling chain under development at Astrium, consists of a 2K heat bath for the dADR provided by 2 Helium-3 Joule Thomson coolers under development at RAL. This 2K stage will in turn be cooled by 3 Stirling coolers with dual temperature stages, one at 16K and one at 102K. Additional cooling support comes from a radiator radiating at ~77K, providing an 80K thermal stage for the cooling chain.

The cooling chain is contained within a cryostat (CVV), designed to house thermal enclosures at each temperature stage provided by the cooling chain (except the upper stage of the Stirling coolers which cools only the Joule Thomson cooler heat exchange pipes, harness and current leads). The initial design of this cryostat, in terms of its structure and primarily its suspension system, were produced based on simple thermal and mechanical analyses. The suspension system consists of a system of metal rings, G10 tubes and S-glass straps between the outer body of the CVV and the 80K thermal enclosure, as well as between the 80K and 16K thermal enclosures. The 2K thermal enclosure is then supported by Kevlar strap suspension from the 16K enclosure. The suspension system was designed to have a first resonant mode >40Hz, and the presented design is predicted to have a first mode at 41.6Hz.

In order to support an external radiator as part of the cooling chain, a feedthrough was designed to allow a thermal link (at ~80K) from the radiator to pass through the

cryostat/CVV wall without suffering a high parasitic heat load from the cryostat wall (at ~300K). Thus, the design was based on purely thermal considerations and consisted of an arrangement of nested G10 cylinders and titanium rings at alternate ends. Thus, a long thermal path is achievable for a given feedthrough radius, and MLI can be insterted between the walls of each cylinder to minimise radiative heat transfer. It was shown that there is an optimal cylinder height which trades off the decrease in conductive load and increase in radiative load (with increasing cylinder height). An optimal thermal design of the feedthrough was found to use four cylinders of 3.5cm height with a feedthrough outer radius of 5.6cm. This design is predicted to impart a heat load of 4.31mW onto the 80K thermal link.

Thermal analysis of the cooling chain showed that it is a feasible design, where for each case of the dADR holding and recycling during both warm and cold redundancy schemes the cooling budget and heat flow maps were presented. The duty cycles of the coolers at each stage were shown to be <100% (note for the radiator it was 101%, but this includes considerable margin and conservatism in the calculations) thus providing a strong evidence that the proposed design would support the MSSL dADR onboard IXO.

It is clear that warm redundancy requires significantly less work from the individual coolers at each stage, thus is recommended for nominal operation in order to maximise reliability over the IXO mission lifetime.

7.2 FURTHER DEVELOPMENTS - MAGNETORESISTIVE HEAT SWITCH

7.2.1 HEAT SWITCH PERFORMANCE RESEARCH

Chapter 5 has shown the potential of a magnetoresistive heat switch as a technology for improving the performance of the ESA ADR and the MSSL IXO dADR. Naturally, this can be extended to include that ADRs in general could see a performance increase from a well engineered heat switch.

It was found that purity differences in the range 99.992% - 99.999% has a dramatic effect on magnetoresistance, and whether a sample is in the 'high field' regime or not. Hence, the performance as a heat switch is a strong function of purity. There is also evidence to suggest that small crystal widths lead to worse performance as a heat switch, primarily by limiting the 'on' state conductivity. Thus, the next stage of development of magnetoresistive heat switches should include the testing of samples of varying purity in the range >99.992% but constant crystal width, for several crystal widths. In addition, samples of equal purity but differing crystal widths (in the range 1mm – 5mm) should be tested, for several crystal purities. The results of such an investigation would allow for the performance as a heat switch, and magnetoresistive effect, to be mapped out over the purity – crystal width parameter space in the range of interest to space ADR heat switch designers. This data would then form the basis for the design of an optimised (in terms of thermal performance) Tungsten magnetoresistive heat switch.

The optimised heat switch configurations could then be investigated further by measuring their performance as an actual heat switch by installing them in an ADR, for example, the ESA ADR. This would then allow for the true performance increase gained by using magnetoresistive heat switches to be determined.

7.2.2 Working towards a Space Qualified Magnetoresistive Heat Switch

In its current state of development, the Tungsten magnetoresistive heat switch remains an immature technology and requires extensive development in order to be qualified for space use. The primary concern regarding using this type of heat switch in space is that Tungsten is a relatively brittle material, and is fragile in the small crystal width, long thermal path designs that have been considered thus far. Thus, it is unlikely that this configuration would survive the vibrations induced during launch and ascent of the spacecraft (see chapter 2 - 2.1.4). Hence, upon completion of sufficient thermal performance development, extensive mechanical/structural development should be undertaken. This could include a further step in development where finite element stress analysis could be used to provide input into the design of test heat switches, which could then be vibration and shock tested to ECSS (European Cooperation for Space Standardization) specified qualification levels (as detailed in ESA ECSS document (101)) with accelerometers attached in order to correlate the models. The subsequent design iteration would then use these results to design a magnetoresistive heat switch that could survive the ECSS qualification levels as well as utilising the thermal performance development detailed in 7.2.1.

If it was found that the thermal performance and mechanical requirements must be traded off in favour of the mechanical/structural requirements such that the thermal performance adversely suffers, further development investigation into modifications to the heat switch design could pursue the direction of encapsulating the Tungsten in some kind of low thermal conductivity protective foam, such as aerogel, or some kind of low thermal conductivity resin.

7.3 FURTHER DEVELOPMENTS – IXO COOLING CHAIN

The IXO cooling chain as described in chapter 6 continues its development at Astrium, where future stages of design will include a full structural and thermal analysis by specialist engineers using finite element techniques. In parallel, a simple test bed could be produced as a breadboard 'proof of concept' for the design. Such a test bed could include a small ADR cooled by a 4K Joule Thomson cooler such as the Planck JT cooler. This in turn would be cooled by a single Astrium 10K cooler, utilising its two temperature stages to provide cooling for thermal enclosures similar to the CVV design presented. This would prove that a cryogen-free combination of space cryogenic technology could support the cooling requirements of an ADR.

Whilst passive technology is extremely reliable, it could be difficult to support a radiator providing the 80K thermal environment in practise, despite a suitable feedthrough having been shown possible from purely thermal considerations. A thermal link and feedthrough between the external radiator and 80K shield would require extensive engineering development in order to be implemented on IXO. Hence, this development should begin as early as possible, including investigations into the structural aspects of the feedthrough. In parallel, the cooling chain evolution could be guided to de-scope the need for an 80K radiator as the individual cryogenic cooling technologies advance in their respective development programmes.

7.4 SUMMARY OF CHAPTER 7

Chapter 7 has summarised the highlights of this thesis by each chapter in turn, and presented the conclusions within the context of the thesis as a whole.

It is clear that X-ray astronomy is an extremely insightful tool into studying some of the most extreme environments in space, and allows for an improvement of our understanding of the laws of physics and the universe itself. Space cryogenics is increasingly required as mission developers and space agencies look to improved resolution and sensitivity in their X-ray spectroscopy instruments, in order to obtain more information from their observations. Cryogen-free systems are increasingly required as future missions such as IXO require long (>5 year) service lifetimes. Thus, reliable, space-proven ADRs capable of millikelvin cooling are of extreme importance to the field of space cryogenics, and to the IXO mission.

Development of millikelvin ADR magnetoresistive heat switches allows for potentially dramatic improvements to the performance of ADRs, and can be extended to any cryogenic system operating in the same temperature range (millikelvin - ~4K). Purity and crystal width are the factors that govern performance of Tungsten as a magnetoresistive heat switch, where higher purity means improved performance, and smaller crystal widths reduces performance. Purity of 99.999% or higher is required for the best heat switch performance, combined with a crystal width that is larger than the electron mean free path (~1.5mm[59]). Further work is needed to map out the parameter space of purity and mean free path to determine the exact relationship of these properties to heat switch performance, and hence design an optimal heat switch. In addition, further considerations are required for qualifying a magnetoresistive heat switch for space use, particularly regarding shock/vibration aspects.

An IXO cooling chain to support the MSSL IXO dADR has been designed at Astrium and the analysis of the thermal and mechanical performance has been presented. It has been shown that the structural suspension design meets the resonant mode criteria, and that the thermal design can support the MSSL dADR as well as the complete cooling chain for all cases considered: ADR holding and recycling for both warm and cold redundancy of the Stirling coolers. Warm redundancy is recommended as the nominal cooling chain operational mode due to the significantly lower stresses experienced by the coolers at each stage in the chain. Further analysis and design work will continue at Astrium to develop the cooling chain into a real functional system.

REFERENCES

1. **The University of Cambridge.** Cambridge X-ray Astronomy. *University of Cambridge Institute of Astronomy.* [Online] [Cited: 27 September 2011.] http://www-xray.ast.cam.ac.uk.

2. *Nobel Lecture: The dawn of x-ray astronomy.* **Giacconi, R.** 3, July 2003, REVIEWS OF MODERN PHYSICS, Vol. 75.

3. **NASA Goddard Space Flight Center.** The Einstein Observatory - HEAO-2. *NASA's HEASARC: Observatories.* [Online] [Cited: 27 September 2011.] http://heasarc.gsfc.nasa.gov/docs/einstein/heao2.html.

4. *X-ray Astronomy Missions.* **Bradt, H. V. D., Ohashi, T., and Pounds, K. A.** 1992, Annual Reviews of Astronomy and Astrophysics, Vol. 30, pp. 391-427.

5. **NASA Goddard Space Flight Center.** Comparison of future and present X-ray missions. *NASA's HEASARC: Observatories.* [Online] [Cited: 27 September 2011.] http://heasarc.nasa.gov/docs/heasarc/missions/comparison.html.

6. **ESA.** IXO Mission Home. *ESA Cosmic Vision .* [Online] [Cited: 14 January 2011.]

7. —. *IXO Revealing the physics of the hot universe: Assessment Study Report.* s.l. : European Space Agency, 2011. ESA/SRE(2011)2.

8. *IXO Payload Definition Document.* **ESA, SRE-PA.** 6, s.l. : SRE-PA, 2009. SRE-PA/2009.019/.

9. *Compton Thick AGN: the dark side of the X-ray background.* **Comastri, A.** Bologna : arXiv, 2004. astro-ph/0403693v1.

10. **Massachussets Institute of Technology (MIT).** Transition Edge Sensors. *MIT Figueroa Group Experimental Cosmology and Astrophysics Laboratory.* [Online] http://web.mit.edu/figueroagroup/ucal/ucal_tes/index.html.

11. **National Institute of Standards and Technology.** About Cryogenics. *NIST Cryogenics Technologies Group.* [Online] http://cryogenics.nist.gov/AboutCryogenics/about%20cryogenics.htm.

12. *A matter of degrees: a brief history of cryogenics.* **Scurlock, R. G.** s.l. : Butterworth-Heinemann Ltd., 1990, Cryogenics, Vol. 30, pp. 483-500.

13. *Cryogenic Cooling Systems in Space.* **Jewell, C. I.** Nordwijk, the Netherlands : ESTEC, 1996. Proceedings of the 30th ESLAB Symposium, "Submillimetre and Far-Infrared Space Instrumentation". pp. 24-26. ESA SP-388.

14. *Cryogenics in space: a review of the missions and of the technologies.* **Collaudin, B., Rando, N.** s.l. : Elsevier, 2000, Cryogenics, Vol. 40, pp. 797-819.

15. **Emes, M. R.** *The Development of a 10mK Refrigeration System for Space (PhD Thesis).* London : University of London, 2000.

16. **ESA.** L2 Orbit of JWST. *ESA Hubble telescope website.* [Online] March 2011. http://www.spacetelescope.org/images/L2_rendering/.

17. **Evans, S. W.** *Natural Environment near the Sun/Earth-Moon L2 Libration Point - Prepared for the NEXT GENERATION SPACE TELESCOPE PROGRAM.* Marshall Space Flight Center. s.l. : NASA. Available at http://snap.lbl.gov/pub/bscw.cgi/d84104/SNAP-TECH-03009.pdf.

18. **Henderson, R. A.** *Spacecraft Systems Engineering.* [ed.] Fortescue P. and Stark J. Second Edition. s.l. : Wiley, 1995.

19. **Arianespace.** Ariane 5 Overview. *Arianespace web site.* [Online] http://www.arianespace.com/launch-services-ariane5/ariane-5-intro.asp.

20. —. *Ariane 5 User's Manual (issue 5).* 2008. Downloadable from Arianespace website.

21. **Lakeshore Cryotronics.** *Lakeshore Cryotronics home.* [Online] http://www.lakeshore.com/pdf_files/Appendices/LSTC_appendixI_l.pdf.

22. **Bowley, R. And Sanchez, M.** *Introductory Statistical Mechanics.* 2nd Edition. Oxford : Oxford Clarendon Press, 1999.

23. **Helsinki University of Technology.** Helium. *Low Temperature Laboratory - Helsinki University of Technology.* [Online] August 2003. http://ltl.tkk.fi/research/theory/helium.html.

24. **Kono, Kimitoshi.** Using superfluid helium-3 to explore new phenomena. *RIKEN research.* [Online] 15 May 2009. Volume 4, Issue 5. http://www.rikenresearch.riken.jp/eng/frontline/5848.

25. **Steijaert, P.** *Thermodynamical aspects of pulse-tube refrigerators.* Eindhoven : Technische Universiteit Eindhoven, 1999. PhD Thesis. ISBN: 90-386-0827-6.

26. *Demonstration of a 10K Stirling Cooler for Space Applications.* **Baker, G.R., Feger, D., Gibson, A. S., Little, A., Bradshaw, T. W., Crook, M. R., Orlowska, A. H., Tomlinson, B. J., Sargeant, A.** s.l. : ESA, 2001. Proceedings of the 9th European Space Mechanisms and Tribology Symposium. pp. 165-170. ISBN: 92-9092-761-5.

27. **The University of Oxford.** Cryogenic Engineering Group | Research - Cryocoolers for space applications. *University of Oxford Cryogenic Engineering Group.* [Online] April 2007. http://www.eng.ox.ac.uk/cryogenics/spacecoolers.html.

28. *Heritage Overview: 20 Years of Commercial Production of Cryocoolers for Space.* **Gibson, A. S., Reed, J., Bradshaw, T. W., Linder, M.** 2008. ADVANCES IN CRYOGENIC

ENGINEERING: Transactions of the Cryogenic Engineering Conference - CEC. Vol. Vol. 53. AIP Conference Proceedings, pp. 493-505.

29. *Pulse Tube Cryocoolers for Cooling Infrared Sensors.* **Radebough, R.** 2000. Proceedings of SPIE, The International Society for Optical Engineering, Infrared Technology and Applications XXVI. Vol. 4130, pp. 363-379.

30. *Low temperature expansion pulse tubes.* **Mikulin, E. I., Tarasov, A. A. and Shkrebyonock, M. P.** New York : Plenum press, 1984, Advances in Cryogenic Engineering, Vol. 29, pp. 629-637.

31. *Development of the Pulse Tube Refrigerator as an Efficient and Reliable Cryocooler.* **Radeborough, R.** London : s.n., 2000, Proc. Institute of Refrigeration, pp. 11-29.

32. *An Overview of NASA Space Cryocooler Programs—2006.* **Ross, R. G., Boyle, R. F.** s.l. : International Cryocooler Conference, 2007. Proceedings of the International Cryocooler Conference.

33. *Status of Air Liquide Space Pulse Tube Cryocoolers.* **Trollier, T., Tanchon, J., Buquet, J., Ravex, A.** [ed.] S.G., Ross, R. G. Miller. s.l. : International Cryocooler Conference, 2009. Cryocoolers 15. pp. 115-123.

34. *Helium 3 Joule-Thomson inversion curve.* **Maytal, B. Z.** s.l. : Elsevier Science Limited, 1996, Cryogenics, Vol. 36, pp. 271-274. 0011-2275/96/.

35. **Atkins, P. and de Paula, J.** *Physical Chemistry.* 8th Edition. Oxford : Oxford University Press, 2006. ISBN 9780198700722.

36. *Joule-Thomson cryocooler for space applications.* **Levenduski, R. and Scarlotti, R.** s.l. : Elsevier Science Limited, 1996, Cryogenics, Vol. 36, pp. 859-866.

37. *Technology developments on the 4 K cooling system for 'Planck' and FIRST.* **Bradshaw, T. W., Orlowska, A. H.** Noordwijk : ESA, 1997. Sixth European Symposium on Space Environmental Control Systems. p. 465. SP-400.

38. **Donabedian, M.** *Spacecraft Thermal Control Handbook: Volume 2.* 2nd Edition. s.l. : AIAA (American Institute of Aeronautics & Astronautics), 2003. Vol. 2.

39. *50 mK cooling solution with an ADR precooled by a sorption cooler.* **Luchier, N., Duval, J.M., Duband, L., Camus, P., Donnier-Valentin, G., Linder, M.** s.l. : Elsevier Science Limited, 2010, Cryogenics, Vol. 50, pp. 591-596.

40. *Dilution refrigerator technology.* **Radebaugh, R. and Siegwarth, J. D.** s.l. : Elsevier, 1971, Cryogenics, pp. 368-384.

41. *A DILUTION REFRIGERATOR INSENSITIVE TO GRAVITY.* **Benoit, A., and Pujol, S.** 169, s.l. : North Holland, 1991, Physica B, pp. 457-458.

42. *Dilution refrigerator for space applications with a cryocooler.* **Benoit, A. and Pujol, S.** 5, s.l. : Elsevier, 1994, Cryogenics, Vol. 34, pp. 421-423.

43. *Successful Qualification of the First PFM Space Dilution Refrigerator.* **Triqueneaux, S., Delmas, J., Camus, P., Guyot, G.** [ed.] S. D. and Ross, R. G. Miller. s.l. : International Cryocooler Conference, 2007. Cryocoolers 14. pp. 535-538.

44. *A closed cycle 3He–4He dilution refrigerator insensitive to gravity.* **Martin, F., Vermeulen, G., Camus, P., Benoit, A.** s.l. : Elsevier, 2010, Cryogenics, Vol. 50, pp. 623-627.

45. **Sato, K. and Hisano, J.** *Energy Budget in the high energy universe.* s.l. : World Scientific Publishing, 2007. ISBN 10: 981-270-010-2.

46. **Hudson, R. P.** *Principles and Applications of Magnetic Cooling.* Amsterdam : North Holland Press, 1972. Vol. 2. ISBN: 0-7204-1257-9.

47. **White, G. K.** *Experimental Techniques in Low-temperature Physics.* 3rd Edition. New York : Oxford University Press, 1989.

48. **Hepburn, I. D. and Smith, A.** Magnetic Refrigeration. [ed.] J. G. Webster. *Wiley Encyclopaedia of Electrical and Electronics Engineering.* s.l. : John Wiley and Sons, Inc., 1999, Vol. 12, pp. 91-96.

49. *Superconducting aluminium heat switch and plated press-contacts for use at ultralow temperatures.* **Mueller, R. M., Buchal, C., Oversluizen, T., and Pobell, F.** 4, 1978, Rev. Sci. Instrum., Vol. 49, pp. 515-518.

50. **Lounasmaa, O. V.** *Experimental Principles and Methods below 1K.* London : Academic Press, 1975.

51. *Passive Gas-Gap Heat Switches for use in Adiabatic Demagnetisation refrigerators.* **Shirron, P., Canavan, E., DiPirro, M., Jackson, M., Panek, J., and Tuttle, J.,.** 2002. Advances in Cryogenic Engineering: Proceedings of the Cryogenic Engineering Conference. Vol. 47, pp. 1175-1182.

52. **Lee, P. J.** *Engineering Superconductivity.* New York : John Wiley & Sons, 2001.

53. *Development of a Cryogen-free continuous ADR for the Constellation-X mission.* **Shirron, P., Canavan, E., DiPirro, M., Francis, J., Jackson, M., Tuttle, J., King, T., and Grabowski, M.** 2004, Cryogenics, Vol. 44, pp. 581-588.

54. *Design of a continuous ADR for the ESA mission XEUS/IXO based on the ESA engineering model ADR.* **Bartlett, J., and Hepburn, I. D.** s.l. : Twenty-First International Cryogenic Engineering Conference, 2006. CryoPrague 2006: Proceedings of ICEC 21. Vol. 1, pp. 347-350.

55. **Bartlett, J. S.** *Design of a 50mK Continuous Adiabatic Demagnetisation Refrigerator for future space missions.* London : The University of London, 2008. PhD Thesis.

56. *Improved performance of an engineering model cryogen free double adiabatic demagnetization refrigerator.* **Bartlett, J., Hardy, G., Hepburn, I.D., Brockley-Blatt, C.,**

Coker, P., Crofts, E., Winter, B., Milward, S., Stafford-Allen, R., Brownhill, M., Reed, J., Linder, M., and Rando, N. s.l. : Elsevier, 2010, Cryogenics, Vol. 50, pp. 582-590.

57. *Design and Development of a Space Engineering Model Cryogen Free ADR for Future ESA Space Missions.* **Hepburn, I. D., Brockley-Blatt, C., Coker, P., Crofts, E., Winter, B., Hardy, G., Milward, S., Stafford-Allen, R., Brownhill, M., Reed, J., Rando, N., and Linder, M.,.** s.l. : Twenty-First International Cryogenic Engineering Conference, 2006. CryoPrague 2006: Proceedings of ICEC 21. Vol. 1, pp. 323-326.

58. *A thermal switch for use at liquid helium temperature in space-borne cryogenic systems.* **Duband, L.** Vail (CO, USA) : Plenum Press, 1995. Proceedings of the 8th international cryocooler conference. pp. 731–741.

59. *Lattice and electronic thermal conductivities of pure tungsten at low temperature.* **Batdalov, A. B., and Red'Ko, N.** 1980, Sov. Phys. Solid State, Vol. 22 , pp. 664-666.

60. *The Suzaku High Resolution X-Ray Spectrometer.* **Kelley, R. L., Mitsuda, K., Allen, C. A., Arsenovic, P., Audley, M. D., Bialas, T. G., Boyce, K. R., Boyle, R. F., Breon, S. R., Brown, G. V., Cottam, J., Dipirro, M. J., Fujimoto, R., Furusho, T.,Gendreau, K. C., Gochar, G. G., Gonzalez, O. et al.** 2007, Publications of the Astronomical Society of Japan, Vol. 59, pp. 77-112. SP1.

61. *Cooling system for the soft X-ray spectrometer onboard Astro-H.* **Ryuichi Fujimoto, Kazuhisa Mitsuda, Noriko Yamasaki, Yoh Takei, Masahiro Tsujimoto, Hiroyuki Sugita, Yoichi Sato, Keisuke Shinozaki, Takaya Ohashi, Yoshitaka Ishisaki, Yuichiro Ezoe, Masahide Murakami, Shunji Kitamoto, Hiroshi Murakami, et al.** s.l. : Elsevier, 2010, Cryogenics, Vol. 50, pp. 488-493.

62. **ESA.** *REQUIREMENTS FOR THE COOLING CHAIN FOR THE XMS ON IXO.* ESTEC. s.l. : ESA, 2009. TN. Issue 1 Revision 1. SRE-PA/2009.022/.

63. **Hepburn, I. D.** *IXO Assessment Study: ADR.* MSSL , UCL. 2010. TN. MSSL/IXO-AS-ADR/TN001.01 .

64. **ESA.** *IXO Payload Definition Document.* ESA SRE/PA. s.l. : ESA, 2009. TN. Issue 6 Revision 1. SRE-PA/2009.019/.

65. *ADR design for the Soft X-ray Spectrometer instrument on the Astro-H mission.* **Shirron, P., Kimball, M., Wegel, D., Miller, F.** 9, 2010, Cryogenics, Vol. 50, pp. 494-499.

66. *Electrical and thermal magnetoconductivities of single-crystal beryllium at low temperatures and its use as a heat switch.* **Radebaugh, R.** 1977, J Low Temp Phys , Vol. 27, pp. 91–105.

67. **Grant, I. S. and Phillips, W. S.** *The elements of physics.* Oxford : Oxford University Press, 2001.

68. **Kittel, C.** *Introduction to Solid State Physics.* 7th edition. New York : John Wiley and sons, 1996.

69. **Ziman, J. M.** *Electrons and Phonons – The theory of transport phenomena in solids.* Oxford : Oxford University Press, 1960.

70. *Lattice conductivity, Lorenz numbers, and Nernst-Ettingshausen effect in tungsten at liquid – helium temperatures.* **Long, J. R.** 8, 1971, Phys. Rev. B. , Vol. 3, pp. 2476–2484.

71. *Lattice thermal conductivity and high-field electrical and thermal magnetoconductivities of tungsten.* **Wagner, D. K.** 2, 1972, Phys. Rev. B., Vol. 5, pp. 336–347.

72. *Resistance Minimum in Dilute Magnetic Alloys.* **Kondo, J.** 1, 1964, Progress of Theoretical Physics, Vol. 32, pp. 37-49.

73. *The Size-Variation of Resistivity for Mercury and Tin.* **Andrew, E. R.** 1949, Proc. Phys. Soc. A, Vol. 77, p. 62.

74. **Laby, Kaye and.** Acoustics: The speed and attenuation of sound. *Kaye and Laby online tables of physical and chemical constants.* [Online] http://www.kayelaby.npl.co.uk/general_physics/2_4/2_4_1.html.

75. **Ashcroft, N. W. and Mermin, N. D.** *Solid State Physics.* s.l. : Saunders, 1976.

76. **Joseph, G. and Kundig, K. J. A.** *Copper: its trade, manufacture, use, and environmental status.* [ed.] K. J. A. Kundig. s.l. : ASM International, 1999. ISBN: 0871706563.

77. **Lifshits, I. M., Azbel', M. Ya., Kaganov, M. I.** *Electron theory of metals.* New York : New York: Consultant's Bureau (A Division of Plenum Publishing Corporation), 1973.

78. **Pippard, A. B.** *Magnetoresistance in metals (Cambridge studies in low temperature physics).* Cambridge : Cambridge University Press, 1989.

79. *Thermal Conductivity and Thermoelectric phenomena in Metals in a Magnetic Field.* **Azbel, M. Ia., Kaganov, M. I., and Lifshitz, I. M.** 5, December 1957, Soviet Physics JETP, Vol. 5, pp. 967-970.

80. *A Magnetoresistive Heat Switch for the Continuous ADR.* **Canavan, E. R., Dipirro, M. J., Jackson, M., Panek, J., Shirron, P. J., Tuttle, J. G.** 2002. Advances in cryogenic engineering: proceedings of the cryogenic engineering conference. Vol. 47, pp. 1183-1190.

81. *Magnetoresistance of gallium – a practical heat switch at liquid helium temperatures.* **Engels, J. M. L., Gorter, F. W., Miedema, A. R.** 2, 1972, Cryogenics, Vol. 12, pp. 141–145.

82. *A cadmium heat switch.* **Laudy, J. and Knol.** 6, 1966, Cryogenics, Vol. 6, pp. 370-371.

83. *Magnetoresistive heat switches and compact superconducting magnets for a miniature adiabatic demagnetization refrigerator.* **Duval, J. M., Cain, B. M., Timbie, P. T.**

New York : Springer Science+Business Media, Inc, 2004, Cryocoolers, Vol. 13, pp. 567-573.

84. *Thermal and electrical transport in a tungsten crystal for strong magnetic fields and low temperatures.* **Long, J. R.** 4, 1971, Phys. Rev. B., Vol. 3, pp. 1197-1205.

85. *Low-temperature electrical and thermal resistivities of tungsten.* **Wagner, D. K., Garland, J.C., Bowers, R.** 10, 1971, Phys. Rev. B. , Vol. 3, pp. 3141-3149.

86. *Anisotropy of the Electronic Work Function of Metals.* **Smoluchowski, R.** 9, 1941, Phys. Rev., Vol. 60, pp. 661-674.

87. *Thermal expansion of some diamondlike crystals .* **Slack, G. A., Bartram, S. F.** 1, 1975, Journal of Applied Physics , Vol. 46, pp. 89-98.

88. **Salerno, L. J. and Kittel, P.** *Thermal Contact Conductance.* AMES Research Center, NASA. s.l. : NASA, 1997. Nasa Technical Memorandum 110429.

89. *PERFORMANCE CHARACTERIZATION OF THE ASTRIUM 10K DEVELOPMENTAL CRYOCOOLER.* **Bruninghaus, C. H. Y., Kallman, J. P., Tomlinson, B. J. Jr., Myrick, E.** [ed.] S. Breon. s.l. : American Institute of Physics, 2002. CP613, Advances in Cryogenic Engineering: Proceedings of the Cryogenic Engineering Conference. Vol. 47. 0-7354-0059-8.

90. **ESA.** The 4 K cooler on the Planck spacecraft. *ESA Science and technology.* [Online] 2009. [Cited:] http://sci.esa.int/science-e/www/object/index.cfm?fobjectid=45516.

91. **Bradshaw, T.** Compact Space Coolers. *Presentation for the Technology Transfer Showcase.* 17 May 2011. A presentation prepared by the leader of the Planck 4K development team..

92. **Astrium UK.** Technical note. Proprietary Astrium Document. TNO-MAX-AST-0007-02.

93. *On the Joule-Thomson integral inversion curves of quantum gases.* **Maytal, B. Z. and Shavit, A.** 1997, Cryogenics, Vol. 37, pp. 33-38.

94. **Bradshaw, T.** 2010. Private Communication with lead developer of 2K JT cooler.

95. **Duband, L.** ESA TRP cooler. s.l. : CEA-SBT. Proprietary CEA-SBT technical note..

96. Multi-Layer Insulation (MLI). *Thermalengineer.com.* [Online] http://www.thermalengineer.com/library/effective_emittance.htm.

97. **Astrium.** *Evaluation of Calorimeter Tests for Herschel Internal MLI.* 2004. Astrium Proprietary document. HP-2-ASED-TN-0083.

98. **ESA.** *Proprietary document detailing IXO XMS detector package.* 2010.

99. **Reed, J.** Proprietory Astrium internal document. Original source unknown to this author..

100. **Young, W. C., and Budynas, R. G.** *Roark's Formulas for Stress and Strain.* 7th Edition. s.l. : McGraw-Hil, 2002. (Table 8.1, Case 1b, section 9.2).

101. **ESA-ESTEC.** *Space engineering: Testing .* Noordwijk : ESA (ECSS - European Cooperation for Space Standardization), 2002. Available at http://www.ecss.nl/. ECSS-E-10-03A.

102. *Bound Electron Pairs in a Degenerate Fermi Gas.* **Cooper, L. N.** 4, 1956, Phys. Rev., Vol. 104, pp. 1189-1190.

103. *Theory of Superconductivity.* **Bardeen, J., Cooper, L. N., Schrieffer, J. R.** 5, 1957, Phys. Rev., Vol. 108, pp. 1175-1204.

104. *Microscopic Theory of Superconductivity.* **Bardeen, J., Cooper, L. N., Schrieffer, J. R.** 1, 1957, Phys. Rev., Vol. 106, pp. 162-164.